

**MODELING FRICTION PHENOMENA AND ELASTOMERIC
DAMPERS IN MULTIBODY DYNAMICS ANALYSIS**

A Thesis
Presented to
The Academic Faculty

by

Changkuan Ju

In Partial Fulfillment
of the Requirements for the Degree
Doctor of Philosophy in the
School of Aerospace Engineering

Georgia Institute of Technology
December 2009

**MODELING FRICTION PHENOMENA AND ELASTOMERIC
DAMPERS IN MULTIBODY DYNAMICS ANALYSIS**

Approved by:

Dr. Olivier A. Bauchau,
Committee Chair
School of Aerospace Engineering
Georgia Institute of Technology

Dr. Olivier A. Bauchau, Advisor
School of Aerospace Engineering
Georgia Institute of Technology

Dr. Dewey H. Hodges
School of Aerospace Engineering
Georgia Institute of Technology

Dr. Massimo Ruzzene
School of Aerospace Engineering
Georgia Institute of Technology

Dr. Andrew Makeev
School of Aerospace Engineering
Georgia Institute of Technology

Dr. Serkan Ozbay
Materials Technologies Corporation

Date Approved: August 18th 2009

ACKNOWLEDGEMENTS

First of all, I would like to express my deep appreciation to Dr. Olivier A. Bauchau, my thesis advisor, for his guidance, suggestions, and encouragement which made possible the successful completion of this dissertation.

I would also like to express my sincere gratitude to my thesis committee members: Drs. Dewey H. Hodges, Massimo Ruzzene, Andrew Makeev, and Serkan Ozbay for their time to serve on my thesis committee and providing valuable suggestions to improve the thesis.

Thanks are also extended to my friends in the School of Aerospace Engineering. Among them are Huimin Song, Dr. Haiying Liu, Dr. Jielong Wang, Dr. Jimmy Ho, Dr. Wei-en Li, Dr. Leihong Li, and Reema Kundu.

Finally, I would like to express my thanks to my wife Xiaoou, for her love and support, and to my son Ziting, for the happiness he brings to me.

The first part of this research work was supported by the Air Force Office of Scientific Research and the second part was sponsored by the National Aeronautics and Space Administration. Their supports are gratefully acknowledged.

Contents

ACKNOWLEDGEMENTS	iii
LIST OF TABLES	ix
LIST OF FIGURES	x
SUMMARY	xv
I INTRODUCTION TO FRICTION PHENOMENA IN MULTIBODY DYNAMICS	1
II KINEMATIC DESCRIPTION OF JOINTS WITH CLEARANCE	4
2.1 Two-Dimensional Case: Planar Clearance Joint	4
2.1.1 Kinematic description	4
2.1.2 Normal contact force	6
2.1.3 Friction force	7
2.2 Three-Dimensional Case: Spatial Clearance Joint	8
2.2.1 Kinematic description	8
2.2.2 Normal contact force	11
2.2.3 Friction force	12
III UNILATERAL CONTACT CONDITIONS	15
3.1 Modeling Unilateral Contact Conditions	15
3.2 Time Step Size Adaptation Procedure	17
IV MODELING FRICTION PHENOMENA	18
4.1 Introduction to Frictional Process	18
4.2 LuGre Friction Model	20
4.2.1 LuGre friction model and its discretization	20
4.2.2 Properties of the proposed discretization	23
4.3 Time Step Size Adaptation Procedure	24
V NUMERICAL EXAMPLES AND CONCLUSIONS	26
5.1 Numerical Examples	26
5.1.1 Spatial mechanism	26
5.1.2 Supercritical rotor	30

5.2	Conclusions	32
VI	INTRODUCTION TO MODELING ELASTOMERIC DAMPERS	35
6.1	Introduction to Behavior of Elastomeric Materials	35
6.2	Motivation	37
6.3	Modeling Approaches of Elastomeric Dampers	38
6.3.1	Device models and first-principles-based models	39
6.3.2	Advantages and disadvantages of the models	39
6.4	Road Map	42
VII	FINITE ELEMENT IMPLEMENTATION	48
7.1	Finite Element Formulation	48
7.1.1	Definition of elastic forces	48
7.1.2	Definition of inertial forces	52
7.1.3	Definition of dissipative forces	53
7.2	Constitutive Law for Hyperelasticity of Elastomeric Materials	54
7.2.1	Strain energy density function	55
7.2.2	The second Piola-Kirchhoff stress tensor	56
7.2.3	Stiffness tensor	57
7.3	Constitutive Law for Inelasticity of Elastomeric Materials	58
VIII	VALIDATION OF THE FINITE ELEMENT IMPLEMENTATION	60
8.1	Static Analysis Validation	60
8.1.1	Cantilever beam	60
8.1.2	Simple elastomeric damper	62
8.2	Dynamic Analysis Validation	63
8.2.1	Eigenvalue analysis	63
8.2.2	Dynamic simulations	66
8.3	Energy Dissipation Validation	68
IX	INTEGRATION OF ELASTOMERIC DAMPERS WITH MULTIBODY DYNAMICS ANALYSIS	70
9.1	Characteristics of the Simple Elastomeric Damper	70
9.1.1	Hysteresis plots	70

	9.1.2 Dual frequency effect	72
	9.2 Integration of Elastomeric Dampers with Multibody Dynamics Analysis .	74
	9.3 Summary	78
X	MODELING HYPERELASTICITY OF ELASTOMERIC MATERIALS . . .	79
	10.1 Introduction	79
	10.2 Invariant-Based Continuum Mechanics Models	80
	10.2.1 Neo-Hookean model	81
	10.2.2 Mooney-Rivlin model	81
	10.2.3 Yeoh model	82
	10.2.4 Biderman model	82
	10.2.5 Haines-Wilson model	82
	10.2.6 Rivlin-Saunders model	83
	10.2.7 Gent-Thomas model	83
	10.2.8 Hart-Smith model	83
	10.2.9 Gent model	84
	10.2.10 Yeoh-Fleming model	85
	10.3 Stretch-Based Continuum Mechanics Models	85
	10.3.1 Valanis-Landel model	85
	10.3.2 Ogden model	85
	10.3.3 Hencky's model	86
	10.4 Statistical Mechanics Models	87
	10.4.1 Three-chain model	88
	10.4.2 Arruda-Boyce model	88
	10.4.3 Constrained junctions model	89
	10.4.4 van der Waals model	90
	10.4.5 Tube model	91
	10.5 Modeling Compressibility	92
	10.6 Summary	93
XI	MODELING INELASTICITY OF ELASTOMERIC MATERIALS	95
	11.1 Introduction	95

11.2	Internal Variables Based Models	96
11.2.1	Multiplicative decomposition of deformation gradient	98
11.2.2	Stress convolution models	108
11.2.3	Anelastic displacement fields model	111
11.3	Fractional Calculus Based Models	112
11.4	Micromechanics Based Models	114
11.5	Summary	116
XII	EVALUATIONS ON ELASTOMERIC MATERIAL MODELS AND MATERIAL PARAMETERS IDENTIFICATION	118
12.1	Simple Shear Deformation	118
12.1.1	Deformation gradient tensor	119
12.1.2	Stress tensors	121
12.2	Haupt-Sedlan Model	122
12.2.1	Constitutive equations for H-S model	123
12.2.2	Characteristics of the structural variable q	125
12.2.3	Storage and loss moduli: response of H-S model under harmonic strain	130
12.2.4	Response of H-S model under relaxation test	140
12.2.5	Identification of material parameters from experimental data	146
12.2.6	Numerical simulations	156
12.2.7	Summary on the evaluations of H-S model	168
12.3	Höfer-Lion Model	172
12.3.1	Constitutive equations for H-L model	172
12.3.2	Storage and loss moduli: response of H-L model under harmonic strain	174
12.3.3	Response of α -0 model under relaxation test	177
12.3.4	Numerical simulations	179
12.3.5	Summary on the evaluations of H-L model	184
12.4	Summary	185
XIII	CONCLUSIONS AND FUTURE WORK	187
13.1	Conclusions	187
13.2	Future work	188

Appendix A	STRAIN MEASURES IN A NONLINEAR CONTINUUM	191
A.1	Kinematics of the Problem	191
A.2	Displacement Field	194
A.3	Strain Measures	194
A.4	Decomposition of Deformation Gradient Tensor	198
A.5	Principal Stretches	201
Appendix B	STRESS MEASURES IN A CONTINUUM MEDIUM	202
B.1	Stress Vector per Unit Area of Deformed Configuration	202
B.2	Cauchy stress tensor	204
B.3	Stress Vector per Unit Area of Reference Configuration	206
B.4	The 1st Piola-Kirchhoff stress tensor	209
B.5	The 2nd Piola-Kirchhoff stress tensor	211
B.6	Relationship Between Cauchy and Piola-Kirchhoff stress tensors	212
Appendix C	GOVERNING EQUATIONS OF FINITE DEFORMATION ELASTIC- ITY	215
C.1	Equations of Equilibrium	215
C.2	Principle of Virtual Work	218
Appendix D	CONSTITUTIVE LAWS FOR A NONLINEAR CONTINUUM	221
D.1	Introduction	221
D.2	Strain Energy Density Function	221
D.3	Linear Elastic Anisotropic Material	222
D.4	Linear Elastic Isotropic Material	223
D.5	Nonlinear Elastic, Isotropic, Incompressible Materials	224
REFERENCES	226

List of Tables

1	Parameters for LuGre friction model	26
2	Sectional properties of spatial mechanism	27
3	Sectional properties of flexible shaft	30
4	Properties of elastic beam	61
5	Properties of hyperelastic beam	61
6	Eigenvalues for elastic cantilever beam [Hz]	65
7	Eigenvalues for hyperelastic cantilever beam [Hz]	65
8	Eigenvalues for simple elastomeric damper [Hz]	66
9	Properties of elastomeric material	71
10	Assumed and identified material parameters	147
11	Stresses [kPa] at $t = 0$ sec to $t = 4\Delta t$	147
12	Sampling times t [sec] and corresponding stresses τ [kPa] after t_0	148
13	Stresses at $t \rightarrow \infty$ [kPa]	148
14	Pseudo-experimental storage modulus G' [kPa]	148
15	Pseudo-experimental loss modulus G'' [kPa]	149
16	Identified elastic and plastic parameters	151
17	Computed elastic stress τ_e [kPa] and plastic stress τ_p [kPa] after t_0	155
18	Over-stresses τ_v [kPa] at sampling times t [sec]	156
19	Storage and loss moduli [kPa]: 200-period simulation for each amplitude	163
20	Storage and loss moduli [kPa]: 10-period simulation for each amplitude	163
21	Assumed material parameters for H-L model	180

List of Figures

1	Configuration of the planar clearance joint.	5
2	Configuration of the spatial clearance joint.	9
3	Relative distance between the candidate contact points.	10
4	Model of a journal bearing using two spatial clearance joints.	14
5	Penetration of contacting deformable bodies.	16
6	Friction coefficient for Coulombs friction law (solid line), and the continuous friction law (dashed line). $\mu_k = 1.0$	19
7	Configuration of the spatial mechanism.	27
8	Relative tangential velocity at the spherical joint for <i>case 2</i>	28
9	Friction force at the spherical joint for <i>case 2</i>	28
10	Beam root forces at point O : F_2 : \diamond , F_3 : \circ . (Solid line: <i>case 2</i> ; dashed line: <i>case 1</i>	29
11	Axial forces at mid-span of link. (Solid line: <i>case 2</i> ; dashed line: <i>case 1</i>	29
12	Time step size used in the simulation for <i>case 2</i>	30
13	Configuration of the supercritical rotor system.	31
14	Time history of the angular velocity of the shaft. The dashed lines indicate the unstable zone of operation: $\Omega \in [44.069, 44.453]$ rad/sec.	31
15	Trajectory of the shaft mid-span point M . (Solid line: $0 < t < 0.875$ sec; dashed line: $0.875 < t < 1.065$ sec; dashed-dotted line: $1.065 < t < 1.340$ sec; dotted line: $1.340 < t < 1.650$ sec.)	32
16	Time history of normal contact force of the spatial clearance joint at point T	33
17	Time history of root bending moments in the shaft at point R . (Solid line: M_2 ; dashed line: M_3 .)	33
18	One-dimensional rheological model featuring elastic, viscous and plastic components.	44
19	Coupling the first-principles-based elastomeric model with multibody systems.	46
20	Geometry of cantilever beam.	60
21	Elastic cantilever beam with tip load $F = 4 \times 10^5$ N. Left: transverse deflection; right: discrepancy between DYMORE: ED2 and ABAQUS.	61
22	Hyperelastic cantilever beam with tip load $F = 10$ N. Left: transverse deflection; right: discrepancy between DYMORE: ED2 and ABAQUS.	62

23	Hyperelastic cantilever beam with tip load $F = 50$ N. Left: transverse deflection; right: discrepancy between DYMORE: ED2 and ABAQUS.	62
24	Simple elastomeric damper model.	63
25	Simple elastomeric damper. Left: deformed top surface; right: discrepancy between DYMORE: ED2 and ABAQUS.	64
26	Simple elastomeric damper. Left: deformed middle surface; right: discrepancy between DYMORE: ED2 and ABAQUS.	64
27	Simple elastomeric damper. Left: deformed bottom surface; right: discrepancy between DYMORE: ED2 and ABAQUS.	64
28	Tip displacement history of elastic cantilever beam. Left: $F = 10 \sin(100\pi t)$ N; right: $F = 4 \times 10^5 \sin(20\pi t)$ N.	67
29	Tip displacement history of hyperelastic cantilever beam. Left: $F = 200 \sin(\pi t)$ N; right: $F = 20 \sin(4\pi t)$ N.	67
30	Displacement history of simple elastomeric damper for $F = 10^4 \sin(10\pi t)$ N. Left: upper-right corner; right: lower-right corner.	67
31	Displacement history of simple elastomeric damper for $F = 10^4 \sin(200\pi t)$ N. Left: upper-right corner; right: lower-right corner.	68
32	Displacement history of elastic cantilever beam with energy dissipation. Left: middle point; right: beam tip.	69
33	Tip displacement history of hyperelastic cantilever beam with energy dissipation.	69
34	Hysteresis plots for simple elastomeric damper (Properties given by Table 5). Left: Displacement history Δ_1 ; Right: Displacement history Δ_2	71
35	Hysteresis plots for simple elastomeric damper (Properties given by Table 9). Left: Displacement history Δ_1 ; right: Displacement history Δ_2	72
36	Reaction forces for simple elastomeric damper with low frequency displacements. Top: Damping constant $\mu = 0.01$ sec; bottom: Damping constant $\mu = 0.05$ sec.	73
37	Reaction forces for simple elastomeric damper with high frequency displacements. Top: Damping constant $\mu = 0.01$ sec; bottom: Damping constant $\mu = 0.05$ sec.	74
38	UH-60 Rotor system with lead-lag elastomeric damper.	75
39	Damper response as a function of azimuth angle. Top: damper stroke; bottom: damper force.	77
40	Rheological models. Left: Zener model; right: Poynting-Thomson model.	97
41	Uniaxial rheological model.	98
42	Elastomer specimen under double-lap shear test	119

43	Haupt-Sedlan Model: one-dimensional version	122
44	History of q under harmonic strain for $\zeta = 2.4$ and $\tau_q = 1000$ sec. Left: $f = 1.6$ Hz; right: $f = 30$ Hz. (Solid lines: $A = 0.01$; dashed lines: $A = 0.30$)	126
45	History of q under harmonic strain for $\zeta = 2.4$ and $\tau_q = 10$ sec. Left: $f = 1.6$ Hz; right: $f = 30$ Hz. (Solid lines: $A = 0.01$; dashed lines: $A = 0.30$)	126
46	History of q under harmonic strain for $\zeta = 24$ and $\tau_q = 10$ sec. Left: $f = 1.6$ Hz; right: $f = 30$ Hz. (Solid lines: $A = 0.01$; dashed lines: $A = 0.30$)	126
47	Steady-state q_s under ramp strain. Left: $k = 0.05 \text{ sec}^{-1}$, right: $k = 0.2 \text{ sec}^{-1}$.	128
48	History of q under ramp strain for $\zeta = 2.4$ and $\tau_q = 1000$ sec. Left: $k = 0.05 \text{ sec}^{-1}$; right: $k = 0.005 \text{ sec}^{-1}$. (Solid lines: numerical solution of Eq. (242); dashed lines: Eq. (245))	128
49	History of q under ramp strain for $\zeta = 2.4$ and $\tau_q = 10$ sec. Left: $k = 0.05 \text{ sec}^{-1}$; right: $k = 0.005 \text{ sec}^{-1}$. (Solid lines: numerical solution of Eq. (242); dashed lines: Eq. (245))	129
50	History of q under ramp strain for $\zeta = 24$ and $\tau_q = 10$ sec. Left: $k = 0.05 \text{ sec}^{-1}$; right: $k = 0.005 \text{ sec}^{-1}$. (Solid lines: numerical solution of Eq. (242); dashed lines: Eq. (245))	129
51	Typical time history of q under relaxation test. Left: $k = 0.05 \text{ sec}^{-1}$, $\zeta = 2.4$ and $\tau_q = 1000$ sec; right: $k = 0.005 \text{ sec}^{-1}$, $\zeta = 2.4$ and $\tau_q = 10$ sec. (Solid lines: numerical solution of Eq. (242); dashed lines: Eq. (251))	130
52	Storage modulus fitting. With symbols: test data from [8]; without symbols: Eq. (272a)	138
53	Loss modulus fitting. With symbols: test data from [8]; without symbols: Eq. (272b)	139
54	Storage modulus with assumed q related parameters. With symbols: test data from [8]; without symbols: numerical simulation	140
55	Loss modulus with assumed q related parameters. With symbols: test data from [8]; without symbols: numerical simulation	141
56	Stress-strain curves for ramp strain: strain rate decreases from top to bottom.	157
57	Stress-strain curves for ramp strain. Material parameters: $c_v = 0.985974$ MPa, $\xi = 10.0$, $\tau_{max} = 1000$ sec, $\tau_{min} = 1$ sec, $\zeta = 100$, $\tau_q = 1000$ sec and $k = 2.5, 0.25, 0.025, 2.5 \times 10^{-3}, 2.5 \times 10^{-4}$, and $2.5 \times 10^{-5} \text{ sec}^{-1}$ from top to bottom.	159
58	Relaxation test. Left: relaxation stress; right: relaxation modulus.	160
59	Relaxation test for $\gamma_0 = 0.06$. Left: relaxation stress; right: relaxation modulus.	160
60	Sinusoidal strain with increasing and decreasing amplitudes	161
61	Time history for q : $f = 3$ Hz and 200-period simulation for each amplitude.	164

62	Time history for q : $f = 3$ Hz and 10-period simulation for each amplitude.	164
63	Storage modulus for different recovery times.	165
64	Sinusoidal strain with static strain offset.	165
65	Effect of static strain offset on dynamic modulus.	166
66	Effect of static strain offset on dynamic modulus (adjusted storage modulus).	168
67	Storage modulus fitting. With symbols: test data from [8]; without symbols: Eq. (272a) with three Maxwell elements	170
68	Loss modulus fitting. With symbols: test data from [8]; without symbols: Eq. (272b) with three Maxwell elements	171
69	Höfer-Lion Model: one-dimensional version	172
70	Storage and loss moduli fitting (average error: 1.61306 MPa). With symbols: test data from [64]; without symbols: α -1 model fitting with one Maxwell element	175
71	Storage and loss moduli fitting (average error: 2.08715 MPa). With symbols: test data from [64]; without symbols: α -0 model fitting with one Maxwell element	175
72	Storage and loss moduli fitting (average error: 0.520227 MPa). With sym- bols: test data from [64]; without symbols: α -1 model fitting with three Maxwell elements	176
73	Storage and loss moduli fitting (average error: 2.02253 MPa). With symbols: test data from [64]; without symbols: α -0 model fitting with three Maxwell elements	176
74	Storage and loss moduli fitting (average error: 0.108241 MPa). With sym- bols: test data from [8]; without symbols: α -1 model fitting with one Maxwell element	177
75	Storage and loss moduli fitting (average error: 0.131517 MPa). With sym- bols: test data from [8]; without symbols: α -0 model fitting with one Maxwell element	177
76	Storage and loss moduli fitting (average error: 0.0364108 MPa. With sym- bols: test data from [8]; without symbols: α -1 model fitting with three Maxwell elements	178
77	Storage and loss moduli fitting (average error: 0.122971 MPa). With sym- bols: test data from [8]; without symbols: α -0 model fitting with three Maxwell elements	178
78	Typical stress histories for α -0 model under relaxation tests. Solid line: $k =$ 0.01 sec^{-1} and $\gamma_0 = 0.30$; dashed line: $k = 0.005 \text{ sec}^{-1}$ and $\gamma_0 = 0.30$	180
79	Relaxation test. Left: relaxation stress; right: relaxation modulus.	181
80	Relaxation test for $\gamma_0 = 0.06$. Left: relaxation stress; right: relaxation modulus.	181

81	Storage modulus for different recovery times.	182
82	Time history for q : $f = 3$ Hz, $\tau_q = 4$ sec. Left: 10-period simulation for each amplitude; right: 200-period simulation for each amplitude.	183
83	Effect of static strain offset on dynamic modulus.	184
84	The reference and deformed configurations of a body.	191
85	The base vectors in the reference and deformed configurations.	193
86	Volume elements in the reference and deformed configurations.	193
87	A body in the reference and deformed configurations.	202
88	A differential element of volume in the deformed configuration	203
89	The Cauchy stress components in a two dimensional case.	204
90	The stress vector per unit area of the reference configuration acting on a convected element of area.	207
91	The tetrahedron in the reference and deformed configurations	208
92	The 1st Piola-Kirchhoff stress components in a two dimensional case.	210
93	The 2nd Piola-Kirchhoff stress components in a two dimensional case.	211
94	Forces acting on a differential element of volume in the deformed configuration.	216

SUMMARY

The first part of this dissertation focuses on the development, implementation and validation of models that capture the behavior of joints in a realistic manner. These models are presented within the framework of finite element based, nonlinear multibody dynamics formulations that ensure unconditional nonlinear stability of the computation for complex systems of arbitrary topology. The proposed approach can be divided into three parts. First, the joint configuration: this purely kinematic part deals with the description of the configuration of the joint and the evaluation of the relative distance and relative tangential velocity between the contacting bodies. Second, the contact conditions: in most cases, contact at the joint is of an intermittent nature. The enforcement of the unilateral contact condition is a critical aspect of the computational procedure. And finally, the contact forces: this last part deals with the evaluation of the forces that arise at the interface between contacting bodies. The advantage of the proposed approach is that the three parts of the problem can be formulated and implemented independently.

Many articulated rotor helicopters use hydraulic dampers, which provide high levels of damping but are also associated with high maintenance costs and difficulties in evaluating their conditions due to the presence of seals, lubricants and numerous moving parts, all operating in a rotating frame. To avoid problems associated with hydraulic dampers, the industry is now switching to elastomeric lead-lag dampers that feature simpler mechanical design, lower part count, and result in “dry” rotors. However, the design of robust elastomeric dampers is hampered by the lack of reliable analytical tools that can be used to predict their damping behavior in the presence of large multi-frequency motions experienced by the rotor and thus the damper. The second part of this dissertation focuses on the development of an elastomeric damper model which predicts the behavior of the elastomeric damper based on a continuum mechanics approach: the configuration of the damper is modeled using a finite element approach, and material behavior is represented

by a set of nonlinear constitutive laws and material parameters. The validated finite element model of the elastomeric damper is then coupled with a comprehensive, multibody dynamics analysis code to predict the behavior of complex systems featuring elastomeric components, for example, rotorcraft with elastomeric lead-lag dampers.

Chapter I

INTRODUCTION TO FRICTION PHENOMENA IN MULTIBODY DYNAMICS

Multibody dynamics analysis is a powerful tool for the comprehensive simulation of the dynamic response of flexible systems of arbitrary topology and complexity. In present formulations, the joints connecting the various flexible bodies are rarely modeled *per se*. The piece of hardware that actually constitutes the joint is not modeled. Rather, only the kinematic constraints they impose on the system are represented by a set of equations.

As multibody formulations become more widely accepted, the need to model a wider array of phenomena increases. In particular, it is necessary to develop methodologies for the analysis of unilateral contact conditions in joints and of the resulting normal and friction forces. For realistic simulations, the actual piece of hardware and contact mechanics should be modeled more precisely. This involves a host of phenomena such as: contact kinematics, nonlinear normal contact forces between inelastic bodies, tangential loading, and sliding contact. Furthermore, the high level of nonlinearity associated with a number of these phenomena implies challenging numerical issues. Although friction forces can be readily evaluated from Coulomb friction laws, the resulting accuracy is questionable. Sticking and slipping can co-exist in different parts of the contact area, a phenomenon known as micro-slip. The actual relationship between the friction force, the normal pressure and the slip motion is not well understood. A further complication is that the accurate evaluation of the normal or pressure forces across the slip plane requires modeling of system dynamics in both normal and slip planes. Hence, joint behavior and system dynamics are intimately coupled. Finally, friction forces depend on the motion in a highly nonlinear way, complicating analytical and numerical solution procedures. Numerous models of friction have been developed and presented in the literature, each addressing some of the above issues.

This research project focuses on the development, implementation and validation of

models that capture the behavior of joints in a realistic manner. These models will be presented within the framework of finite element based, nonlinear multibody dynamics formulations that ensure unconditional nonlinear stability of the computation for complex systems of arbitrary topology. The proposed approach can be divided into three parts. First, the joint configuration: this purely kinematic part of the problem deals with the description of the configuration of the joint and the evaluation of the relative distance, q , and the relative tangential velocity, v^t , between the contacting bodies. Second, the contact conditions: in most cases, contact at the joint is of an intermittent nature. When contact occurs, normal contact forces and friction forces will arise. This unilateral contact condition is readily expressed in terms of the relative distance as $q \geq 0$. The enforcement of the unilateral contact condition is a critical aspect of the computational procedure. And finally, the contact forces: this last part of the problem deals with the evaluation of the forces that arise at the interface between contacting bodies. The contact forces must be computed based on suitable phenomenological laws. A survey of the multibody literature reveals that very simple models have been used thus far. For instance, the normal contact forces have been modeled using a quadratic potential that corresponds to a linear force-approach relationship, or the potential corresponding to Hertz's problem [124]. The classical form of Coulomb's law has been the basis for the modeling of frictional phenomena [111].

Increasing the versatility and accuracy of unilateral contact models in multibody systems is the focus of this project. To achieve this goal, the three parts of the model must be considerably expanded. The kinematics of the contacting bodies must be generalized so as to allow a wide variety of joint configurations to be considered. The proper enforcement of the contact condition is central to the numerical stability of the proposed procedure. Robust schemes must be used to treat this challenging numerical problem. Finally, contact and friction forces must be modeled in an accurate manner. Note that the problem is highly coupled because contact and friction forces depend on the overall dynamic response of the system; joint behavior cannot be investigated without modeling the entire system.

The advantage of the proposed approach is that the three parts of the problem can be formulated and implemented independently. For instance, once a given friction law has been

implemented, it can be used for various types of joints and for systems of arbitrary configurations. It is also possible to evaluate the performance of various friction laws for a given joint configuration by comparing their predictions with experimental measurements. Because the formulation is developed within the framework of finite element based multibody dynamics, it can deal with systems of arbitrary configurations.

The first part of this dissertation is laid out as follows: Chapter 2 describes the kinematic aspects of both two- and three-dimensional joints with clearance. The candidate contact points and the relative distance q between the contact points are obtained from relatively simple geometric considerations. The evaluations of the normal contact force and friction force follow. The unilateral contact conditions associated with the clearance are discussed in Chapter 3. In Chapter 4, after a brief introduction to the friction process, the details of the LuGre friction model is discussed. Finally, numerical examples of the proposed procedure appear in Chapter 5, followed by conclusions.

Chapter II

KINEMATIC DESCRIPTION OF JOINTS WITH CLEARANCE

The kinematic description of joints with clearance will be divided into two- and three-dimensional models. For two-dimensional problems, a revolute joint with clearance, called the *planar clearance joint*, is viewed as a planar joint with a unilateral constraint. The clearance, or distance between the inner and outer races, can be evaluated from the kinematic variables associated with the planar joint. A similar approach can be applied to spherical joints with clearance. In the three-dimensional case, a *spatial clearance joint* is developed; the clearance can still be related to the kinematic variables of the joint, although this relationship is more complex.

2.1 Two-Dimensional Case: Planar Clearance Joint

2.1.1 Kinematic description

A revolute joint with clearance can be modeled as a planar joint with the appropriate addition of a unilateral contact condition. Consider the planar joint depicted in Fig. 1; the outer and inner races of the joint are modeled as bodies K and L , respectively. The kinematic description of these bodies in their reference and deformed configurations will make use of three orthogonal triads. First, an inertial triad, denoted $\mathcal{I}(\bar{i}_1, \bar{i}_2, \bar{i}_3)$, is used as a global reference for the system. In the reference configuration, the position of body K is defined by its position vector \underline{u}_0^k and its orientation is determined by a body attached orthonormal basis $\mathcal{B}_0^k = (\bar{e}_{10}^k, \bar{e}_{20}^k, \bar{e}_{30}^k)$, with \bar{e}_{30}^k normal to the plane of joint. The rotation tensor from \mathcal{I} to \mathcal{B}_0^k is represented by R_0^k . The radius of the outer race is denoted ρ^k . In the deformed configuration, body K undergoes a displacement \underline{u}^k and a rotation R^k which results in an orthonormal basis $\mathcal{B}^k = (\bar{e}_1^k, \bar{e}_2^k, \bar{e}_3^k)$ from basis \mathcal{B}_0^k . The kinematic variables associated with body L , which represents the inner race of the revolute joint, are defined in a similar manner.

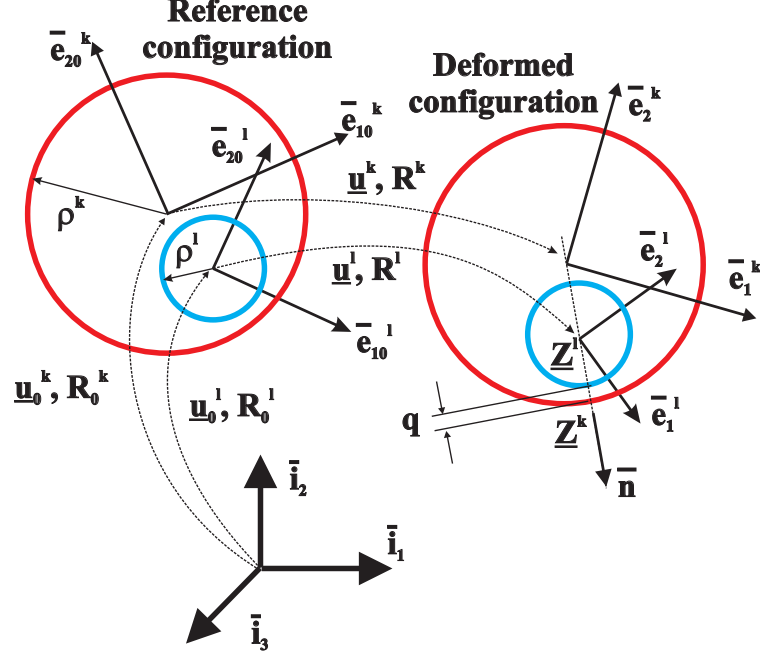


Figure 1: Configuration of the planar clearance joint.

The planar joint is associated with the following constraint conditions

$$\begin{aligned}
 \mathcal{C}_1 &= \bar{e}_1^{\ell T} \bar{e}_3^k = 0; \\
 \mathcal{C}_2 &= \bar{e}_2^{\ell T} \bar{e}_3^k = 0; \\
 \mathcal{C}_3 &= \bar{e}_3^{kT} (\underline{u}_0 + \underline{u}) = 0,
 \end{aligned} \tag{1}$$

where $\underline{u}_0 = \underline{u}_0^\ell - \underline{u}_0^k$ and $\underline{u} = \underline{u}^\ell - \underline{u}^k$. Kinematic condition $\mathcal{C}_3 = 0$ implies that body L remains in the plane normal to \bar{e}_3^{kT} . Conditions $\mathcal{C}_1 = \mathcal{C}_2 = 0$ imply that \bar{e}_3^ℓ remains normal to that same plane. The implementation of the holonomic constraints, Eqs. (1), is discussed in [17], where a constraint potential, $\underline{\lambda}^T \underline{\mathcal{C}}$, is added to the strain energy of the system with $\underline{\lambda} = (\lambda_1, \lambda_2, \lambda_3)^T$ as the Lagrange multipliers and $\underline{\mathcal{C}} = (\mathcal{C}_1, \mathcal{C}_2, \mathcal{C}_3)^T$. The corresponding constraint force can be derived from the constraint potential.

Contact may occur between the inner and outer races of the joint. As shown in Fig. 1, the candidate contact points [111] are readily found as

$$\begin{aligned}
 \underline{Z}^k &= \underline{u}_0^k + \underline{u}^k + \rho^k \bar{n}, \\
 \underline{Z}^\ell &= \underline{u}_0^\ell + \underline{u}^\ell + \rho^\ell \bar{n},
 \end{aligned} \tag{2}$$

where $\bar{n} = (\underline{u}_0 + \underline{u}) / \|\underline{u}_0 + \underline{u}\|$ is the unit vector joining the centers of the two races. The

relative distance between the races then becomes

$$\begin{aligned} q &= \bar{n}^T(\underline{Z}^k - \underline{Z}^\ell) \\ &= \rho^k - \rho^\ell - \|\underline{u}_0 + \underline{u}\|. \end{aligned} \quad (3)$$

2.1.2 Normal contact force

The virtual work done by the normal contact force is

$$\begin{aligned} \delta W &= f^n \bar{n}^T \delta(\underline{Z}^k - \underline{Z}^\ell) \\ &= f^n \bar{n}^T \delta(\underline{u}^k - \underline{u}^\ell) = f^n \delta q, \end{aligned} \quad (4)$$

where f^n is the magnitude of the normal contact force and $\delta(\cdot)$ represents the variation of (\cdot) . Expanding this result yields

$$\delta W = \begin{bmatrix} \delta \underline{u}^k \\ \delta \underline{u}^\ell \end{bmatrix}^T \underline{F}^n = \begin{bmatrix} \delta \underline{u}^k \\ \delta \underline{u}^\ell \end{bmatrix}^T f^n \begin{bmatrix} \bar{n} \\ -\bar{n} \end{bmatrix}. \quad (5)$$

The discretization of the system is based on its configurations at the beginning and end times of a typical time step, denoted t_i and t_f , respectively, and the subscripts $(\cdot)_i$ and $(\cdot)_f$ denote the value of a quantity at t_i and t_f , respectively. The normal contact force is taken to be constant over a time step and is discretized as

$$\underline{F}_m^n = f_m^n \begin{bmatrix} \underline{n}_m \\ -\underline{n}_m \end{bmatrix}, \quad (6)$$

where $\underline{n}_m = 2(\underline{u}_0 + \underline{u}_m) / (\|\underline{u}_0 + \underline{u}_f\| + \|\underline{u}_0 + \underline{u}_i\|)$, $\underline{u}_m = (\underline{u}_f + \underline{u}_i)/2$, and f_m^n the constant magnitude of the contact force over the time step. It is readily verified that this discretization implies that the work done by the normal contact force over a time step is

$$\Delta W = f_m^n (q_f - q_i). \quad (7)$$

Note that the work done by the normal contact force over a time step is in general not zero since the contacting bodies are flexible.

2.1.3 Friction force

Next, the friction forces will be evaluated. The time derivatives of the candidate contact point positions are, from Eqs. (2),

$$\begin{aligned}\dot{\underline{Z}}^k &= \dot{\underline{u}}^k + \rho^k \tilde{\omega}^k \bar{n}, \\ \dot{\underline{Z}}^\ell &= \dot{\underline{u}}^\ell + \rho^\ell \tilde{\omega}^\ell \bar{n},\end{aligned}\tag{8}$$

where $(\dot{\cdot})$ denotes a derivative with respect to time, $(\tilde{\cdot})$ denotes the skew-symmetric matrix formed with the components of (\cdot) . $\underline{\omega}^k$ and $\underline{\omega}^\ell$ are the angular velocity vectors of bodies K and L , respectively, given by

$$\begin{aligned}\tilde{\omega}^k &= \dot{R}^k R^{kT}, \\ \tilde{\omega}^\ell &= \dot{R}^\ell R^{\ell T}.\end{aligned}\tag{9}$$

The relative velocity, \underline{V}^r , and the relative tangential velocity, \underline{V}^t , are, respectively

$$\begin{aligned}\underline{V}^r &= \dot{\underline{Z}}^\ell - \dot{\underline{Z}}^k, \\ \underline{V}^t &= P \underline{V}^r,\end{aligned}\tag{10}$$

where $P = U - \bar{n}\bar{n}^T$ is the operator that projects the relative velocity vector onto the common tangential plane at the point of contact; U is the identity matrix. The unit vector along the relative tangential velocity is denoted

$$\bar{e} = \underline{V}^t / V^t,\tag{11}$$

where $V^t = \|\underline{V}^t\|$.

The virtual work done by the friction force is

$$\delta W = -f^t \bar{e}^T (\delta \underline{Z}^\ell - \delta \underline{Z}^k),\tag{12}$$

where f^t is the magnitude of the frictional force. Expanding this expression yields

$$\delta W = \begin{bmatrix} \underline{\delta u}^k \\ \underline{\delta \psi}^k \\ \underline{\delta u}^\ell \\ \underline{\delta \psi}^\ell \end{bmatrix}^T \underline{F}^t = \begin{bmatrix} \underline{\delta u}^k \\ \underline{\delta \psi}^k \\ \underline{\delta u}^\ell \\ \underline{\delta \psi}^\ell \end{bmatrix}^T f^t \begin{bmatrix} \bar{e} \\ \rho^k \tilde{n} \bar{e} \\ -\bar{e} \\ -\rho^\ell \tilde{n} \bar{e} \end{bmatrix},\tag{13}$$

where $\underline{\delta\psi}^k$ and $\underline{\delta\psi}^\ell$ are virtual rotation vectors of bodies K and L , respectively, and can be defined in an analogous manner to the angular velocity vectors, Eqs (9), as

$$\begin{aligned}\widetilde{\delta\psi}^k &= \delta R^k R^{kT}, \\ \widetilde{\delta\psi}^\ell &= \delta R^\ell R^{\ell T}.\end{aligned}\tag{14}$$

Note that there is no vector $\underline{\psi}$ such that $\delta(\underline{\psi})$ is the virtual rotation vector; to emphasize this important fact, the notation $\underline{\delta\psi}$, rather than $\delta\underline{\psi}$, is used to indicate the virtual rotation vector.

The discretized friction force is selected as

$$\underline{F}_m^t = f_m^t \begin{bmatrix} \bar{e}_m \\ \rho^k \widetilde{n}_m \bar{e}_m \\ -\bar{e}_m \\ -\rho^\ell \widetilde{n}_m \bar{e}_m \end{bmatrix}.\tag{15}$$

The work done by the friction forces over a single time step then becomes

$$\Delta W = -f_m^t \Delta t V_m^t,\tag{16}$$

provided the following definitions are made: $\underline{V}_m^t = (U - \underline{n}_m \underline{n}_m^T) \underline{V}_m^r$, $\bar{e}_m = \underline{V}_m^t / V_m^t$ and $\Delta t \underline{V}_m^r = (\underline{u}_f - \underline{u}_i) + \rho^\ell \widetilde{n}_m^T \underline{r}^\ell - \rho^k \widetilde{n}_m^T \underline{r}^k$, where \underline{r}^k and \underline{r}^ℓ are the incremental rotations of bodies K and L , respectively. If the friction is dissipative, $f^t \Delta t V^t \geq 0$, and the above discretization guarantees that

$$\Delta W = -f_m^t \Delta t V_m^t \leq 0,\tag{17}$$

i.e., the discretization of the frictional process is dissipative.

Note that the formulation presented in this section for the two-dimensional planar clearance joint is also valid for a spherical joint with clearance.

2.2 Three-Dimensional Case: Spatial Clearance Joint

2.2.1 Kinematic description

When the motion of the joint cannot be assumed to remain planar, a more complex, three-dimensional configuration must be considered, such as that presented in Fig. 2. The outer

race of the joint, denoted body K , is idealized as a cylinder of radius ρ^k . The inner race, denoted body L , is idealized as a thin disk of radius ρ^ℓ . Here again the kinematic description of these bodies in their reference and deformed configurations will make use of three orthogonal triads. First, an inertial triad, denoted $\mathcal{I}(\bar{i}_1, \bar{i}_2, \bar{i}_3)$, is used as a global reference for the system. In the reference configuration, the position of the outer race is defined by the position vector \underline{u}_0^k of its center and its orientation is determined by a body attached orthonormal basis $\mathcal{B}_0^k = (\bar{e}_{10}^k, \bar{e}_{20}^k, \bar{e}_{30}^k)$, with \bar{e}_{30}^k along the axis of the cylinder. The rotation tensor from \mathcal{I} to \mathcal{B}_0^k is represented by R_0^k . In the deformed configuration, the outer race center undergoes a displacement \underline{u}^k and a rotation R^k which results in an orthonormal basis $\mathcal{B}^k = (\bar{e}_1^k, \bar{e}_2^k, \bar{e}_3^k)$ from basis \mathcal{B}_0^k . The kinematic variables associated with body L are defined in a similar manner, with \bar{e}_{30}^ℓ normal to the plane of the disk.

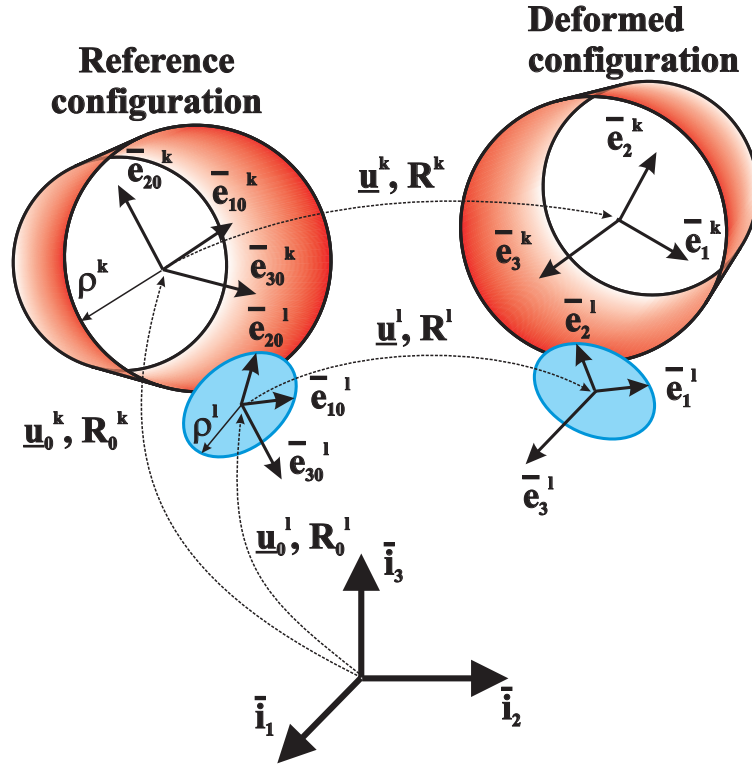


Figure 2: Configuration of the spatial clearance joint.

An orthonormal basis $\bar{d}_1^k, \bar{d}_2^k, \bar{d}_3^k$ is now defined in the following manner: $\bar{d}_3^k = \bar{e}_3^k$ is along

the axis of the cylinder, \bar{d}_1^k makes an arbitrary angle ϕ with \bar{e}_1^k , and \bar{d}_2^k completes the basis

$$\begin{aligned}\bar{d}_1^k &= \cos \phi \bar{e}_1^k + \sin \phi \bar{e}_2^k; \\ \bar{d}_2^k &= -\sin \phi \bar{e}_1^k + \cos \phi \bar{e}_2^k; \\ \bar{d}_3^k &= \bar{e}_3^k.\end{aligned}\tag{18}$$

Consider the plane tangent to the cylinder, defined by vectors \bar{d}_2^k and \bar{d}_3^k , as depicted in Fig. 3. Point \underline{P} , of position vector $\underline{u}_0^k + \underline{u}^k + \rho^k \bar{d}_1^k$, belongs to this plane. The relative distance \bar{q} between disk L and this tangent plane is now evaluated.

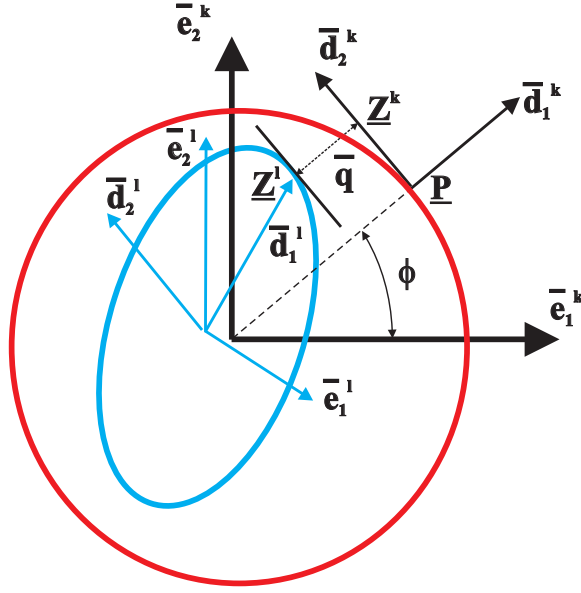


Figure 3: Relative distance between the candidate contact points.

The candidate contact points on the plane and disk are denoted \underline{z}^k and \underline{z}^ℓ , respectively, see Fig. 3. The tangent to the disk at the candidate contact point must be in the plane of the disk and parallel to the contacting plane, *i.e.*, normal to \bar{e}_3^ℓ and \bar{d}_1^k , respectively. The following basis is now defined

$$\begin{aligned}\bar{d}_2^\ell &= -\frac{\tilde{d}_1^k \bar{e}_3^\ell}{h_1}; \\ \bar{d}_3^\ell &= \bar{e}_3^\ell; \\ \bar{d}_1^\ell &= \tilde{d}_2^\ell \bar{e}_3^\ell,\end{aligned}\tag{19}$$

where $h_1 = \|\tilde{d}_1^k \bar{e}_3^\ell\|$. Clearly, \bar{d}_2^ℓ is parallel to the tangent at the candidate contact point, \bar{d}_1^ℓ points toward the candidate contact point, and \bar{d}_3^ℓ is normal to the plane of the disk. The

vector from point \underline{P} to point \underline{Z}^ℓ is

$$\begin{aligned}\underline{PZ}^\ell &= \left[(\underline{u}_0^\ell + \underline{u}^\ell) + \rho^\ell \bar{d}_1^\ell \right] - \left[(\underline{u}_0^k + \underline{u}^k) + \rho^k \bar{d}_1^k \right] \\ &= \underline{u}_0 + \underline{u} + \rho^\ell \bar{d}_1^\ell - \rho^k \bar{d}_1^k,\end{aligned}\tag{20}$$

where $\underline{u}_0 = \underline{u}_0^\ell - \underline{u}_0^k$, and $\underline{u} = \underline{u}^\ell - \underline{u}^k$. The relative distance \bar{q} is found by projecting \underline{PZ}^ℓ along the unit vector $-\bar{d}_1^k$, see Fig. 3, to find

$$\begin{aligned}\bar{q} &= -\bar{d}_1^{kT} \underline{PZ}^\ell \\ &= -\bar{d}_1^{kT} (\underline{u}_0 + \underline{u}) - \rho^\ell \bar{d}_1^{kT} \bar{d}_1^\ell + \rho^k.\end{aligned}\tag{21}$$

As shown in Fig. 3, the candidate contact point \underline{Z}^k is in the tangent plane, but not necessarily on the cylindrical surface defining the outer race of the joint. The relative distance \bar{q} defined by Eq. (21) is clearly a function of the angle ϕ that defines the location of the tangent plane around the cylinder. The relative distance q between the cylinder and disk is found by minimizing \bar{q} with respect to the choice of ϕ , *i.e.*, by setting $d\bar{q}/d\phi = 0$ to find

$$\bar{d}_2^{kT} \left[\rho^\ell \frac{g_1}{h_1} \bar{e}_3^\ell - (\underline{u}_0 + \underline{u}) \right] = 0,\tag{22}$$

where $g_1 = \bar{e}_3^{\ell T} \bar{d}_1^k$ and $h_1 = \|\tilde{d}_1^k \bar{e}_3^\ell\| = \bar{d}_1^{kT} \bar{d}_1^\ell$. Note that for small angles $g_1 \approx 0$ and $h_1 \approx 1$. The same result could be obtained by imposing the condition that \underline{PZ}^ℓ be orthogonal to \bar{d}_2^k . In summary, the relative distance between the inner and outer races of the joint is

$$q = \rho^k - \rho^\ell h_1 - \bar{d}_1^{kT} (\underline{u}_0 + \underline{u}),\tag{23}$$

with angle ϕ implicitly defined by Eq. (22).

2.2.2 Normal contact force

If contact occurs, the virtual work done by the normal contact force is

$$\begin{aligned}\delta W &= f^n \bar{d}_1^{kT} \delta(\underline{Z}^k - \underline{Z}^\ell) \\ &= f^n \bar{d}_1^{kT} \delta(q \bar{d}_1^k) = f^n \delta q,\end{aligned}\tag{24}$$

where f^n is the magnitude of the normal contact force. Expanding this result yields

$$\delta W = \begin{bmatrix} \delta \underline{u}^k \\ \delta \psi^k \\ \delta \underline{u}^\ell \\ \delta \psi^\ell \end{bmatrix}^T \quad \underline{F}^n = \begin{bmatrix} \delta \underline{u}^k \\ \delta \psi^k \\ \delta \underline{u}^\ell \\ \delta \psi^\ell \end{bmatrix}^T \quad f^n \begin{bmatrix} \bar{d}_1^k \\ (\rho^\ell g_1/h_1) \underline{h}_1 - \tilde{d}_1^k(\underline{u}_0 + \underline{u}) \\ -\bar{d}_1^k \\ -(\rho^\ell g_1/h_1) \underline{h}_1 \end{bmatrix}, \quad (25)$$

where $\underline{h}_1 = \tilde{d}_1^k \bar{e}_3^\ell$. The proposed discretization of the normal contact force, taken to be constant over a time step, is

$$\underline{F}_m^n = f_m^n \begin{bmatrix} \underline{d}_{1m}^k \\ (\rho^\ell g_{1m}/h_{1m}) \underline{h}_{1m} - \tilde{d}_{1m}^k(\underline{u}_0 + \underline{u}_m) \\ -\underline{d}_{1m}^k \\ -(\rho^\ell g_{1m}/h_{1m}) \underline{h}_{1m} \end{bmatrix}, \quad (26)$$

where $\underline{d}_{1m}^k = (\bar{d}_{1f}^k + \bar{d}_{1i}^k)/2$, $\underline{e}_{3m}^\ell = (\bar{e}_{3f}^\ell + \bar{e}_{3i}^\ell)/2$, $\underline{h}_{1m} = \tilde{d}_{1m}^k \underline{e}_{3m}^\ell$, $h_{1m} = (h_{1f} + h_{1i})/2$, and $g_{1m} = (g_{1f} + g_{1i})/2$. It is readily verified that this discretization implies that the work done by the normal contact force over a time step is

$$\Delta W = f_m^n (q_f - q_i). \quad (27)$$

2.2.3 Friction force

Next, the friction forces will be evaluated. The time derivatives of the candidate contact point positions are

$$\begin{aligned} \dot{\underline{Z}}^k &= \dot{\underline{u}}^k + \tilde{\omega}^k \underline{\lambda}, \\ \dot{\underline{Z}}^\ell &= \dot{\underline{u}}^\ell + \rho^\ell \tilde{\omega}^\ell \bar{d}_1^\ell, \end{aligned} \quad (28)$$

where $\underline{\lambda} = (\underline{u}_0 + \underline{u}) + \rho^\ell \bar{d}_1^\ell + q \bar{d}_1^k$. The relative velocity is

$$\underline{V}^r = \dot{\underline{Z}}^\ell - \dot{\underline{Z}}^k, \quad (29)$$

and the relative tangential velocity, \underline{V}^t , then becomes

$$\underline{V}^t = P \underline{V}^r, \quad (30)$$

where $P = U - \bar{d}_1^k \bar{d}_1^{kT}$ is the operator that projects the relative velocity vector onto the common tangential plane at the point of contact. The unit vector along the relative tangential velocity is denoted $\bar{e} = \underline{V}^t / V^t$, where $V^t = \|\underline{V}^t\|$. The virtual work done by the friction force is

$$\delta W = -f^t \bar{e}^T (\delta \underline{Z}^\ell - \delta \underline{Z}^k), \quad (31)$$

where f^t is the magnitude of the frictional force. Expanding this expression yields

$$\delta W = \begin{bmatrix} \delta \underline{u}^k \\ \delta \psi^k \\ \delta \underline{u}^\ell \\ \delta \psi^\ell \end{bmatrix}^T \underline{F}^t = \begin{bmatrix} \delta \underline{u}^k \\ \delta \psi^k \\ \delta \underline{u}^\ell \\ \delta \psi^\ell \end{bmatrix}^T f^t \begin{bmatrix} \bar{e} \\ \tilde{\lambda} \bar{e} \\ -\bar{e} \\ -\rho^\ell \tilde{d}_1^\ell \bar{e} \end{bmatrix}. \quad (32)$$

The discretized friction force is selected as

$$\underline{F}_m^t = f_m^t \begin{bmatrix} \bar{e}_m \\ \tilde{\lambda}_m \bar{e}_m \\ -\bar{e}_m \\ -\rho^\ell \tilde{d}_{1m}^\ell \bar{e}_m \end{bmatrix}. \quad (33)$$

The work done by the friction forces over a single time step then becomes

$$\Delta W = -f_m^t \Delta t V_m^t, \quad (34)$$

provided the following definitions are made: $\underline{V}_m^t = (U - \underline{d}_{1m}^k \underline{d}_{1m}^{kT}) \underline{V}_m^r$, $\bar{e}_m = \underline{V}_m^t / V_m^t$ and $\Delta t \underline{V}_m^r = (\underline{u}_f - \underline{u}_i) + \rho^\ell \tilde{d}_{1m}^{\ell T} \underline{r}^\ell - \tilde{\lambda}_m^T \underline{r}^k$, where \underline{r}^k and \underline{r}^ℓ are the incremental rotations of bodies K and L , respectively. If the friction is dissipative, $f^t \Delta t V^t \geq 0$, and the above discretization guarantees that $\Delta W = -f_m^t \Delta t V_m^t \leq 0$, *i.e.*, the discretization of the frictional process is dissipative.

A realistic model of a journal bearing with clearance is obtained by using two spatial clearance joints connected by a rigid body, as depicted in Fig. 4.

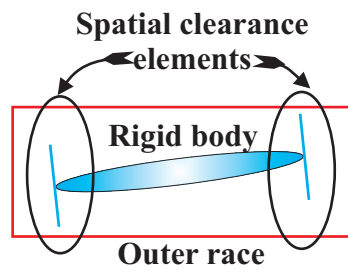


Figure 4: Model of a journal bearing using two spatial clearance joints.

Chapter III

UNILATERAL CONTACT CONDITIONS

3.1 Modeling Unilateral Contact Conditions

The approaches to the modeling of unilateral contact conditions can be categorized in two main classes. The first one considers impact to be an impulsive phenomenon of null duration [76, 77]. The configuration of the system is “frozen” during the impact, and an appropriate model is used to relate the states of the system immediately before and immediately after the event. There are two alternative formulations of this theory: Newton’s and Poisson’s methods. The first relates the relative normal velocities of the contacting bodies through the use of an appropriate restitution coefficient. The second divides the impact in two phases. At first, a compression phase brings the relative normal velocity of the bodies to zero through the application of an impulse at the contact location. Then, an expansion phase applies an impulse of opposite sign. The restitution coefficient relates the magnitudes of these two impulses. Although these methods have been used with success for multibody contact/impact simulations, it is clear that their accuracy is inherently limited by the assumption of a vanishing impact duration.

In the second approach, contact/impact events are of finite duration, and the time history of the resulting interaction forces is computed as a byproduct of the simulation [78, 33]. The contacting bodies are assumed to be deformable in a small region near the contact point. In this case, the centers of mass of the bodies are allowed to approach each other closer than what would be allowed for rigid bodies. This quantity is defined as the *approach* and is denoted a . $a > 0$ when penetration occurs, as depicted in Fig. 5.

The approach a is obtained at each instant of the simulation by solving a set of kinematic equations that also express the minimum distance between the bodies when they are not in contact, such as Eqs. (3) or (23). When the bodies are in contact, the relationship between the normal contact force and the approach is given by a constitutive law; various laws can

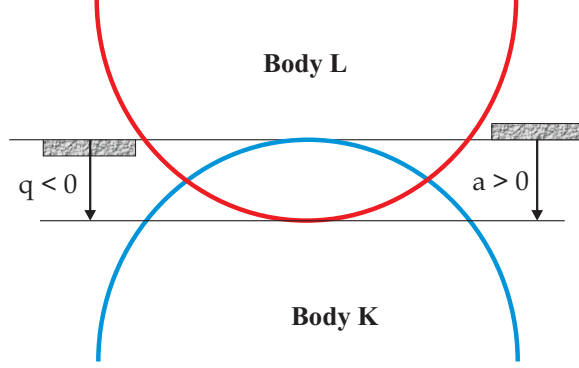


Figure 5: Penetration of contacting deformable bodies.

be used, but the classical solution of the static contact problem presented by Hertz [124] has been used by many investigators. Energy dissipation can be added in an appropriate manner, as proposed by Hunt and Crossley [70]. If the normal contact forces can be derived from a potential, $V(q)$, the work done by these forces over a time step of the simulation is $\Delta W = f_m^n(q_f - q_i)$, as implied by the time discretizations proposed in section 2. The work done by these forces then becomes $\Delta W = V(q_f) - V(q_i)$, as expected, if the normal forces are discretized as $f_m^n = (V(q_f) - V(q_i))/(q_f - q_i)$.

The contact model used in this work consists of elastic and dissipative components. Accordingly, the normal contact force f^n can be written as the sum of an elastic force f^e and a dissipative force f^d ,

$$f^n = f^e + f^d. \quad (35)$$

The relationship between the elastic contact force and the approach a is assumed to be given by the solution of the Hertz contact problem [124]

$$f^e = ka^{3/2}, \quad (36)$$

where k is the stiffness coefficient. The dissipative force is represented by a linear damper as

$$f^d = \mu\dot{a}, \quad (37)$$

where μ is the linear damping coefficient.

3.2 Time Step Size Adaptation Procedure

To be successful, the approach described above must be complemented with a time step size selection procedure. When contact between the two bodies is about to take place, the contact model will dictate the time step for the analysis. Let q_0 and q_1 be the relative distance between the bodies for two consecutive time steps of size Δt_0 and Δt_1 , respectively. To avoid large penetration distances and the ensuing large normal contact forces at the first time step after contact, the time step size will be selected so that the change in relative distance, $\Delta q = q_1 - q_0$, be of the order of a user defined “characteristic penetration distance,” ε_p . To achieve this goal, the desired change in relative distance is selected as

$$\Delta q = \varepsilon_p \begin{cases} 1 & \text{if } \kappa \leq 1 \\ \kappa^\alpha & \text{if } \kappa > 1 \end{cases}, \quad (38)$$

where the quantity κ , defined as $\kappa = (q_1/\varepsilon_p)/\bar{q}_{\min}$, measures the proximity to contact. The desired time step size is then estimated as

$$\Delta t_{\text{new}} = (\Delta q)/v_m, \quad (39)$$

where $v_m = 2(q_1 - q_0)/(\Delta t_0 + \Delta t_1)$ is the average relative velocity during the previous time step. The following values were found to give good results for a wide range of problems: $\bar{q}_{\min} = 5$ and $\alpha = 1.2$.

Chapter IV

MODELING FRICTION PHENOMENA

4.1 Introduction to Frictional Process

The detailed modeling of frictional forces poses unique computational challenges that will be illustrated using Coulomb’s law as an example. When sliding takes place, Coulomb’s law states that the friction force, \underline{F}^f , is proportional to the magnitude of the normal contact force, f^n ,

$$\underline{F}^f = -\mu_k(v) f^n \underline{v}/v, \quad (40)$$

where $\mu_k(v)$ is the coefficient of kinetic friction and v the magnitude of the relative velocity vector tangent to the friction plane, \underline{v} . If the relative velocity vanishes, sticking takes place. In this case, the frictional force is

$$|\underline{F}^f| \leq \mu_s f^n, \quad (41)$$

where μ_s is the coefficient of static friction, which is usually larger than the coefficient of kinetic friction, μ_k , for the same interface.

Application of Coulomb’s law involves discrete transitions from sticking to sliding and vice-versa, as dictated by the vanishing of the relative velocity and the magnitude of the friction force. These discrete transitions can cause numerical difficulties that are well documented, and numerous authors have advocated the use of a continuous friction law [104], [21], [117], [33], typically written as

$$\underline{F}^f = -\mu_k(v) f^n \frac{\underline{v}}{v} (1 - e^{-|v|/v_s}), \quad (42)$$

where $(1 - e^{-|v|/v_s})$ is a “regularization factor” that smoothes out the friction force discontinuity, as depicted in Fig. 6, and v_s a characteristic velocity usually chosen to be small compared to the maximum relative velocity encountered during the simulation. The continuous friction law describes both sliding and sticking behavior, *i.e.*, it completely replaces Coulomb’s law. Sticking is replaced by “creeping” between the contacting bodies with a

small relative velocity. Various forms of the regularizing factor have appeared in the literature; a comparison between these various models appears in [15].

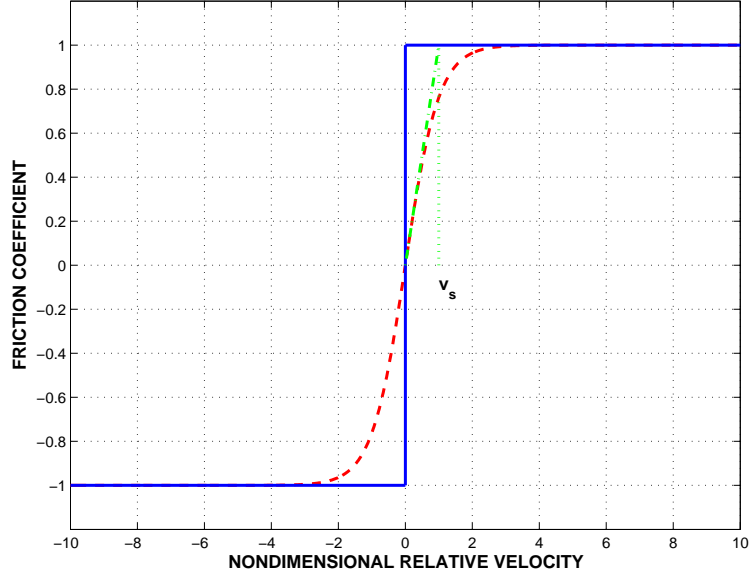


Figure 6: Friction coefficient for Coulomb's friction law (solid line), and the continuous friction law (dashed line). $\mu_k = 1.0$

Replacing Coulomb's friction law by a continuous friction law is a practice widely advocated in the literature; however, this practice presents a number of shortcomings [18]. First, it alters the physical behavior of the system and can lead to the loss of important information such as abrupt variations in frictional forces; second, it negatively impacts the computational process by requiring very small time step sizes when the relative velocity is small; and finally it does not appear to be able to deal with systems with different values of the static and kinetic coefficients of friction.

In reality, frictional forces do not present the discontinuity described by Coulomb's law but rather, a velocity dependent, rapid variation. The regularization factor discussed in the previous paragraph smoothes the discontinuity through a purely mathematical artifact that makes no attempt to more accurately represent the physical processes associated with the friction phenomenon. On the other hand, physics based models address the behavior of the frictional interface under small relative velocity. Typically, these micro-slip models allow

small relative displacements to take place during “sticking”; the frictional interface then behaves like a very stiff viscous damper. Of course, such models are incapable of capturing the tangential stiffness of the joint during micro-slip. The most common micro-slip model is the Iwan model [71], also named elastic-perfectly plastic model [44]. In this approach, the frictional interface is modeled as a spring in series with a Coulomb friction element featuring a friction force of magnitude μf^n . When the force in the spring reaches this magnitude, the force in the Iwan model saturates until the direction of slip reverses. An alternative approach to the treatment of micro-slip involves modification of the friction law itself.

Over the years, several friction models have been proposed that more accurately model various physical aspects of the friction process, such as the Valanis model [128]. Dahl [37] proposed a model that is able to emulate the hysteretic force-displacement behavior that characterizes micro-slip using a differential relationship. The primary shortcoming of the Dahl model is that it does not include the dependence of the friction coefficient on slip velocity. In particular, it does not capture the rapid decrease in the friction coefficient as the interface begins to slip, which is known as Stribeck effect [6] and is a major contributor to stick-slip oscillations. The omission of the Stribeck effect could be a major drawback of the Dahl model in its application to joint dynamics. More recently, Canudas de Wit *et al.* have proposed the LuGre model [32] that is based on a phenomenological description of friction. This model is able to capture experimentally observed phenomena such as pre-sliding displacements, the hysteretic relationship between the friction force and the relative velocity, the variation of the break-away force as a function of force rate, and stick-slip motion associated with the Stribeck effect. The LuGre model has further been refined by Swevers *et al.* [123] and Lampaert *et al.* [84].

4.2 LuGre Friction Model

4.2.1 LuGre friction model and its discretization

The state of the art in friction modeling was advanced using the paradigm of intermeshing “bristles” to explain the friction forces between two contacting bodies [54]. The bristle model captures micro-slip and also accounts for the drop in friction force as the sliding speed is

increased. However, according to its authors, the model is computationally burdensome. One of the more promising friction models developed from the bristle paradigm is the LuGre model [32] which captures the variation in friction force with slip velocity, making it a good candidate for studies involving stick-slip oscillations. Also, when linearized for very small motions, the LuGre model is shown to be equivalent to a linear spring/damper arrangement.

The LuGre model is an analytical friction model summarized by the following two equations

$$\mu = \sigma_0 z + \sigma_1 \frac{dz}{dt} + \sigma_2 v; \quad (43a)$$

$$\frac{dz}{dt} = v - \frac{\sigma_0 |v|}{\mu_k + (\mu_s - \mu_k) e^{-|v/v_s|^\gamma}} z. \quad (43b)$$

The first equation predicts the instantaneous friction coefficient μ as a function of the relative velocity, v , of the two contacting bodies and an internal state of the model, z , that represents the average deflection of elastic bristles whose interaction results in equal and opposite friction forces on the two bodies. The coefficients σ_0 , σ_1 , and σ_2 are parameters of the model. σ_0 is an equivalent stiffness for the deflection-force relationship, and σ_1 can be considered as the micro-viscous damping coefficient of the bristles. The third term in the first equation, which is proportional to the relative velocity, is added to account for the viscous friction. The second equation is an evolution equation for the average bristle deflection. μ_s and μ_k are the static and kinetic friction coefficients, respectively; v_s the characteristic Stribeck velocity; and γ a final model parameter is often selected as $\gamma = 2$. The friction force acting between the bodies is then

$$f^f = \mu f^n, \quad (44)$$

where f^n is the normal contact force.

The parameters of the LuGre friction model for particular contacting surfaces are usually identified from experimental data. Swevers *et al.* identified the friction model parameters for a joint of a industrial robot [123]. For the identification, the parameters of the model were divided into two groups: those that have significant effect during the sliding regime and those that mainly influence the pre-sliding response. The first group of parameters was

determined based on constant velocity tests over the full velocity range of the joint using a weighted least-squares estimator. The second group of parameters was identified from a pre-sliding experiment in which the applied force was slowly ramped up or down. In this case, the dynamical effects, the micro-viscous damping and the viscous friction were all neglected.

For convenience, the LuGre friction model can be rewritten in a nondimensional form as

$$\bar{\mu} = (1 - \bar{\beta}\bar{\sigma}_1)\bar{z} + (\bar{\sigma}_1 + \bar{\sigma}_2)\bar{v}; \quad (45a)$$

$$\dot{\bar{z}} = \bar{v} - \bar{\beta}\bar{z}, \quad (45b)$$

where $\bar{\mu} = \mu/\mu_k$, $\bar{v} = v/v_s$, $\bar{z} = \sigma_0 z/\mu_k$, $\bar{\sigma}_1 = \sigma_1 v_s/\mu_k$ and $\bar{\sigma}_2 = \sigma_2 v_s/\mu_k$. The nondimensional time is $\tau = \Omega t$, where

$$\Omega = \frac{\sigma_0 v_s}{\mu_k} \quad (46)$$

is the inverse of the time constant of the LuGre model. The notation $(\cdot)'$ indicates a derivative with respect to the nondimensional time. Finally, $\bar{\beta} = |\bar{v}|/\bar{g}(\bar{v})$, where

$$\bar{g}(\bar{v}) = 1 + (\mu_s/\mu_k - 1)e^{-|\bar{v}|^\gamma}. \quad (47)$$

The evolution equation of the LuGre model, Eq. (45b), will be discretized in the following manner, based on a time discontinuous Galerkin procedure [74]

$$\frac{z_f - z_i}{\Delta\tau} + \beta_g \frac{z_f + z_j}{2} = v_g, \quad (48a)$$

$$\frac{z_j - z_i}{\Delta\tau} - \beta_g \frac{z_f - z_j}{6} = 0, \quad (48b)$$

where, for simplicity, the over bar was dropped from all symbols. The subscripts $(\cdot)_i$ and $(\cdot)_f$ denote quantities at the beginning and end of the time step, whereas the subscripts $(\cdot)_j$ indicates a quantity after the initial discontinuity. The subscript $(\cdot)_g$ indicates the following average $(\cdot)_g = [(\cdot)_f + (\cdot)_j]/2$.

4.2.2 Properties of the proposed discretization

For steady state solutions $z_f = z_j = z_i = z_{ss}$, Eq. (48b) is identically satisfied, whereas Eq. (48a) implies $\beta_{ss} z_{ss} = v_{ss}$, which can be written as

$$|v|_{ss} [s_{v_{ss}} s_{z_{ss}} - |z|_{ss}/g(v_{ss})] = 0, \quad (49)$$

where $s_{v_{ss}} = \text{sign}(v_{ss})$ and $s_{z_{ss}} = \text{sign}(z_{ss})$. The first solution of Eq. (49) is $|v|_{ss} = 0$, which corresponds to sticking. The second is $|z|_{ss} = g(v_{ss})$ with $s_{v_{ss}} s_{z_{ss}} = 1$, which corresponds to steady state sliding. For large sliding velocity, $g(v_{ss}) \approx 1$, and hence, $|z|_{ss} \approx 1$.

The discretization also implies an important evolution law for the strain energy of the bristles. This evolution law is obtained by summing up Eqs. (48a) and (48b) multiplied by $(z_f + z_j)/2$ and $-(z_f - z_j)/2$, respectively, to yield

$$\frac{V_f - V_i}{\Delta\tau} = -|z|_g |v|_g \left[\frac{|z|_g}{g(v_g)} - s_{v_g} s_{z_g} \right] - \frac{1}{2\Delta\tau} \left(1 + \frac{6}{\beta_g \Delta\tau} \right) (z_j - z_i)^2, \quad (50)$$

where $V = z^2/2$ is the strain energy stored in the bristles. The second term of the evolution law, Eq. (50), is a numerical dissipation term that is always negative. As the time step decreases, $z_j \rightarrow z_i$ as implied by the time discontinuous Galerkin approximation, and the numerical dissipation vanishes. The first term is negative whenever $s_{v_g} s_{z_g} = -1$, or when $s_{v_g} s_{z_g} = 1$ and $|z|_g/g(v_g) > 1$. In summary, $(V_f - V_i)/\Delta\tau < 0$ when $|z|_g > g(v_g)$. This implies the decreasing of the strain energy of the elastic bristles whenever $|z|_g > g(v_g)$. Since the strain energy is a quadratic form of the bristle average deflection, this implies the decreasing of the bristle deflection under the same conditions. Consequently, the bristle deflection must remain smaller than the upper bound of $g(v_g)$, which, in view of Eq. (47), is equal to μ_s/μ_k . It follows that $|z|_g < \mu_s/\mu_k$. This inequality implies the finiteness of the bristle deflection and of its strain energy.

The discretizations of the friction forces for the clearance joints proposed in this work, Eqs. (15) and (33), imply that the work done by the friction force over one time step is

$$\Delta W = -f_m^t \Delta t V_m^t = -\mu_g f_g^n \Delta t v_g; \quad (51)$$

introducing Eq. (45a) then yields

$$\frac{\sigma_0 \Delta W}{\mu_k^2 \Delta\tau f_g^n} = -[(1 - \beta_g \sigma_1) z_g + (\sigma_1 + \sigma_2) v_g] v_g. \quad (52)$$

With the help of Eq. (50), this work can be expressed as

$$\begin{aligned} \frac{\sigma_0 \Delta W}{\mu_k^2 \Delta \tau f_g^n} &= -\sigma_2 v_g^2 - \frac{z_g^2}{g(v_g)} |v|_g - \frac{V_f - V_i}{\Delta \tau} - \sigma_1 \left[1 - \frac{|z|_g}{g(v_g)} s_{v_g} s_{z_g} \right] v_g^2 \\ &\quad - \frac{1}{2 \Delta \tau} \left(1 + \frac{6}{\beta_g \Delta \tau} \right) (z_j - z_i)^2. \end{aligned} \quad (53)$$

The first two terms are always dissipative, with the second term corresponding to the main energy dissipation during sliding. The third term corresponds to the change in the potential of the elastic deformation of the bristles. Although this term can be positive or negative, it is finite since the potential is, itself, finite. As discussed earlier, when $|z|_g > g(v_g)$, $(V_f - V_i)/\Delta \tau < 0$ and the potential energy of the bristle deflection is released to the system. Under a similar condition, $s_{v_g} s_{z_g} = 1$ and $|z|_g > g(v_g)$, the fourth term also becomes positive. Clearly, the third and fourth terms are non-dissipative only when the potential of the elastic bristles is released. As discussed earlier, this potential is finite and increases in its value stem from work done against friction forces; it is this very work that could be released at a later time. Finally, the last term is a numerical dissipation term. Note that as the time step size is decreased, $(z_j - z_i)^2$ rapidly decreases, and the numerical dissipation vanishes. In summary, the proposed discretization of LuGre model guarantees the dissipative nature of the friction forces, when combined with the proposed discretizations for the friction forces, Eqs. (15) and (33).

4.3 Time Step Size Adaptation Procedure

To be successful, the approach described above must be complemented with a time step size selection procedure. When friction occurs, the friction model will dictate the time step for the analysis. In view of the rapid variation of the function $g(v)$ for small relative velocities, the time step size must be reduced when the relative velocity is of the order of the Stribeck velocity v_s . To achieve this goal, the time step size for the next time step is selected as

$$\Omega \Delta t_{\text{new}} = \Delta \tau_{\text{min}} \begin{cases} 1 & \text{if } \nu \leq 1 \\ \nu^\alpha & \text{if } \nu > 1 \end{cases}, \quad (54)$$

where Ω , given by Eq. (46), is the inverse of the time constant of the LuGre model and the quantity ν , defined as $\nu = (V_r/v_s)/(\bar{v}_{\text{min}})$, measures the smallness of the relative velocity.

The existence of a time constant, $1/\Omega$, associated with the friction process as described by the LuGre model, enables a rational time adaptivity strategy. The following values of the parameters give good results for a wide range of problems: $\Delta\tau_{\min} = 0.02$, $\bar{v}_{\min} = 5$, $\alpha = 1.2$.

Chapter V

NUMERICAL EXAMPLES AND CONCLUSIONS

5.1 Numerical Examples

Two examples will be studied in this section. The same contact model and friction model were used for both examples. A linear spring with a stiffness constant $k = 15$ MN/m was used for the intermittent contact model, and the linear damping coefficient for dissipative force is $\mu = 10^{-3}$. The parameters for the time adaptivity algorithm described earlier are: $\varepsilon_p = 3.0 \times 10^{-6}$, $\bar{q}_{\min} = 5$, and $\alpha = 1.2$. The LuGre model was used to model the friction phenomena with the following parameters, see Table 1.

Table 1: Parameters for LuGre friction model

σ_0 [m ⁻¹]	10 ⁵
σ_1 [sec/m]	0.0
σ_2 [sec/m]	0.0
v_s [m/sec]	10 ⁻³
μ_k	0.30
μ_s	0.30
γ	2.0

5.1.1 Spatial mechanism

The spatial mechanism depicted in Fig. 7 consists of a crank of length $L_a = 0.2$ m connected to the ground at point **S** by means of a revolute joint that allows rotation about an axis parallel to \bar{v}_1 . The motion of the crank is prescribed as $\theta = \Omega t$, where $\Omega = 20$ rad/sec. At point **P**, the crank connects to a link of length $L_b = 1$ m through a universal joint that allows rotations about axes \bar{v}_2 and \bar{v}_3 . The other end of the link attaches to a spherical joint at point **Q**. In turns, this joint connects to a prismatic joint of mass $m_Q = 5$ kg that allows relative displacements along axis \bar{v}_1 . Finally, this prismatic joint is attached to a flexible beam, cantilevered at point **O**. The physical properties of the flexible beam, link and crank are listed in Table 2.

Two cases were contrasted in this example; for *case 1*, the spherical joint at point **Q**

Table 2: Sectional properties of spatial mechanism

	Flexible beam	Link	Crank
Bending stiffnesses I_{22} [kN·m ²]	23.0	12.0	23.2
Bending stiffnesses I_{33} [kN·m ²]	23.0	12.0	29.8
Torsional stiffness GJ [kN·m ²]	18.0	9.00	28.0
Mass per unit span m [kg/m]	1.60	0.85	1.60

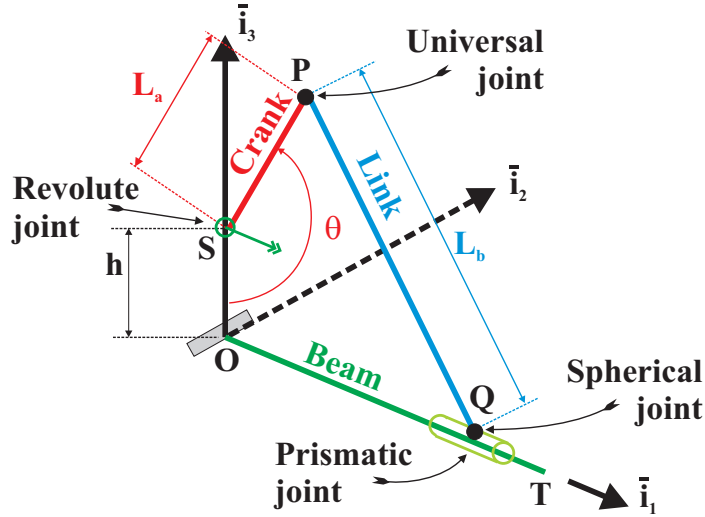


Figure 7: Configuration of the spatial mechanism.

was treated as a kinematic constraint, whereas in *case 2*, the same spherical joint features the clearance model described in section 2.1 with $\rho^k = 50$ and $\rho^\ell = 49.5$ mm. For *case 1*, the simulation was run at a constant time step of $\Delta t = 10^{-3}$ sec; for *case 2*, the time adaptivity algorithms were used. Simulations were run for a total of six revolutions of the crank to obtain a periodic solution, and results will be presented for the fifth revolution of the crank.

The relative tangential velocity at the clearance joint is shown in Fig. 8 for *case 2*. Note the several occurrences of nearly vanishing relative velocities at crank angular positions from 150 to 250 degrees. The resulting frictional force is shown in Fig. 9. Note that at crank angle of about 275 degrees, contact in the joint is lost and the friction force vanishes. This intermittent contact behavior, coupled with the elastic response of the system, creates rapid variations in the normal contact force that are reflected in the friction force.

Fig. 10 shows the time history of the root forces in the beam at point **O**. Whereas

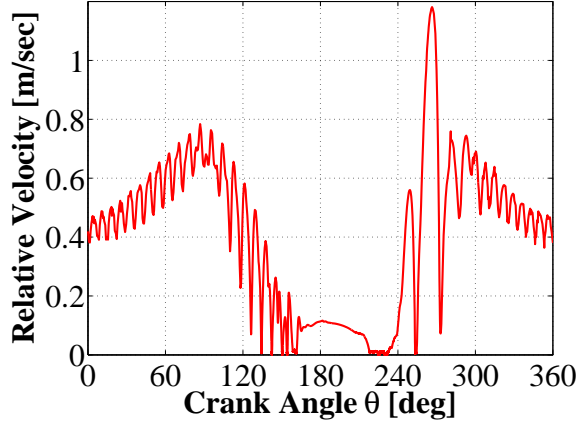


Figure 8: Relative tangential velocity at the spherical joint for *case 2*.

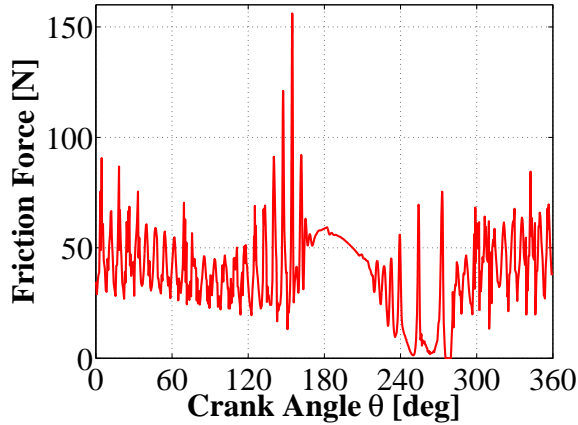


Figure 9: Friction force at the spherical joint for *case 2*.

the overall responses for *cases 1* and *2* are qualitatively similar, it is clear that the strong variations in both normal and tangential contact forces excite the elastic modes of the system, resulting in full coupling between the dynamic response of the system and the behavior of the contact forces. The frequency of the response variation for *cases 2* is about 46 Hz. This frequency is close to one of the bending frequencies of the link when it is considered as a simply supported beam, and is much higher than the frequency of the prescribed rotation at point **S**, about 3.2 Hz. The same comments can be made concerning the axial forces at the mid-span of link, as shown in Fig. 11; the oscillatory component of the stresses would strongly impact the fatigue life of these structural components.

It is interesting to note that the change of the relative velocity at crank angular positions

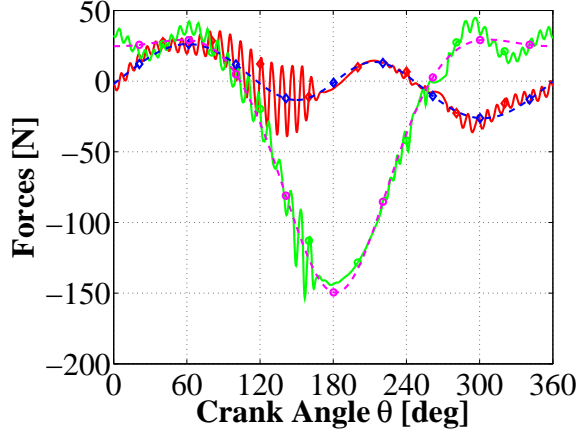


Figure 10: Beam root forces at point O : F_2 : \diamond , F_3 : \circ . (Solid line: *case 2*; dashed line: *case 1*).

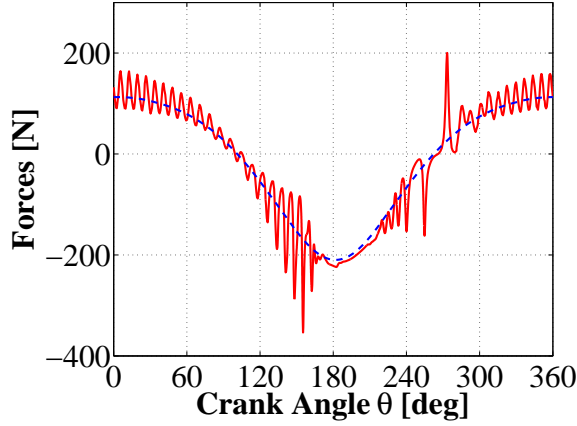


Figure 11: Axial forces at mid-span of link. (Solid line: *case 2*; dashed line: *case 1*).

from 170 to 210 degrees is slow, see Fig. 8, although the overall change of the relative velocity is rapid. This slow change in the relative velocity leads to a smooth contact force and then the friction force in Fig. 9 for the same crank angular positions. Accordingly, the high frequency components in the response of the system are not seen in Figs. 10 and 11 for the same crank angular positions.

Finally, the implication of the varying relative velocity on the time step size used in the simulation is evident in Fig. 12; clearly, for this problem, the time step size for the simulation is driven by the friction model. The parameters associated with the time step size control are: $\Delta\tau_{\min} = 5.0 \times 10^{-4}$, $\bar{v}_{\min} = 5$, $\alpha = 1.5$.

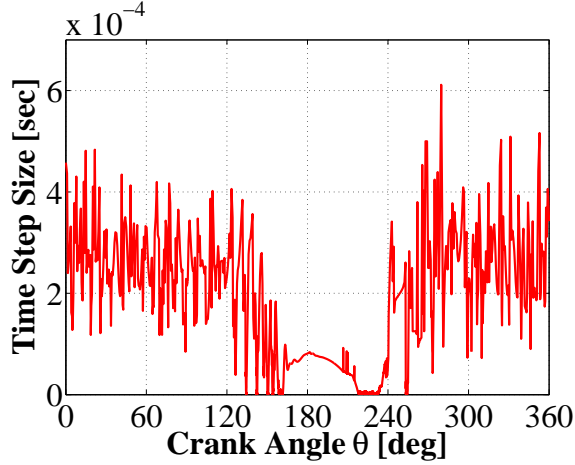


Figure 12: Time step size used in the simulation for *case 2*.

5.1.2 Supercritical rotor

The simple rotor system depicted in Fig. 13 features a flexible shaft of length $L_s = 6$ m with a mid-span rigid disk of mass $m_d = 5$ kg and radius $R_d = 15$ mm. The shaft is a thin-walled, circular tube of mean radius $R_m = 50$ mm and thickness $t = 5$ mm; its sectional properties are listed in Table 3. The center of mass of the shaft is located at a 1 mm offset from its geometric center. At point **R**, the shaft is connected to the ground by means of a revolute joint; at point **T**, it is supported by a spatial clearance joint. The radius of the cylinder is $\rho^k = 80.8$ mm and that of the disk is $\rho^\ell = 80$ mm.

Table 3: Sectional properties of flexible shaft

Bending stiffnesses I_{22} [kN·m ²]	28.20
Bending stiffnesses I_{33} [kN·m ²]	28.70
Torsional stiffness GJ [kN·m ²]	22.10
Mass per unit span m [kg/m]	0.848

At first, the natural frequencies of the shaft were computed and the critical speed zone was found to correspond to shaft angular speeds $\Omega \in [44.069, 44.453]$ rad/sec.

The system is initially at rest and a torque is applied at point **R** with the following schedule

$$Q(t) = Q_0 \begin{cases} (1 - \cos 2\pi t) & t \leq t_s \\ (1 - \cos 2\pi t_s) & t > t_s \end{cases}, \quad (55)$$

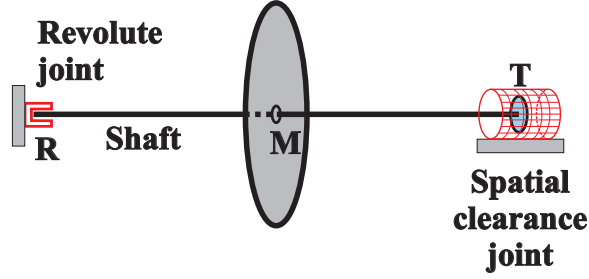


Figure 13: Configuration of the supercritical rotor system.

where $Q_0 = 0.825 \text{ N}\cdot\text{m}$ and $t_s = 0.93 \text{ sec}$. The time history of the resulting angular velocity of the shaft is depicted in Fig. 14 which also indicates the unstable region. After 2 sec, the rotor has crossed the unstable region of operation and stabilizes at a supercritical speed of about 50 rad/sec. The trajectory of the mid-span point **M** is shown in Fig. 15. Since the shaft must first cross the unstable operation zone, the trajectory first spirals away from the axis of rotation of the shaft, as expected. Once the unstable zone is crossed, the shaft regains equilibrium and due to the friction in the spatial clearance joint, the amplitude of the motion decreases. Since in supercritical operation the shaft is self centering, a displacement of about 1 mm (corresponding to the center of mass offset) is expected for point **M**.

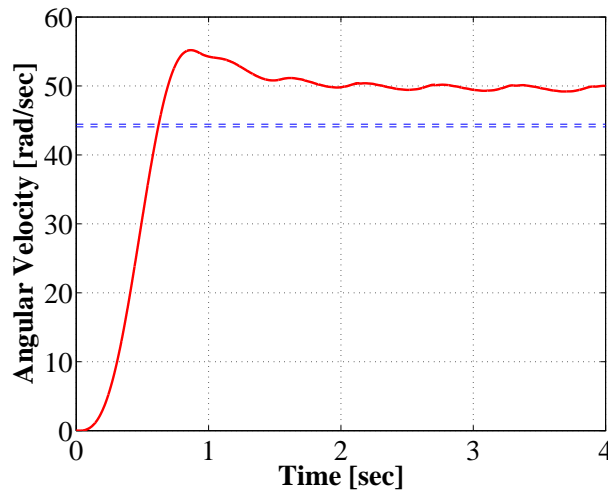


Figure 14: Time history of the angular velocity of the shaft. The dashed lines indicate the unstable zone of operation: $\Omega \in [44.069, 44.453] \text{ rad/sec}$.

The time history of the normal contact force is depicted in Fig. 16; large contact forces

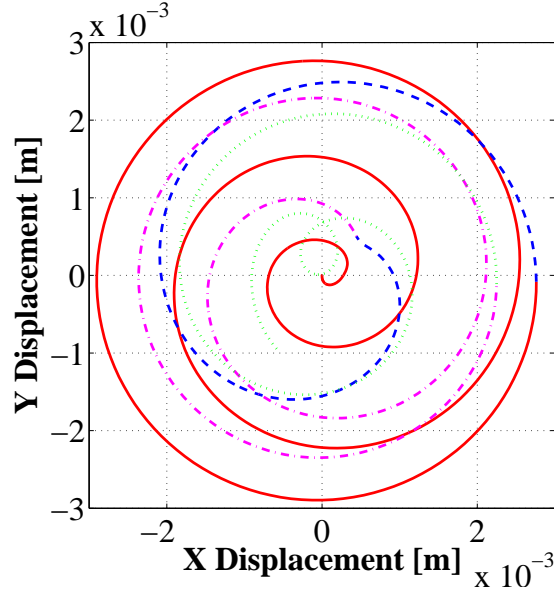


Figure 15: Trajectory of the shaft mid-span point M. (Solid line: $0 < t < 0.875$ sec; dashed line: $0.875 < t < 1.065$ sec; dashed-dotted line: $1.065 < t < 1.340$ sec; dotted line: $1.340 < t < 1.650$ sec.)

are generated as the shaft crosses the unstable zone, however, while regaining stability, intermittent contact episodes are observed, at 2.1 and 2.7 sec into the simulation. When contact is restored, large impact forces are experienced, up to about 100 N (not shown in Fig. 16), *i.e.*, an order of magnitude larger than that during the continuous contact regime. In supercritical operation, the contact force decreases to smaller levels. Similar behavior is observed in Fig. 17 that depicts the bending moments at the root of the shaft.

In this problem, the relative velocity at the spatial clearance joint always remains much larger than the Stribeck velocity; hence, the friction model has little impact on the computation strategy. The parameters associated with the time step size control for this example were selected as: $\Delta\tau_{\min} = 0.1$, $\bar{v}_{\min} = 500$, $\alpha = 1.2$.

5.2 Conclusions

The present research has proposed an approach to increase the versatility and accuracy of unilateral contact models in multibody systems. Two joint configurations were developed, the planar and spatial clearance joints that can deal with typical configurations where contact and clearance are likely to occur. More general configurations could be developed

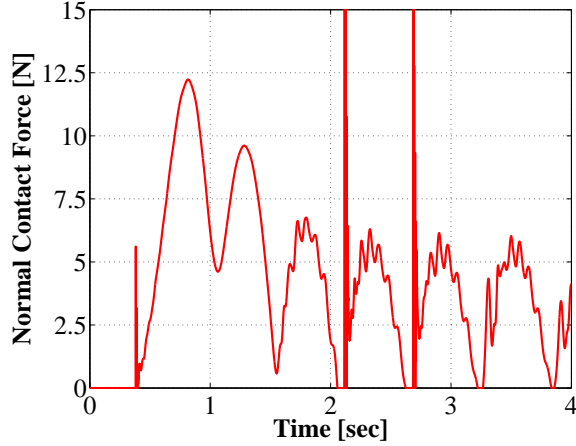


Figure 16: Time history of normal contact force of the spatial clearance joint at point **T**.

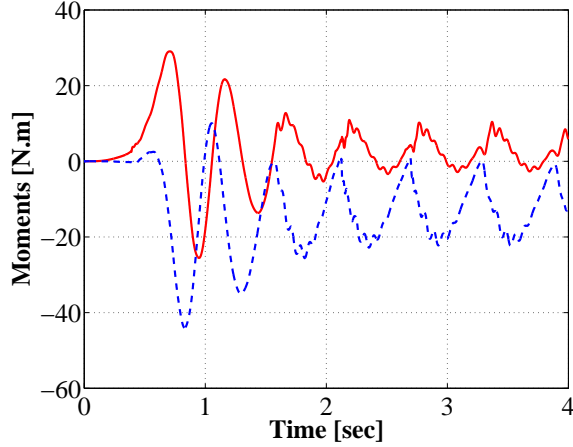


Figure 17: Time history of root bending moments in the shaft at point **R**. (Solid line: M_2 ; dashed line: M_3 .)

based on the same principles.

The kinematic analysis of the joint yields two important quantities: the relative distance between the bodies that drives the intermittent contact model and the relative tangential velocity between the bodies that drives the friction model. An arbitrary contact force-approach relationship can be used for the contact model. For the friction model, the use of the LuGre model was proposed in this work. This physics based model is capable of capturing a number of experimentally observed phenomena associated with friction [32, 123, 84]. From a numerical standpoint, it eliminates the discontinuity associated with Coulomb's

friction law. Discretizations were proposed for both normal contact force and friction force that imply an energy balance for the former and energy dissipation for the latter. When combined with the energy decaying schemes used in this effort, these properties of the discretizations guarantee the nonlinear stability of the overall numerical process.

The numerical simulations rely on time step adaptivity; simple, yet effective strategies were given to evaluate the required time step size when contact and friction are occurring. The efficiency of the proposed approach was demonstrated by realistic numerical examples that demonstrate the coupling between contact and friction forces and the overall dynamic response of the system.

Chapter VI

INTRODUCTION TO MODELING ELASTOMERIC DAMPERS

6.1 Introduction to Behavior of Elastomeric Materials

After John Dunlop in England invented the first commercially successful pneumatic tire in 1889, which was at that time used for bicycles [122], elastomeric materials have become one of the most widely used engineering materials with applications including tires, engine mounts, shock-absorbing bushes, seals, etc. However, unvulcanized elastomers are generally not very strong, do not maintain their shapes after a large deformation, and can be very sticky; thus, most useful elastomeric products require vulcanization, a process that increases elasticity and reduces the amount of permanent deformation remaining after removal of the deforming force. Thus vulcanization increases elasticity and decreases plasticity of elastomeric materials [97].

For elastomers to become suitable for specific applications, special fillers, for example, carbon-black or silica, are usually added to improve the strength and toughness properties of elastomers during vulcanization. The reinforcement of elastomers by adding fillers has been extensively studied in the past, particularly in the 1960s and 1970s [97]. The use of reinforcing fillers induces a simultaneous increase in modulus and deformation at failure. These increases characterize elastomer reinforcement. Curiously, the replacement of a part of the deformable matrix by solid objects does not reduce its deformability. This fascinating paradox explains the ability of reinforced elastomers to provide unique material properties and applications and justify their success in different technological fields.

The addition of fillers to elastomers considerably enhances the properties such as strength, tear and abrasion resistance, and stiffness [35]. The fillers also serve to greatly alter the inelastic behavior and temperature dependence of the filled elastomers, often resulting in completely different behavior than exhibited by the neat elastomers. For example, small

amounts of filler may significantly alter the temperature coefficient of the modulus of elasticity, even change the sign of the coefficient. Similarly, the addition of reinforcing fillers leads to a strongly pronounced nonlinear behavior, even under small deformations. Applications of filled elastomers are numerous and important and include automotive engine mounts, flexible couplings and seismic and vibration isolation systems. An example of advanced applications of elastomeric materials is a lead-lag damper used in rotorcraft to dampen the inplane motions of the rotor blades. This is a demanding application that is crucial to the performance of the helicopter.

The experimentally observed mechanical response of a filled elastomer can usually be subdivided into four parallel fundamental effects which together characterize the typical overall response of filled elastomers [98]:

1. **Finite elasticity.** The elasticity of elastomeric materials can be modeled by a hyperelastic model, which is by definition perfectly elastic for finite deformation. It follows that their stress-strain behavior may be described by a strain energy density function, representing the work that must be done on unit volume of the material in the reference state to deform it to the current configuration [100].
2. **Finite viscoelasticity.** Viscoelasticity leads to rate-dependent hysteresis such as relaxation and creep phenomena and is apparent in creep and relaxation tests. Cyclic loading tests show a typical frequency-dependent hysteresis as well where the area of the hysteresis loop increases with increasing stretch rates. This phenomenon can be explained micromechanically by a rearrangement of secondary weak bonds between polymer chains in the deformation process.
3. **Finite elastoplasticity.** This elastoplastic effect is responsible for rate-independent hysteresis phenomena associated with relaxed equilibrium states. This phenomenological effect observed in filled elastomeric materials is called *Payne's effect* [108, 107, 45], which is a partial rate-independent response. This phenomenon can be identified as a hysteresis of the relaxed equilibrium response within cyclic deformation processes and is usually denoted as a plastic effect. Due to Payne's effect, the stiffness of the

filled elastomers under dynamic deformations is strongly dependent on the amplitude of the deformations. Increasing strain amplitudes leads to a decrease in the dynamic stiffness.

4. **Rate-independent damage response.** Under cyclic loading, *filled elastomers* develop a significant stress-softening during the first several loading cycles. This is the so-called *Mullins' effect* [101, 102, 56]. This effect can be interpreted as a damage effect where the evolution of the damage depends critically on the maximum stretch obtained in the deformation history.

6.2 *Motivation*

Elastomeric materials have found increasing use in many vehicles, from cars and trucks to helicopters. In helicopters, the need to stabilize the very lightly damped lead-lag motions of rotor blades has necessitated the use of external dampers. Many articulated rotor helicopters use hydraulic dampers, which provide high levels of damping but are also associated with high maintenance costs and difficulties in evaluating their conditions due to the presence of seals, lubricants and numerous moving parts, all operating in a rotating frame.

The motivation to avoid problems associated with hydraulic dampers prompted the industry to switch to elastomeric lead-lag dampers that feature simpler mechanical design, lower part count, and result in “dry” rotors. In the near future, it is quite likely that the older hydraulic dampers will be targeted for replacement with more modern elastomeric components when the rotorcraft systems are being upgraded.

Bearingless and hingeless rotor configurations typically utilize elastomeric dampers to provide the required lead-lag damping to avoid problems associated with hydraulic dampers. However, the design of robust elastomeric dampers is hampered by a lack of reliable analytical tools that can be used to predict their damping behavior in the presence of the large multi-frequency nonlinear motions experienced by the rotor and thus the damper. Clearly, there is a need to develop advanced modeling tools for the analysis and design of elastomeric components.

Indeed, the behavior of elastomeric dampers is complex, and a large number of factors

influence their response. Elastomeric materials feature hyperelastic behavior, nonlinear dissipation characterized by complex hysteresis loops, and dependence on amplitude, frequency, and temperature. The need for accurate modeling of elastomeric materials was recognized early, and highly simplified analysis procedures based on table look-up methods were initially developed. Next, simple linearized models were developed based on Kelvin chains and Maxwell models [46]; the parameters of the models were identified from experimental measurements. In view of the observed nonlinear behavior of the dampers, more complex material models were developed; the stiffness and damping parameters were allowed to be nonlinear functions of the amplitude of damper stroke [43], or of the force acting in the element [49].

Recently, more sophisticated models were derived based on the concept of *augmented thermodynamic fields* (ATF) [85] and *an-elastic displacement fields* (ADF) [86]. In these models, internal variables are introduced that interact with the mechanical displacement field of continuum mechanics. A nonlinear ADF model was developed to model elastomeric dampers [120], [28]; the parameters of the model were identified using experimentally measured stress levels under various harmonic shear strain amplitudes. Applications of this model to helicopter dampers were presented in [121]. The ADF model was further refined to reduce the errors between the measured and predicted material complex moduli. A rate-independent, friction-spring element (Iwan model) was added to the ADF model to allow for low frequency material stiffness that is different from their high amplitude counterpart. The inclusion of both rate-dependent (inherent to the ADF model) and rate-independent (associated with the Iwan element) nonlinearities was found necessary for capturing the frequency and amplitude dependence of elastomeric dynamic behavior [29]. This refined model was shown to be suitable for the prediction of rotor aeroelastic response [30].

6.3 Modeling Approaches of Elastomeric Dampers

Various approaches to the modeling of dampers were reviewed by Kunz [82] who points out that “Some of the damper models performed quite well, but all were saddled with severe restrictions.” These severe restrictions, coupled with the nature of the models themselves

(see below) result in poor predictive capabilities that hamper many industry applications of elastomers and motivate the proposed effort described herein.

6.3.1 Device models and first-principles-based models

All the models discussed above are *device* or *lumped parameters models*; in fact, all models are combinations of Kelvin chains, Maxwell models and Iwan models featuring linear and/or nonlinear material parameters. A device model is a “black box” approach: a relationship is sought between the time-dependent stroke of the damper and the resulting force; the actual components of the device are not modeled *per se*. That is, one could not take the materials and geometry of particular conceptual design for a damper and predict its behavior based on these models. Instead, a host of experiments must be undertaken to first identify the *device* parameters. Thus, the damper must first exist and it must be tested. On the other hand, a first-principles model predicts the behavior of the device based on a continuum mechanics approach: the configurations of the various components of the device are modeled using a finite element approach, and material behavior is represented by an appropriate set of nonlinear constitutive laws and *material* parameters. Thus, such a model would not require the damper to exist; indeed, it could be used to design dampers.

The state of the art in first-principles modeling of elastomeric dampers is reflected in the approaches of Miehe and Keck [98], or Austrell *et al.* [9], for instance. The former researchers developed continuum mechanics based formulations to predict the response of filled, damaged, rubbery polymers. Their material model superimposes the finite responses from elastic, plastic, viscoelastic, and thermodynamic sources. The kinematics are based on logarithmic principal strains and a scalar damage variable. The second law of thermodynamics is invoked, which provides a scientific basis for relationships among the various physical phenomena being modeled. Such a material model can be used to create a finite element scheme which, in turn, could be used to model elastomeric dampers. Some other approaches for modeling elastomeric materials will be discussed in Chapter 11

6.3.2 Advantages and disadvantages of the models

The advantages of the device model approach are as follows.

1. The approach leads to simple models: typically, a small number of nonlinear differential equations are obtained that can be readily included in a comprehensive analysis of the vehicle.
2. The user of the model does not need to understand how the elastomeric device works.

However, the device model approach also suffers serious drawbacks.

1. Costly experimental programs are required to identify device parameters. Tests must be run at various amplitude levels, frequencies, and temperatures. If the tests are performed at only one harmonic test, it is impossible to ascertain the validity of the model in the time domain under arbitrary excitations.
2. Device model parameters are not *material parameters*, such as Young's modulus or the bulk modulus of a material; rather, they are *device parameters*, in the sense that they characterize the behavior of a specific device. Device model parameters cannot be used to characterize the behavior of another device presenting a different configuration, even if the same elastomer is used.
3. Device parameters represent the combined effects of material nonlinear elastic and damping characteristics, and device configuration. Consequently, these parameters are not expected to directly relate to either material characteristics or geometric configuration.
4. The complexity of device models is not the consequence of an intrinsically complex behavior of device components, but rather, reflects the fact that device model is a convolution of both material properties and configuration.
5. The device model approach can lead to erroneous identification of "physical phenomena." For instance, the response of dampers under dual frequency excitation was identified early on as a difficult problem: the responses of the device at two different frequencies cannot be superimposed to yield its response under the combined excitation. In a device model approach, this appears to be a new phenomenon. Actually, it

is a simple consequence of the fact that superposition cannot be used in the presence of nonlinear material characteristics; the superposition principle only applies to linear problems. Dual frequency effects complicate a device model, which must include additional parameters to properly capture this behavior and an increased amount of experimental data is required to identify these additional parameters.

On the other hand, the advantages of approaching the modeling from first-principles are as follows:

1. It makes use of the extensive engineering knowledge readily available for the various components of the device. For instance, the theory of rubber elasticity is well developed and simple constitutive laws exist to model this complex behavior. The Ogden model [106, 105], among many others, reliably predicts the hyperelastic behavior of elastomeric materials from very small to large strain levels. Yet, this model only involves two or three parameters, and these are truly *material parameters*. Such models are implemented in many commercial finite element packages and are routinely used to predict the behavior of complex parts such as rubber seals, bushings and dampers.
2. Although finite element modeling of quasi-incompressible materials such as elastomer offers some challenges to numerical analysts, techniques to overcome these problems are now well documented and readily available.
3. First-principles models enable the design of devices that will present desirable, possibly nonlinear characteristics. Rather than selecting a specific device from a manufacturer's catalog that might not suit his needs, a vehicle designer would approach a manufacturer with a potential design that features close to ideal behavior. Because both manufacturer and designer describe the device in terms of the functionality and properties of its components, the device selection process can be significantly shortened; expensive, time-consuming iterations and tests will be avoided; and a better device will be obtained in the final design.

The disadvantage of the first-principles-based modeling approach is that experimental testings are required to identify the material properties/parameters. Although some material properties for certain elastomeric materials are available in the literature, material parameters for a particular elastomer have to be identified from experimental data.

6.4 Road Map

The discussion presented in the previous section clearly indicates the need for more *accurate, first-principles-based models of elastomeric dampers*. The first objective of this research is to develop a finite element based tool for modeling the response of complex components made of elastomeric materials. Next, this tool will be integrated with a finite element based, multibody dynamics analysis code to accurately simulate the dynamic response of vehicles using elastomeric components, such as cars, trucks or rotorcraft.

The fundamental theories (elasticity and viscoelasticity) for the elastomeric materials are available in the literature; however, applications of these first-principles-based models in the multibody dynamics community, specifically rotorcraft industry, are very limited. The current analyses are heavily dependent on the lumped-parameter based device models and consequently, the effects of configuration and dissipative nonlinearities on the damper behavior are not accurately accounted for. The proposed first-principles-based analytical simulation approach will bridge this gap between the continuum mechanics based models and the comprehensive dynamic analysis tools. Such computationally efficient modeling applications will enable the design of devices that possess desirable, nonlinear characteristics and account for the true dissipative nature of elastomeric materials. To implement the first-principles-based model of elastomeric material within a comprehensive analysis framework the following steps are required:

1. **Finite element formulation for elastomeric components.** In the first-principles-based elastomeric damper model, the configuration of the elastomeric component should be considered. Thus, a two-dimensional continuum finite element will first be developed and implemented. This element is capable of modeling plane strain, plane

stress and axisymmetric problems. A finite element tool, which consists of the two-dimensional continuum element, mesh tool, numerical solver and different material models will then be developed. The material models will include elastic models (for validation purpose) and elastomeric material models (which will be developed next).

2. **Model elastic behavior of elastomers.** The three-dimensional constitutive laws for the elastic behavior of elastomeric materials will be reviewed and an appropriate set of them, suitable for carbon-black filled elastomeric materials, will then be selected. The constitutive laws for the hyperelastic behavior of elastomeric materials, which are typically developed from an assumed strain energy function, are well understood and many accurate models are well documented in the literature. For instance, the Ogden model [106, 105] or the Yeoh model [132] provide excellent correlation with experimental measurements over a wide range of strain levels.

3. **Model inelastic behavior of elastomers.** The constitutive laws for the inelastic behavior of elastomeric materials will be reviewed and an appropriate set of them will then be selected. While the elastic behavior of elastomers has received extensive scrutiny, the *nonlinear inelastic behavior* of the same materials is far less investigated: little literature is available on the subject. This is easily understood because elastomeric materials are most often used as *isolators* rather than dampers. For instance, in automotive applications, tires isolate the car from the road to improve ride comfort, but do not provide energy dissipation. Indeed, if tires dissipate energy, they would rapidly heat up and deteriorate; tire manufacturers formulate the elastomeric material used to make such component so as to minimize energy dissipation. Consequently, the damping characteristics of the material are ignored in the modeling of tires as they have little effect on their dynamic response. The inelastic behavior of the material is altogether ignored in the constitutive laws.

The situation is sharply different when elastomeric materials are used to produce dampers, rather than isolators. Consider, for instance, the design of a rotorcraft lead-lag damper in a ground resonance situation. It is well known that the stability of

the system is controlled by the product of the damping coefficients in the fixed and rotating systems. If the lead-lag damper is made of elastomeric material, the damping characteristics of the device become a crucial element of the problem.

Considering the complexity and scarcity of literature devoted to the nonlinear inelastic behavior of the elastomers, a one-dimensional inelastic model will be first set up. The one-dimensional inelastic behavior of elastomeric materials can be adequately captured through a combination of simple elements [8]. A typical rheological model of both elastic and inelastic behavior includes one elastic component, in parallel with one or more viscous components, and one or more plastic components, as depicted in Fig. 18. The viscous components model the viscous damping (*i.e.*, rate-dependent damping) that is prevalent in the rubber base of elastomers, whereas the plastic components model the rate-independent damping that is prevalent in the rubber-carbon and carbon-carbon interfaces of carbon-black filled elastomers. All elements are subjected to the same strain, the total stress is the sum of the elastic, viscous and plastic components. Various options of one-dimensional inelastic models in literature will be investigated and the most appropriate one will be selected.

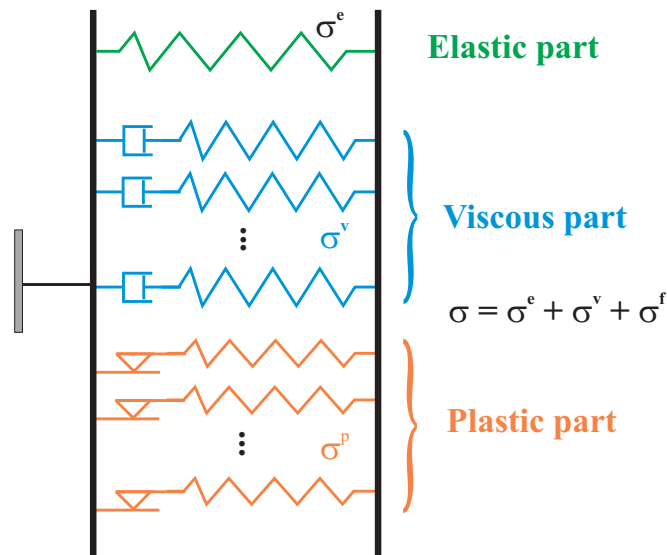


Figure 18: One-dimensional rheological model featuring elastic, viscous and plastic components.

The one-dimensional model for the inelastic behavior of elastomers will then be generalized to deal with the general, three-dimensional case of elastomers under multi-axial loading condition. Few constitutive laws for the nonlinear, three-dimensional inelastic behavior of elastomeric materials have appeared in the literature, but are of critical importance to the success of this work. The relative merits of the three-dimensional inelastic models in literature will be assessed and the most appropriate formulation will be selected.

4. **Implement and validate the first-principles-based elastomer model.** The constitutive laws developed earlier will be implemented in the finite element tool. The models to be developed must be *computationally efficient* since they are to be coupled with comprehensive, vehicle dynamics analysis software. The constitutive laws and their finite element implementation will then be validated. The validation will be fulfilled in two steps. First, the predictions from the developed model for simple elastomeric components will be compared with results from other commercial software, for example, ABAQUS. Second, the developed model must also be validated against experimental data. The same damper model will be set up using the developed first-principle-based elastomeric model and be simulated under the same conditions as in the experiments. The numerical predictions will be validated against the corresponding experimental results. Before the predictions can be compared with experimental data, material properties for the elastomer from which the damper is made must be identified through simple experiments. Although some material properties for certain elastomeric materials are available in the literature, material parameters for specific elastomeric material have to be identified from experimental data. A parameter identification procedure needs to be developed.
5. **Couple the first-principles-based elastomeric model with multibody dynamics code.** The validated finite element model of elastomeric components will be coupled with a comprehensive, multibody dynamics analysis to predict the behavior of complex systems featuring elastomeric components, for instance, rotorcraft with

elastomeric lead-lag dampers. Fig. 19 depicts the overall coupling strategy. The finite element based multibody dynamics code [17], [19] predicts the displacements of all elements of the system, and in particular the damper stroke, Δ . This stroking is the input to the first-principles-based finite element model for the elastomeric damper. Based on the constitutive laws described above and a set of material parameters, this model predicts the force, F , generated by the damper. This force is added to all other forces applied on the multibody system to predict the system response.

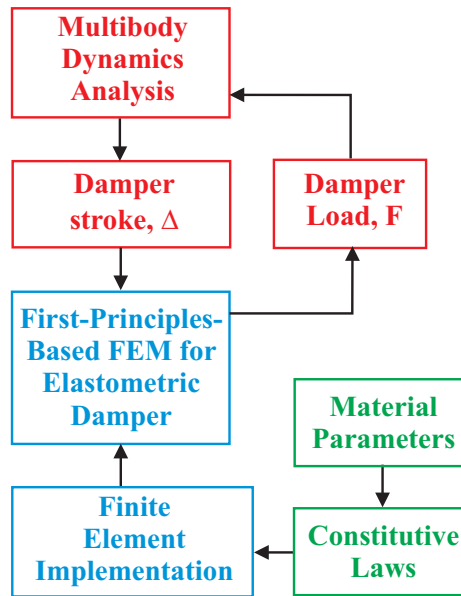


Figure 19: Coupling the first-principles-based elastomeric model with multibody systems.

Simulations of a rotorcraft with elastomeric lead-lag dampers will be performed to further verify the development of the first-principles-based damper model and the feasibility of the coupling strategy. This validation will conclude this research work.

At the conclusion of this work, a validated, first-principles-based formulation for the modeling of elastomeric devices will be available. This tool will be coupled to a finite element based, multibody dynamics formulation for the comprehensive simulation of vehicles such as cars, trucks or helicopters. The elastomeric material models will be validated by comparing their predictions against results from other commercial software and/or experimental measurements, upon the availability. The models of elastomeric devices will be

validated by comparing predictions of the developed models with experimental force/stroke measurements on rotorcraft lead-lag dampers. Finally, the coupling of these models with comprehensive vehicle dynamics models will be validated by running comprehensive rotorcraft modeling including elastomeric components.

The second part of this dissertation for modeling elastomeric dampers in multibody dynamics analysis is organized as follows: In Chapter 7, finite element formulations for the two-dimensional continuum finite element are derived. The polynomial type of hyperelastic model and a simple linear inelastic model for elastomeric materials are also discussed in the same chapter; followed by validations of the finite element implementation in Chapter 8. The coupling of a simple elastomeric damper with a realistic helicopter appears in Chapter 9 to verify the feasibility of the coupling strategy; this verification concludes the developing procedure. After the feasibility of the developing procedure is verified, the focus of the research moves to the elastomeric material models: Different hyperelastic models for elastomeric materials are reviewed in Chapters 10. Also modeling the compressibility of elastomeric materials are discussed in the same chapter. Chapter 11 discusses the modeling of the inelastic behavior of elastomeric materials; and two candidate elastomeric models in the literature are thoroughly studied and compared in Chapter 12. Chapter 13 concludes the elastomeric damper modeling and possible future work is recommended. Finally, some fundamentals for the finite deformation elasticity are included in the Appendices.

Chapter VII

FINITE ELEMENT IMPLEMENTATION

In this chapter the finite element formulations for a two-dimensional continuum finite element, called ED2, will be first derived. This finite element has nine nodes, and is capable of modeling plane strain, plane stress, and axisymmetric problems. A finite element tool is then developed in the framework of DYMORE, a finite element based multibody dynamics analysis code. The finite element tool consists of the ED2 element, mesh tool, numerical solver and different material models. The material models include elastic model (for validation purpose) and elastomeric material model.

At this time, a polynomial form of hyperelastic model and a simple linear inelastic model for the elastomeric materials will be used for verifying the feasibility of the road map proposed in Section 6.4. The elastomeric material models in literature will be reviewed in Chapter 10 for hyperelastic models and in Chapters 11 and 12 for inelastic models. The constitutive equations for the elastic materials are presented in Appendix D. The details for the mesh tool and numerical solver for the finite element tool can be found in the User's Manual for DYMORE [20].

7.1 Finite Element Formulation

7.1.1 Definition of elastic forces

According to the principle of virtual work, Eq. (491), the virtual work done by the internal stresses can be written as

$$\delta W_I = \int_v \sigma_{ij} \delta e_{ij} dv, \quad (56)$$

where v is the volume of the structure in the reference configuration, σ_{ij} the components of the 2nd Piola-Kirchhoff stress tensor defined in Eq. (456), and e_{ij} the components the Green-Lagrange strain tensor defined in Eq. (386).

For the two-dimensional case, the components the Green-Lagrange strain tensor are

$$e_{11} = u_{1,1} + \frac{1}{2} (u_{1,1}^2 + u_{2,1}^2), \quad (57a)$$

$$e_{22} = u_{2,2} + \frac{1}{2} (u_{1,2}^2 + u_{2,2}^2), \quad (57b)$$

$$2e_{12} = u_{1,2} + u_{2,1} + u_{1,1}u_{1,2} + u_{2,1}u_{2,2}, \quad (57c)$$

$$e_{33} = \frac{u_1}{x_1} + \frac{1}{2} \left(\frac{u_1}{x_1} \right)^2, \quad (57d)$$

and zero for other components. In Eqs. (57), u_i for $i = 1, 2$ denotes the displacement along i -axis and $u_{i,j} = \partial u_i / \partial x_j$. Similar notations will be adopted throughout this chapter. Note that e_{33} component of the Green-Lagrange strain tensor does not show up for the plane stress and plane strain problems and is for axisymmetric problems only. Variations of the components of the Green-Lagrange strain tensor are then readily obtained as

$$\delta e_{11} = (1 + u_{1,1})\delta u_{1,1} + u_{2,1}\delta u_{2,1}, \quad (58a)$$

$$\delta e_{22} = u_{1,2}\delta u_{1,2} + (1 + u_{2,2})\delta u_{2,2}, \quad (58b)$$

$$2\delta e_{12} = u_{1,2}\delta u_{1,1} + (1 + u_{1,1})\delta u_{1,2} + (1 + u_{2,2})\delta u_{2,1} + u_{2,1}\delta u_{2,2}, \quad (58c)$$

$$\delta e_{33} = \frac{\delta u_1}{x_1} + \frac{u_1}{x_1} \frac{\delta u_1}{x_1}. \quad (58d)$$

In finite element formulations, the displacement field within an element, $\underline{u}(x_1, x_2)$, is discretized using shape functions as

$$\underline{u}(x_1, x_2) = h_k(x_1, x_2)\hat{\underline{u}}_k, \quad (59)$$

where $h_k(x_1, x_2)$ is the shape function and $\hat{\underline{u}}_k$ the nodal displacements of k th node for $k = 1, 2, \dots, 9$. Expressions for the shape functions can be found in finite element textbooks such as [16]. Summation over the nodes is implied by the repeated index k . It now becomes possible to express variations of the strains in a compact matrix notation as

$$\delta \underline{e} = B_L \delta \hat{\underline{u}} = (B_{L0} + B_{L1}) \delta \hat{\underline{u}}. \quad (60)$$

The virtual strain array is defined as

$$\delta \underline{e} = \begin{Bmatrix} \delta e_{11} \\ \delta e_{22} \\ 2\delta e_{12} \\ \delta e_{33} \end{Bmatrix}, \quad (61)$$

whereas the nodal virtual displacement array is

$$\delta \hat{\underline{u}} = \begin{Bmatrix} \vdots \\ \delta \hat{\underline{u}}_k \\ \vdots \end{Bmatrix}. \quad (62)$$

Finally, the strain interpolation matrix B_{L0} is

$$B_{L0} = \left[\begin{array}{c} \dots \\ \dots \\ \dots \\ \dots \end{array} \left\| \begin{array}{cc} h_{k,1} & 0 \\ 0 & h_{k,2} \\ h_{k,2} & h_{k,1} \\ \frac{h_k}{x_1} & 0 \end{array} \right\| \dots \right], \quad (63)$$

whereas B_{L1} is

$$B_{L1} = \left[\begin{array}{c} \dots \\ \dots \\ \dots \\ \dots \end{array} \left\| \begin{array}{cc} u_{1,1}h_{k,1} & u_{2,1}h_{k,1} \\ u_{1,2}h_{k,2} & u_{2,2}h_{k,2} \\ u_{1,2}h_{k,1} + u_{1,1}h_{k,2} & u_{2,2}h_{k,1} + u_{2,1}h_{k,2} \\ \frac{u_1}{x_1}h_k & 0 \end{array} \right\| \dots \right]. \quad (64)$$

The array of 2nd Piola-Kirchhoff stress tensor components is defined as

$$\underline{\sigma} = \begin{Bmatrix} \sigma_{11} \\ \sigma_{22} \\ \sigma_{12} \\ \sigma_{33} \end{Bmatrix}. \quad (65)$$

Introducing Eq. (60), the virtual work done by the internal stresses, Eq. (56), now becomes

$$\delta W_I = \int_v \underline{\sigma}^T \delta \underline{e} \, dv = \delta \hat{\underline{u}}^T \int_v B_L^T \underline{\sigma} \, dv = \delta \hat{\underline{u}}^T \underline{F}^e, \quad (66)$$

where the elastic force array, \underline{F}^e , was defined as

$$\underline{F}^e = \int_v B_L^T \underline{\sigma} \, dv. \quad (67)$$

7.1.1.1 Linearization of elastic forces

Since the expression for the elastic forces is nonlinear, the computational process requires a linearization. To facilitate the process, the following notation is introduced

$$B_L^T \underline{\sigma} = B_{NL}^T \Sigma B_{NL} \hat{\underline{u}}, \quad (68)$$

where the nonlinear strain interpolation matrix is defined as

$$B_{NL} = \begin{bmatrix} \left[\begin{array}{c} h_{k,1} \\ \dots \\ h_{k,2} \\ \dots \\ 0 \\ 0 \\ \frac{h_k}{x_1} \end{array} \right] & \left[\begin{array}{c} 0 \\ \dots \\ 0 \\ \dots \\ h_{k,1} \\ h_{k,2} \\ 0 \end{array} \right] \end{bmatrix}, \quad (69)$$

and the 2nd Piola-Kirchhoff stress tensor component matrix is

$$\Sigma = \begin{bmatrix} \sigma_{11} & \sigma_{12} & 0 & 0 & 0 \\ \sigma_{12} & \sigma_{22} & 0 & 0 & 0 \\ 0 & 0 & \sigma_{11} & \sigma_{12} & 0 \\ 0 & 0 & \sigma_{12} & \sigma_{22} & 0 \\ 0 & 0 & 0 & 0 & \sigma_{33} \end{bmatrix}. \quad (70)$$

The linearization of the elastic forces now yields

$$\begin{aligned} \Delta [B_L^T \underline{\sigma}] &= [\Delta B_L^T] \underline{\sigma} + B_L^T \Delta \underline{\sigma} \\ &= B_{NL}^T \Sigma B_{NL} \Delta \hat{\underline{u}} + B_L^T \frac{\partial \underline{\sigma}}{\partial \underline{e}} \Delta \underline{e} \\ &= [B_{NL}^T \Sigma B_{NL} + B_L^T C B_L] \Delta \hat{\underline{u}}, \end{aligned} \quad (71)$$

where the material stiffness matrix was defined as

$$C = \frac{\partial \underline{\sigma}}{\partial \underline{e}}. \quad (72)$$

The linearization of the elastic forces now simply writes

$$\Delta \underline{F}^e = [K_L + K_{NL}] \Delta \hat{\underline{u}}, \quad (73)$$

where the linear and nonlinear stiffness matrices are, respectively,

$$K_L = \int_v B_L^T C B_L \, dv, \quad (74a)$$

$$K_{NL} = \int_v B_{NL}^T \Sigma B_{NL} \, dv. \quad (74b)$$

7.1.2 Definition of inertial forces

According to the principle of virtual work, Eq. (491), the virtual work done by the inertial forces can be written as

$$\delta W_E = - \int_v \delta \underline{u}^T \rho \ddot{\underline{u}} \, dv, \quad (75)$$

where v is the volume of the structure in the reference configuration, ρ the material density in the reference configuration, and \underline{u} the displacement vector. The displacement field can be interpolated using the shape function defined earlier

$$\underline{u} = H \hat{\underline{u}}, \quad (76)$$

where the displacement interpolation matrix is

$$H = \left[\begin{array}{c|c|c} \dots & h_k & 0 \\ \dots & 0 & h_k \\ \dots & \dots & \dots \end{array} \right]. \quad (77)$$

Introducing this interpolation, the virtual work done by the inertial forces, Eq. (75), now becomes

$$\delta W_E = -\delta \hat{\underline{u}}^T \int_v H^T \rho \ddot{\underline{u}} \, dv = -\delta \hat{\underline{u}}^T \underline{F}^i, \quad (78)$$

where the inertial force array, \underline{F}^i , was defined as

$$\underline{F}^i = \int_v H^T \rho \ddot{\underline{u}} \, dv. \quad (79)$$

7.1.2.1 Linearization of inertial forces

Since the expression for the inertial forces is nonlinear, the computational process requires a linearization. The linearization of the inertial forces now simply writes

$$\Delta \underline{F}^i = -M \Delta \ddot{\underline{u}}, \quad (80)$$

where the mass matrix is

$$M = \int_v H^T \rho H \, dv. \quad (81)$$

7.1.3 Definition of dissipative forces

For dissipative stresses of the form $\underline{\sigma}^d = \mu C \underline{\dot{\epsilon}}$, the dissipative forces can be written as, by analogy with the elastic forces defined in Eq. (67),

$$\underline{F}^d = \int_v B_L^T \mu C \underline{\dot{\epsilon}} \, dv = \int_v B_L^T \underline{\sigma}^d \, dv, \quad (82)$$

where μ is a dissipation parameter. The strain rates are easily computed as

$$\dot{\epsilon}_{11} = (1 + u_{1,1})\dot{u}_{1,1} + u_{2,1}\dot{u}_{2,1}, \quad (83a)$$

$$\dot{\epsilon}_{22} = u_{1,2}\dot{u}_{1,2} + (1 + u_{2,2})\dot{u}_{2,2}, \quad (83b)$$

$$2\dot{\epsilon}_{12} = u_{1,2}\dot{u}_{1,1} + (1 + u_{1,1})\dot{u}_{1,2} + (1 + u_{2,2})\dot{u}_{2,1} + u_{2,1}\dot{u}_{2,2}, \quad (83c)$$

$$\dot{\epsilon}_{33} = \frac{\dot{u}_1}{x_1} + \frac{u_1}{x_1} \frac{\dot{u}_1}{x_1}, \quad (83d)$$

and can be expressed in a compact manner as

$$\underline{\dot{\epsilon}} = B_L \dot{\underline{u}} = (B_{L0} + B_{L1}) \dot{\underline{u}}, \quad (84)$$

where the strain interpolation matrices B_{L0} and B_{L1} are defined in Eqs. (63) and (64), respectively.

7.1.3.1 Linearization of dissipative forces

Since the expression for the dissipative forces is nonlinear, the computational process requires a linearization. To facilitate the process, the following notation is introduced

$$B_L^T \underline{\sigma}^d = B_{NL}^T \Sigma^d B_{NL} \hat{\underline{u}}, \quad (85)$$

where the dissipative stress rate tensor component matrix is

$$\Sigma^d = \begin{bmatrix} \sigma_{11}^d & \sigma_{12}^d & 0 & 0 & 0 \\ \sigma_{12}^d & \sigma_{22}^d & 0 & 0 & 0 \\ 0 & 0 & \sigma_{11}^d & \sigma_{12}^d & 0 \\ 0 & 0 & \sigma_{12}^d & \sigma_{22}^d & 0 \\ 0 & 0 & 0 & 0 & \sigma_{33}^d \end{bmatrix}. \quad (86)$$

The linearization of the dissipative forces now yields

$$\begin{aligned}\Delta \left[B_L^T \underline{\sigma}^d \right] &= [\Delta B_L^T] \underline{\sigma}^d + B_L^T \Delta \underline{\sigma}^d \\ &= B_{NL}^T \Sigma^d B_{NL} \Delta \hat{\underline{u}} + B_L^T \mu C \Delta \dot{\underline{e}}.\end{aligned}\tag{87}$$

Note that for simplicity, the stiffness matrix was assumed to remain constant in the linearization process. Strain rate increments can be computed as

$$\Delta \dot{\underline{e}} = (B_{L0} + B_{L1}) \Delta \dot{\hat{\underline{u}}} + B_D \Delta \hat{\underline{u}},\tag{88}$$

where the strain interpolation matrices B_{L0} and B_{L1} are defined in Eqs. (63) and (64), respectively, and the strain rate interpolation matrix, B_D , is

$$B_D = \left[\begin{array}{c} \dots \\ \left\| \begin{array}{cc} \dot{u}_{1,1} h_{k,1} & \dot{u}_{2,1} h_{k,1} \\ \dot{u}_{1,2} h_{k,2} & \dot{u}_{2,2} h_{k,2} \\ \dot{u}_{1,2} h_{k,1} + \dot{u}_{1,1} h_{k,2} & \dot{u}_{2,2} h_{k,1} + \dot{u}_{2,1} h_{k,2} \\ \frac{\dot{u}_1}{x_1^2} h_k & 0 \end{array} \right\| \dots \end{array} \right].\tag{89}$$

The linearization of the dissipative forces now simply writes

$$\Delta \underline{F}^d = \left[K_L^d + K_{NL}^d \right] \Delta \hat{\underline{u}} + G^d \Delta \dot{\hat{\underline{u}}},\tag{90}$$

where the linear and nonlinear stiffness matrices are, respectively,

$$K_L^d = \int_v B_L^T \mu C B_D \, dv,\tag{91a}$$

$$K_{NL}^d = \int_v B_{NL}^T \Sigma^d B_{NL} \, dv;\tag{91b}$$

and the gyroscopic matrix is

$$G^d = \int_v B_L^T \mu C B_L \, dv.\tag{92}$$

7.2 Constitutive Law for Hyperelasticity of Elastomeric Materials

In this section, the constitutive law for hyperelastic materials will be derived. The derivation is based on a strain energy density function with the general polynomial form Eq. (148).

The implementation of the hyperelastic constitutive law itself is straightforward.

7.2.1 Strain energy density function

A hyperelastic material is an elastic material for which the stress-strain relationship can be derived from a *strain energy density function*. In this work, a polynomial form of the strain energy density function is selected

$$W = W(\bar{I}_1, \bar{I}_2, J) = \sum_{i+j=1}^N C_{ij}(\bar{I}_1 - 3)^i(\bar{I}_2 - 3)^j + \sum_{i=1}^N \frac{1}{D_i}(J - 1)^{2i}, \quad (93)$$

where W is the strain energy per unit of reference volume, \bar{I}_1 and \bar{I}_2 the first two invariants of the deviatoric part of the right Cauchy-Green deformation tensor defined in Eqs. (421), J the determinant of the deformation gradient tensor defined in Eq. (380), N the number of terms used in the expansion, and C_{ij} and D_i temperature-dependent material parameters. The second term of Eq. (93) considers the compressibility of the elastomeric materials, as discussed in Section 10.5. For the incompressible material, the relative change in volume of a material element in the reference and deformed configurations is zero, *i.e.*, $J = 1$, from Eq. (396), then the second term in Eq. (93) vanishes.

The hyperelastic material is assumed to be isotropic, *i.e.*, its properties are identical in all material directions. This implies that the strain energy density function should be a sole function of the invariants of the deformations. In this work, the measure of deformation will be taken as the right Cauchy-Green deformation tensor G_{ij} as defined in Eq.(381), and hence, $W = W(I_1, I_2, I_3)$, where I_1 , I_2 , and I_3 are the invariants of G_{ij} as defined in Eqs.(418). Hyperelastic materials are often nearly incompressible, *i.e.*, deformation of these materials occurs under nearly constant material volume. It seems appropriate to reflect this fact in the functional dependency of the strain energy density function, which will be written as a function of the first two invariants of the deviatoric part of the right Cauchy-Green deformation tensor, \bar{I}_1 and \bar{I}_2 , and of the determinant of the deformation gradient tensor, J . In view of Eqs. (421) and (418), this simply corresponds to a change of variables, and leads to the assumed form of the strain energy density function, $W = W(\bar{I}_1, \bar{I}_2, J)$. For cases where the nominal strains are small or only moderately large ($< 100\%$), the first terms in the polynomial series usually provide a sufficiently accurate model.

In the unstrained configuration of the body, $G_{ij} = \delta_{ij}$, and hence, $I_1 = I_2 = 3$ and

$I_3 = 1$. This leads to $\bar{I}_1 = \bar{I}_2 = 3$ and $J = 1$. Clearly, the strain energy density function given by Eq. (93) vanishes when the material is undeformed, as expected.

7.2.2 The second Piola-Kirchhoff stress tensor

The *second Piola-Kirchhoff stress tensor*, σ_{ij} , is defined as the partial derivative of the strain energy density function with respect to the Green-Lagrange strain tensor, e_{ij} , *i.e.*,

$$\begin{aligned}\sigma_{ij} &= \frac{\partial W}{\partial e_{ij}} = \frac{\partial W}{\partial G_{kl}} \frac{\partial G_{kl}}{\partial e_{ij}} = 2 \frac{\partial W}{\partial G_{ij}} \\ &= 2 \left(\frac{\partial W}{\partial \bar{I}_1} \frac{\partial \bar{I}_1}{\partial G_{ij}} + \frac{\partial W}{\partial \bar{I}_2} \frac{\partial \bar{I}_2}{\partial G_{ij}} + \frac{\partial W}{\partial J} \frac{\partial J}{\partial G_{ij}} \right),\end{aligned}\tag{94}$$

where $\partial G_{kl}/\partial e_{ij} = 2$ which can be easily obtained from Eq. (383), and the chain rule for derivatives was used. The derivatives of the strain energy density function with respect to \bar{I}_1 , \bar{I}_2 and J are readily computed from Eq. (93) to find

$$\begin{aligned}\frac{\partial W}{\partial \bar{I}_1} &= \sum_{i+j=1}^N i C_{ij} (\bar{I}_1 - 3)^{i-1} (\bar{I}_2 - 3)^j, \\ \frac{\partial W}{\partial \bar{I}_2} &= \sum_{i+j=1}^N j C_{ij} (\bar{I}_1 - 3)^i (\bar{I}_2 - 3)^{j-1}, \\ \frac{\partial W}{\partial J} &= \sum_{i=1}^N \frac{2i}{D_i} (J - 1)^{2i-1},\end{aligned}\tag{95}$$

respectively. Next, the derivatives of \bar{I}_1 , \bar{I}_2 and J with respect to the components of the right Cauchy-Green deformation tensor will be evaluated. First, the derivatives of the invariants I_1 , I_2 and I_3 with respect to the components of the right Cauchy-Green deformation tensor, G_{ij} are computed as

$$\frac{\partial I_1}{\partial G_{ij}} = \delta_{ij},\tag{96a}$$

$$\frac{\partial I_2}{\partial G_{ij}} = I_1 \delta_{ij} - G_{ij},\tag{96b}$$

$$\frac{\partial I_3}{\partial G_{ij}} = I_3 G_{ij}^{-1}.\tag{96c}$$

Using the chain rule and combining Eqs. (421) and (96) one can find

$$\frac{\partial \bar{I}_1}{\partial G_{ij}} = \frac{\partial \bar{I}_1}{\partial I_1} \frac{\partial I_1}{\partial G_{ij}} + \frac{\partial \bar{I}_1}{\partial I_2} \frac{\partial I_2}{\partial G_{ij}} + \frac{\partial \bar{I}_1}{\partial I_3} \frac{\partial I_3}{\partial G_{ij}} = I_3^{-1/3} \left(\delta_{ij} - \frac{1}{3} I_1 G_{ij}^{-1} \right), \quad (97a)$$

$$\frac{\partial \bar{I}_2}{\partial G_{ij}} = \frac{\partial \bar{I}_2}{\partial I_1} \frac{\partial I_1}{\partial G_{ij}} + \frac{\partial \bar{I}_2}{\partial I_2} \frac{\partial I_2}{\partial G_{ij}} + \frac{\partial \bar{I}_2}{\partial I_3} \frac{\partial I_3}{\partial G_{ij}} = I_3^{-2/3} \left(I_1 \delta_{ij} - G_{ij} - \frac{2}{3} I_2 G_{ij}^{-1} \right), \quad (97b)$$

$$\frac{\partial J}{\partial G_{ij}} = \frac{\partial J}{\partial I_1} \frac{\partial I_1}{\partial G_{ij}} + \frac{\partial J}{\partial I_2} \frac{\partial I_2}{\partial G_{ij}} + \frac{\partial J}{\partial I_3} \frac{\partial I_3}{\partial G_{ij}} = \frac{1}{2} I_3^{1/2} G_{ij}^{-1}. \quad (97c)$$

Finally, the components of the second Piola-Kirchhoff stress tensor are obtained by substituting Eqs. (95) and (97) into Eq. (94).

7.2.3 Stiffness tensor

When linearizing the nonlinear equations for the behavior of hyperelastic materials, it is necessary to evaluate the effective stiffness of the material, *i.e.*, the derivative of the second Piola-Kirchhoff stress tensor with respect to the Green-Lagrange strain tensor, to find the *tangent stiffness tensor*

$$c_{ijkl} = \frac{\partial \sigma_{ij}}{\partial e_{kl}} = \frac{\partial \sigma_{ij}}{\partial G_{pq}} \frac{\partial G_{pq}}{\partial e_{kl}} = 2 \frac{\partial \sigma_{ij}}{\partial G_{kl}}. \quad (98)$$

To simplify the computation and enable index notation, the following variables are defined:

$\iota_1 = \bar{I}_1$, $\iota_2 = \bar{I}_2$ and $\iota_3 = J$. In view of Eq. (94), the tangent stiffness tensor becomes

$$\begin{aligned} c_{ijkl} &= 4 \frac{\partial}{\partial G_{kl}} \left(\frac{\partial W}{\partial \iota_p} \frac{\partial \iota_p}{\partial G_{ij}} \right) = 4 \left[\frac{\partial}{\partial G_{kl}} \left(\frac{\partial W}{\partial \iota_p} \right) \frac{\partial \iota_p}{\partial G_{ij}} + \frac{\partial W}{\partial \iota_p} \frac{\partial^2 \iota_p}{\partial G_{ij} \partial G_{kl}} \right] \\ &= 4 \left(\frac{\partial^2 W}{\partial \iota_p \partial \iota_q} \frac{\partial \iota_q}{\partial G_{kl}} \right) \frac{\partial \iota_p}{\partial G_{ij}} + 4 \frac{\partial W}{\partial \iota_p} \frac{\partial^2 \iota_p}{\partial G_{ij} \partial G_{kl}}. \end{aligned} \quad (99)$$

The second derivatives of the strain energy density function with respect to its variables are readily obtained from Eqs. (95)

$$\begin{aligned} \frac{\partial^2 W}{\partial \bar{I}_1 \partial \bar{I}_1} &= \sum_{i+j=1}^N i(i-1) C_{ij} (\bar{I}_1 - 3)^{i-2} (\bar{I}_2 - 3)^j, \\ \frac{\partial^2 W}{\partial \bar{I}_1 \partial \bar{I}_2} &= \frac{\partial^2 W}{\partial \bar{I}_2 \partial \bar{I}_1} = \sum_{i+j=1}^N ij C_{ij} (\bar{I}_1 - 3)^{i-1} (\bar{I}_2 - 3)^{j-1}, \\ \frac{\partial^2 W}{\partial \bar{I}_2 \partial \bar{I}_2} &= \sum_{i+j=1}^N j(j-1) C_{ij} (\bar{I}_1 - 3)^i (\bar{I}_2 - 3)^{j-2}, \\ \frac{\partial^2 W}{\partial J \partial J} &= \sum_{i=1}^N \frac{2i(2i-1)}{D_i} (J-1)^{2(i-1)}, \\ \frac{\partial^2 W}{\partial \bar{I}_1 \partial J} &= \frac{\partial^2 W}{\partial J \partial \bar{I}_1} = \frac{\partial^2 W}{\partial \bar{I}_2 \partial J} = \frac{\partial^2 W}{\partial J \partial \bar{I}_2} = 0. \end{aligned} \quad (100)$$

Finally, the second derivative of the variables ι_p with respect to the components of the right Cauchy-Green deformation tensor are evaluated based on Eqs. (97) and (96) to find

$$\begin{aligned}
\frac{\partial^2 \bar{I}_1}{\partial G_{ij} \partial G_{kl}} &= \frac{\partial}{\partial G_{kl}} \left[I_3^{-1/3} \left(\delta_{ij} - \frac{I_1}{3} G_{ij}^{-1} \right) \right] \\
&= -\frac{1}{3} I_3^{-1/3} \left(\delta_{ij} G_{kl}^{-1} + \delta_{kl} G_{ij}^{-1} - \frac{I_1}{3} G_{ij}^{-1} G_{kl}^{-1} - I_1 \frac{\partial G_{ij}^{-1}}{\partial G_{kl}} \right), \\
\frac{\partial^2 \bar{I}_2}{\partial G_{ij} \partial G_{kl}} &= \frac{\partial}{\partial G_{kl}} \left[I_3^{-2/3} \left(I_1 \delta_{ij} - G_{ij} - \frac{2}{3} I_2 G_{ij}^{-1} \right) \right] \\
&= I_3^{-2/3} \left[\delta_{ij} \delta_{kl} - \frac{1}{2} (\delta_{ki} \delta_{lj} + \delta_{kj} \delta_{li}) + \frac{2}{3} (G_{ij}^{-1} G_{kl} + G_{ij} G_{kl}^{-1}) \right] \\
&\quad - \frac{2}{3} I_3^{-2/3} \left[I_1 \left(\delta_{ij} G_{kl}^{-1} + \delta_{kl} G_{ij}^{-1} \right) - I_2 \left(\frac{2}{3} G_{ij}^{-1} G_{kl}^{-1} - \frac{\partial G_{ij}^{-1}}{\partial G_{kl}} \right) \right], \\
\frac{\partial^2 J}{\partial G_{ij} \partial G_{kl}} &= \frac{\partial}{\partial G_{kl}} \left(\frac{1}{2} I_3^{1/2} G_{ij}^{-1} \right) = \frac{1}{2} I_3^{1/2} \left(\frac{1}{2} G_{ij}^{-1} G_{kl}^{-1} + \frac{\partial G_{ij}^{-1}}{\partial G_{kl}} \right).
\end{aligned} \tag{101}$$

The tangent stiffness tensor is then obtained by introducing Eqs. (100) and (101) into Eq. (99). To complete the computations, it is necessary to evaluate $\partial G_{ij}^{-1} / \partial G_{kl}$. Since $G_{ij}^{-1} G_{jk} = \delta_{ik}$, it follows that

$$\begin{aligned}
\frac{\partial G_{ij}^{-1}}{\partial G_{mn}} G_{jk} &= -G_{ij}^{-1} \frac{\partial G_{jk}}{\partial G_{mn}} = -\frac{1}{2} G_{ij}^{-1} (\delta_{mj} \delta_{nk} + \delta_{mk} \delta_{nj}) \\
&= -\frac{1}{2} (G_{im}^{-1} \delta_{nk} + \delta_{mk} G_{in}^{-1}).
\end{aligned} \tag{102}$$

Multiplying by the inverse of of the right Cauchy-Green deformation tensor then yields

$$\begin{aligned}
\frac{\partial G_{ij}^{-1}}{\partial G_{mn}} G_{jk} G_{kl}^{-1} &= -\frac{1}{2} G_{kl}^{-1} (G_{im}^{-1} \delta_{nk} + \delta_{mk} G_{in}^{-1}) \\
&= -\frac{1}{2} (G_{im}^{-1} G_{nl}^{-1} + G_{ml}^{-1} G_{in}^{-1}),
\end{aligned}$$

and finally

$$\frac{\partial G_{ij}^{-1}}{\partial G_{kl}} = -\frac{1}{2} (G_{ik}^{-1} G_{lj}^{-1} + G_{kj}^{-1} G_{il}^{-1}). \tag{103}$$

7.3 Constitutive Law for Inelasticity of Elastomeric Materials

At this time a complicated inelastic constitutive model for elastomeric materials has not been chosen and implemented. Instead, a simple linear inelastic material model is proposed and implemented for verifying the feasibility of the road map proposed in Section 6.4. After the feasibility of the development approach has been validated, complex inelastic constitutive models will be evaluated in Chapters 11 and 12.

The inelastic behavior of the material is modeled by a dissipative stress, σ_{ij}^d , proportional to the rate of the Green-Lagrange strain, \dot{e}_{ij} ,

$$\sigma_{ij}^d = \mu c_{ijkl} \dot{e}_{kl}, \quad (104)$$

where μ is the damping coefficient and c_{ijkl} the stiffness tensor defined by Eq. (98). The stress-strain relation for the elastomeric material is then

$$\sigma_{ij} = \sigma_{ij}^d + c_{ijkl} e_{kl}. \quad (105)$$

Chapter VIII

VALIDATION OF THE FINITE ELEMENT IMPLEMENTATION

In order to validate the implementation of the ED2 element and the elastomeric material model, several finite element models were constructed and analyzed using the developed finite element tool and ABAQUS. Results from these two tools were then compared against each other.

8.1 *Static Analysis Validation*

8.1.1 Cantilever beam

The validation started with static analysis of cantilever beams made of elastic and hyperelastic materials, respectively. The dimensions of the beam are depicted in Fig. 20, and the thickness of the beam is 0.05 m for the elastic case and 1.0 m for the hyperelastic case. The properties for the elastic material are listed in Table 4; and those for the hyperelastic beam in terms of the coefficients in the strain energy function, see Eq. (93), are in Table 5. Different vertical forces were applied on the tip of the cantilever beam, and the transverse deflections of the beam were computed using DYMORE with ED2 element and ABAQUS, respectively; and the results from these two tools were compared.

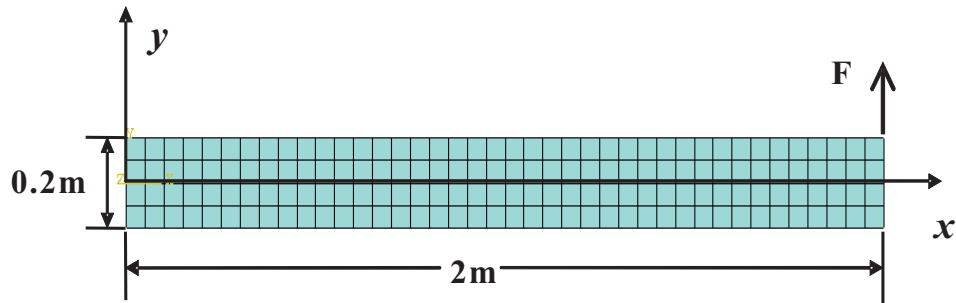


Figure 20: Geometry of cantilever beam.

In the analysis, same mesh size (40×4) was maintained for both DYMORE: ED2 and

Table 4: Properties of elastic beam

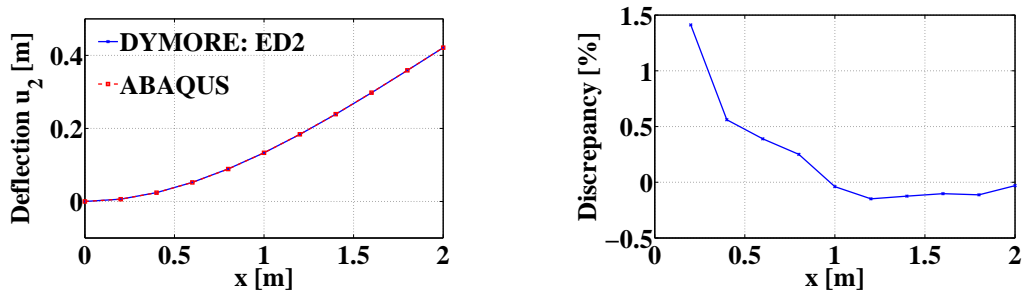
Young's modulus E [kPa]	7.3×10^7
Poison's ratio ν	0.3
Mass density ρ [kg/m ³]	2680

Table 5: Properties of hyperelastic beam

C_{10} [kPa]	60.951
C_{20} [kPa]	21.463
C_{30} [kPa]	17.258
$C_{01}, C_{11}, C_{02}, C_{21}, C_{12}, C_{03}$ [kPa]	0
D_1, D_2, D_3 [kPa ⁻¹]	1
Mass density ρ [kg/m ³]	1100

ABAQUS. Plane stress analysis was conducted for the elastic beam, whereas plane strain analysis for the hyperelastic case. The elements used in ABAQUS were the eight-node plane stress element (CPS8) and the eight-node plane strain element (CPE8), respectively. In DYMORE both ED2 plane stress and plane strain elements have nine nodes.

Fig. 21 presents the transverse deflection of the elastic beam under a tip load $F = 4 \times 10^5$ N and the discrepancy between results from DYMORE: ED2 and from ABAQUS. Figs. 22 and 23 show similar results for hyperelastic cantilever beam under different tip loads. From the figures, very good agreement was found between the results from ABAQUS and DYMORE with ED2 element, especially around the beam tip. These results validate the ED2 element formulation as well as the accuracy of the meshing tools and the FE solver used in the process. The hyperelastic cases also demonstrate the validity of the implementation of hyperelastic material constitutive law.

**Figure 21:** Elastic cantilever beam with tip load $F = 4 \times 10^5$ N. Left: transverse deflection; right: discrepancy between DYMORE: ED2 and ABAQUS.

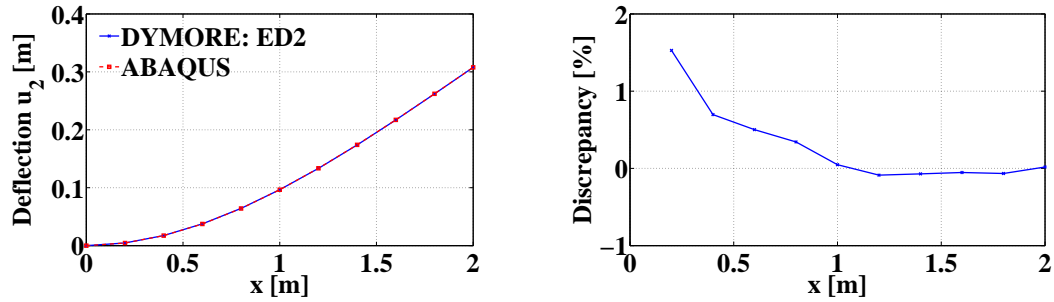


Figure 22: Hyperelastic cantilever beam with tip load $F = 10$ N. Left: transverse deflection; right: discrepancy between DYMORE: ED2 and ABAQUS.

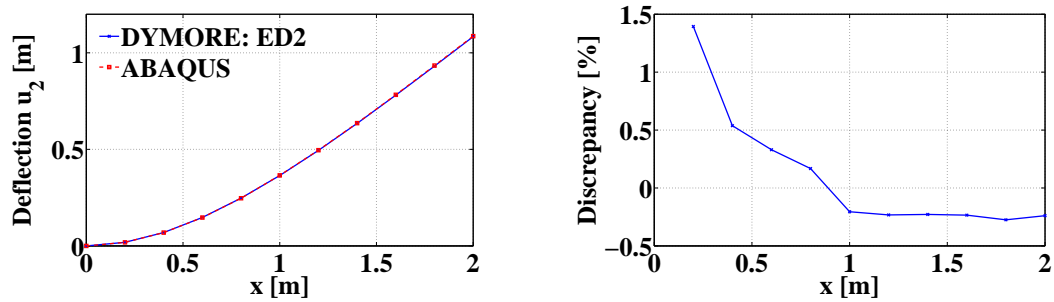


Figure 23: Hyperelastic cantilever beam with tip load $F = 50$ N. Left: transverse deflection; right: discrepancy between DYMORE: ED2 and ABAQUS.

8.1.2 Simple elastomeric damper

The second example for the static analysis is a simple, yet typical, elastomeric damper as illustrated in Fig. 24. The figure also depicts a typical configuration of a helicopter rotor with an elastomeric lead-lag damper. For this particular design, two dampers are used, one on each side of the blade. The damper consists of a parallelepiped of elastomeric material sandwiched between two aluminum plates. These plates connect the damper to the rotor blade on one side and to the rotor hub on the other. The damper was modeled as a two-dimensional problem using the plane strain assumption and its thickness is 0.1 m. The left aluminum plate was connected to the ground, whereas a force $F = 160$ N was applied at the lower right corner of the right aluminum plate. The material properties for the outer aluminum plates and the inner elastomeric parallelepiped are same as those shown in Table 4 and 5, respectively. This problem was analyzed using DYMORE with ED2 element

and ABAQUS with CPE8 element, respectively, with the same mesh density (the length of element is 5 mm).

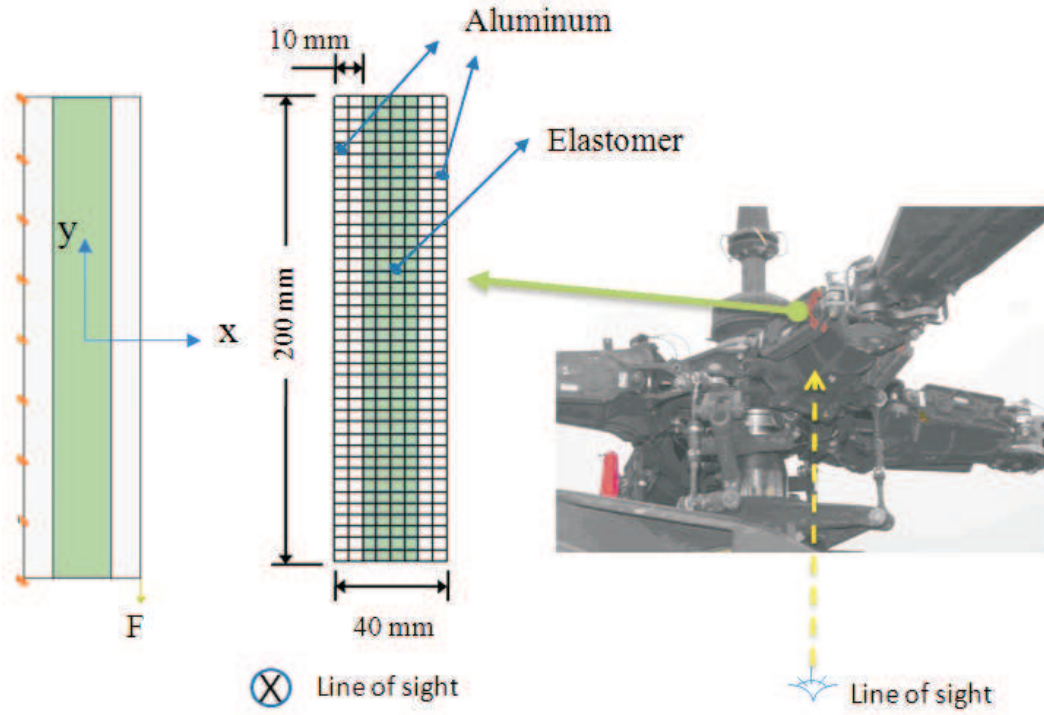


Figure 24: Simple elastomeric damper model.

Figs. 25 to 27 show the deformation, within the plane of paper, of the top, middle and bottom surfaces of the simple elastomeric damper, respectively. The discrepancy between the results from DYMORE: ED2 and ABAQUS are also provided. It can be seen that the results are matched within a 3% maximum discrepancy. Under the applied load, the elastomeric components were observed to be strained up to 10%, which is consistent with typical strain levels encountered in elastomeric damper applications.

8.2 *Dynamic Analysis Validation*

8.2.1 Eigenvalue analysis

After successfully verified the ED2 element and the hyperelastic material model for the static behavior of the cantilever beam and of the simple elastomeric damper, the validation moves to the cases of dynamic analysis, which is a more challenging work than the static

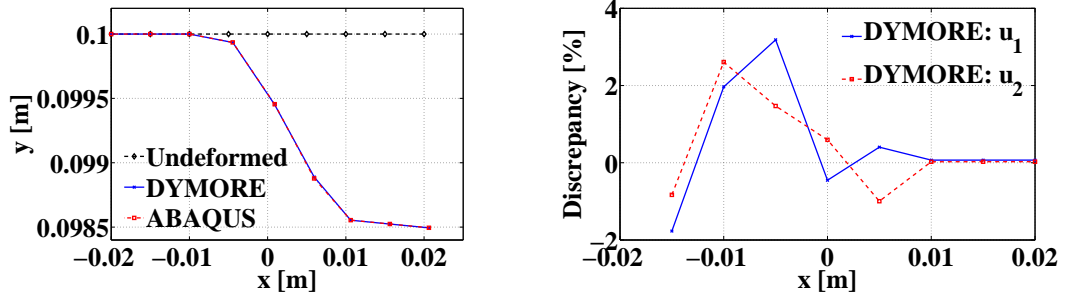


Figure 25: Simple elastomeric damper. Left: deformed top surface; right: discrepancy between DYMORE: ED2 and ABAQUS.

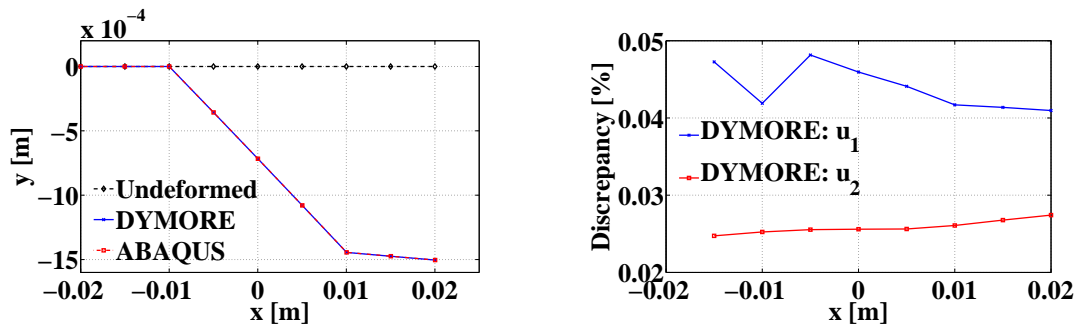


Figure 26: Simple elastomeric damper. Left: deformed middle surface; right: discrepancy between DYMORE: ED2 and ABAQUS.

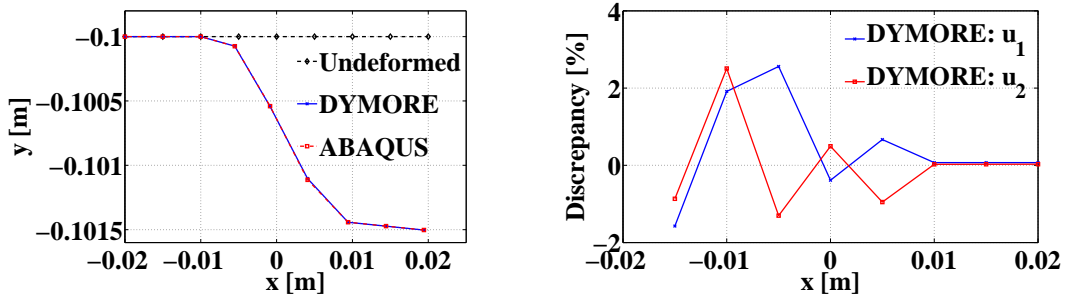


Figure 27: Simple elastomeric damper. Left: deformed bottom surface; right: discrepancy between DYMORE: ED2 and ABAQUS.

case. First, the eigenvalue analysis was performed for the elastic and hyperelastic cantilever beam as well as for the simple elastomeric damper. For the elastic cantilever beam, plane stress assumption was adopted and CPS8 element was used in ABAQUS; however, for the hyperelastic beam and the simple elastomeric damper, plane strain assumption was adopted and CPE8 element was used in ABAQUS. For all three examples, the mesh sizes are the same as those used in the static analysis. Tables 6 to 8 present the first ten eigenvalues for these three cases, respectively. Good agreements between the ABAQUS and DYMORE: ED2 results for all three cases indicate a successful implementation of the inertial effects in the developed finite element tool.

Table 6: Eigenvalues for elastic cantilever beam [Hz]

	DYMORE: ED2	ABAQUS
1	41.880	41.885
2	251.25	251.29
3	653.98	653.19
4	661.83	661.93
5	1202.8	1202.9
6	1834.4	1834.6
7	1958.1	1958.2
8	2525.7	2525.9
9	3256.2	3256.3
10	3258.5	3258.6

Table 7: Eigenvalues for hyperelastic cantilever beam [Hz]

	DYMORE: ED2	ABAQUS
1	0.086567	0.086592
2	0.52818	0.52831
3	1.3455	1.3456
4	1.4213	1.4215
5	2.6441	2.6444
6	4.0290	4.0293
7	4.1216	4.1217
8	5.7845	5.7842
9	6.6893	6.6898
10	7.5801	7.5789

Table 8: Eigenvalues for simple elastomeric damper [Hz]

	DYMORE: ED2	ABAQUS
1	61.424	61.429
2	76.975	76.980
3	79.894	79.906
4	246.11	245.95
5	250.96	250.78
6	273.30	273.27
7	278.53	278.51
8	286.58	286.58
9	298.21	298.17
10	299.03	299.56

8.2.2 Dynamic simulations

Next, dynamic simulations were performed on the same structures under sinusoidal loadings with different amplitudes and frequencies, respectively. The assumptions for stress/strain states, types of elements used in ABAQUS analysis, and the mesh sizes are the same as those used in the eigenvalue analysis for the elastic and hyperelastic cantilever beams and simple elastomeric damper, respectively. Fig. 28 depicts the tip displacements of the elastic cantilever beam under two different loading histories, $F = 10 \sin(100\pi t)$ N and $F = 4 \times 10^5 \sin(20\pi t)$ N, respectively. In the figures, the results from both DYMORE with ED2 element and ABAQUS are shown. Similar results for the hyperelastic beam are presented in Fig. 29 for tip loadings $F = 200 \sin(\pi t)$ N and $F = 20 \sin(4\pi t)$ N, respectively. It can be seen that the results from ABAQUS and DYMORE with ED2 are in excellent agreement.

Fig. 30 presents the displacements for the simple hyperelastic damper under loading $F = 10^4 \sin(10\pi t)$ N. The left figure shows the displacement for the upper-right corner of the damper and the right figure for the lower-right corner. It can be seen that DYMORE with ED2 element predicts the transient response accurately. Fig. 31 shows similar results with $F = 10^4 \sin(200\pi t)$ N, which has a higher frequency.

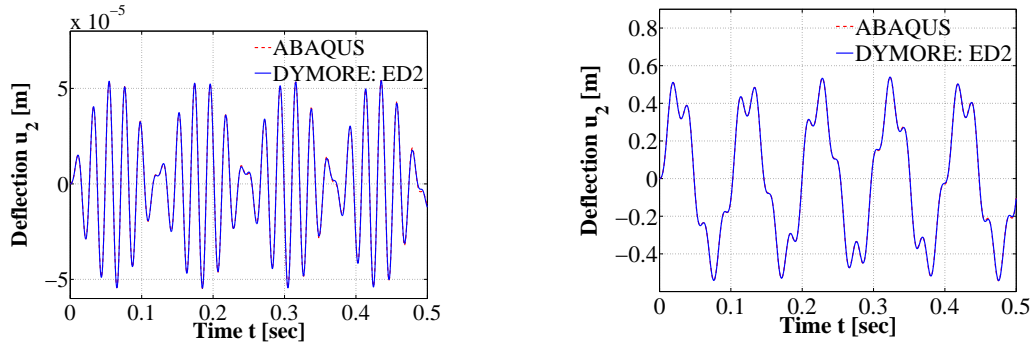


Figure 28: Tip displacement history of elastic cantilever beam. Left: $F = 10 \sin(100\pi t)$ N; right: $F = 4 \times 10^5 \sin(20\pi t)$ N.

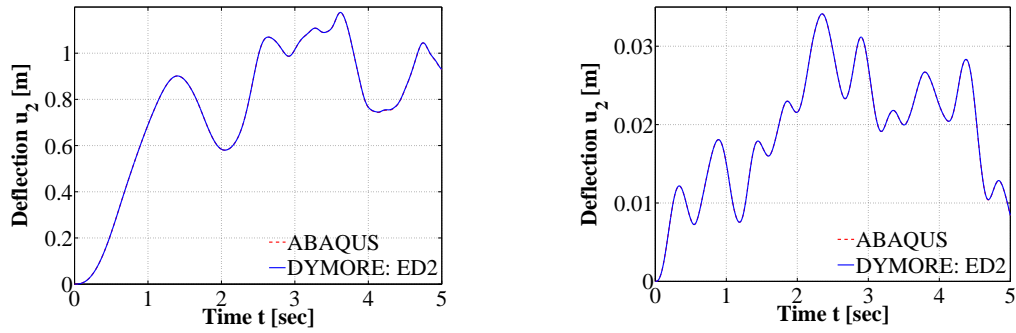


Figure 29: Tip displacement history of hyperelastic cantilever beam. Left: $F = 200 \sin(\pi t)$ N; right: $F = 20 \sin(4\pi t)$ N.

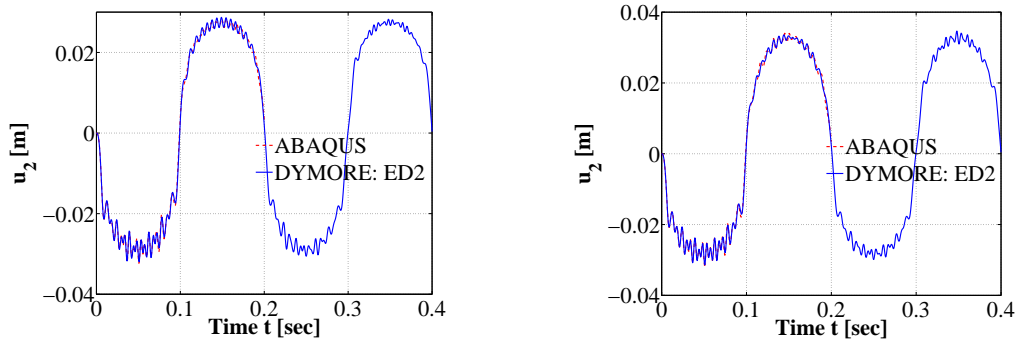


Figure 30: Displacement history of simple elastomeric damper for $F = 10^4 \sin(10\pi t)$ N. Left: upper-right corner; right: lower-right corner.

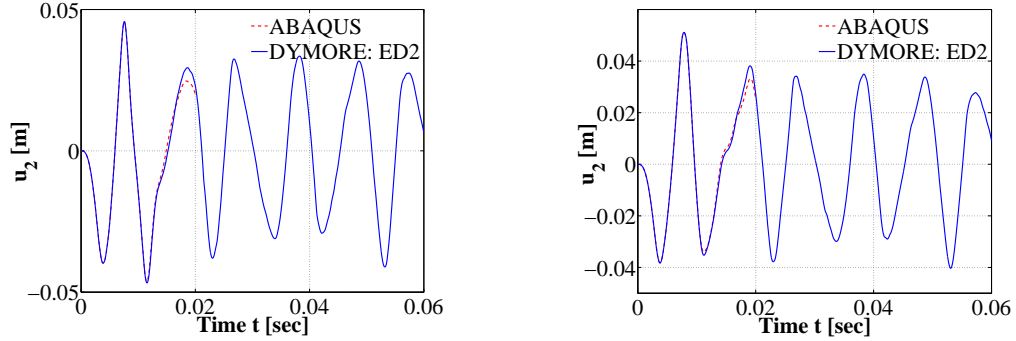


Figure 31: Displacement history of simple elastomeric damper for $F = 10^4 \sin(200\pi t)$ N. Left: upper-right corner; right: lower-right corner.

8.3 Energy Dissipation Validation

At this time a linear inelastic model is implemented for the elastomeric material; see Eq. (104), in which the damping stress is proportional to the strain rate. The correctness of the implementation of this damping term was verified by the comparison of the results between DYMORE with ED2 element and DYMORE with BEAM element for the elastic cantilever beam. Note that the BEAM element in DYMORE has already been well verified, so the results with BEAM element will serve as benchmark data.

Fig. 32 illustrates the displacement response for the elastic cantilever beam, which was modeled as a plane stress problem, impacted by a force $F = 2 \times 10^4$ N at the tip. The figure depicts decaying displacement amplitude for nonzero damping constant μ . A good correlation can be observed between the results from the case based on ED2 element with a linear dissipative term and those based on DYMORE BEAM element.

Fig. 33 presents the tip displacement for the hyperelastic cantilever beam, which was modeled as a plane strain problem, under a tip force $F = 2 \sin(20\pi t)$ N with different values of damping constant μ . It can be seen that the peaks of the displacement history are decreasing with increasing of the damping constant, as expected. This example concludes the verification of the implementation of the ED2 element and elastomeric material model.

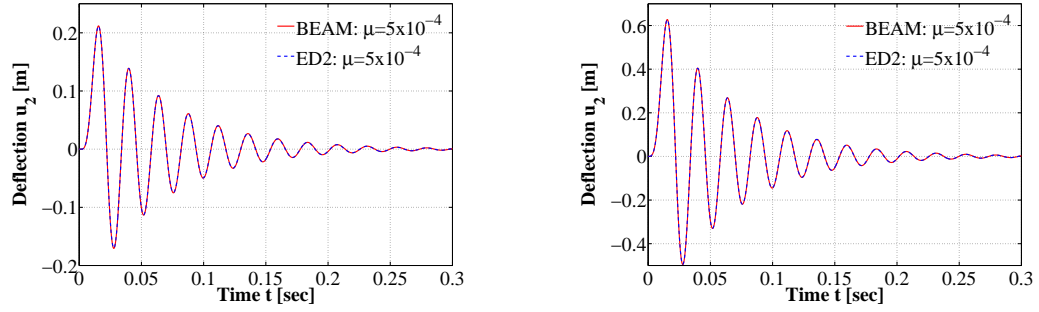


Figure 32: Displacement history of elastic cantilever beam with energy dissipation. Left: middle point; right: beam tip.

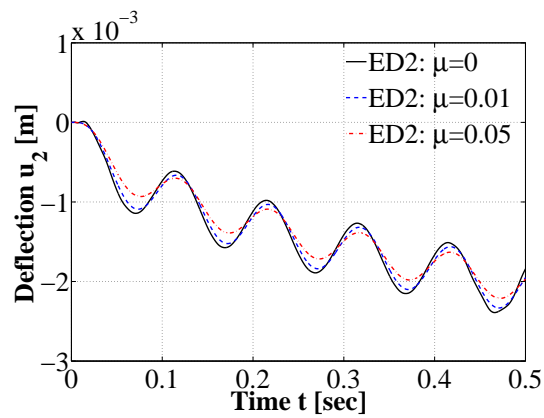


Figure 33: Tip displacement history of hyperelastic cantilever beam with energy dissipation.

Chapter IX

INTEGRATION OF ELASTOMERIC DAMPERS WITH MULTIBODY DYNAMICS ANALYSIS

Now with implementation and validation of the ED2 element and the elastomeric material model dealt with, they are now integrated with a multibody dynamics analysis code, DYMORE, for a coupled comprehensive simulation of the dynamic response of structure systems involving elastomeric components, such as rotorcraft and automobiles. The coupling strategy is depicted in Fig. 19 and explained in Section 6.4

In this chapter, the simple elastomeric damper discussed in the previous chapter will be integrated with the UH-60 rotor for a demonstration. The UH-60 rotor with a spring/dashpot type damper model is chosen as the baseline system, and then the spring/dashpot type damper is replaced by the simple elastomeric damper. The rotor with elastomeric damper will be simulated in the forward flight regime using DYMORE and the damper response will be compared with the baseline case.

9.1 Characteristics of the Simple Elastomeric Damper

Before the simple elastomeric damper is integrated with multibody dynamics systems, some of its fundamental characteristics, such as the hysteresis loop and the dual frequency effect, will be studied.

9.1.1 Hysteresis plots

In order to obtain the force-displacement hysteresis plots for the simple elastomeric damper model, the damper was excited with different loadings, which was fulfilled through prescribing different relative displacements between the two aluminum plates. Two sinusoidal

displacements with different amplitudes and frequencies were used

$$\Delta_1 = 0.025 \sin(8.6\pi t) \text{ [ft]}, \quad (106a)$$

$$\Delta_2 = 0.00833 \sin(2\pi t) \text{ [ft]}. \quad (106b)$$

Fig. 34 shows the hysteresis plots (reaction force against the prescribed displacement) for the elastomeric damper under strain histories Eqs. (106) with different damping constant μ , respectively. Fig. 35 presents similar results for an elastomeric damper with different material properties as shown in Table 9. These figures demonstrate the effects of the material properties, damping constant, and the amplitude and frequency of the strain history on the energy dissipated by the elastomeric damper. It can also be found from the figures that a greater damping constant results in more energy dissipation per cycle, which is represented by the area of the hysteresis loop, if the strain history is kept the same for both cases. It is worth mentioning that the ED2 element combined with the elastomeric material model captures typical hysteresis curves as expected.

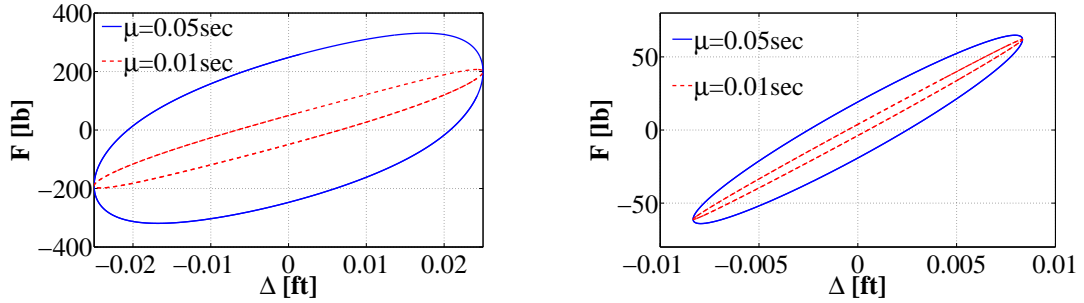


Figure 34: Hysteresis plots for simple elastomeric damper (Properties given by Table 5). Left: Displacement history Δ_1 ; Right: Displacement history Δ_2 .

Table 9: Properties of elastomeric material

C_{10} [kPa]	36.5706
C_{20} [kPa]	12.8778
C_{30} [kPa]	10.3548
$C_{01}, C_{11}, C_{02}, C_{21}, C_{12}, C_{03}$ [kPa]	0
D_1, D_2, D_3 [kPa ⁻¹]	0.8
Mass density ρ [kg/m ³]	1100

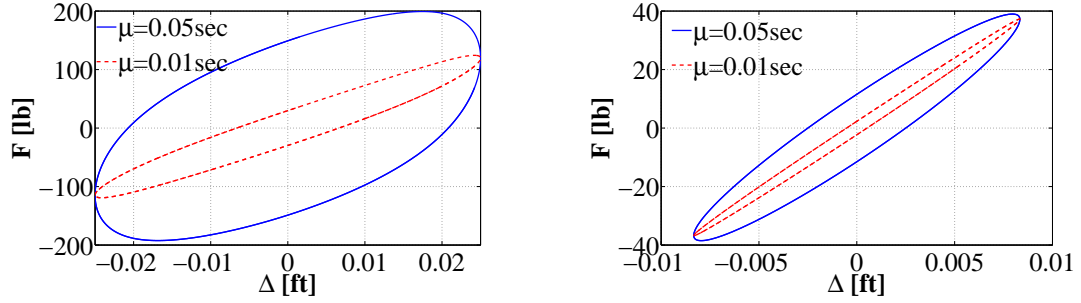


Figure 35: Hysteresis plots for simple elastomeric damper (Properties given by Table 9). Left: Displacement history Δ_1 ; right: Displacement history Δ_2 .

9.1.2 Dual frequency effect

The dual frequency effect was investigated by measuring the responses of the simple elastomeric damper model under dual frequency excitation. By prescribing the displacement histories with different amplitudes and frequencies, as those in Eqs. (106), and $\Delta_3 = \Delta_1 + \Delta_2$; the corresponding reaction forces were measured as F_1 , F_2 , and F_3 , respectively, and shown in Fig. 36 for different damping constants. The results indicate that F_3 is not simply the superposition of F_1 and F_2 , *i.e.*, $F_3 \neq F_1 + F_2$. This phenomenon is expected, as the superposition principle cannot be applied for this problem with nonlinearities; it only applies to linear problems. It is found that the developed first-principles-based elastomeric damper model exhibits a dual frequency effect for this simple elastomeric damper because it is an intrinsically nonlinear material model.

Although $F_3 \neq F_1 + F_2$ in Fig. 36, it can be seen that the difference between F_3 and $F_1 + F_2$ is small except at the peaks. This might be due to the fact that the frequencies of the prescribed displacements are quite low, so that the influence of the frequency itself on the response is not significant. Hence, in a second case, displacements with higher frequency were prescribed to see how significantly the frequency of the loading (prescribed displacement) affects the dual frequency effect. The prescribed displacements are

$$\Delta_1 = 0.04 \sin(10\pi t) \text{ [ft]}, \quad (107a)$$

$$\Delta_2 = 0.02 \sin(200\pi t) \text{ [ft]}. \quad (107b)$$

Fig. 37 shows the reaction forces for cases with different damping constant, respectively.

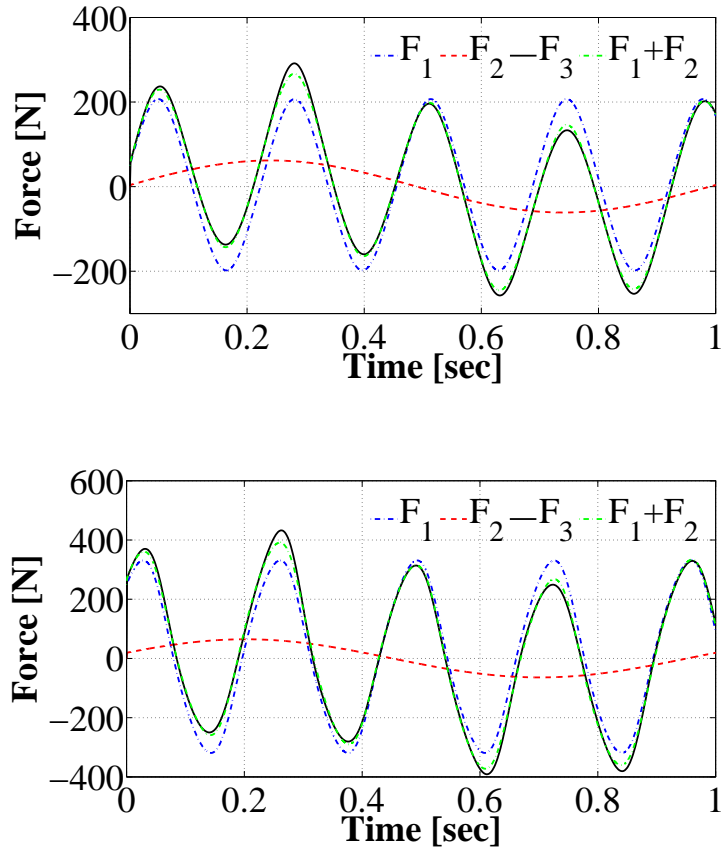


Figure 36: Reaction forces for simple elastomeric damper with low frequency displacements. Top: Damping constant $\mu = 0.01$ sec; bottom: Damping constant $\mu = 0.05$ sec.

It can be seen from the figures that the difference between F_3 and $F_1 + F_2$ in this case is much more significant than that in the previous case. Hence, when determining if the dual frequency effect is important for a system or not, the frequency of the loading is an important factor to be considered. Another observation is that the peak value of F_3 is much larger than the peak value of the superposition of F_1 and F_2 in this case, indicating the importance of accounting for the dual frequency effect in the dynamic analysis of elastomeric materials since the difference between the forces computed by the nonlinear model and the principle of superposition might be quite large.

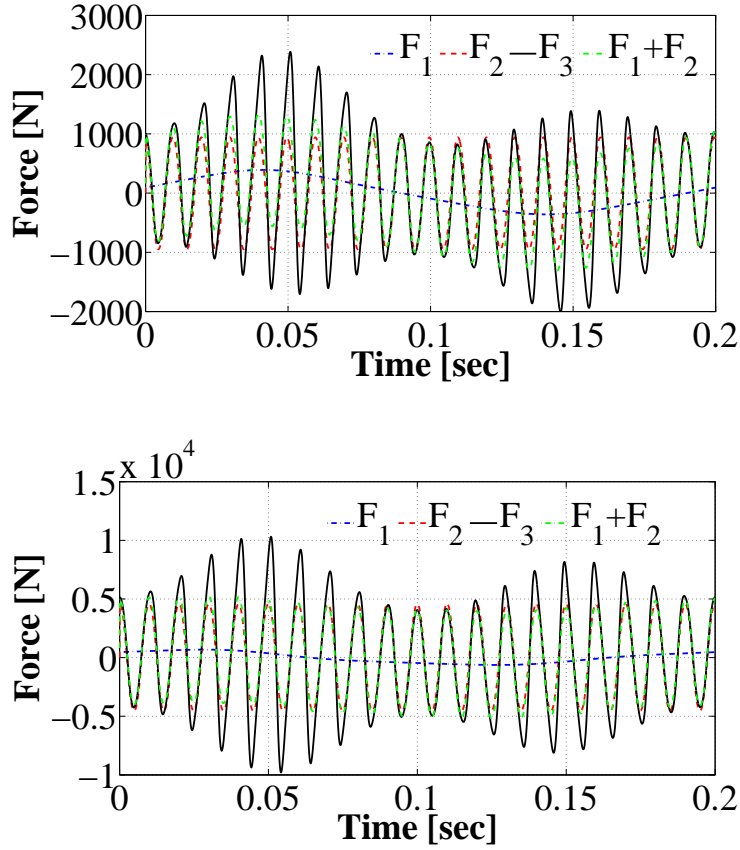


Figure 37: Reaction forces for simple elastomeric damper with high frequency displacements. Top: Damping constant $\mu = 0.01$ sec; bottom: Damping constant $\mu = 0.05$ sec.

9.2 *Integration of Elastomeric Dampers with Multibody Dynamics Analysis*

After the characteristics of the elastomeric damper have been investigated, the developed damper model was used for the simulation of a realistic helicopter rotor, the UH-60 utility helicopter. The structural model involves four blades connected to the hub through blade root retention structures and lead-lag dampers. Fig. 38 illustrates the configuration of a typical blade, which was discretized by means of ten cubic beam elements using the finite element based multibody dynamics code DYMORE, as described in [19]. The root retention structure, connecting the hub to the blade, was separated into three segments labeled segment 1, 2 and 3, respectively. The first segment, modeled by one beam element, was attached to the hub. The flap and lead-lag hinges and the pitch bearing of the blade

were modeled by three revolute joints connecting the first two segments of the root retention structure. The physical characteristics of the elastomeric bearing were represented by springs and dampers in the joints to model the stiffness and energy dissipation characteristics of the elastomeric material. The last two segments, each modeled by two beam elements, were rigidly connected to each other and to the pitch horn. Finally, the last segment was rigidly connected to the blade and damper horn. The pitch angle of the blade was set by the following control linkages: the swash-plate, pitch link, and pitch horn. The pitch link, modeled by three cubic beam elements, was attached to the rigid swash-plate by means of a universal joint and to the rigid pitch horn by a spherical joint. The damper arm and damper horn were modeled as rigid bodies. The lead-lag damper was modeled as a prismatic joint; its end points were connected to the damper arm and horn. Finally, the lead-lag damper, *per se*, was modeled using the proposed first-principles-based finite element formulation for elastomeric materials.

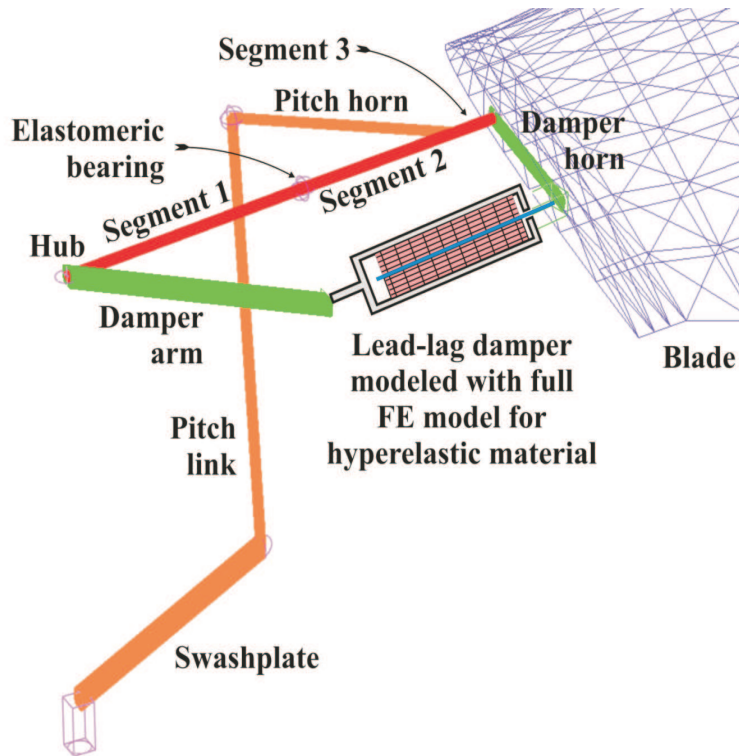


Figure 38: UH-60 Rotor system with lead-lag elastomeric damper.

Next, the performance of the proposed model of the elastomeric damper was assessed in the forward flight regime. The model described above with a 7.3° forward tilt was used; the rotor speed is set to its nominal speed $\Omega = 258.0$ RPM or 27.02 rad/sec and the forward speed is 157.9 knots, corresponding to an advance ratio of 0.368 . The aerodynamic model combines thin airfoil theory with a three-dimensional dynamic inflow model. The inflow velocities at each spanwise location were computed using the finite state induced flow model developed by Peters *et al.* [110, 109]. The airfoil has a constant lift curve slope, $a_0 = 5.73$, drag coefficient, $c_d = 0.018$, and a vanishing moment coefficient about the quarter-chord. The number of inflow harmonics was selected as $m = 5$, corresponding to 21 aerodynamic inflow states for this problem.

First, the baseline model with simple linear spring/dashpot damper model was simulated; the spring and dashpot constants were selected to match that predicted by the proposed model under small strokes. Those two parameters are identified as $k = 0.5$ lb/ft and $c = 245.0$ lb-sec/ft, respectively. The damper reaction force for this model with stroke history Δ is then given by $F = k\Delta + c\dot{\Delta}$. Next, the proposed simple elastomeric damper model was used with different material properties as given by Tables 5 and 9, respectively. These two cases will be denoted Elastomer 1 and Elastomer 2 in the following discussion, respectively. Elastomer 1 was run with a damping constant $\mu = 0.05$ sec; while for Elastomer 2 $\mu = 0.01$ sec. In all cases, the response of the rotor was simulated until a periodic solution of the problem was obtained.

Fig. 39 shows the damper's stroke and force for the last revolution of the simulation, as a function of the azimuthal angle. To a large extent, the stroking of the damper is dictated by the lag motion of the blade, which itself depends on the aerodynamic drag forces applied on the rotor, the damper force, and its in-plane dynamics. The damper force is small compared to all other forces for this UH-60 rotor; consequently, the damper stroke for the elastomeric dampers and spring/dashpot damper are nearly identical, as shown in the top figure of Fig. 39.

The damper force, however, is dictated by the properties of the damper. As shown in the bottom figure of Fig. 39, the damper forces predicted by the elastomeric and simplified

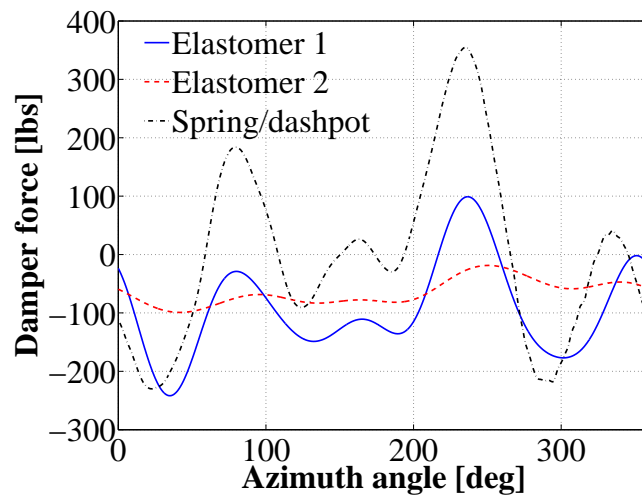
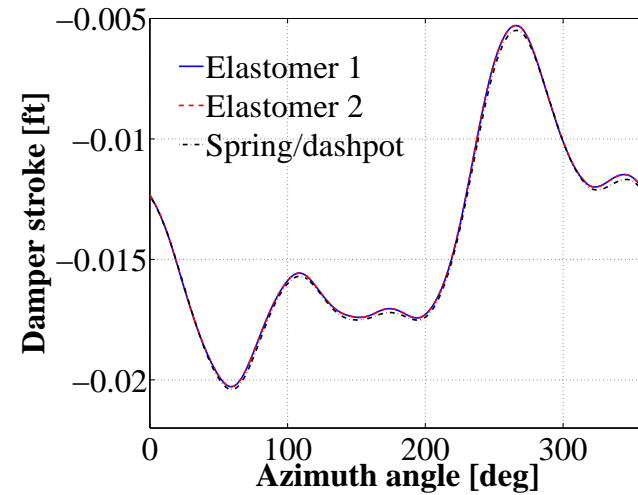


Figure 39: Damper response as a function of azimuth angle. Top: damper stroke; bottom: damper force.

models are very different: for the simplified spring/dashpot model, the peak-to-peak force in the damper is nearly 600 lbs, whereas those predicted by the elastomeric models are 350 and 100 lbs, respectively, depending on the elastomeric material parameters. However, this is not a general trend because the damper force for elastomeric dampers may be greater than that of the spring/dashpot dampers when different parameters are selected. Clearly, the nonlinear behavior of the damper dramatically affects the forces it applies on the blade and hub. In turn, these forces dramatically affect the fatigue characteristics of the system.

9.3 Summary

At this point, a first-principles-based elastomeric damper model has been developed. This model takes the damper's geometric configuration into account and its behavior is represented by the constitutive laws of the elastomeric materials. This model is also capable of capturing some fundamental properties/phenomena inherent in elastomeric materials, for instance, the hysteresis loop and dual frequency effect, by nature. A strategy to couple the developed first-principles-based elastomeric damper model with the finite element based multibody dynamics analysis code was also proposed and its feasibility was verified by the numerical simulations of UH-60 helicopter with elastomeric lead-lad dampers.

However, in the previous implementation and simulation, the details of the elastomeric material model have not been exploited. Especially, a simple linear inelastic model for the elastomeric materials was used, which is not complex enough for modeling the behavior of real elastomeric materials. In addition, the inelastic behavior of elastomeric materials acts a key role for the behavior of elastomeric dampers, which work as energy dissipating components. Hence, more complicated elastomeric material models are needed in practice. In the following chapters, the elastomeric material models, hyperelasticity and inelasticity, from the literature will be thoroughly reviewed.

Chapter X

MODELING HYPERELASTICITY OF ELASTOMERIC MATERIALS

10.1 Introduction

Elastomeric materials are predominantly elastic and capable of large strains, thus the elastic model of the elastomers should be capable of capturing nonlinear material elasticity and the kinematic nonlinearity associated with large strains. This chapter will discuss the hyperelasticity of the elastomeric materials.

Hyperelastic materials are by definition perfectly elastic for finite deformation; it follows that their stress-strain behavior may be described by a strain energy density function, representing the work that must be done on unit volume of the material in the reference state to deform it to the current configuration [100]. In the last decade, developments in computational mechanics, specially in finite element analysis, have enabled three-dimensional, large strain analysis of complex elastomeric products to be an integral component of the design process. In this context, an appropriate constitutive model is an essential prerequisite for good numerical predictions. These developments have also fueled further development of constitutive models of rubber elasticity.

In general, an efficient hyperelastic model usually meets the following criteria [34]:

- It should be able to accurately reproduce the whole S-shaped response of elastomeric materials; *i.e.*, it should be capable of capturing the characteristics of the stress-strain curve of elastomeric materials. For the elastomeric materials under loading, Young's modulus decreases at first with the increasing of the strain until it is of the order of one-third of its initial value. After that the Young's modulus increases rapidly with the increasing of strain. This leads to an S-shaped stress-strain curve for the elastomeric materials [73].
- The relevant material parameters must be as few as possible in order to reduce the number of experimental measurements needed for the identification. It is obvious that

one can make the model to be suitable for complex deformation states by including more parameters in the model. However, this will result in more experiments to be done when calibrating the material parameters, which is prohibitively expensive.

- The change of deformation modes should not be problematic. Usually the identification of the material parameters is conducted through experiments with simple deformation states, for example, a uniaxial tensile test or simple shear test; occasionally, a biaxial or planar deformation mode might also be tested. However, the deformation state of an actual elastomeric component is often complex and three-dimensional. The model should accurately predict the complex deformation state using the parameters identified from relatively simpler tests.
- The mathematical formulation has to be simple to ease the numerical implementation of the model. When the elastomeric component is integrated with the comprehensive multibody analysis code, the computational efficiency must be taken into consideration.

The hyperelastic constitutive models for elastomeric materials in the literature fall mainly into two approaches: *continuum mechanics* approach and *statistical mechanics* approach, the former can further be divided into invariant-based model and stretch-based model. These models will be reviewed in the following sections.

10.2 Invariant-Based Continuum Mechanics Models

Most continuum mechanics treatments of rubber elasticity begin with the fundamental basis of continuum mechanics for an isotropic, hyperelastic material which is that the strain energy density depends on stretch via one or more of the three strain invariants, I_1 , I_2 , and I_3 (or $J = \sqrt{I_3}$), of the right Cauchy-Green deformation tensor which is also called metric tensor (see Appendix A for the description of deformation in a continuum). If the elastomeric material is approximated as incompressible, then I_3 is taken as constant and equal to unity so that it does not contribute to strain energy. The most classical forms of

the strain energy potential are the polynomial in the invariants,

$$W = \sum_{i+j=1}^N C_{ij}(I_1 - 3)^i(I_2 - 3)^j, \quad (108)$$

where C_{ij} are material parameters. This form is also referred to as *generalized Mooney-Rivlin model* [114, 115]. By truncating the series to terms of different orders, many classical polynomial models can be obtained from Eq. (108).

10.2.1 Neo-Hookean model

The *neo-Hookean model* is the simplest form of a rubber elastic potential, which can be obtained by setting $N = 1$ and $C_{01} = 0$ in Eq. (108). The strain energy density function is then

$$W = C_{10}(I_1 - 3). \quad (109)$$

The linear structure of neo-Hookean model does not allow for nonlinear shape of the stress-strain curve as it is common in large strain state for elastomeric materials. However, this model may serve as a prototype for a rubber model in the absence of accurate material data if the application is restricted to small strains. When considering small strains, physical significance can be given to the constant, $C_{10} = E/6$, where E is the elastic modulus, which should be thought of as the slope of the uniaxial stress-strain curve at zero strain [1].

10.2.2 Mooney-Rivlin model

Mooney [99] noted that in the simple shear loading condition of a cuboid of rubber, the shear stress of rubber was directly proportional to the shear angle. On the basis of this observation, a stress-strain relation was hypothesized that is equivalent to assuming a strain energy density function of the following type, by keeping two terms in Eq. (108),

$$W = C_{10}(I_1 - 3) + C_{10}(I_2 - 3). \quad (110)$$

Although the *Mooney-Rivlin model* shows a good agreement with tensile test data, it has been found inadequate in describing the compression mode of deformation. Moreover, the Mooney-Rivlin material model fails to account for the stiffening of the material at large strains. The inclusion of higher order terms in the generalized Mooney-Rivlin polynomial

function of strain energy density function leads to a better agreement with test data for both unfilled and filled rubbers.

10.2.3 Yeoh model

It should be noted that the dependence of the strain energy density on the second invariant, I_2 , at least for strains larger than 20%, is generally much weaker than that on the first invariant, I_1 . Yeoh proposed a model which depends only on the first invariant I_1 , but with a higher order [133]

$$W = C_{10}(I_1 - 3) + C_{20}(I_1 - 3)^2 + C_{30}(I_1 - 3)^3. \quad (111)$$

Using higher order I_1 terms in the strain energy function has been shown to work well in capturing different deformation states for elastomeric materials at moderate to large deformations. Since the second invariant I_2 is not used in the strain energy density function, the Yeoh model is also called *reduced polynomial model*.

10.2.4 Biderman model

Biderman modified the Yeoh model to make the strain energy depending on the second invariant I_2 to the first order. This leads to the *Biderman model* [24]

$$W = C_{10}(I_1 - 3) + C_{20}(I_1 - 3)^2 + C_{30}(I_1 - 3)^3 + C_{01}(I_2 - 3). \quad (112)$$

Very good correlation is exhibited between experiment and Biderman model for uniaxial tension, uniaxial compression and plane strain of a thin rubber sheet (pure shear). However, if Eq. (112) is evaluated for the equi-biaxial stressing of the thin sheet, a comparison with the experiments of Treloar [127] shows poor correlation, indicating that this form for the strain energy density function does not seem to be valid for all types of deformations.

10.2.5 Haines-Wilson model

James *et al.* [72] chose the first six terms in Eq. (108) and obtained the *Haines-Wilson model*

$$\begin{aligned} W = & C_{10}(I_1 - 3) + C_{01}(I_2 - 3) + C_{11}(I_1 - 3)(I_2 - 3) \\ & + C_{20}(I_1 - 3)^2 + C_{02}(I_2 - 3)^2 + C_{30}(I_1 - 3)^3. \end{aligned} \quad (113)$$

This model was used to predict the shapes and pressures of inflated diaphragms and tubes, and was found that it leads to accurate results even at relatively high extensions.

10.2.6 Rivlin-Saunders model

Some other hyperelastic models have forms other than the polynomial form although they are invariants-based models. Rivlin and Saunders [116] used a biaxial tensile tester to obtain experimental conditions for which I_1 and I_2 are set as constants. They observed that for a carbon-black filled elastomer $\frac{\partial W}{\partial I_1}$ does not depend on I_1 and I_2 , and $\frac{\partial W}{\partial I_2}$ does not depend on I_1 . They also showed that the ratio $\frac{\partial W}{\partial I_2} / \frac{\partial W}{\partial I_1}$ decreases with I_2 and they proposed the following *Rivlin-Saunders model*

$$W = C(I_1 - 3) + f(I_2 - 3), \quad (114)$$

where f is a function to be determined by experimental data. If a reasonably simple form can be found for f , Rivlin-Saunders model is amenable to analytical solutions for a wide range of deformations and stress configurations.

10.2.7 Gent-Thomas model

The Rivlin-Saunders model in Eq. (114) is only a general form since the function is not specified. Gent and Thomas [51] proposed the *Gent-Thomas model* with an empirical function for f

$$W = C(I_1 - 3) + C_2 \ln \left(\frac{I_2}{3} \right). \quad (115)$$

This model was shown to be considerably superior to the Mooney-Rivlin model in describing the behavior of vulcanized rubber.

10.2.8 Hart-Smith model

Hart-Smith [55] observed that $\frac{\partial W}{\partial I_1}$ is constant for $I_1 < 12$, but that it increases for higher values of I_1 . This was explained by invoking the limit of extensibility of macromolecules which leads to strain-hardening phenomenon observed during mechanical tests. An exponential term was proposed in the strain energy density, W , to model this strain-hardening

phenomenon,

$$\frac{\partial W}{\partial I_1} = G \exp [k_1(I_1 - 3)^2], \quad (116a)$$

$$\frac{\partial W}{\partial I_2} = G \frac{k_2}{I_2}; \quad (116b)$$

or equivalently in an integral form,

$$W = C_1 \int \exp [C_3(I_1 - 3)^2] dI_1 + C_2 \ln \left(\frac{I_2}{3} \right), \quad (117)$$

where C_1 , C_2 , and C_3 are material constants and can be related with G , k_1 , and k_2 . In Eq. (117), the first right-hand side term, which depends on I_1 , describes the global response of the material. The second term that involves I_2 is the same as the second term in Gent-Thomas model. The Hart-Smith model is able to reproduce the response of rubberlike materials for the entire range of deformation endured by rubbers.

10.2.9 Gent model

At very high strains the shear behavior of unfilled polymer shows a rising tangent stiffness, usually ascribed to finite extensibility of the polymer chains. To take this effect into account, Gent [50] proposed a simple form for the strain energy function

$$W = -\frac{G}{2} J_m \ln \left[1 - \frac{J_1}{J_m} \right], \quad (118)$$

where $J_1 = I_1 - 2$ and J_m denotes the maximum value of J_1 , at which the material reaches its limiting state. This model gives similar predictions to the *Arruda-Boyce model*, which will be discussed later in Section 10.4.2, but its simpler form avoids the temptation to truncate the infinite series expression in Arruda-Boyce model, which can seriously impair its predictive capability.

Note that when the natural logarithm term in Eq. (118) is expanded, the polynomial form of the *Gent model* is obtained

$$W = -\frac{G}{2} J_m \left[(I_1 - 3) + \frac{1}{2J_m} (I_1 - 3)^2 + \cdots + \frac{1}{(k+1)J_m^k} (I_1 - 3)^{k+1} \right]. \quad (119)$$

10.2.10 Yeoh-Fleming model

Yeoh and Fleming [134] performed tensile, simple shear, compression and equi-biaxial experiments and found that $\frac{\partial W}{\partial I_1}$ is much greater than $\frac{\partial W}{\partial I_2}$. So they proposed to neglect the second term and modified the Gent model to a new model that involves two additional material parameters,

$$W = \frac{A}{B} J_m \left(1 - e^{-\frac{B J_1}{J_m}} \right) - C_{10} J_m \ln \left[1 - \frac{J_1}{J_m} \right]. \quad (120)$$

10.3 *Stretch-Based Continuum Mechanics Models*

Strain energy density functions based on the principal stretches as opposed to the invariants have also been proposed by several researchers although this type of models is much less often used than invariants-based models.

10.3.1 Valanis-Landel model

An early effort may be due to Valanis and Landel [129], who proposed a model with the strain energy function as separable functions of the principal stretches

$$W = w(\lambda_1) + w(\lambda_2) + w(\lambda_3). \quad (121)$$

Note that the functions for all three principal stretches have the same form; however, a specific analytical expression for the form of w was not given in [129] and it should be obtained experimentally. Biaxial tests in which one stretch is held constant while another is varied were used to characterize the data pairs as $(\lambda_i, w(\lambda_i))$ for $\lambda_j = \text{constant}$ with $j \neq i$.

10.3.2 Ogden model

Following a similar approach, Ogden [106] proposed a specific form for the strain energy function in terms of principal stretches,

$$W = \sum_{n=1}^N \frac{\mu_n}{\alpha_n} (\lambda_1^{\alpha_n} + \lambda_2^{\alpha_n} + \lambda_3^{\alpha_n} - 3). \quad (122)$$

where μ_n and α_n are material constants which should satisfy $\mu_n \alpha_n > 0$. *Ogden model* is one of the most widely used models for large strain problems, even if the determination of the

parameters leads to some difficulties. The degree of the sum may be adjusted as needed to the experimental data and reasonable fits to data have been achieved by Ogden for $n \geq 3$ in which the minimum number of independently adjustable parameters is six.

10.3.3 Hencky's model

Hencky's model is an isotropic finite elastic model, generalized from the classical Hooke's law for isotropic infinitesimal elasticity by replacing the Cauchy stress tensor and the infinitesimal strain tensor with the Kirchhoff stress tensor and Hencky or logarithmic strain tensor, respectively. Xiao and Chen [131] proved that the Hencky's model is exactly a hyperelastic model, derivable from a quadratic strain energy function of the Hencky strain tensor.

The classical strain energy function for infinitesimal isotropic elasticity is, see Eq. (506),

$$W = \mu (\varepsilon_1^2 + \varepsilon_2^2 + \varepsilon_3^2) + \frac{\Lambda}{2} (\varepsilon_1 + \varepsilon_2 + \varepsilon_3)^2, \quad (123)$$

where ε_i are the principal strains of the infinitesimal strain tensor, and Λ and μ are the Lamé's constants. Hencky's strain energy function for finite deformation can be obtained by replacing the infinitesimal strain tensor, ε_i , in Eq. (123) with the Hencky strain tensor [62, 63], *i.e.*,

$$\varepsilon_i = \ln \lambda_i, \quad (124)$$

where λ_i as the principal stretches.

Anand [4] showed that the Hencky's model is in good accord with experiments for metals and rubbers in uniaxial strain, simple tension and compression, and pure shear for moderately large deformations ($\lambda \approx 0.7$ to 1.3). He also validated the agreement between the Hencky's model and experimental data for vulcanized natural rubbers in simple torsion and combined extension-torsion [5]. Here again the accordance is up to moderate deformation. The advantage of the Hencky's model is that it contains only two material parameters, the Lamé's constants, and they can be determined from the infinitesimal deformations.

10.4 Statistical Mechanics Models

The statistical mechanics approach assumes that the elastomeric material consists of long molecular chains and they are randomly oriented. When the elastomeric material is under loading/deformation, the chain stretches and its configurational entropy decreases. Considering a deformation state with principal stretches $(\lambda_1, \lambda_2, \lambda_3)$, under which the chain length does not approach its fully extended length, the elastic strain energy density function can be derived from the change in configurational entropy and found to be [125, 126]

$$W = \frac{1}{2}Nk\theta(\lambda_1^2 + \lambda_2^2 + \lambda_3^2 - 3), \quad (125)$$

where N is the number of chains, k the Boltzmann's constant, and θ the absolute temperature. It can be seen that Eq. (125) is actually the neo-Hookean model discussed in Section 10.2.1.

The derivation of Eq. (125) uses a Gaussian statistical distribution and is based on the assumption that the length of the chain is significantly less than its fully extended length during the deformation. This Gaussian statistics model is found to be able to provide a reasonable prediction for the stress-stretch behavior up to moderate stretches. When the stretch becomes large the non-Gaussian behavior of real materials becomes evident and the prediction from Eq. (125) then departs significantly from the experimental observations.

In order to consider the finite extensibility of chain stretch, Kuhn and Grün [81] used a non-Gaussian theory to take into account the limiting extensibility of polymer chains and derived the strain energy of a single chain as

$$w = nk\theta \left[\beta \frac{\lambda}{\sqrt{n}} + \ln \frac{\beta}{\sinh \beta} \right], \quad (126)$$

where n is the number of links in the chain and

$$\beta = \mathcal{L}^{-1} \left(\frac{\lambda}{\sqrt{n}} \right) \quad (127)$$

with \mathcal{L}^{-1} denoting the inverse Langevin function defined by

$$\mathcal{L}(x) = \coth(x) - \frac{1}{x}. \quad (128)$$

The incorporation of this more accurate individual chain strain energy into constitutive models leads to several physically based models that are found to be capable of capturing the non-Gaussian nature of the stress-stretch behavior at moderate and large deformations.

10.4.1 Three-chain model

In the *three-chain model* [130, 73], it is assumed that the chains are equally distributed along the axes of an initially cubic cell, *i.e.*, the N chains are distributed upon the three axes with a density equal to $N/3$ in each direction. The chain deforms affinely with the cell and the stretch on each chain then corresponds to a principal stretch. The resulting strain energy density function is given by

$$W = \frac{Nk\theta}{3}n \sum_{i=1}^3 \left[\beta_i \frac{\lambda_i}{\sqrt{n}} + \ln \left(\frac{\beta_i}{\sinh \beta_i} \right) \right], \quad (129)$$

where $\beta_i = \mathcal{L}^{-1}(\lambda_i/\sqrt{n})$ for $i = 1, 2, 3$. The three-chain model is capable of capturing the non-Gaussian nature of the stress-stretch behavior in uniaxial tension. However, the predictions from the three-chain model are dominated by the contribution of the chains which lie along the maximum principal stretch directions. Therefore, it does not effectively sample the network response of the underlying structure, but only the response of the chain lying along the maximum stretch direction [27].

10.4.2 Arruda-Boyce model

Recently, Arruda and Boyce [7] proposed a *eight-chain model* with a distribution of chains upon eight directions corresponding to the vertices of a cubic cell inscribed in a unit sphere. This model is governed by the stretch of the diagonal of the cube. The chains in the eight-chain network deform in a cooperative manner where the chains extend with any imposed deformation and rotate toward the maximum principal stretch axes. Due to the symmetry of the chain structure, the interior junction point remains centrally located throughout the deformation and the stretch on each chain in the diagonal can be obtained as

$$\lambda_{chain} = \sqrt{\frac{\lambda_1^2 + \lambda_2^2 + \lambda_3^2}{3}} = \sqrt{\frac{I_1}{3}}. \quad (130)$$

The corresponding strain energy function is given by, from Eq. (126),

$$W = Nk\theta n \left(\beta_{chain} \frac{\lambda_{chain}}{\sqrt{n}} + \ln \frac{\beta_{chain}}{\sinh \beta_{chain}} \right), \quad (131)$$

where $\beta_{chain} = \mathcal{L}^{-1}(\lambda_{chain}/\sqrt{n})$. The eight-chain model is found to predict the significant differences between equi-biaxial tension and uniaxial tension. It is also capable of capturing the behavior of a complicated network in a very simple way although affine deformation is not assumed for all chains.

Note that the strain energy function for the Arruda-Boyce model, Eq. (131), is actually I_1 -based since the chain stretch, λ_{chain} , is equal to $\sqrt{I_1/3}$ from Eq. (130). Thus, the strain energy function for the Arruda-Boyce model, Eq. (131) can be expanded in a polynomial form of I_1

$$W = Nk\theta \left[\frac{1}{2}(I_1 - 3) + \frac{1}{20n}(I_1^2 - 3^2) + \frac{11}{1050n^2}(I_1^3 - 3^3) + \frac{19}{7000n^3}(I_1^4 - 3^4) + \frac{519}{673750n^4}(I_1^5 - 3^5) + \dots \right]. \quad (132)$$

One can find that the Arruda-Boyce model is actually a polynomial form model with high order I_1 terms. This is the reason for its success since high order I_1 terms mimic the physics of the non-Gaussian statistics models.

When comparing Eq. (132) with Eq. (119), one can find that the Arruda-Boyce model is essentially equivalent to the Gent model. That is the reason why these two models provide similar results; both of them give good predictions.

10.4.3 Constrained junctions model

While the models based on non-Gaussian statistics capture the effects of the limiting extensibility of the chain stretch on the stress-stretch curves at large deformations, they do not account for discrepancies between experimental data and Gaussian statistical models at small to moderate deformations. The reason might be due to the so-called phantom assumption which does not account for chains entanglement and through which chains can pass mutually. Several models [47, 42, 14, 48] have introduced the idea of entanglement constraints and proposed to separate the strain energy function as,

$$W = W_{ph} + W_c, \quad (133)$$

where W_{ph} is the strain energy of phantom network and W_c the energy for the cross-linking.

Based on this general theory, Flory and Erman [47, 42, 48] developed a model in which the junction points between chains are constrained to move in a restricted neighborhood due to other chains. The strain energy of phantom network of the model is described by a factor of the neo-Hookean model, Eq. (125)

$$W_{ph} = \frac{1}{2} \xi k \theta (\lambda_1^2 + \lambda_2^2 + \lambda_3^2 - 3), \quad (134)$$

with

$$\xi = \left(1 - \frac{2}{\phi}\right) N, \quad (135)$$

where $\phi > 2$ is the number of chains meeting at a junction point. The contribution of the constraints to the strain energy is given by

$$W_c = \frac{1}{2} N k \theta \sum_{i=1}^3 [B_i + D_i - \ln(B_i + 1) - \ln(D_i + 1)], \quad (136)$$

where

$$B_i = \kappa^2 \frac{\lambda_i^2 - 1}{(\lambda_i^2 + \kappa)^2}, \quad (137)$$

$$D_i = \frac{\lambda_i^2}{\kappa} B_i,$$

and κ is a measure of the strengths of the constraints. The inclusion of W_c term improves the performance of the neo-Hookean model by leading better agreement with experimental data at moderate strains. However, the use of the neo-Hookean model for the phantom part limits the *constrained junctions model* to stretch lower than 300% for uniaxial extension.

10.4.4 van der Waals model

The *van der Waals model* [80, 79], also known as *Kilian model*, takes into account the van der Waals forces, and the rubber network is treated as a gas where the interaction forces are applied between quasi-particles. The strain energy function of van der Waals model is given as

$$W = \mu \left\{ -(\lambda_m^2 - 3) [\ln(1 - \eta) + \eta] - \frac{2}{3} a \left(\frac{\tilde{I} - 3}{2} \right)^{3/2} \right\}, \quad (138)$$

where λ_m is the locking stretch, and η a material parameter

$$\eta = \sqrt{\frac{\tilde{I} - 3}{\lambda_m^2 - 3}}. \quad (139)$$

\tilde{I} is a generalized invariant [2], [41], which is a linear combination of the first and second invariants,

$$\tilde{I} = (1 - \beta)I_1 + \beta I_2. \quad (140)$$

The parameter $0 \leq \beta \leq 1$ has no physical meaning, which makes this model empirical in nature even if it is primarily based on molecular considerations.

10.4.5 Tube model

Recently, Heinrich and Kaliske [61] proposed a model which assumes that the molecular chains are constrained in a tube formed by surrounding chains. This assumption is attributed to the high degree of entanglement of the rubber network. The confinement of chains is governed by a topology restoring potential, which is determined by using the statistical mechanics,

$$W = G_c I^*(2) - \frac{2G_e}{\beta} I^*(-\beta), \quad (141)$$

where $I^*(\alpha)$ is the first invariant of the generalized α -order strain tensor e_{ik} , given by

$$e_{ik}(\alpha) = \frac{b_{ik}^{\alpha/2} - \delta_{ik}}{\alpha}, \quad (142)$$

where b_{ik} denotes the Finger's deformation tensor

$$b_{ik} = \sum_{j=1}^3 \frac{\partial x_i(t)}{\partial x_j(0)} \frac{\partial x_k(t)}{\partial x_j(0)}. \quad (143)$$

The first term in the right-hand side of Eq. (141) represents the crosslink contribution to the total strain energy, while the second represents the constraint contribution.

This model is limited to moderate deformation and is not able to reproduce strain-hardening. This limitation is inherent to its foundations which refer to entanglement constraints but not to the extensibility. In order to overcome this limitation, Kaliske and Heinrich [75] replaced the Gaussian distribution by the non-Gaussian one and introduced an inextensibility parameter δ . They then replaced the crosslink contribution term of the strain energy function with a new one

$$W = \frac{G_c}{2} \left\{ \frac{(1 - \delta^2)(I_1 - 3)}{1 - \delta^2(I_1 - 3)} + \ln [1 - \delta^2(I_1 - 3)] \right\}, \quad (144)$$

while the constraint contribution term in Eq. (141) is not changed. This is often called the *extended tube model*. Kaliske and Heinrich showed that the predictions from the extended tube model are at least as good as the results obtained using the Yeoh model which turned out to be one of the best phenomenological formulations.

10.5 Modeling Compressibility

In the models of the elasticity of elastomeric materials discussed above, the materials are assumed to be incompressible, which means the volume ratio $J = \sqrt{I_3} = 1$. However, in reality the elastomeric materials are compressible or nearly incompressible, which means $J \neq 1$ and the volumetric strain $\Delta = J - 1 \neq 0$; thus, an accurate constitutive model of elastomeric material should include the consideration of the compressibility. The considerations of the compressibility have traditionally fallen along two lines, both of which start from removing the incompressible restriction, $J = 1$ [27].

The first approach assumes the strain energy can be separated as a deviatoric strain energy and a spherical strain energy, *i.e.*,

$$W = W_d(\bar{I}_1, \bar{I}_2) + W_h(J), \quad (145)$$

where $\bar{I}_1 = J^{-2/3}I_1$ and $\bar{I}_2 = J^{-4/3}I_2$ are the invariants of the deviatoric deformation tensor, see Section A.5. Note that in this approach, the first term in the formulation is a function of \bar{I}_1 and \bar{I}_2 only, which means this term considers the deviatoric contribution only; while the second term considers the contribution due to the volume change only.

The second compressibility modeling approach appends a bulk strain energy term to an existing strain energy function like any of those discussed previously

$$W = W_a(I_1, I_2, J) + W_b(J). \quad (146)$$

Note that in this approach, both terms in the formulation contain contributions due to the volume change, which is reflected by the fact that the first term is a function of I_1 , I_2 , and J .

A typical form of the spherical strain energy W_h is given by

$$W_h = \sum_{i=1}^N \frac{1}{D_i} (J - 1)^{2i}, \quad (147)$$

which may be appended to the general polynomial strain energy function, Eq. (108), with changing on its dependence on \bar{I}_1 and \bar{I}_2 , to get a compressible version of the general polynomial form of strain energy function

$$W = \sum_{i+j=1}^N C_{ij} (\bar{I}_1 - 3)^i (\bar{I}_2 - 3)^j + \sum_{i=1}^N \frac{1}{D_i} (J - 1)^{2i}. \quad (148)$$

Some other specific compressibility models were also developed by different authors. One widely used model is the compressible Ogden model [105]

$$W = \sum_{n=1}^N \frac{\mu_n}{\alpha_n} (\lambda_1^{\alpha_n} + \lambda_2^{\alpha_n} + \lambda_3^{\alpha_n} - 3 - \ln J) + W_b(J), \quad (149)$$

with $W_b(J)$ given by

$$W_b(J) = \frac{\kappa}{\beta^2} \left(\beta \ln J + \frac{1}{J^\beta} - 1 \right), \quad (150)$$

where $\beta > 0$ is an empirical coefficient, and κ a material constant.

Recently, a compressible model based on the Arruda-Boyce model, see Section 10.4.2, was proposed as the following form [25]

$$W = Nk\theta n \left[\beta_{chain} \frac{\lambda_{chain}}{\sqrt{n}} + \ln \left(\frac{\beta_{chain}}{\sinh \beta_{chain}} \right) + \frac{\beta_0}{3\sqrt{n}} \ln \left(\frac{1}{J} \right) \right] + W_b(J), \quad (151)$$

where $\beta_0 = \mathcal{L}^{-1}(1/\sqrt{n})$, and $W_b(J)$ is the bulk strain energy, given by

$$W_b(J) = \frac{B}{\alpha^2} \{ \cosh[\alpha(J - 1)] - 1 \}. \quad (152)$$

This model satisfies all the restrictions owing to stability and physically realistic volume changes. When comparing with the experimental data, this model was shown to be capable of reproducing the pressure versus volume response of elastomeric materials in hydrostatic compression, as well as the stress versus stretch and the volume change versus stress data during uniaxial tension. However, the form of the bulk strain energy was found to be inadequate to capture the nonlinear pressure versus volume data exhibited by several elastomeric materials in hydrostatic compression.

10.6 Summary

In this chapter, different hyperelastic material models in the literature were reviewed. Each individual model has its own advantages and drawbacks. In general, the continuum mechanics models are more common and have simpler expressions than the statistical mechanics

models. The general polynomial form of strain energy function, Eq. (148), has been chosen to model the hyperelasticity of elastomeric materials and implemented in a finite element framework in this work due to its simple polynomial form and prevalence in commercial software. The advantages of this general polynomial form of strain energy function are that many other models reviewed previously can be derived from it by setting different coefficients and that the manipulations on a polynomial form are much easier than on other types of functions, for instance, the logarithmic and exponential functions. Another advantage is that the number of polynomial terms for this model can be adjusted, which gives flexibility in the applications of this model. In general, more terms included in the strain energy function will lead to more accurate results.

Chapter XI

MODELING INELASTICITY OF ELASTOMERIC MATERIALS

11.1 Introduction

As discussed in the previous chapter, the primary behavior of elastomeric materials is the hyperelasticity; however, the study of the inelastic behavior of elastomeric materials is of critical importance. When the elastomeric materials work as energy dissipation components, for instance, elastomeric dampers, the inelastic behavior of the elastomeric materials acts as a crucial role for the response of those energy dissipation components.

The first inelastic behavior of the elastomeric materials is the nonlinear rate-dependent viscous effects, which is apparent in relaxation and creep tests. Cyclic loading tests show a typical frequency-dependent hysteresis as well where the width of the hysteresis increases with increasing stretch rates.

The dynamic stiffness, which is the ratio of the load amplitude to the displacement amplitude during a cyclic loading test, is an important property of many elastomeric materials. It is observed that the dynamic stiffness of elastomeric materials tends to decrease with the increasing of the strain amplitude, specially at small to moderate strain levels. This is the so-called Payne effect [108, 107, 45] which is more pronounced in the filled elastomers than in the unfilled elastomers. Another inelastic phenomenon, equilibrium hysteresis, can be observed during cyclic loadings with a series of relaxation periods with sufficiently long duration [90]. The stress is then dependent on not only the strain/deformation, but also on the loading history. In terms of the micromechanics, this hysteresis effect may be attributed to irreversible slip processes between adjacent filler particles. The amplitude dependence and equilibrium hysteresis are usually modeled by the theory of plasticity.

The Mullins effect is another important inelastic behavior, specially for filled elastomeric materials. The Mullins effect is a strain induced stress-softening during the first couple of loading cycles [101, 102, 56]. During a cyclic testing with constant strain amplitude, the

materials soften in the first several loading cycles, and then a steady hysteresis loop is reached. After that, if the strain amplitude increases, this stress softening phenomenon will appear again, and the material will achieve another steady hysteresis loop. Most of the softening appears in the first loading cycle and the magnitude of the softening depends on the maximum amplitude of the strain. The Mullins effect can be traced back micromechanically to a destruction of bonds between the polymer chains and the filler particles and can be considered as a side effect of the filler. The Mullins effect may be eliminated by a preconditioning process. This process will be a cyclic strain testing with a strain amplitude equal to or greater than the maximum strain amplitude at which the elastomeric material will work. The Mullins effect can usually be modeled by a damage model.

11.2 Internal Variables Based Models

The kinetic theory of elasticity for elastomeric materials provides a self-consistent molecular theory of the relation between stress and strain under various types of deformations [125, 126, 73]. According to this theory the stiffness of the elastomeric materials is proportional to the concentration of network chains, and the rates of bond breaking and bond reforming must be exactly the same under deformation. However, this theory does not consider the relaxation effects of the elastomeric materials.

Green and Tobolsky [53] extended the kinetic theory of elasticity to include the relaxation effects with a reasonable explanation for the stress decay phenomenon at constant extension. The only reasonable explanation for this phenomenon, which occurs in spite of the fact that bond breaking and bond reformation are proceeding at equal rates, is that the reforming of bonds does not contribute to the stress at constant extension, whereas the breaking of bonds relaxes the stress in chains that are in a stretched condition. Incorporating this assumption in the kinetic theory results in linear differential equations for strain-like “internal variables” which represent the “internal shear” or “internal length” of a chain. These variables are the values of the shear or of the length to which the elastomeric network would return if the external stresses are removed.

Based on Green and Tobolsky’s work Lubliner [96] proposed a approach of multiplicative

decomposition of the deformation gradient tensor into elastic and inelastic parts and interpreted Green and Tobolsky’s “internal strains” as inelastic strains. The inelastic strains are in turn governed by evolution equations. Lubliner further split the free energy of a viscoelastic solid into two parts, one for the rate-independent behavior and one for the time-dependent effects. Following this approach, many researchers developed models with different evolution laws to model the inelasticity of elastomeric materials.

These internal variables based models are mainly based on the generalizations of two types of three-parameter solids: Zener model and Poynting-Thomson model, as depicted in Fig. 40. A Zener model consists of a spring and a Maxwell element in parallel. One way to generalize the Zener model is to include more than one Maxwell elements in parallel to represent different relaxation times of the material, leading to a viscoelastic material model [113, 3, 26, 69]. Another approach of the generalization is to add additional plastic elements to the generalized Zener model from the beginning [93, 59]. The plastic elements model the amplitude-dependence and/or equilibrium hysteresis of the behavior of the elastomeric materials. The Maxwell and plastic elements are all independent of each other in the Zener model generalizations. A Poynting-Thomson model consists of a leading spring and a Kelvin model in series. The generalization of the Poynting-Thomson model usually adds additional Kelvin models in series. In this case, the Kelvin models in series are coupled to each other.



Figure 40: Rheological models. Left: Zener model; right: Poynting-Thomson model.

11.2.1 Multiplicative decomposition of deformation gradient

11.2.1.1 Concept of decomposition of deformation gradient in uniaxial model

The concept of multiplicative decomposition of deformation gradient tensor can be explained using an uniaxial rheological model [59, 93], as illustrated in Fig. 41. This model is a generalization of the Zener model with an additional plastic element. The spring at the top is introduced to represent the nonlinear elastic behavior. The Maxwell element in the middle is attributed to the rate-dependent part of the stress. Finally the plastic element at the bottom describes the rate-independent equilibrium hysteresis effects. These three branches are assumed to be independent of each other and subjected to the same strain. All the springs in the model must be nonlinear and thus stand for nonlinear functions of the strains ε , ε^{ev} , and ε^{ep} , respectively.

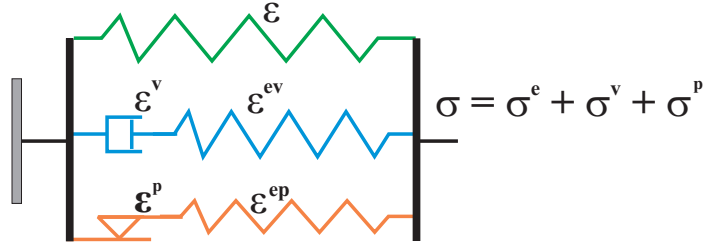


Figure 41: Uniaxial rheological model.

The stresses in each branch are the equilibrium elastic stress, the over-stress and the equilibrium plastic stress, denoted σ^e , σ^v , and σ^p , respectively. The total stress of this uniaxial model is the sum of the above three types of stresses

$$\sigma = \sigma^e + \sigma^v + \sigma^p. \quad (153)$$

The total strain of this uniaxial model, ε , may be decomposed into elastic and viscous strains for Maxwell element, which means

$$\varepsilon = \varepsilon^{ev} + \varepsilon^v; \quad (154)$$

or into elastic and plastic strains for the plastic branch as

$$\varepsilon = \varepsilon^{ep} + \varepsilon^p. \quad (155)$$

For physical reasons the strain energy function is assumed to be sum of three strain energy functions, which are related to three springs in the model, respectively,

$$\psi = \psi_0(\varepsilon) + \psi_v(\varepsilon^{ev}) + \psi_p(\varepsilon^{ep}). \quad (156)$$

In Eq. (156), ψ_0 is a function depending on the total strain ε ; the strain energy of the spring in Maxwell element ψ_v is a function depending on the elastic strain ε^{ev} ; and the strain energy of the spring in the plastic branch ψ_p is a function depending on the elastic strain ε_{ep} .

For isothermal processes the entropy inequality reduces to the statement that the stress power minus the rate of change of free energy must be non-negative, i.e.,

$$\sigma \dot{\varepsilon} - \dot{\psi} \geq 0. \quad (157)$$

Inserting Eqs. (153) and (156) into Eq. (157) and using Eqs. (154) and (155), one obtains the following expression

$$\left(\sigma^e - \frac{\partial \psi_0}{\partial \varepsilon} \right) \dot{\varepsilon} + \left(\sigma^v - \frac{\partial \psi_v}{\partial \varepsilon^{ev}} \right) \dot{\varepsilon} + \left(\sigma^p - \frac{\partial \psi_p}{\partial \varepsilon^{ep}} \right) \dot{\varepsilon} + \frac{\partial \psi_v}{\partial \varepsilon^{ev}} \dot{\varepsilon}^v + \frac{\partial \psi_p}{\partial \varepsilon^{ep}} \dot{\varepsilon}^p \geq 0. \quad (158)$$

In Eq. (158) all coefficients of the total strain rate $\dot{\varepsilon}$ should be zero because the springs are assumed to be elastic; thus, one has

$$\sigma^e = \frac{\partial \psi_0}{\partial \varepsilon} = f_e(\varepsilon), \quad (159a)$$

$$\sigma^v = \frac{\partial \psi_v}{\partial \varepsilon^{ev}} = f_v(\varepsilon^{ev}) = f_v(\varepsilon - \varepsilon^v), \quad (159b)$$

$$\sigma^p = \frac{\partial \psi_p}{\partial \varepsilon^{ep}} = f_p(\varepsilon^{ep}) = f_p(\varepsilon - \varepsilon^p), \quad (159c)$$

and the entropy inequality reduces to

$$\frac{\partial \psi_v}{\partial \varepsilon^{ev}} \dot{\varepsilon}^v + \frac{\partial \psi_p}{\partial \varepsilon^{ep}} \dot{\varepsilon}^p \geq 0. \quad (160)$$

This inequality shows that the choices of the evolution equations for the inelastic strains ε^v and ε^p are not arbitrary if the model is required to be compatible with the entropy inequality.

This inequality can be satisfied in the sense of sufficient conditions by appropriate flow rules

$$\dot{\varepsilon}^v = \frac{1}{\eta_v} \sigma^v \quad (161a)$$

$$\dot{\varepsilon}^p = \frac{1}{\eta_p} |\dot{\varepsilon}| \sigma^p, \quad (161b)$$

where $\eta_v > 0$ is the viscosity and $\eta_p > 0$ is a material constant. Since the rate-dependent response is nonlinear and the relaxation behavior depends on the loading history, the viscosity should be a function of process quantities. Note that Eq. (161a) is simply a viscosity relation, and that Eq. (161b) is the simplest kind of flow rule of rate-independent plasticity without a yield surface. Different flow rules can be used as long as they satisfy Eq. (160).

11.2.1.2 Three-dimensional model based on decomposition of deformation gradient

The uniaxial model discussed above can be generalized to a three-dimensional version [59, 93]. In this case the additive decomposition of the strain in the uniaxial model corresponds to a multiplicative decomposition of the deformation gradient tensor F . Thus, corresponding to Eqs. (154) and (155), the deformation gradient can be decomposed into elastic and viscous parts, and elastic and plastic parts, respectively,

$$F = F_{ev}F_v. \quad (162a)$$

$$F = F_{ep}F_p, \quad (162b)$$

The decompositions in Eqs. (162) introduce two intermediate configurations \mathcal{F}_v and \mathcal{F}_p , respectively.

Inserting the decomposition of the deformation gradient, Eqs. (162), into the Green-Lagrangian strain tensor

$$E = \frac{1}{2}(G - U), \quad (163)$$

with

$$G = F^T F \quad (164)$$

as the right Cauchy-Green strain tensor and U identity tensor; one has

$$E = \frac{1}{2}(F_p^T G_{ep} F_p - U), \quad (165a)$$

$$E = \frac{1}{2}(F_v^T G_{ev} F_v - U), \quad (165b)$$

where $G_{ev} = F_{ev}^T F_{ev}$ and $G_{ep} = F_{ep}^T F_{ep}$ are tensors similar to the right Cauchy-Green strain tensor, Eq. (164), but related to F_{ev} and F_{ep} , respectively.

When expressing Eqs. (165) in configurations \mathcal{F}_v and \mathcal{F}_p , respectively, one obtains,

$$(F_v^T)^{-1} E F_v^{-1} = \frac{1}{2} (G_{ev} - U) + \frac{1}{2} (U - B_v^{-1}) =: E_{ev} + E_v; \quad (166a)$$

$$(F_p^T)^{-1} E F_p^{-1} = \frac{1}{2} (G_{ep} - U) + \frac{1}{2} (U - B_p^{-1}) =: E_{ep} + E_p, \quad (166b)$$

where $B_v = F_v F_v^T$ and $B_p = F_p F_p^T$. It is clear that the strain tensors, when expressed in the intermediate configurations, can be additively decomposed into a purely elastic part and a purely inelastic part. Further one can define the deformation rates for the total, viscous and plastic deformations, respectively, as

$$L = \dot{F} F^{-1}, \quad (167a)$$

$$L_v = \dot{F}_v F_v^{-1}, \quad (167b)$$

$$L_p = \dot{F}_p F_p^{-1}; \quad (167c)$$

and their symmetric parts as

$$D = \frac{1}{2} (L + L^T), \quad (168a)$$

$$D_v = \frac{1}{2} (L_v + L_v^T), \quad (168b)$$

$$D_p = \frac{1}{2} (L_p + L_p^T). \quad (168c)$$

Corresponding to the uniaxial rheological model, the second Piola-Kirchhoff stress tensor S is decomposed into a rate-dependent over-stress tensor, S_v , and a rate-independent equilibrium stress tensor, the latter is in turn a sum of a elastic part, S_e , and a history dependent-hysteretic part, S_p ,

$$S = S_e + S_v + S_p. \quad (169)$$

Note that the stress decomposition in Eq. (169) is associated to the reference configuration, whereas the strain decomposition, Eqs. (166), are related to the intermediate configurations \mathcal{F}_v and \mathcal{F}_p , respectively. Hence the over-stress tensor, S_v , and the hysteretic stress tensor, S_p , should be transformed to configurations \mathcal{F}_v and \mathcal{F}_p , respectively, in order to relate the corresponding strain and stress tensors by the constitutive equations. The elastic part, S_e , of the equilibrium stress tensor does not need to be transformed because the corresponding

strain tensor, the Green-Lagrangian strain E , operates on the reference configuration. The over-stress tensor and the hysteretic part of the equilibrium stress tensor, when transformed into configurations \mathcal{F}_v and \mathcal{F}_p , can be written as, respectively,

$$\tau_v := F_v S_v F_v^T, \quad (170a)$$

$$\tau_p := F_p S_p F_p^T. \quad (170b)$$

Accordingly, the second Piola-Kirchhoff stress tensor S , Eq. (169), becomes

$$S = S_e + F_v^{-1} \tau_v (F_v^T)^{-1} + F_p^{-1} \tau_p (F_p^T)^{-1}. \quad (171)$$

In the context of the uniaxial rheological model, the free energy is the sum of the strain energies of all spring elements. Accordingly the strain energy in this three-dimensional model may be assumed as

$$\psi = \psi_0(G) + \psi_v(G_{ev}) + \psi_p(G_{ep}). \quad (172)$$

The entropy inequality is generalized into three dimensional version as

$$S \cdot \dot{E} - \dot{\psi} \geq 0. \quad (173)$$

After inserting Eq. (171) and some calculations, the entropy inequality becomes,

$$\begin{aligned} & \left(S_e - 2 \frac{d\psi_0}{dG} \right) \cdot \dot{E} + \left(\tau_v - 2 \frac{d\psi_v}{dG_{ev}} \right) \cdot \left[(F_v^T)^{-1} E F_v^{-1} \right] \\ & + \left(\tau_p - 2 \frac{d\psi_p}{dG_{ep}} \right) \cdot \left[(F_p^T)^{-1} E F_p^{-1} \right] + [(U + 2E_{ev}) \tau_v] \cdot D_v + [(U + 2E_{ep}) \tau_p] \cdot D_p \geq 0. \end{aligned} \quad (174)$$

Coleman and Noll standard arguments [36] then lead to the stress relations

$$\begin{aligned} S_e &= 2 \frac{d\psi_0}{dG} = f(G), \\ \tau_v &= 2 \frac{d\psi_v}{dG_{ev}} = f_v(G_{ev}), \\ \tau_p &= 2 \frac{d\psi_p}{dG_{ep}} = f_p(G_{ep}); \end{aligned} \quad (175)$$

and the entropy inequality reduces to

$$[(U + 2E_{ev}) \tau_v] \cdot D_v + [(U + 2E_{ep}) \tau_p] \cdot D_p \geq 0. \quad (176)$$

In order to state sufficient conditions for the entropy inequality, Eq. (176), one may specify the evolution equations for the inelastic strains by the following flow rules

$$D_v = \frac{1}{\eta_v} (U + 2E_{ev}) 2 \frac{d\psi_v}{dG_{ev}}, \quad (177a)$$

$$D_p = \frac{1}{\eta_p} \|(F_p^T)^{-1} \dot{E} F_p^{-1}\| (U + 2E_{ep}) 2 \frac{d\psi_p}{dG_{ep}}, \quad (177b)$$

where $\eta_p > 0$ is a material constant and $\eta_v > 0$ the viscosity. Since the rate-dependent response is nonlinear and the relaxation behavior depends on the loading history, the viscosity should be a function of process quantities.

As Haupt and Sedlan [59] pointed out, the viscosity, η_v , should be a function of process variables; and they proposed a simple equation that relates the viscosity to the strain rate as,

$$\frac{1}{\eta_v} = \frac{1}{\mu \|B\|} \left(\xi \|D\| + \frac{1}{\tau_0} \right), \quad (178)$$

where $B = FF^T$ is the left Cauchy-Green deformation tensor and μ and ξ are material constants. The relaxation time τ_0 is further allowed to vary between a minimum value τ_{min} and a maximum value τ_{max} ,

$$\tau_0 = \tau_{max}(1 - q) + \tau_{min}q, \quad (179)$$

and in turn, the structural variable q is governed by an initial-value problem

$$\dot{q} = \varphi \|D\| (1 - q) - \frac{1}{\tau_q} q^\kappa, \quad q(0) = 0, \quad (180)$$

where φ , κ , and τ_q are additional material parameters.

11.2.1.3 Evolution laws

Note that the temporal evolution equations, for instance, Eqs. (177), governing the internal variables, are not unique as long as they satisfy the second law of thermodynamics, for example, Eq. (173) for isothermal processes. Some researchers proposed models based on the multiplicative decomposition of the deformation gradient tensor but with different evolution laws, as introduced in the following. These models are all based on the generation of Zener model.

• Reese and Govindjee [113] proposed a finite deformation viscoelastic model with a non-linear evolution law. Thus, the model is not restricted to states close to the thermodynamic equilibrium. In their derivations, the residual dissipation inequality takes the following form

$$-\tau_v : \frac{1}{2}(\mathcal{L}_v B_{ev})B_{ev}^{-1} \geq 0, \quad (181)$$

with

$$\tau_v = 2F_{ev} \frac{d\psi_v}{dG_{ev}} F_{ev}^T, \quad (182a)$$

$$\mathcal{L}_v B_{ev} = F (G_v^{-1})' F^T, \quad (182b)$$

$$B_{ev} = F_{ev} F_{ev}^T. \quad (182c)$$

A sufficient condition fulfilling Eq. (181) gives the evolution equation

$$-\frac{1}{2}(\mathcal{L}_v B_{ev})B_{ev}^{-1} = \mathcal{V}^{-1} : \tau_v, \quad (183)$$

with

$$\mathcal{V}^{-1} = \frac{1}{2\eta_D} \left(U^4 - \frac{1}{3}U \otimes U \right) + \frac{1}{9\eta_V} U \otimes U, \quad (184)$$

where U^4 is the fourth order symmetric identity tensor, and η_D and η_V are the deviatoric and volumetric viscosities, respectively, possibly deformation dependent. The final form of the evolution equation is, by inserting Eq. (184) into Eq.(183),

$$-\frac{1}{2}(\mathcal{L}_v B_{ev})B_{ev}^{-1} = \frac{1}{\eta_D} \text{dev}[\tau_v] + \frac{2}{9\eta_V} (\tau_v : U)U, \quad (185)$$

where $\text{dev}[\cdot] = (\cdot) - \text{tr}(\cdot)U/3$ is the deviator of the indicated argument. This evolution law is valid for large deformations and large perturbations away from thermodynamic equilibrium.

• Amin *et al.* [3] investigated the rate-dependent behavior of filled natural rubber and high damping rubber in compression and shear regimes. They identified the constitutive equation for the viscosity directly from the experimental data. They followed Huber and Tsakmakis's procedure [69, 68], in which the evolution equation is expressed in Mandel stress tensor,

$$D_v = \frac{1}{\eta_v} (P - P_{ev})^D, \quad (186)$$

with $P = F_{ev}^{-1} S F_{ev}$, with $P_{ev} = F_{ev}^{-1} S_{ev} F_{ev}$ called Mandel stress tensor by analogy to that used in plasticity theory, and with superscript D indicating the deviatoric part of the argument.

Based on their experiments and identification scheme, they proposed an evolution equation using a power law to represent the effects of internal variable on viscosity phenomena, which is

$$\frac{1}{\eta_v} = \frac{1}{\eta_0 \|B\|^\phi} \left(\frac{\|P_v\|}{\pi} \right)^\delta, \quad (187)$$

where δ , ϕ and η_0 are material parameters; and $\pi = 1\text{MPa}$ is a constant introduced for dimensional reasons. Comparing Eq. (187) with Eq. (178), one can find that the dependence of the viscosity η_v on the left Cauchy-Green tensor $B = FF^T$ is similar for both models. The difference is that, in Eq. (178), an inverse dependence of η_v on the total strain rate $D = \frac{1}{2}(L + L^T)$ is suggested, while in Amin *et al.*'s model, the over-stress P_v is introduced as a variable in the evolution equation. This model has shown an encouraging correlation with the experiments conducted on natural rubber and high damping rubber in both compression and shear deformations. Amin *et al.* also proposed a different viscosity for the unloading path in order to consider the weak rate dependency during unloading,

$$\eta_v = \left\{ \eta_1 + (\eta_0 - \eta_1) \frac{1}{2} [1 + \tanh(\xi S D)] \right\} \left(\frac{\pi}{\|P_v\|} \right)^\delta \|B\|^\phi. \quad (188)$$

- Bonet [26] proposed a large strain viscoelastic constitutive model, which is also based on the multiplicative decomposition of the deformation gradient, with a nonlinear rate type of evolution equations for the internal variables. Bonet started the derivation from a Maxwell rheological model, for which the following equations can be written for the dashpot and spring, respectively,

$$\sigma = \eta_v \dot{\varepsilon}_v, \quad (189a)$$

$$\sigma = E(\varepsilon - \varepsilon_v); \quad (189b)$$

where η_v and E are the viscosity for the dashpot and spring constant, respectively. Keeping the total strain ε as constant, and substituting $\dot{\varepsilon}_v$ from Eq. (189a) into the time derivative

of Eq. (189b), one has

$$\dot{\sigma}|_{\varepsilon=\text{constant}} = -\frac{1}{\tau_v}\sigma, \quad (190)$$

where $\tau_v = \eta_v/E$ is the relaxation time for the Maxwell model. Eq. (190) is then extended to a three dimensional version by replacing the stress with the second Piola-Kirchhoff stress tensor, S_v , and the strain by the right Cauchy-Green strain tensor, G ,

$$\frac{dS_v}{dt}|_{G=\text{constant}} = -\frac{1}{\tau_v}S_v. \quad (191)$$

Given that S_v is a function of G_v , Eq. (191) becomes, using the chain rule,

$$\frac{\partial S_v}{\partial G_v} : \dot{G}_v = -\frac{1}{\tau_v}S_v. \quad (192)$$

This leads to the nonlinear evolution equation for the internal variable G_v ,

$$\dot{G}_v = -\frac{1}{\tau_v}M_v^{-1} : S_v, \quad (193)$$

with

$$M_v = 2\frac{\partial^2\psi_v(G, G_v)}{\partial G\partial G_v}. \quad (194)$$

It should be noted that although the evolution equations Eqs. (193) and (194) for the internal variables G_v are nonlinear, the underlying relaxation in Eq. (191) is linear. One may construct a fully nonlinear evolution model by replacing the right-hand side of Eq. (191) with an appropriate flow rule.

- Miehe and Keck [98] proposed a constitutive model for elastomeric materials which in some sense includes all four fundamental material behavior of the elastomers introduced previously. This phenomenological material model superimposes finite elastic, viscoelastic, and plastic response, together with a damage model for modeling the stress-softening effect. This model is suitable for the simulation of carbon-black filled rubbers in monotonic and cyclic deformation processes under isothermal conditions. This model decomposes the local stress response into three constitutive branches that act in parallel: an elastic stress response, a rate-dependent viscoelastic over-stress response of the Maxwell type and a rate-independent plastoelastic over-stress response. The damage is assumed to act isotropically on all three branches. These three branches are represented in a completely analogous

format within separate eigenvalue spaces, and the viscoelasticity and elastoplasticity are described within a framework of finite inelasticity based on the notion of developing reference metric tensors. This framework provides an extremely compact representation of isotropic finite inelasticity in a complete analogous representation of the three constitutive branches, and the representation of the viscous and plastic flow rules in the form of evolution equations for eigenvector are obtained from general eigenvalue problems.

11.2.1.4 *Generalization of Poynting-Thomson model*

All the models discussed above are based on generalizations of Zener's model. Huber and Tsakmakis applied the multiplicative decomposition of the deformation gradient tensor approach to a Poynting-Thomson model in [69, 68]. Laiarinandrasana *et al.* [83] developed a constitutive model for a Poynting-Thomson model using the same approach. They postulated that there exists a dissipation pseudo-potential, which relates the thermodynamical forces to their corresponding fluxes. They also included a damage model to account for the Mullins effect. The Mullins effect was described as a continuum damage model driven by the maximum strain. A damage factor $D \in [0, 1)$, which measures the relative damage area, was introduced, and the nominal strain energy was assumed as

$$W = (1 - D)W_0, \tag{195}$$

where W_0 is the effective energy with respect to the undamaged material.

11.2.1.5 *Thermal effects*

Several authors [60, 91, 94] used the concept of multiplicative decomposition of the deformation gradient tensor to consider the thermal effects during the deformation of elastomeric materials. The deformation gradient tensor was first decomposed into thermal and mechanical parts, the latter being further decomposed into elastic and inelastic parts.

It is worth noting that in this modeling approach, the evolution equations are obtained through the enforcement of the second law of thermodynamics; thus, all of these models are thermodynamically consistent. In the next section, another modeling approach, stress convolution model, will be discussed. The evolution equations in some of those models are

proposed by postulation. The consistency with the second law of thermodynamics for those models is questionable, especially for the finite deformation cases.

11.2.2 Stress convolution models

11.2.2.1 Concept of stress decomposition

Another approach to model the inelastic behavior of the elastomeric materials is to additively decompose the second Piola-Kirchhoff stress tensor, instead of the deformation gradient tensor, into equilibrium and non-equilibrium parts. The equilibrium response is assumed to be governed by a free energy function $\psi_{eq}(G)$. The non-equilibrium response of the material is characterized by a set of non-equilibrium free energy functions $\psi_{neq}^k(G)$, where k represents the k th relaxation mechanism in the material and each of them is associated with a non-equilibrium stress Q^k [52]. One or more relaxation mechanisms may be considered in the model. Note that both parts of the strain energy are functions of the total strain G , which is different from the deformation decomposition based models. The second Piola-Kirchhoff stress tensor reads, for a generalized Zener model,

$$S(t) = S_{eq} + S_{neq} = 2 \frac{d\psi_{eq}(G)}{dG} + \sum_{k=1}^N Q^k(t). \quad (196)$$

A simple linear evolution equation which governs the non-equilibrium stress is postulated as [118, 65],

$$\frac{d}{dt} Q^k(t) + \frac{1}{\tau^k} Q^k(t) = \frac{d}{dt} \left[2 \frac{d\psi_{neq}^k(G)}{dG} \right], \quad (197a)$$

$$Q^k(t)|_{t=0} = Q_0^k \quad (197b)$$

where τ^k is the relaxation time related to the k th relaxation mechanism. Eq. (197) can be written in a convolution form as

$$Q^k(t) = Q_0^k \exp\left(-\frac{t}{\tau^k}\right) + \int_{-\infty}^t \exp\left[-\frac{t-s}{\tau^k}\right] \frac{d}{ds} \left[2 \frac{d\psi_{neq}^k(G)}{dG} \right] ds. \quad (198)$$

This model is well known to be computationally efficient; however, it has not been conclusively proven to satisfy the second law of thermodynamics for all admissible processes. In the small deformation case this model simply reduces to that of the generalized standard linear solid, which is known to satisfy the second law of thermodynamics.

Simo [118] also employed a continuum damage mechanics to develop a simple isotropic damage mechanism, which incorporates stress-softening behavior (Mullins effect) under deformation, and leads to progressive degradation of the storage modulus in a cyclic test with increasing amplitude.

Holzappel and Simo [66] investigated the thermal effect during the deformation through adding an additional term, which contains temperature dependent material parameters and vanishes for isothermal processes, to the right-hand side of Eq. (197a)

$$\frac{d}{dt}Q^k(t) + \frac{1}{\tau^k}Q^k(t) = \frac{d}{dt} \left[2 \frac{d\psi_{neq}^k(G)}{dG} \right] - Q_{cpl}^k(t). \quad (199)$$

The additional term is in turn governed by another set of internal variables, Γ^k , through

$$Q_{cpl}^k(t) = 2\dot{\mu}^k\Gamma^k(t), \quad (200)$$

where $\mu^k \geq 0$ are temperature dependent parameters.

11.2.2.2 A finite viscoplastic model based on stress decomposition

Lion [90] developed a constitutive model of finite strain viscoplasticity based on the stress decomposition concept. The idea of the proposed model can be explained in a uniaxial model of viscoplasticity as follows.

First the total stress is decomposed into an equilibrium stress σ_{eq} and an over-stress σ_{ov} ,

$$\sigma = \sigma_{eq} + \sigma_{ov}. \quad (201)$$

The rate-dependent behavior of the material is related to the over-stress, while the rate-independent behavior to the equilibrium stress. The rate of the over-stress is assumed to be governed by a differential equation,

$$\dot{\sigma}_{ov} = (\sigma_{sp} - \sigma_{eq})' - \frac{1}{z_0 M(|\sigma_{ov}|)} \sigma_{ov}, \quad (202)$$

where σ_{sp} is the spontaneous stress, z_0 a material constant and M a material function depending on the amplitude of the over-stress. In order to represent the nonlinearity of the rate-dependent behavior, a stress dependent relaxation time $z_0 M(|\sigma_{ov}|)$ was proposed.

In a similar manner, the equilibrium stress, σ_{eq} , is split into two parts, $\sigma_{eq\infty}$ and σ_{eqov} , relating to the elastic behavior and the rate-independent hysteresis behavior, respectively,

$$\sigma_{eq} = \sigma_{eq\infty} + \sigma_{eqov}. \quad (203)$$

The later is further related to the arclength presentation through a differential equation,

$$\dot{\sigma}_{eqov} = (\sigma_{eq0} - \sigma_{eq\infty})' - b\dot{z}\sigma_{eqov}. \quad (204)$$

The variable z can be set as $\dot{z} = |\dot{\varepsilon}|$. In this model, three energy potentials ψ_{sp} , ψ_{eq0} , and $\psi_{eq\infty}$ should be specified and the stress components σ_{sp} , σ_{eq0} , and $\sigma_{eq\infty}$ can be derived from them, respectively, as

$$\sigma_{sp} = \frac{d\psi_{sp}(\varepsilon)}{d\varepsilon} = f_{sp}(\varepsilon), \quad (205a)$$

$$\sigma_{eq0} = \frac{d\psi_{eq0}(\varepsilon)}{d\varepsilon} = f_{eq0}(\varepsilon), \quad (205b)$$

$$\sigma_{eq\infty} = \frac{d\psi_{eq\infty}(\varepsilon)}{d\varepsilon} = f_{eq\infty}(\varepsilon). \quad (205c)$$

The extension of the uniaxial model to a three-dimensional finite strain viscoplastic model is straightforward if the concept of dual variables is adopted [57]. Some numerical simulations in the paper demonstrate that the proposed model is able to represent the experimentally observed phenomena qualitatively and quantitatively with a sufficient level of accuracy for carbon-black filled elastomeric materials.

The Mullins effect is also considered by a continuum damage model, where the evolution of the damage is controlled by the maximum strain. Two additional internal variables are introduced to model the damage. The first one is the relative measure of the damage area $D \in [0, 1)$. The effective stress in the damaged material would be the applied stress divided by a factor $(1 - D)$. This damage variable D is governed by the following different equation,

$$\dot{D} = \alpha_D |\dot{\varepsilon}| [1 - f(g)D], \quad f(0) \geq 1, \quad f(\infty) = 1, \quad f' \leq 0, \quad (206)$$

where $\alpha_D \geq 0$ is a material parameter, and g the second internal variable, which is defined as the maximum value of ε^2 over the past history up to the current time. g can be computed

from the following differential equations,

$$\begin{aligned} \dot{g} &= \varepsilon \dot{\varepsilon} \quad \text{if} \quad \frac{\partial \varphi}{\partial \varepsilon} \dot{\varepsilon} \geq 0 \quad \text{and} \quad \psi = 0, \\ \dot{g} &= 0 \quad \text{in all other cases,} \end{aligned} \tag{207}$$

where φ is defined as

$$\varphi = \frac{1}{2} \varepsilon^2 - g. \tag{208}$$

11.2.3 Anelastic displacement fields model

Recently, the anelastic displacement fields (ADF) method was proposed by Lesieutre and his colleagues [86, 87] to describe the frequency dependent behavior of linear elastomeric materials, as well as the temperature dependence [88]. ADF model is a special kind of augmenting thermodynamic fields (AFT) model [89, 85]. The AFT model is based on the notion of scalar internal variables or augmenting thermodynamic fields that describe the interaction of the usual mechanical displacement field of continuum structural dynamics with irreversible processes occurring at the material level. The techniques of non-equilibrium irreversible thermodynamics, namely that the time rate of change of the state variable describing an irreversible process is proportional to the corresponding conjugate quantity, are used to develop coupled material constitutive equations and coupled partial differential equations of evolution. In the ADF approach, the effects of the thermodynamic processes are focused on the displacement fields.

In the ADF method, the displacement/strain field is split into elastic and anelastic parts. The anelastic part is essentially the internal variable that accounts for the material relaxation process. A single ADF model is mechanically analogous to a Poynting-Thomson model, which consists of a leading spring and a Kelvin element in series, as depicted in Fig. 40. From the mechanical analogy, the stress in the leading spring is determined by its modulus and the elastic strain across it. The elastic strain is the difference between the total observable strain and the total internal anelastic strain. The stress in the dashpot is the difference between the stress in leading spring and the secondary spring in the Kelvin element that is in parallel with the dashpot. This dashpot stress is also equivalent to the dashpot constant multiplied by the time rate of change of the anelastic strain; this relation

gives the evolution equation for the internal anelastic field.

The anelastic displacement/strain may be further subdivided, where each individual anelastic strain represents a relaxation process in the viscoelastic material. This leads to the multi-ADF model. Each of the subdivided anelastic fields is governed by an evolution equation, and these evolution equations are decoupled each other, however coupled with the total material strain.

The nonlinearity can be introduced into ADF model by replacing the linear ADF parameters with nonlinear ones that are nonlinear functions of the total and anelastic strains. Brackbill *et al.* [28, 31] improved the nonlinear ADF model by adding rate-independent nonlinearity, in which multiple friction damping and linear spring elements in parallel with the baseline nonlinear ADF model were used to provide additional amplitude dependent relaxation behavior. The ADF approach has been reported to model elastomeric lead-lag dampers in rotorcraft [82, 31, 67].

Currently, the ADF method is mainly applied to one-dimensional viscoelastic problems, such as uniaxial rods [85, 86], and simple shear deformations [88, 31]. The three-dimensional ADF model is not common in the literature. Lesieutre and Bianchini [87] developed a three-dimensional linear viscoelastic model for isotropic materials using ADF approach. A key feature of the model is the absence of explicit time dependence in the constitutive equations. Apparent time-dependent behavior is described instead by evolution equations that govern the relaxation of the anelastic displacement fields. These coupled governing equations are developed in a parallel fashion, involving the divergence of appropriate stress tensors.

11.3 Fractional Calculus Based Models

In 1920s Nutting [103] observed that the stress relaxation process could be modeled by fractional powers of time instead of decaying exponentials. After that many researchers employed the time derivative of fractional order to model Nutting's observation or the viscoelastic phenomena [119, 11, 13, 92, 95]. Slonimsky [119] related the fractional calculus models to the chain structure of macromolecules and supermolecular structure of the polymeric materials. An advantage of the fractional derivative models is that they produce

compact analytical representations of complex modulus, well behaved in both the frequency and time domains [12]. A fractional derivative model is able to provide a continuous relaxation spectrum for the viscoelastic materials, comparing with the discrete relaxation spectrum which can be expressed as linear combination of finite number of decreasing exponentials. This leads to relaxation functions very close to the relaxation behavior of real materials [58].

The stress and strain relation of standard linear viscoelastic materials can be represented as a series of time derivatives acting on the stress and strain fields [10],

$$\sigma(t) + \sum_{m=1}^M b_m \frac{d^m \sigma(t)}{dt^m} = E_0 \varepsilon(t) + \sum_{n=1}^N E_n \frac{d^n \varepsilon(t)}{dt^n}. \quad (209)$$

For viscoelastic materials that are frequency dependent over a wide range of frequencies, the number of time derivatives M and N is large; consequently the number of empirical parameters in the model is also large. This will result in a high-order differential equation of motion. However, when fractional derivative is introduced, the general form of the viscoelastic model may be represented as

$$\sigma(t) + \sum_{m=1}^M b_m D_m^\beta \langle \sigma(t) \rangle = E_0 \varepsilon(t) + \sum_{n=1}^N E_n D_n^\alpha \langle \varepsilon(t) \rangle, \quad (210)$$

where $D^\alpha \langle f(t) \rangle$ is the fractional derivatives defined by

$$D^\alpha \langle f(t) \rangle = \frac{1}{\Gamma(1-\alpha)} \frac{d}{dt} \int_0^t \frac{f(\tau)}{(t-\tau)^\alpha} d\tau, \quad 0 < \alpha < 1; \quad (211)$$

with Γ the Gamma function. Experimental observations indicate that many viscoelastic materials can be modeled by retaining the first fractional derivative term in both sides of Eq. (210), thus the fractional derivative model reduces to five parameters, b , E_0 , E_1 , α , and β , as

$$\sigma(t) + b D^\beta \langle \sigma(t) \rangle = E_0 \varepsilon(t) + E_1 D^\alpha \langle \varepsilon(t) \rangle. \quad (212)$$

Lion [92] investigated uniaxial and three-dimensional viscoelastic models at constant temperature in combination with fractional differential operator. Sufficient conditions for the Clausius-Duhem inequality was specified, and it was shown that the rheological models consisting of springs and fractional dashpots are compatible with the dissipation principle.

The author also presented a systematic method for deriving the free energy functionals for fractional systems, which can be derived as a generalization of related discrete systems. Drozdov [38] proposed a new class of constitutive models for viscoelastic media capable of finite strains with the help of the so-called fractional derivatives of tensor functions. The models were verified by comparison with experimental data for viscoelastic solids and fluids. It is shown that the fractional Kelvin-Voigt model provides excellent predictions, whereas the fractional Maxwell model ensures fair agreement between experimental data and results of numerical simulation.

Taking Fourier transform of the fractional derivative operator, Eq. (211), one has

$$F[D^\alpha \langle f(t) \rangle] = (i\omega)^\alpha F[f(t)]. \quad (213)$$

It is convenient to model the viscoelastic model in frequency domain. Bagley and Torvik [13] examined the consistency of the fractional derivative model with the thermodynamic principles. The development of constraints on parameters of the model ensures that the model predicts a nonnegative rate of energy dissipation and a nonnegative internal work. These constraints led the model to predict realistic sinusoidal response as well as realistic relaxation and creep responses. Lu [95] developed a form of fractional derivative viscoelastic model for characterizing frequency dependent complex moduli of elastomeric materials.

11.4 Micromechanics Based Models

Unlike the molecular approach to the theory of rubber elasticity which can be traced back at least to 1930s, the micromechanics based models for modeling the inelastic behavior of elastomeric materials are quite recent. One main reason is the limited information about the microstructure of the elastomeric materials. In this approach, the elastomeric material is usually treated as a network of long chains bridged by permanent and temporary junctions associated at the micro-level with chemical crosslinks and active entanglements, respectively. A strand between two junctions is thought of as a sequence of statistically independent segments linked by covalent bonds [40].

Bergström and Boyce [22] proposed a viscoelastic model based on the assumption that

the molecular network may be decomposed into two parts: an equilibrium network corresponding to the state that is approached in long time stress relaxation tests; and a second network capturing the nonlinear rate-dependent deviation from the equilibrium state. The time-dependence of the second network is further assumed to be governed by the rotational motion of molecules having the ability to significantly change conformation and thereby relaxing the overall stress state. The stress-strain relationship for the equilibrium network is governed by a compressible version of the eight-chain network model of Arruda and Boyce [7] as discussed in section 10.4.2. The time-dependent behavior of the second network is based on a decomposition of the strain into elastic and inelastic parts and the stress-strain relationship for this network is then obtained in the same manner as for the equilibrium network, but based on the decomposed elastic strain only. The inelastic strain is further determined by an evolution equation. This constitutive model predicts rate-dependence and relaxation behavior well for uniaxial compression and plane strain compression. This model was further extended by same authors to account for the effect of filler particles on the time-dependent, hysteretic stress-strain behavior [23]. The influence of filler particles is modeled by amplification of scalar equivalent values of the stretch and shear stress. The amplification factor is dependent on the volume fraction and distribution of filler particles. A direct comparison between the new model and experimental data indicates that the new model framework successfully captures the observed behavior in experiments.

Drozdov and Dorfmann [39] studied the isothermal time-dependent response of particle reinforced elastomeric materials at finite strains based on the concept of rigid-rod networks. The main assumption in the theory of rubber elasticity is that the configurational entropy of a chain substantially exceeds its mechanical energy, so that the latter may be neglected in the calculations. However, some experimental observations showed that the mechanical energy of chains may substantially exceed the contribution of their configurational energy into the free energy of elastomeric materials. In their rigid-rod concept based model, the strand between two neighboring junctions is treated as a sequence of rigid rods connected by bonds. In the stress-free state, a bond may be in one of two stable conformations: flexed and extended. An explicit expression was developed for the free energy of a network.

Stress-strain relations and kinetic equations for the concentrations of bonds in various conformations were derived using the laws of thermodynamics. Fair agreement is demonstrated between the experimental results and the numerical simulation results.

Reese [112] extended the concept of transient network, which is based on the assumption that the chains in the material are steadily breaking and reforming, to the finite viscoelasticity. This means the new model is capable for the states far away from the thermodynamic equilibrium. A crucial assumption for the concept of transient network is the idea of a stress-free intermediate configuration, which is related in the continuum mechanical context to the elastic-inelastic multiplicative decomposition of the deformation gradient. This is motivated by the observation that the deformation in single crystals can be decomposed into the inelastic slip on the crystallographic slip planes and elastic lattice distortions and rigid rotations. In section 11.2.1, this idea of stress-free intermediate configuration is used in the approach of multiplicative decomposition of the deformation gradient tensor at a macromechanical level, while it is used at the micromechanical level in the transient network theory.

11.5 Summary

Among the modeling approaches for the inelastic behavior of elastomeric materials discussed above, the internal variables based models are very common, whereas the micromechanics based models are few and relatively new, due to the limited knowledge about the microstructure of the elastomeric materials. Some shortcomings for the micromechanics based models are their fundamental difficulties in the description of stress-softening, *i.e.*, the Mullins effect, for elastomeric materials under cyclic loading, thermal recovery of rubbery polymers, and fracture of reinforced rubbers [40]. Although the fractional calculus based models are well behaved in both frequency and time domains and lead to continuous relaxation functions very close to the relaxation behavior of real materials, this type of models with equilibrium hysteresis effect is not seen in the literature.

The anelastic displacement fields model is an internal variables based model developed recently and has been applied for several lead-lag elastomeric dampers for helicopters.

However, the applications for ADF models are mainly in their one-dimensional forms, *i.e.*, uniaxial model or simple shear model. The current extension of ADF to three-dimensional model focuses on linear viscoelasticity only.

Three-dimensional internal variables based models derived from the decomposition of the deformation gradient or from the stress convolution are very common in the literature. These two types of models are capable to capturing all the inelastic behavior of elastomeric materials and suitable for finite viscoelasticity, for example, the models in [90, 93, 98, 59]. Either the models based on the multiplicative decomposition of the deformation gradient tensor or the stress convolution models might be an option for implementation in this research.

Chapter XII

EVALUATIONS ON ELASTOMERIC MATERIAL MODELS AND MATERIAL PARAMETERS IDENTIFICATION

In this chapter, two elastomeric material models from the literature, one is based on the multiplicative decomposition of the deformation gradient tensor and another one based on the concept of stress decomposition, will be thoroughly evaluated. Their behavior under different strain histories will be compared with experimental data to establish which experimentally observed phenomena these models are able to capture and which they are not. In addition, each material model involves material parameters. These parameters should be identified from experimental data. A material parameters identification procedure will be proposed for each evaluated material model in this chapter, and the experiments needed for identifying the material parameters will be suggested.

12.1 Simple Shear Deformation

To easily and clearly understand the fundamental characteristics of the elastomeric material models, the models will be evaluated based on a simple shear deformation, which is very close to the deformation state for lead-lag dampers used in rotorcraft. Fig. 42 depicts an elastomer specimen under a double-lap shear test. Typically, the fixture is much stiffer than the elastomer specimen so that the width of the specimen, W , can be considered to remain constant during deformation. The left part of the figure shows one elastomeric sample in its reference (solid line) and deformed (dashed line) configurations. The deformation is assumed as plane strain state and the ratio of the length L to the width W of the specimen is assumed to be much greater than unity, *i.e.*, $L/W \gg 1$.

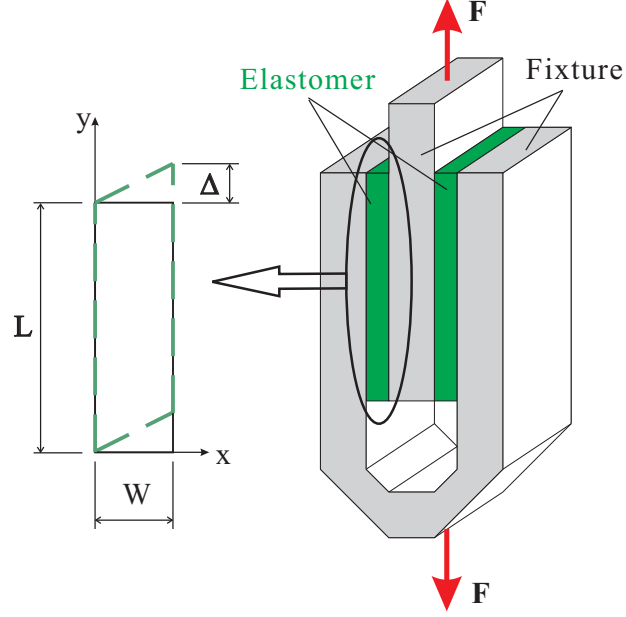


Figure 42: Elastomer specimen under double-lap shear test

12.1.1 Deformation gradient tensor

For a material point with coordinates $\underline{x} = (x, y, z)$ in the reference configuration, its coordinates will become $\underline{X} = (x, y + \gamma x, z)$ in the deformed configuration, where

$$\gamma = \frac{\Delta}{W} \quad (214)$$

is the shear strain. From the definition of deformation gradient $F = d\underline{X}/d\underline{x}$, see Eq. (375), one can obtain

$$F = \begin{bmatrix} 1 & 0 & 0 \\ \gamma & 1 & 0 \\ 0 & 0 & 1 \end{bmatrix}. \quad (215)$$

The right Cauchy-Green strain tensor, Eq. (381), can then be computed as

$$G = F^T F = \begin{bmatrix} 1 + \gamma^2 & \gamma & 0 \\ \gamma & 1 & 0 \\ 0 & 0 & 1 \end{bmatrix}. \quad (216)$$

The invariants of the right Cauchy-Green strain tensor can be computed as, from Eqs. (418),

$$I_1 = \text{tr}(G) = 3 + \gamma^2, \quad (217a)$$

$$I_2 = \frac{1}{2} [(\text{tr}G)^2 - \text{tr}(GG)] = 3 + \gamma^2, \quad (217b)$$

$$I_3 = \det(G) = 1. \quad (217c)$$

It can be seen, from $I_3 = 1$, that this is a volume preserving deformation.

Note that the additive splitting of the shear strain corresponds to a multiplicative decomposition of the deformation gradient for this problem. This can be verified by assuming

$$\gamma = \gamma_1 + \gamma_2, \quad (218)$$

then one has

$$F_1 F_2 = \begin{bmatrix} 1 & 0 & 0 \\ \gamma_1 & 1 & 0 \\ 0 & 0 & 1 \end{bmatrix} \begin{bmatrix} 1 & 0 & 0 \\ \gamma_2 & 1 & 0 \\ 0 & 0 & 1 \end{bmatrix} = \begin{bmatrix} 1 & 0 & 0 \\ \gamma_1 + \gamma_2 & 1 & 0 \\ 0 & 0 & 1 \end{bmatrix} = F, \quad (219)$$

where F_1 and F_2 are the deformation gradient tensors corresponding to shear strains γ_1 and γ_2 , respectively, see Eq. (215). Hence, when the shear strain is split as elastic and plastic parts or elastic and viscous parts,

$$\gamma = \gamma_{ep} + \gamma_p, \quad (220a)$$

$$\gamma = \gamma_{ev} + \gamma_v, \quad (220b)$$

the corresponding decomposition of the deformation gradient tensors will be

$$F = F_{ep} F_p, \quad (221a)$$

$$F = F_{ev} F_v, \quad (221b)$$

where F_{ep} , F_p , F_{ev} , and F_v are deformation gradient tensors corresponding to shear strain γ_{ep} , γ_p , γ_{ev} , and γ_v , respectively.

12.1.2 Stress tensors

When a strain energy function ψ is assumed, the second Piola-Kirchhoff stress tensor can be derived from the strain energy function as, considering $I_3 = 1$,

$$\sigma_{ij} = 2 \frac{\partial \psi}{\partial G_{ij}} = 2 \left(\frac{\partial \psi}{\partial I_1} \frac{\partial I_1}{\partial G_{ij}} + \frac{\partial \psi}{\partial I_2} \frac{\partial I_2}{\partial G_{ij}} \right). \quad (222)$$

The derivatives of the invariants of the right Cauchy-Green strain tensor with respect to the components of the same strain tensor can be computed as, see Eqs. (96a) and (96b),

$$\frac{\partial I_1}{\partial G_{ij}} = \delta_{ij}, \quad (223a)$$

$$\frac{\partial I_2}{\partial G_{ij}} = I_1 \delta_{ij} - G_{ij}. \quad (223b)$$

Thus the second Piola-Kirchhoff stress tensor can be computed as

$$\sigma_{ij} = 2 \frac{\partial \psi}{\partial I_1} \begin{bmatrix} 1 & 0 & 0 \\ 0 & 1 & 0 \\ 0 & 0 & 1 \end{bmatrix} + 2 \frac{\partial \psi}{\partial I_2} \begin{bmatrix} I_1 - (1 + \gamma^2) & -\gamma & 0 \\ -\gamma & I_1 - 1 & 0 \\ 0 & 0 & I_1 - 1 \end{bmatrix} = \begin{bmatrix} \sigma_{11} & \sigma_{12} & 0 \\ \sigma_{21} & \sigma_{22} & 0 \\ 0 & 0 & \sigma_{33} \end{bmatrix}, \quad (224)$$

with

$$\sigma_{11} = 2 \frac{\partial \psi}{\partial I_1} + 4 \frac{\partial \psi}{\partial I_2}, \quad (225a)$$

$$\sigma_{12} = \sigma_{21} = -2\gamma \frac{\partial \psi}{\partial I_2}, \quad (225b)$$

$$\sigma_{22} = \sigma_{33} = \sigma_{11} - \gamma \sigma_{12}. \quad (225c)$$

The second Piola-Kirchhoff stress tensor, Eq. (224), can be transformed to the Cauchy stress tensor based on the following formulation,

$$\tau_{ij} = F \sigma_{ij} F^T = \begin{bmatrix} \sigma_{11} & \gamma \sigma_{11} + \sigma_{12} & 0 \\ \gamma \sigma_{11} + \sigma_{21} & \gamma^2 \sigma_{11} + \gamma(\sigma_{12} + \sigma_{21}) + \sigma_{22} & 0 \\ 0 & 0 & \sigma_{33} \end{bmatrix}. \quad (226)$$

This Cauchy stress can be further decomposed into spherical and deviatoric parts. The spherical part can be computed as

$$p = \frac{1}{3} (\tau_{11} + \tau_{22} + \tau_{33}) = \sigma_{11} + \frac{1}{3} \gamma^2 \sigma_{11}, \quad (227)$$

where Eqs. (225) were used. Then, the deviatoric part of the Cauchy stress becomes

$$\tau_{ij}^{dev} = \tau_{ij} - p\delta_{ij} = \begin{bmatrix} -\frac{1}{3}\gamma^2\sigma_{11} & \gamma\sigma_{11} + \sigma_{12} & 0 \\ \gamma\sigma_{11} + \sigma_{21} & \frac{2}{3}\gamma^2\sigma_{11} + \gamma\sigma_{12} & 0 \\ 0 & 0 & -\frac{1}{3}\gamma^2\sigma_{11} - \gamma\sigma_{12} \end{bmatrix}. \quad (228)$$

Note that the deviatoric stress components τ_{11}^{dev} , τ_{22}^{dev} , and τ_{33}^{dev} in Eq. (228) are higher order terms in term of the shear strain γ compared with τ_{12} . Hence, when γ is assumed to be small, these components can be neglected. In the following discussions, only the shear strain γ and shear stress τ_{12} will be considered. In other words, this simple shearing deformation is considered as a one-dimensional problem. The subscript for the shear stress τ_{12} will be omitted in the following discussions.

12.2 Haupt-Sedlan Model

The first material model to be evaluated was proposed by Haupt and Sedlan [59], which will be referred as H-S model in the following. This model is based on the decomposition of the deformation gradient tensor and its one-dimensional version can be represented by Fig. 43.

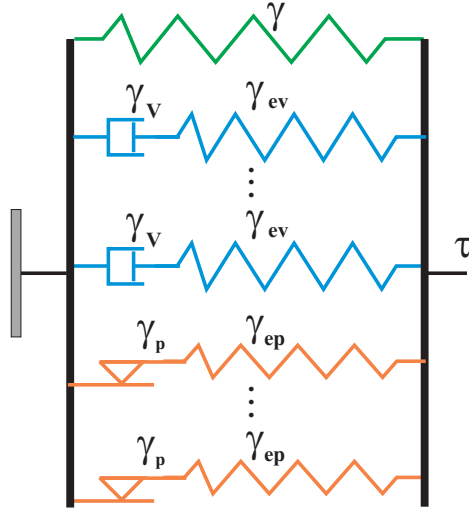


Figure 43: Haupt-Sedlan Model: one-dimensional version

12.2.1 Constitutive equations for H-S model

According to Fig. 43, the total shear stress can be written as

$$\tau = \tau_e + \sum_m \tau_p + \sum_n \tau_v, \quad (229)$$

where τ_e , τ_p , and τ_v are the elastic, plastic and viscous contributions to the total response, respectively. m and n are the number of plastic and viscous branches the model may include, respectively. The total strain in the plastic and viscous branches will be decomposed as elastic and plastic parts, and elastic and viscous parts, respectively, see Eqs. (220). The evolution laws governing the plastic and viscous strains will be assumed the following forms, respectively,

$$\dot{\gamma}_p = \frac{1}{\eta_p} |\dot{\gamma}| \tau_p, \quad (230a)$$

$$\dot{\gamma}_v = \frac{1}{\eta_v} \tau_v; \quad (230b)$$

where $\eta_v > 0$ is the viscosity and $\eta_p > 0$ a material constant. Since the rate-dependent response is nonlinear and the relaxation behavior depends on the loading history, the viscosity should be a function of process variables, and a simple equation that relates the viscosity to the strain rate can be assumed as,

$$\eta_v = \frac{c_v}{\xi |\dot{\gamma}| + 1/\tau_0}, \quad (231)$$

where c_v and ξ are material constants. The relaxation time τ_0 is further allowed to vary between a minimum τ_{min} and a maximum value τ_{max} ,

$$\tau_0 = \tau_{max}(1 - q) + \tau_{min}q, \quad (232)$$

through the introduction of a structural variable q , which is governed by an initial-value problem and should be between 0 and 1,

$$\dot{q} = \zeta |\dot{\gamma}| (1 - q) - \frac{1}{\tau_q} \sqrt{q}, \quad q(0) = 0, \quad (233)$$

where ζ and τ_q are additional material parameters.

The elastic equilibrium stress τ_e , hysteretic equilibrium stress τ_p and over-stress τ_v can be related to the shear strain γ , plastic strain γ_p and viscous strain γ_v , respectively, through

strain energy density functions. As an example, the strain energy functions corresponding to τ_e , τ_p and τ_v are assumed to take the forms, respectively, as

$$\psi_e = c_1(I_1 - 3) + c_2(I_2 - 3) + c_3(I_1 - 3)(I_2 - 3) + c_4(I_2 - 3)^2 + c_5(I_1 - 3)^3, \quad (234a)$$

$$\psi_{ep} = c_{p1}(I_{ep1} - 3) + c_{p2}(I_{ep2} - 3), \quad (234b)$$

$$\psi_{ev} = c_{v1}(I_{ev1} - 3); \quad (234c)$$

where I_{ep1} and I_{ev1} are the first invariants of the right Cauchy-Green strain tensor corresponding to the deformation gradient tensor F_{ep} and F_{ev} , respectively. From these strain energy functions the stresses can be derived.

Taking the elastic equilibrium stress as an example, one has

$$\frac{\partial \psi_e}{\partial I_1} = c_1 + c_3(I_2 - 3) + 3c_5(I_1 - 3)^2 = c_1 + c_3\gamma^2 + 3c_5\gamma^4, \quad (235a)$$

$$\frac{\partial \psi_e}{\partial I_2} = c_2 + c_3(I_1 - 3) + 2c_4(I_2 - 3) = c_2 + (c_3 + 2c_4)\gamma^2; \quad (235b)$$

and, from Eqs. (225),

$$\sigma_{11}^e = (2c_1 + 4c_2) + (6c_3 + 8c_4)\gamma^2 + 6c_5\gamma^4, \quad (236a)$$

$$\sigma_{12}^e = \sigma_{21}^e = -2c_2\gamma - (2c_3 + 4c_4)\gamma^3, \quad (236b)$$

$$\sigma_{22}^e = \sigma_{33}^e = (2c_1 + 4c_2) + (2c_2 + 6c_3 + 8c_4)\gamma^2 + (2c_3 + 4c_4 + 6c_5)\gamma^4. \quad (236c)$$

Thus, the elastic equilibrium shear stress can be computed as, from Eq. (228),

$$\begin{aligned} \tau_e = \tau_{12}^e &= \gamma\sigma_{11}^e + \sigma_{12}^e = 2(c_1 + c_2)\gamma + 4(c_3 + c_4)\gamma^3 + 6c_5\gamma^5 \\ &\equiv c_{e1}\gamma + c_{e2}\gamma^3 + c_{e3}\gamma^5. \end{aligned} \quad (237)$$

In a similar procedure, one can obtain the hysteretic equilibrium stress and over-stress as, respectively,

$$\tau_p = \frac{d\psi_{ep}}{d\gamma_{ep}} = 2(c_{p1} + c_{p2})\gamma_{ep} \equiv c_p(\gamma - \gamma_p), \quad (238a)$$

$$\tau_v = \frac{d\psi_{ev}}{d\gamma_{ev}} = 2c_{v1}\gamma_{ev} \equiv c_v(\gamma - \gamma_v). \quad (238b)$$

Each of them may be further considered as a sum of several such stresses.

Eqs. (229) to (233) and Eqs.(237) to (238) define the complete H-S material model. The behavior of this model will be studied in the following sections.

12.2.2 Characteristics of the structural variable q

Considering Eqs. (231) to (233), one can find that the introduction of the structural variable q makes the relaxation time τ_0 to be process dependent. After a close look to the q equation, Eq. (233), it can be found that it is difficult, if not impossible, to find an analytical solution for q , except few special cases. In this section, the characteristics of the structural variable q will be investigated for two special cases: harmonic strain and relaxation test.

12.2.2.1 Characteristics of the structural variable q under harmonic strain

For a harmonic strain history, for instance,

$$\gamma = A \sin(\omega t), \quad (239)$$

it can be expected that the steady state of the structural variable q will also be harmonic. In this case it is impossible to obtain closed-form expression for q . Figs. 44 to 46 present some numerical solutions of q for different material parameters and different harmonic strains. Note that the curves in these figures are all harmonic but with small amplitudes. Key observations from the figures are:

- the structural variable saturates to a steady state faster for high frequency (or amplitude) harmonic strains than for low frequency (or amplitude) strains;
- the steady state of q for low frequency (or amplitude) harmonic strains is smaller than that for high frequency (or amplitude) harmonic strains;
- the combination of high frequency and high amplitude of the strain results in a quicker saturation of q to a larger steady state, which is almost 1 for most cases, than the low frequency and low amplitude strain does;
- a larger τ_q implies a longer saturation time for q to achieve its steady state; and
- increase in ζ can dramatically decrease the saturation time and increase the steady state of q .

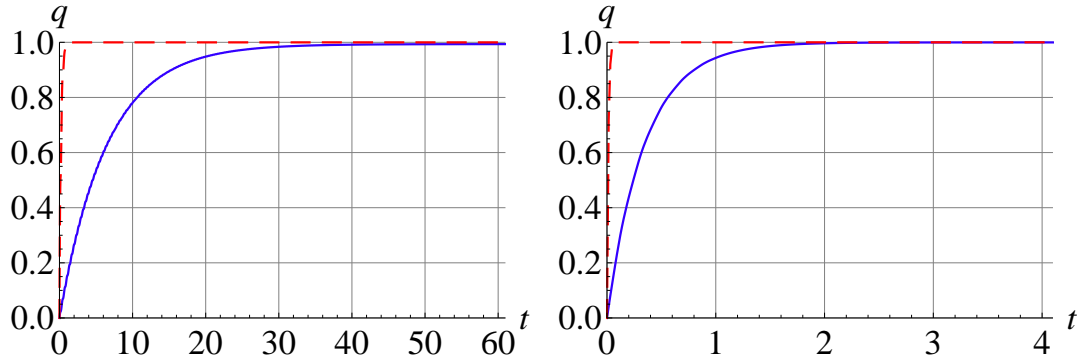


Figure 44: History of q under harmonic strain for $\zeta = 2.4$ and $\tau_q = 1000$ sec. Left: $f = 1.6$ Hz; right: $f = 30$ Hz. (Solid lines: $A = 0.01$; dashed lines: $A = 0.30$)

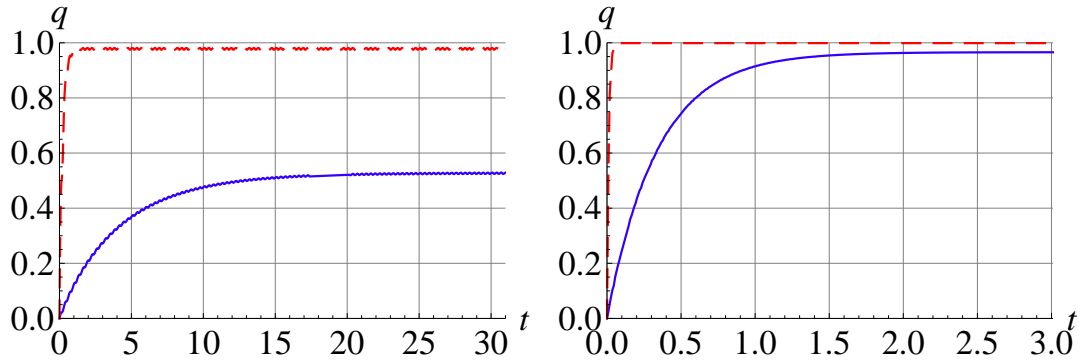


Figure 45: History of q under harmonic strain for $\zeta = 2.4$ and $\tau_q = 10$ sec. Left: $f = 1.6$ Hz; right: $f = 30$ Hz. (Solid lines: $A = 0.01$; dashed lines: $A = 0.30$)

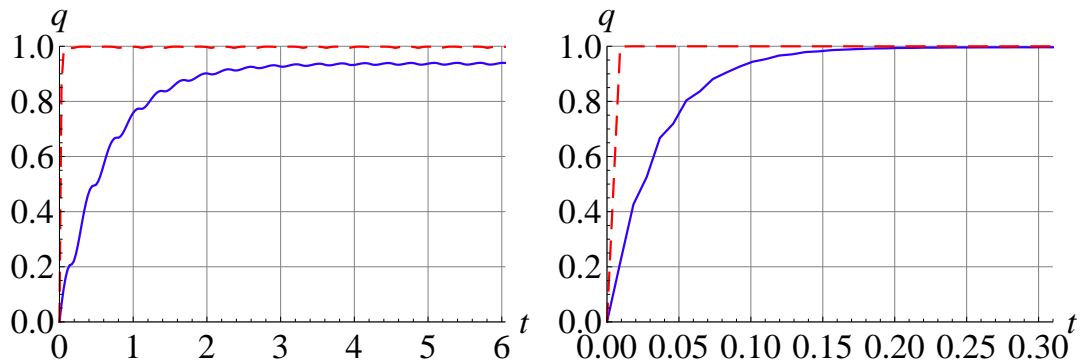


Figure 46: History of q under harmonic strain for $\zeta = 24$ and $\tau_q = 10$ sec. Left: $f = 1.6$ Hz; right: $f = 30$ Hz. (Solid lines: $A = 0.01$; dashed lines: $A = 0.30$)

12.2.2.2 Characteristics of the structural variable q under relaxation test

For a relaxation test, the strain history is

$$\gamma(t) = kt, \quad (0 \leq t \leq t_0), \quad (240a)$$

$$\gamma(t) = kt_0 \equiv \gamma_0, \quad (t > t_0); \quad (240b)$$

where k is the positive constant strain rate. The strain rate can be obtained as

$$\dot{\gamma}(t) = k, \quad (0 \leq t \leq t_0), \quad (241a)$$

$$\dot{\gamma}(t) = 0, \quad (t > t_0). \quad (241b)$$

For this relaxation test, the history of q can be obtained from Eq. (233). For the case $0 \leq t \leq t_0$, one has

$$\dot{q} = \zeta k(1 - q) - \frac{1}{\tau_q} \sqrt{q}, \quad q(0) = 0, \quad 0 \leq q \leq 1. \quad (242)$$

It is not possible to obtain an analytical solution for q from Eq. (242); however, one can find a steady-state q_s in this case, by setting $\dot{q} = 0$. Hence, one has

$$\zeta k(1 - q_s) = \frac{1}{\tau_q} \sqrt{q_s}. \quad (243)$$

Solving this equation, one obtains

$$q_s = \frac{\left(\sqrt{4k^2\zeta^2 + \lambda_q^2} - \lambda_q\right)^2}{4k^2\zeta^2}, \quad (244)$$

where $\lambda_q = 1/\tau_q$. Note that q_s satisfies $0 \leq q_s \leq 1$. Thus q increases from zero up to q_s when the time is long enough under a ramp strain.

Fig. 47 depicts q_s versus ζ and λ_q for $k = 0.05$ and $k = 0.2 \text{ sec}^{-1}$, respectively. It can be seen that the steady-state q_s increases with increasing of strain rate k , and ζ ; while decreases with increasing of λ_q .

Solving Eq. (242) numerically using symbolic manipulators, for example, *Mathematica*, one can obtain the history of q for different k , ζ , and λ_q . Based on these numerical solutions, the following approximation for the history of q may be proposed, for $0 \leq t \leq t_0$,

$$q(t) = q_s \left[1 - e^{-(\zeta k + \lambda_q)t}\right], \quad (245)$$

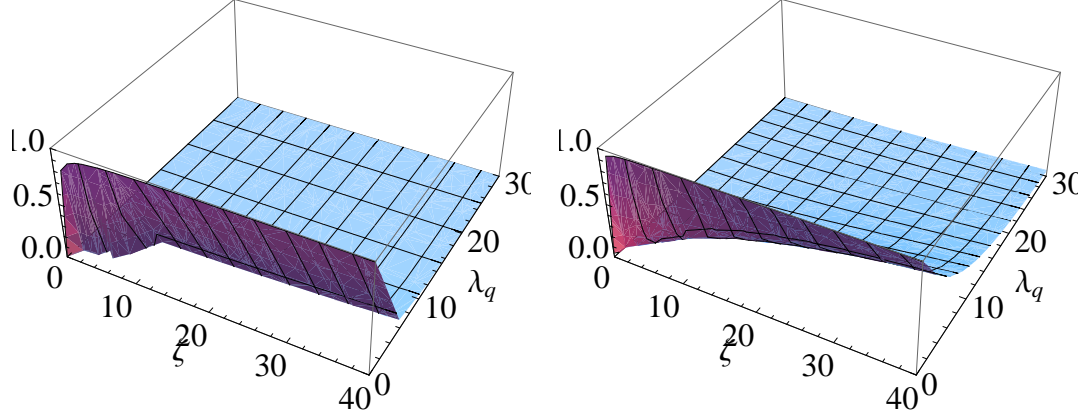


Figure 47: Steady-state q_s under ramp strain. Left: $k = 0.05 \text{ sec}^{-1}$, right: $k = 0.2 \text{ sec}^{-1}$.

where q_s is given by Eq. (244). Figs. 48 to 50 show the numerical and approximate q for cases with different k , ζ , and λ_q . It can be found that Eq. (245) gives good approximation for q except the case with a very small steady-state q_s .

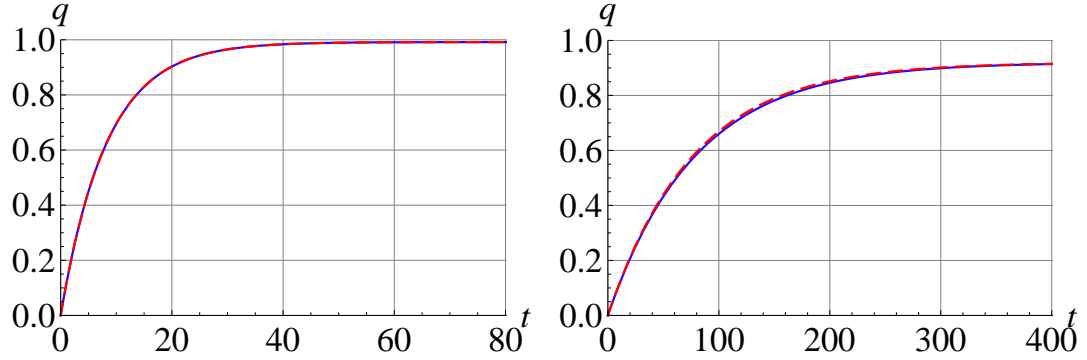


Figure 48: History of q under ramp strain for $\zeta = 2.4$ and $\tau_q = 1000 \text{ sec}$. Left: $k = 0.05 \text{ sec}^{-1}$; right: $k = 0.005 \text{ sec}^{-1}$. (Solid lines: numerical solution of Eq. (242); dashed lines: Eq. (245))

For the case $t > t_0$, Eq. (233) becomes

$$\dot{q} = -\lambda_q \sqrt{q}, \quad q(t_0) = q_0, \quad 0 \leq q \leq 1; \quad (246)$$

where q_0 can be obtained from Eq. (245). Eq. (246) can be solved for \sqrt{q} ,

$$\sqrt{q} = -\frac{1}{2}\lambda_q t + C; \quad (247)$$

where integration constant C can be determined from $q(t_0) = q_0$,

$$C = \sqrt{q_0} + \frac{1}{2}\lambda_q t_0. \quad (248)$$

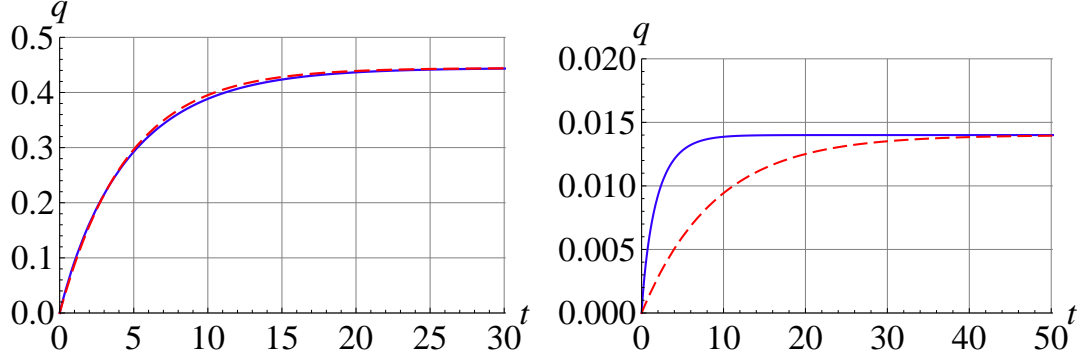


Figure 49: History of q under ramp strain for $\zeta = 2.4$ and $\tau_q = 10$ sec. Left: $k = 0.05$ sec^{-1} ; right: $k = 0.005$ sec^{-1} . (Solid lines: numerical solution of Eq. (242); dashed lines: Eq. (245))

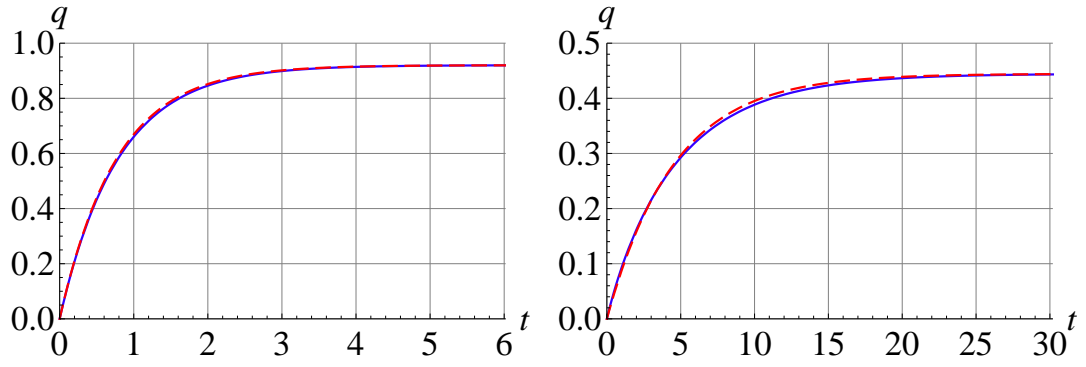


Figure 50: History of q under ramp strain for $\zeta = 24$ and $\tau_q = 10$ sec. Left: $k = 0.05$ sec^{-1} ; right: $k = 0.005$ sec^{-1} . (Solid lines: numerical solution of Eq. (242); dashed lines: Eq. (245))

Hence, one has

$$\sqrt{q} = \sqrt{q_0} - \frac{1}{2}\lambda_q(t - t_0). \quad (249)$$

It can be seen, from Eq. (249), that q decreases from q_0 , and at some time $t = t_{rec}$ it becomes 0. After that q will remain 0 due to the constraint $0 \leq q \leq 1$. The recovery time t_{rec} can be computed from Eq. (249), by setting $q = 0$,

$$t_{rec} = \frac{2\sqrt{q_0}}{\lambda_q} + t_0. \quad (250)$$

Finally, the history of q under a relaxation test can be obtained as, from Eqs. (245)

and (249),

$$q(t) = \begin{cases} q_s [1 - e^{-(\zeta k + \lambda_q)t}] & (0 \leq t \leq t_0) \\ [\sqrt{q_0} - \frac{1}{2}\lambda_q(t - t_0)]^2 & (t_0 < t \leq t_{rec}) \\ 0 & (t > t_{rec}) \end{cases} \quad (251)$$

where q_s is given by Eq. (244), and $q_0 = q_s [1 - e^{-(\zeta k + \lambda_q)t_0}]$. Fig. 51 illustrates two typical time histories for q . It can be seen from the figures that q increases during the ramp strain region and decreases in the relaxation region in which the strain remains constant. After enough time, q becomes and remains zero. When the strain rate is high, q increases fast; however, if the strain rate is low, q increases slowly and is saturated to a steady-state q_s . Also, a large τ_q implies a long relaxation time for q .

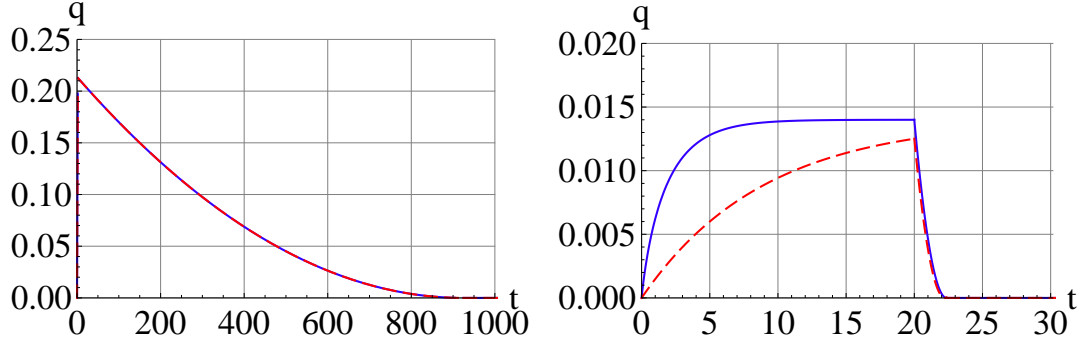


Figure 51: Typical time history of q under relaxation test. Left: $k = 0.05 \text{ sec}^{-1}$, $\zeta = 2.4$ and $\tau_q = 1000 \text{ sec}$; right: $k = 0.005 \text{ sec}^{-1}$, $\zeta = 2.4$ and $\tau_q = 10 \text{ sec}$. (Solid lines: numerical solution of Eq. (242); dashed lines: Eq. (251))

12.2.3 Storage and loss moduli: response of H-S model under harmonic strain

Since the storage and loss moduli are often measured in laboratory for elastomeric materials, one may try to identify the material parameters from such testing data. In this case, a harmonic strain history will be prescribed, such as the one in Eq. (239). Then the corresponding steady state stress history is

$$\tau = c_0 + c_1 \cos(\omega t) + d_1 \sin(\omega t) + c_2 \cos(2\omega t) + d_2 \sin(2\omega t) + \dots \quad (252)$$

From these strain and stress histories, one can compute the storage modulus, G' , and loss modulus, G'' , as follows, respectively,

$$G' = \frac{d_1}{A}, \quad (253a)$$

$$G'' = \frac{c_1}{A}. \quad (253b)$$

These expressions can then be fitted to experimental data to identify the material parameters.

Since it is not easy to obtain a closed-form expression for the structural variable q when a harmonic strain is applied, the relaxation time τ_0 is assumed to be constant and independent of q in the following discussions. After the harmonic behavior of the model with constant relaxation time is studied, the influence of q on the storage and loss moduli will be discussed.

The steady state stress, Eq. (252), of the H-S material model under a harmonic strain, Eq. (239), will be first derived. Note that in this approach, the terms of interest in the stress are those that have the same frequency as the input strain history. Hence, in the following discussions, the terms with frequencies higher than ω will be ignored.

12.2.3.1 Elastic response

The elastic response of the material can be obtained by substituting Eq. (239) into Eq. (237)

$$\begin{aligned} \tau_e &= c_{e1}A \sin(\omega t) + c_{e2} [A \sin(\omega t)]^3 + c_{e3} [A \sin(\omega t)]^5 \\ &= c_{e1}A \sin(\omega t) + c_{e2}A^3 \left[\frac{3}{4} \sin(\omega t) + \dots \right] + c_{e3}A^5 \left[\frac{5}{8} \sin(\omega t) + \dots \right] \\ &= \left(c_{e1}A + \frac{3}{4}c_{e2}A^3 + \frac{5}{8}c_{e3}A^5 \right) \sin(\omega t) + \dots \end{aligned} \quad (254)$$

12.2.3.2 Plastic response

To obtain the plastic response of the material, the amplitude of the strain rate is needed, which is

$$\frac{|\dot{\gamma}|}{A\omega} = |\cos(\omega t)|. \quad (255)$$

Fourier transformation on Eq. (255) gives

$$\frac{|\dot{\gamma}|}{A\omega} = |\cos(\omega t)| = a_0 + \sum_{k=1}^{\infty} [a_k \cos(k\omega t)] + \sum_{k=1}^{\infty} [b_k \sin(k\omega t)], \quad (256)$$

with

$$a_0 = \frac{\omega}{2\pi} \int_{-\pi/\omega}^{\pi/\omega} |\cos(\omega t)| dt = \frac{2}{\pi}, \quad (257a)$$

$$a_k = \frac{\omega}{\pi} \int_{-\pi/\omega}^{\pi/\omega} |\cos(\omega t)| \cos(k\omega t) dt = \begin{cases} 0, & (k = 2n - 1) \\ (-1)^{k/2+1} \frac{4}{\pi(k^2-1)}, & (k = 2n) \end{cases}, \quad (257b)$$

$$b_k = \frac{\omega}{\pi} \int_{-\pi/\omega}^{\pi/\omega} |\cos(\omega t)| \sin(k\omega t) dt = 0. \quad (257c)$$

Thus, Eq (256) becomes

$$\frac{|\dot{\gamma}|}{A\omega} = |\cos(\omega t)| = \frac{2}{\pi} + \sum_{n=1}^{\infty} \left[(-1)^{n+1} \frac{4}{\pi(4n^2-1)} \cos(2n\omega t) \right]. \quad (258)$$

Substituting Eq. (258) into Eq. (230a), together with Eq. (238a), one has

$$\dot{\gamma}_p = u \left\{ \frac{2}{\pi} + \sum_{n=1}^{\infty} \left[(-1)^{n+1} \frac{4}{\pi(4n^2-1)} \cos(2n\omega t) \right] \right\} [A \sin(\omega t) - \gamma_p], \quad (259)$$

with $u = c_p A \omega / \eta_p$. It can be expected that the steady state response of γ_p has the form

$$\gamma_p = c_{p0} + \sum_{k=1}^{\infty} [c_{pk} \cos(k\omega t)] + \sum_{k=1}^{\infty} [d_{pk} \sin(k\omega t)]. \quad (260)$$

Substituting Eq. (260) into Eq. (259) and rewriting the products and powers of trigonometric functions in terms of trigonometric functions with combined arguments, Eq. (259) can then be written as

$$0 = g_0 + \sum_{m=1}^{\infty} [g_m \cos(m\omega t)] + \sum_{m=1}^{\infty} [h_m \sin(m\omega t)], \quad (261)$$

where g_0 , g_m , and h_m are functions of c_{p0} , c_{pk} , and d_{pk} . By setting

$$g_0 = 0, \quad g_m = 0, \quad h_m = 0, \quad (262)$$

one can solve for c_{p0} , c_{pk} , and d_{pk} ; and the plastic response is then given by Eq. (260).

Since the above procedure involves summation of infinite series, one has to approximate the summation with truncation of finite number of terms in practice. For demonstration purpose, one harmonic term is kept in the Fourier transformation of $|\dot{\gamma}|$ in the following

derivation, *i.e.*, the maximum of n is 1 in Eq. (258). In this case, Eqs. (259) and (260) become, respectively,

$$\dot{\gamma}_p = u \left[\frac{2}{\pi} + \frac{4}{3\pi} \cos(2\omega t) \right] [A \sin(\omega t) - \gamma_p], \quad (263a)$$

$$\gamma_p = c_{p0} + c_{p1} \cos(\omega t) + d_{p1} \sin(\omega t) + c_{p2} \cos(2\omega t) + d_{p2} \sin(2\omega t). \quad (263b)$$

Substituting Eq. (263b) into Eq. (263a) and rewriting the products and powers of trigonometric functions in terms of trigonometric functions with combined arguments, one obtains

$$\begin{aligned} 0 = & \frac{1}{3\pi} [(6uc_{p0} + 2uc_{p2}) \\ & + (8uc_{p1} + 3\pi\omega d_{p1}) \cos(\omega t) + (-4uA - 3\pi\omega c_{p1} + 4ud_{p1}) \sin(\omega t) \\ & + (4uc_{p0} + 6uc_{p2} + 6\pi\omega d_{p2}) \cos(2\omega t) + (-6\pi\omega c_{p2} + 6ud_{p2}) \sin(2\omega t) \\ & + 2uc_{p1} \cos(3\omega t) + (-2uA + 2ud_{p1}) \sin(3\omega t) \\ & + 2uc_{p2} \cos(4\omega t) + 2ud_{p2} \sin(4\omega t)]. \end{aligned} \quad (264)$$

Setting the constant term and the coefficients for $\cos(\omega t)$, $\sin(\omega t)$, $\cos(2\omega t)$, and $\sin(2\omega t)$ to be zero gives

$$0 = 6uc_{p0} + 2uc_{p2}, \quad (265a)$$

$$0 = 8uc_{p1} + 3\pi\omega d_{p1}, \quad (265b)$$

$$0 = -4uA - 3\pi\omega c_{p1} + 4ud_{p1}, \quad (265c)$$

$$0 = 4uc_{p0} + 6uc_{p2} + 6\pi\omega d_{p2}, \quad (265d)$$

$$0 = -6\pi\omega c_{p2} + 6ud_{p2}. \quad (265e)$$

From this system of equations, one can obtain

$$c_{p0} = 0, \quad (266a)$$

$$c_{p1} = \frac{-12\pi u A \omega}{32u^2 + 9\pi^2 \omega^2} = \frac{-12\pi A \left(\frac{u}{\omega}\right)}{32 \left(\frac{u}{\omega}\right)^2 + 9\pi^2}, \quad (266b)$$

$$d_{p1} = \frac{32u^2 A}{32u^2 + 9\pi^2 \omega^2} = \frac{32A \left(\frac{u}{\omega}\right)^2}{32 \left(\frac{u}{\omega}\right)^2 + 9\pi^2}, \quad (266c)$$

$$c_{p2} = 0, \quad (266d)$$

$$d_{p2} = 0. \quad (266e)$$

Since $u/\omega = Ac_p/\eta_p$ is frequency independent, c_{p1} and d_{p1} are not dependent on the frequency, but on the amplitude only. Note also that with solutions in Eqs. (266), $\cos(3\omega t)$, $\sin(3\omega t)$, $\cos(4\omega t)$, and $\sin(4\omega t)$ do not necessarily vanish. This is due to the truncation of the infinite series.

Substituting Eqs. (266) into Eq. (263b), one can obtain the plastic strain history of the material and the plastic stress history is given by Eq. (238a),

$$\tau_p = c_p [A \sin(\omega t) - c_{p1} \cos(\omega t) - d_{p1} \sin(\omega t)] + \dots \quad (267)$$

When two harmonic terms are kept in the Fourier transformation of $|\dot{\gamma}|$ (see Eq. (258)), the same procedure will give the coefficients c_{p0} , c_{pk} , and d_{pk} . The ones of interest are

$$c_{p1} = \frac{-900\pi A \left[76 \left(\frac{u}{\omega}\right)^3 + 225\pi^2 \left(\frac{u}{\omega}\right) \right]}{172672 \left(\frac{u}{\omega}\right)^4 + 650700\pi^2 \left(\frac{u}{\omega}\right)^2 + 151875\pi^4}, \quad (268a)$$

$$d_{p1} = \frac{64A \left[2698 \left(\frac{u}{\omega}\right)^4 + 8775\pi^2 \left(\frac{u}{\omega}\right)^2 \right]}{172672 \left(\frac{u}{\omega}\right)^4 + 650700\pi^2 \left(\frac{u}{\omega}\right)^2 + 151875\pi^4}. \quad (268b)$$

Note that c_{p1} and d_{p1} are not dependent on the frequency, but on the amplitude only.

With the help of *Mathematica*, the coefficients c_{p1} and d_{p1} were also derived for the case with five harmonic terms in the Fourier transformation of $|\dot{\gamma}|$ (see Eq. (258)). They are not presented here due to the length of the expressions.

The differences among the coefficients for cases with one, two and five harmonic terms were studied, the maximum difference was found to be less than 5% with reasonable material parameters and strain amplitude and frequency. More harmonic terms are preferred to be kept in the Fourier transformation when one has no prior knowledge of the material; however, more terms will lead to difficulties in the parameter identification procedure. As a compromise between accuracy, computational efficiency and quality of the curve fitting, results with two harmonic terms, Eqs. (268), will be used in the following identification procedure.

12.2.3.3 Viscous response

Following the same procedure for deriving the plastic response, the viscous response can be obtained. Substituting Eq. (258) into Eq. (230b), together with Eq. (238b), one has

$$\dot{\gamma}_v = \left\{ v \left[\frac{2}{\pi} + \sum_{n=1}^{\infty} \left((-1)^{n+1} \frac{4}{\pi(4n^2 - 1)} \cos(2n\omega t) \right) \right] + \lambda_0 \right\} [A \sin(\omega t) - \gamma_v], \quad (269)$$

with $v = \xi A \omega$. Substituting the same steady state response as in Eq. (260) for viscous response into Eq. (269) and rewriting the products and powers of trigonometric functions in terms of trigonometric functions with combined arguments, Eq. (269) can then be written as the same form as Eq. (261). Setting the coefficients in Eq. (261) to be zero, one can solve for c_{v0} , c_{vk} , and d_{vk} ; the viscous response has the same form as Eq. (260), but with different coefficients c_{v0} , c_{vk} , and d_{vk} .

If one harmonic term is kept in the Fourier transformation of $|\dot{\gamma}|$ (see Eq. (258)), the coefficients c_{v1} and d_{v1} are

$$c_{v1} = \frac{-3\pi A \omega (4v + 3\pi \lambda_0)}{32v^2 + 9\pi^2 \omega^2 + 36\pi v \lambda_0 + 9\pi^2 \lambda_0^2}, \quad (270a)$$

$$d_{v1} = \frac{A(8v + 3\pi \lambda_0)(4v + 3\pi \lambda_0)}{32v^2 + 9\pi^2 \omega^2 + 36\pi v \lambda_0 + 9\pi^2 \lambda_0^2}. \quad (270b)$$

Note that in this case c_{v1} and d_{v1} are dependent on both frequency and amplitude of the strain. The viscous stress history is given by Eq. (238b),

$$\tau_v = c_v [A \sin(\omega t) - c_{v1} \cos(\omega t) - d_{v1} \sin(\omega t)] + \dots \quad (271)$$

Here again the cases with two and five harmonic terms kept in the Fourier transformation of $|\dot{\gamma}|$ (see Eq. (258)) were also studied with the help of *Mathematica*, and the coefficients c_{v1} and d_{v1} were derived. They are not presented here due to the length of the expressions. The differences among the coefficient for cases with one, two and five harmonic terms were studied, the maximum difference was again less than 5% with reasonable material parameters and strain amplitude and frequency. In the following identification procedure, the coefficients for case with two harmonic terms will be used.

12.2.3.4 Storage and loss moduli

The total response of the material is the summation of the elastic, plastic and viscous responses. Hence, the storage and loss moduli can also be separated as elastic, plastic and viscous moduli as

$$G' = G'_e + G'_p + G'_v, \quad (272a)$$

$$G'' = G''_e + G''_p + G''_v. \quad (272b)$$

Considering only the terms with the same frequency as the input strain history, the storage and loss moduli, Eq. (253), can then be obtained for elastic, plastic and viscous contributions using Eqs. (254), (267), and (271), respectively,

$$G'_e = c_{e1} + \frac{3}{4}c_{e2}A^2 + \frac{5}{8}c_{e3}A^4, \quad (273a)$$

$$G''_e = 0; \quad (273b)$$

$$G'_p = c_p \left(1 - \frac{d_{p1}}{A}\right), \quad (274a)$$

$$G''_p = -c_p \frac{c_{p1}}{A}; \quad (274b)$$

and

$$G'_v = c_v \left(1 - \frac{d_{v1}}{A}\right), \quad (275a)$$

$$G''_v = -c_v \frac{c_{v1}}{A}. \quad (275b)$$

It can be expected that the elastic modulus is amplitude dependent only and has no out-of-phase component and that the plastic moduli are amplitude dependent but not frequency dependent. However, the viscous parts of the moduli are both amplitude and frequency dependent. The expressions for the moduli, Eqs. (272), can be used to identify the material parameters.

12.2.3.5 Fitting to experimental data

Once the analytical formulations for the storage and loss moduli are determined, these expressions can be used to identify unknown material parameters by fitting the expressions onto test data. The identification will essentially try to minimize the error between Eqs. (272) and the test data. The error function is constructed as

$$\|e\|^2 = (\underline{G}' - \underline{G}'_{exp})^T (\underline{G}' - \underline{G}'_{exp}) + (\underline{G}'' - \underline{G}''_{exp})^T (\underline{G}'' - \underline{G}''_{exp}), \quad (276)$$

where \underline{G}' and \underline{G}'' are results from Eqs. (272) and \underline{G}'_{exp} and \underline{G}''_{exp} are experimental test data. *Mathematica* was used to minimize the error function.

The test data used for the fitting procedure is from [8], where dynamic modulus G_{dyn} and phase angle δ were reported. The storage and loss moduli can be computed from the dynamic modulus and phase angle through

$$G' = \frac{G_{dyn}}{\sqrt{1 + \delta^2}}, \quad (277a)$$

$$G'' = \delta G'. \quad (277b)$$

The test data was measured for sinusoidal strains with different amplitudes and frequencies, given by

$$A = \{0.02, 0.05, 0.10, 0.15\}, \quad (278a)$$

$$f = \{1.0, 5.0, 10.0, 15.0, 20.0\} \text{ Hz}. \quad (278b)$$

Figs. 52 and 53 present the fitted non-dimensional storage and loss moduli together with the test data, respectively. It can be seen that this material model with constant relaxation time is capable of fitting both the storage and loss moduli quite well, especially the storage modulus.

In applications where one of the storage and loss moduli is more important than the other, one may define a weighted error function, as

$$\|e\|^2 = \alpha(\underline{G}' - \underline{G}'_{exp})^T (\underline{G}' - \underline{G}'_{exp}) + (1 - \alpha)(\underline{G}'' - \underline{G}''_{exp})^T (\underline{G}'' - \underline{G}''_{exp}), \quad (279)$$

where $0 \leq \alpha \leq 1$ is a weight. When $\alpha = 1$, the fitting procedure is actually using the storage modulus data only; while if $\alpha = 0$, it is fitting only the loss modulus.

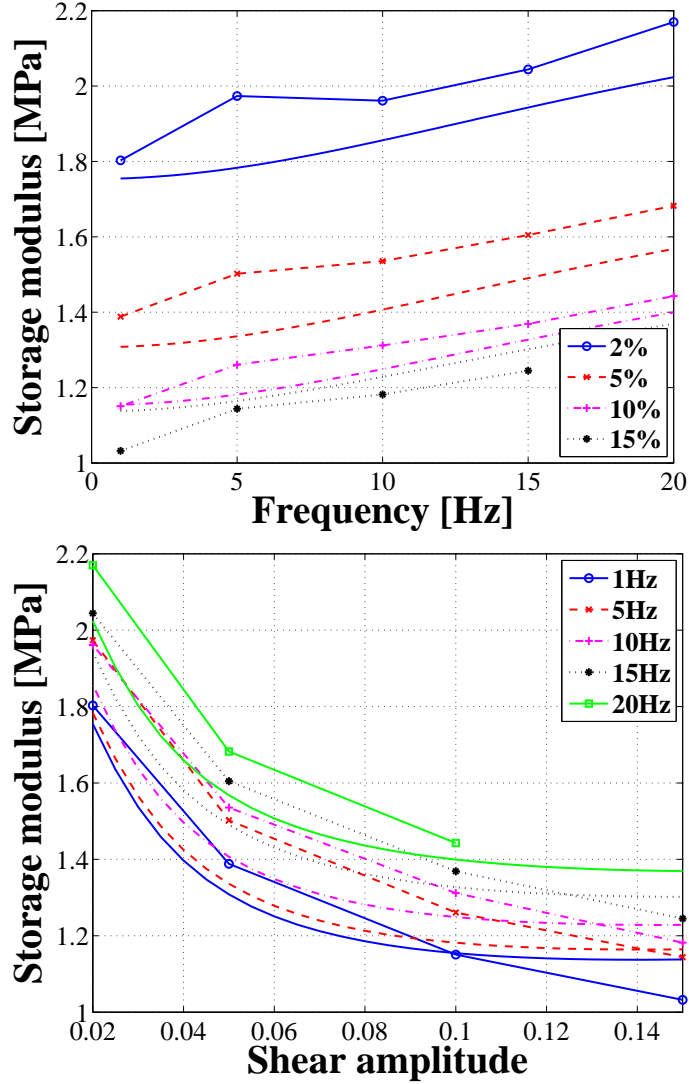


Figure 52: Storage modulus fitting. With symbols: test data from [8]; without symbols: Eq. (272a)

12.2.3.6 *H-S model with non-constant relaxation time: harmonic response*

In the previous section, for the ease of calculation the relaxation time is assumed to be constant. Next the model predictions will be investigated with varied structural variable q . Numerical simulations were performed with material parameters identified from the fitting procedure for Figs. 52 and 53 together with assumed parameters involved in q equation.

In the simulations, the stress response of the material was computed with harmonic strain, Eq. (239), as input. The Fourier transformation was then performed on the stress history to obtain the components with the same frequency as that of the input strain.

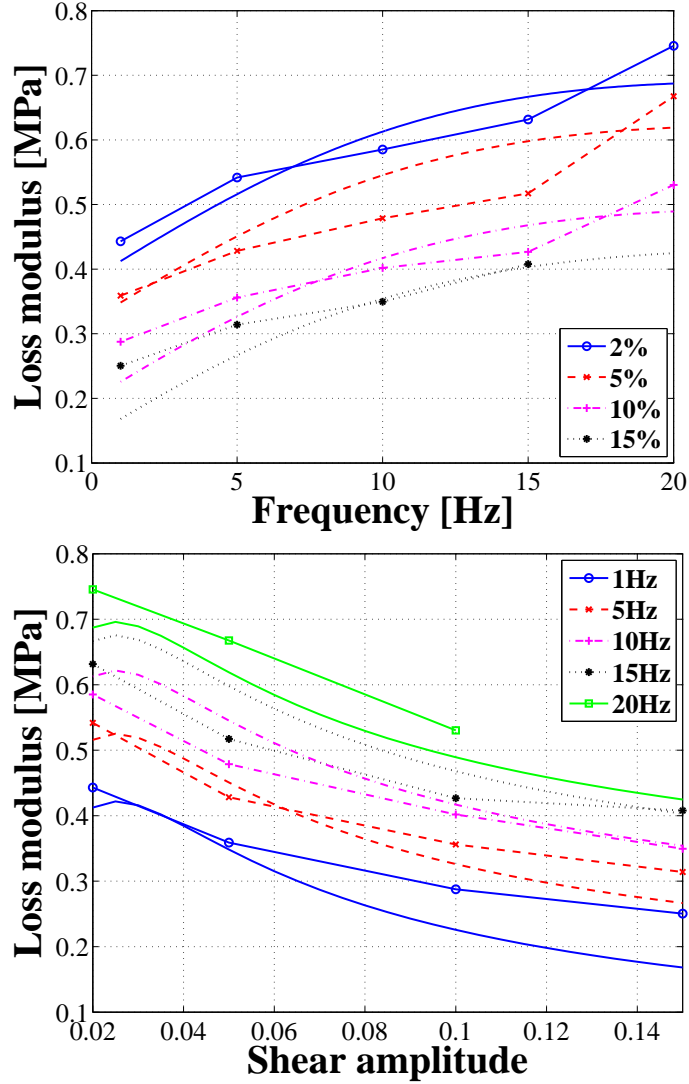


Figure 53: Loss modulus fitting. With symbols: test data from [8]; without symbols: Eq. (272b)

Finally, the storage and loss moduli were calculated from Eqs. (253), and the results are presented in Figs. 54 and 55. From these figures, it is found that the loss modulus is better fitted than those in Fig. 53, where τ_0 was assumed to be constant. The model now captures the general form of the loss modulus variation with strain amplitude and frequency. It is believed that, if the material parameters are better tuned, the H-S model would be able to predict the experimental data.

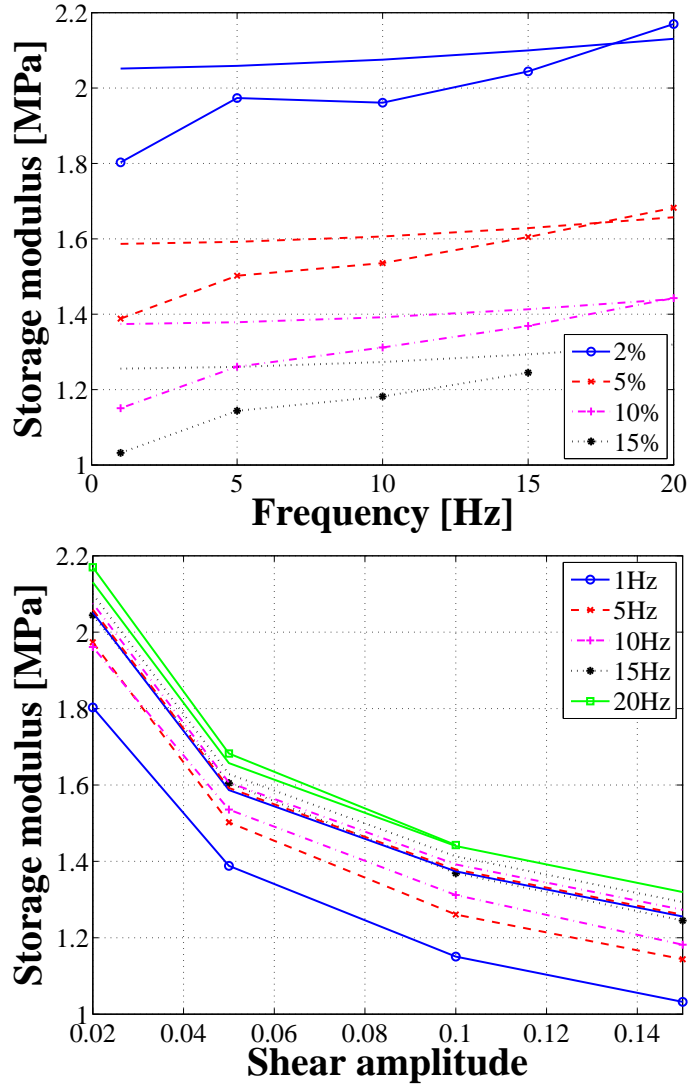


Figure 54: Storage modulus with assumed q related parameters. With symbols: test data from [8]; without symbols: numerical simulation

12.2.4 Response of H-S model under relaxation test

In this section the response of the H-S model under a relaxation test will be studied. The strain history and strain rate in this test are given by Eqs. (240) and (241), respectively.

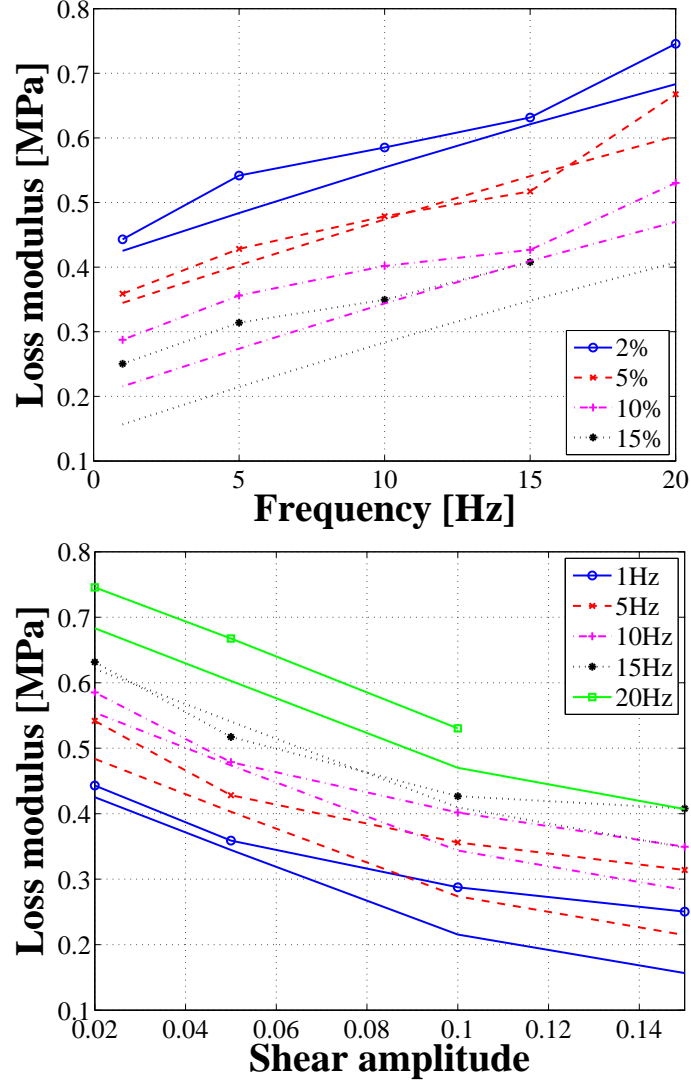


Figure 55: Loss modulus with assumed q related parameters. With symbols: test data from [8]; without symbols: numerical simulation

12.2.4.1 Elastic response

The elastic contribution to the material response can be obtained by substituting Eq. (240) into Eq. (237)

$$\tau_e = c_{e1}(kt) + c_{e2}(kt)^3 + c_{e3}(kt)^5, \quad (0 \leq t \leq t_0), \quad (280a)$$

$$\tau_e = c_{e1}\gamma_0 + c_{e2}\gamma_0^3 + c_{e3}\gamma_0^5, \quad (t > t_0). \quad (280b)$$

Note that for $t > t_0$, the elastic stress is constant.

12.2.4.2 Plastic response

With the strain history, Eq. (240), the governing equation for the plastic strain, Eq. (230a), becomes

$$\dot{\gamma}_p = \frac{kc_p}{\eta_p}(kt - \gamma_p), \quad (0 \leq t \leq t_0), \quad (281a)$$

$$\dot{\gamma}_p = 0, \quad (t > t_0). \quad (281b)$$

The solution of Eq. (281a) can be obtained as follows:

1. Write Eq. (281a) as

$$\dot{\gamma}_p + \frac{kc_p}{\eta_p}\gamma_p = \frac{kc_p}{\eta_p}kt. \quad (282)$$

2. The general solution of the homogeneous form of Eq. (282) can be obtained as

$$\gamma_p = Ce^{-\frac{c_p}{\eta_p}kt}. \quad (283)$$

3. The solution of Eq. (282) takes the same form as Eq. (283) while the integration constant C is considered as a unknown time function $C(t)$. Thus, one has

$$\dot{\gamma}_p = \dot{C}(t)e^{-\frac{c_p}{\eta_p}kt} - \frac{kc_p}{\eta_p}C(t)e^{-\frac{c_p}{\eta_p}kt}. \quad (284)$$

4. Substituting Eqs. (283) and (284) into Eq. (282), one obtains

$$\dot{C}(t) = \frac{kc_p}{\eta_p}kte^{\frac{c_p}{\eta_p}kt}. \quad (285)$$

5. Integrating Eqs. (285) gives

$$\begin{aligned} C(t) &= \int \frac{kc_p}{\eta_p}kte^{\frac{c_p}{\eta_p}kt} dt + C_1 \\ &= \left(kt - \frac{\eta_p}{c_p}\right) e^{\frac{c_p}{\eta_p}kt} + C_1, \end{aligned} \quad (286)$$

where C_1 is a constant to be determined.

6. The solution of Eq. (282) is then, by substituting Eq. (286) into Eq. (283),

$$\gamma_p(t) = \left(kt - \frac{\eta_p}{c_p}\right) + C_1 e^{-\frac{c_p}{\eta_p}kt}. \quad (287)$$

7. Using the initial condition $\gamma_p(0) = 0$, the constant C_1 can be determined

$$C_1 = \frac{\eta_p}{c_p}. \quad (288)$$

8. Finally, the solution of Eq. (281a) for $0 \leq t \leq t_0$ is obtained as

$$\gamma_p(t) = kt + \frac{\eta_p}{c_p} \left(e^{-\frac{c_p}{\eta_p} kt} - 1 \right), \quad (0 \leq t \leq t_0). \quad (289)$$

The solution of Eq. (281b) for $t > t_0$ can be easily obtained as

$$\begin{aligned} \gamma_p(t) &= \gamma_p(t_0) = kt_0 + \frac{\eta_p}{c_p} \left(e^{-\frac{c_p}{\eta_p} kt_0} - 1 \right) \\ &= \gamma_0 + \frac{\eta_p}{c_p} \left(e^{-\frac{c_p}{\eta_p} \gamma_0} - 1 \right), \quad (t > t_0). \end{aligned} \quad (290)$$

The plastic contribution to the total stress becomes

$$\tau_p(t) = \eta_p \left(1 - e^{-\frac{c_p}{\eta_p} kt} \right), \quad (0 \leq t \leq t_0), \quad (291a)$$

$$\tau_p(t) = \eta_p \left(1 - e^{-\frac{c_p}{\eta_p} \gamma_0} \right), \quad (t > t_0). \quad (291b)$$

The plastic contribution to the total stress is also constant for $t > t_0$.

12.2.4.3 Viscous response for case with constant relaxation time τ_0

As stated earlier, in the H-S model, the relaxation time τ_0 is not a constant but related to a structural variable q . This results in the difficulty of obtaining an analytical expression for the viscous response; especially, when it is impossible to obtain analytical solutions for q . Thus, the case with constant relaxation time τ_0 will be studied first.

With the strain history, Eq. (240), the governing equation for the viscous strain, Eq. (230b), becomes

$$\dot{\gamma}_v = \left(k\xi + \frac{1}{\tau_0} \right) (kt - \gamma_v), \quad (0 \leq t \leq t_0), \quad (292a)$$

$$\dot{\gamma}_v = \frac{1}{\tau_0} (\gamma_0 - \gamma_v), \quad (t > t_0). \quad (292b)$$

The solution of Eq. (292a) can be obtained from a procedure similar to the one applied to

Eq. (281a). The key steps are listed as:

$$\gamma_v = C(t)e^{-\left(k\xi + \frac{1}{\tau_0}\right)t}, \quad (293a)$$

$$\dot{\gamma}_v = \dot{C}(t)e^{-\left(k\xi + \frac{1}{\tau_0}\right)t} - \left(k\xi + \frac{1}{\tau_0}\right)C(t)e^{-\left(k\xi + \frac{1}{\tau_0}\right)t}, \quad (293b)$$

$$\dot{C}(t) = \left(k\xi + \frac{1}{\tau_0}\right)kte^{\left(k\xi + \frac{1}{\tau_0}\right)t}, \quad (293c)$$

$$C(t) = \left(kt - \frac{k}{k\xi + \frac{1}{\tau_0}}\right)e^{\left(k\xi + \frac{1}{\tau_0}\right)t} + C_2. \quad (293d)$$

The integration constant C_2 can be determined using the initial condition $\gamma_v(0) = 0$,

$$C_2 = \frac{k}{k\xi + \frac{1}{\tau_0}}. \quad (294)$$

Then the solution of Eq. (292a) for $0 \leq t \leq t_0$ can be written as

$$\gamma_v(t) = kt + \frac{k}{k\xi + \frac{1}{\tau_0}} \left[e^{-\left(k\xi + \frac{1}{\tau_0}\right)t} - 1 \right], \quad (0 \leq t \leq t_0). \quad (295)$$

The solution of Eq. (292b) can be obtained in a similar procedure as

$$\gamma_v(t) = \gamma_0 + C_3 e^{-\frac{1}{\tau_0}t}; \quad (296)$$

where C_3 can be determined by the continuity of the viscous strain γ_v at $t = t_0$. From Eqs. (295) and (296), one has, respectively,

$$\gamma_v(t_0) = \gamma_0 + \frac{k}{k\xi + \frac{1}{\tau_0}} \left[e^{-\left(k\xi + \frac{1}{\tau_0}\right)t_0} - 1 \right]; \quad (297a)$$

$$\gamma_v(t_0) = \gamma_0 + C_3 e^{-\frac{1}{\tau_0}t_0}. \quad (297b)$$

Thus, one can obtain

$$C_3 = \frac{k}{k\xi + \frac{1}{\tau_0}} \left[e^{-\left(k\xi + \frac{1}{\tau_0}\right)t_0} - 1 \right] e^{\frac{1}{\tau_0}t_0}, \quad (298)$$

and the solution of Eq. (292b) becomes

$$\gamma_v(t) = \gamma_0 + \frac{k}{k\xi + \frac{1}{\tau_0}} \left[e^{-\left(k\xi + \frac{1}{\tau_0}\right)t_0} - 1 \right] e^{-\frac{1}{\tau_0}(t-t_0)}, \quad (t > t_0). \quad (299)$$

The viscous contribution to the total stress then becomes

$$\tau_v(t) = \frac{c_v k}{k\xi + \frac{1}{\tau_0}} \left[1 - e^{-\left(k\xi + \frac{1}{\tau_0}\right)t} \right], \quad (0 \leq t \leq t_0), \quad (300a)$$

$$\tau_v(t) = \frac{c_v k}{k\xi + \frac{1}{\tau_0}} \left[1 - e^{-\left(k\xi + \frac{1}{\tau_0}\right)t_0} \right] e^{-\frac{1}{\tau_0}(t-t_0)}, \quad (t > t_0). \quad (300b)$$

12.2.4.4 Viscous response for case with non-constant relaxation time τ_0

With the approximated expressions for q , Eq. (251), the equation governing the viscous strain, Eq. (230b), can be written as

$$\dot{\gamma}_v + \left[\xi k + \frac{1}{\tau_{max} + (\tau_{min} - \tau_{max})q} \right] \gamma_v = \left[\xi k + \frac{1}{\tau_{max} + (\tau_{min} - \tau_{max})q} \right] kt, \quad (0 \leq t \leq t_0) \quad (301a)$$

$$\dot{\gamma}_v + \frac{1}{\tau_{max} + (\tau_{min} - \tau_{max})q} \gamma_v = \frac{1}{\tau_{max} + (\tau_{min} - \tau_{max})q} kt_0, \quad (t_0 < t \leq t_{rec}) \quad (301b)$$

$$\dot{\gamma}_v + \frac{1}{\tau_{max}} \gamma_v = \frac{1}{\tau_{max}} kt_0, \quad (t > t_{rec}) \quad (301c)$$

Note that Eqs. (301) have the same form as

$$\dot{\gamma}_{vi} + r_i(t) \gamma_{vi} = s_i(t), \quad (i = 1, 2, 3); \quad (302)$$

where γ_{vi} for $i = 1, 2, 3$ are the viscous strains for $0 \leq t \leq t_0$, $t_0 < t \leq t_{rec}$, and $t > t_{rec}$, respectively; and

$$r_1(t) = \xi k + \frac{1}{\tau_{max} + (\tau_{min} - \tau_{max})q}, \quad s_1(t) = \left[\xi k + \frac{1}{\tau_{max} + (\tau_{min} - \tau_{max})q} \right] kt, \quad (303a)$$

$$r_2(t) = \frac{1}{\tau_{max} + (\tau_{min} - \tau_{max})q}, \quad s_2(t) = \frac{1}{\tau_{max} + (\tau_{min} - \tau_{max})q} kt_0, \quad (303b)$$

$$r_3(t) = \frac{1}{\tau_{max}}, \quad s_3(t) = \frac{1}{\tau_{max}} kt_0. \quad (303c)$$

The general solution to Eq. (302) is

$$\gamma_{vi} = e^{-\int r_i(t) dt} \left[\int s_i(t) e^{\int r_i(t) dt} dt + C_i \right]. \quad (304)$$

The integration constants C_i can be determined from the initial conditions $\gamma_v(0) = 0$, and the continuity of γ_v at $t = t_0$ and $t = t_{rec}$ for Eqs. (301b) and (301c), respectively,

$$C_1 = - \left. \int s_1 e^{\int r_1 dt} dt \right]_{t=0}, \quad (0 \leq t \leq t_0) \quad (305a)$$

$$C_2 = \left. \int s_1 e^{\int r_1 dt} dt \right]_{t=t_0} - \left. \int s_2 e^{\int r_2 dt} dt \right]_{t=t_0}, \quad (t_0 < t \leq t_{rec}) \quad (305b)$$

$$C_3 = \left. \int s_2 e^{\int r_2 dt} dt \right]_{t=t_{rec}} - \left. \int s_3 e^{\int r_3 dt} dt \right]_{t=t_{rec}}, \quad (t > t_{rec}) \quad (305c)$$

Substituting Eqs. (305) into Eqs. (304), one can obtain the history of the viscous strain $\gamma_v(t)$

$$\gamma_{v1} = e^{-\int r_1 dt} \int_0^t s_1 e^{\int r_1 dt} dt, \quad (0 \leq t \leq t_0) \quad (306a)$$

$$\gamma_{v2} = e^{-\int r_2 dt} \int_{t_0}^t s_2 e^{\int r_2 dt} dt + \gamma_{v1}(t_0) e^{-\int_{t_0}^t r_2 dt}, \quad (t_0 < t \leq t_{rec}) \quad (306b)$$

$$\gamma_{v3} = e^{-\int r_3 dt} \int_{t_{rec}}^t s_3 e^{\int r_3 dt} dt + \gamma_{v2}(t_{rec}) e^{-\int_{t_{rec}}^t r_3 dt}, \quad (t > t_{rec}) \quad (306c)$$

The over-stress can be calculated from the viscous strains as

$$\tau_v = c_v(\gamma - \gamma_v). \quad (307)$$

Note that τ_v is a function of c_v , ξ , τ_{max} , τ_{min} , ζ , and τ_q . Particularly, the viscous strain and over-stress for $t > t_{rec}$ can be explicitly written as, respectively,

$$\gamma_{v3} = kt_0 - [kt_0 - \gamma_{v2}(t_{rec})] e^{-\frac{t-t_{rec}}{\tau_{max}}}; \quad (308)$$

and

$$\tau_{v3} = c_v [kt_0 - \gamma_{v2}(t_{rec})] e^{-\frac{t-t_{rec}}{\tau_{max}}}. \quad (309)$$

12.2.5 Identification of material parameters from experimental data

Closed-form expressions for the response of the material model under harmonic strain and relaxation test were obtained in the previous sections. These expressions can be used to identify the material parameters based on experimental data.

12.2.5.1 Pseudo-experimental data

Since complete experimental data (except for some experimentally measured storage and loss moduli data found in literature) are not available at this time, in the following demonstration, two sets of assumed experimental data were created. One is the storage and loss moduli, G'_{exp} and G''_{exp} , and another set is the stress histories $\tau_{exp}(t)$ for relaxation tests. These pseudo-experimental test data were generated using numerical simulations based on assumed material parameters shown in Table 10, in which the identified values for those parameters and the discrepancy between the assumed and identified values are also included.

Table 10: Assumed and identified material parameters

	Assumed values	Identified values	Discrepancy [%]
c_{e1} [kPa]	578.325	578.325	0.0
c_{e2} [kPa]	-225.309	-225.309	0.0
c_{e3} [kPa]	-1546.62	-1546.62	0.0
c_p [kPa]	63.0344	63.0344	0.0
η_p [kPa]	1.04223	1.04223	0.0
c_v [kPa]	197.195	195.816	-0.70
ξ	1.92091	2.07435	7.99
τ_{max} [sec]	0.76946	0.777411	1.03
τ_{min} [sec]	0.0019236	0.00197659	2.75
ζ	2.40	2.4142	0.59
τ_q [sec]	1000.0	744.564	-25.54

The parameters identification procedure in essence tries to trace back these parameters from the pseudo-experimental data.

The relaxation tests for generating the pseudo-experimental data were simulated at a constant starting ramp strain rate $k = 0.05 \text{ sec}^{-1}$ and followed by six different maximum strain amplitudes, see Eqs. (240),

$$\underline{\gamma}_0 = \{0.01, 0.03, 0.06, 0.10, 0.20, 0.30\}. \quad (310)$$

In other words, six relaxation tests were simulated with $k = 0.05 \text{ sec}^{-1}$ and

$$\underline{t}_0 = \{0.20, 0.60, 1.2, 2.0, 4.0, 6.0\} \text{ sec}. \quad (311)$$

Some results that are necessary for the material parameters identification are extracted and illustrated here. The stresses at $t = 0 \text{ sec}$ to $t = 4\Delta t$ with $\Delta t = 0.01 \text{ sec}$ are presented in Table 11. Note that these stresses are the same for all six strain levels since the strain history are the same for all the relaxation tests within this time range. The stresses right after t_0 were sampled for each relaxation test. The sampling time instants and the corresponding stresses for each test are shown in Table 12. Finally, the stresses at $t \rightarrow \infty$, for each strain level, are listed in Table 13,

Table 11: Stresses [kPa] at $t = 0 \text{ sec}$ to $t = 4\Delta t$

t	0.0	Δt	$2\Delta t$	$3\Delta t$	$4\Delta t$
$\tau(t)$	0.0	0.418116	0.833951	1.24754	1.65894

Table 12: Sampling times t [sec] and corresponding stresses τ [kPa] after t_0

$\gamma_0 = 0.01$					
t	0.25	0.40	0.55	0.70	0.90
τ	7.86262	7.57184	7.3337	7.13866	6.93238
$\gamma_0 = 0.03$					
t	0.65	0.75	0.90	1.05	1.20
τ	21.8893	21.4107	20.8071	20.3175	19.9205
$\gamma_0 = 0.06$					
t	1.30	1.50	1.70	1.80	1.90
τ	40.3106	39.1065	38.2145	37.8594	37.5537
$\gamma_0 = 0.10$					
t	2.10	2.20	2.40	2.55	2.70
τ	63.4898	62.7509	61.5933	60.9442	60.4373
$\gamma_0 = 0.20$					
t	4.10	4.20	4.45	4.60	4.70
τ	118.272	117.543	116.267	115.767	115.511
$\gamma_0 = 0.30$					
t	6.10	6.30	6.50	6.65	6.80
τ	167.577	166.393	165.696	165.369	165.149

Table 13: Stresses at $t \rightarrow \infty$ [kPa]

γ_0	0.01	0.03	0.06	0.10	0.20	0.30
τ_∞	6.256	18.216	35.6642	58.6315	114.41	164.698

Another type of test is the harmonic test. In this test, the stress response of the material was computed with harmonic strain, Eq. (239), as input. The Fourier transformation was then performed on the stress history to obtain the components with same frequency as that of the input strain. Finally, the storage and loss moduli, G'_{exp} and G''_{exp} , were calculated from Eqs. (253), and are shown in Tables 14 and 15, respectively, for different frequencies and amplitudes.

Table 14: Pseudo-experimental storage modulus G' [kPa]

	$A = 0.20$	$A = 0.30$
$f = 15$ [Hz]	578.236	562.185
$f = 30$ [Hz]	592.278	575.092

Table 15: Pseudo-experimental loss modulus G'' [kPa]

	$A = 0.20$	$A = 0.30$
$f = 15$ [Hz]	39.242	36.3395
$f = 30$ [Hz]	63.8909	59.4031

12.2.5.2 Identification of elastic and plastic material parameters from relaxation tests

From the viscous response, Eq. (300b) or (308), for relaxation test, it can be found that $\tau_v \rightarrow 0$ when $t \rightarrow \infty$. Hence, when the strain increases from zero to certain level, γ_0 , and keeps unchanged for enough time, the over-stress will vanish and the measured stress is actually the contribution of the elastic and plastic response. The total stress is then the sum of τ_e and τ_p only, from Eqs. (280) and (291),

$$\tau_\infty = \tau_e + \tau_p = c_{e1}\gamma_0 + c_{e2}\gamma_0^3 + c_{e3}\gamma_0^5 + \eta_p \left(1 - e^{-\frac{c_p}{\eta_p}\gamma_0}\right). \quad (312)$$

It can be seen that this stress is not a function of time, but a function of the strain amplitude γ_0 . This makes it possible to identify the parameters involved in the elastic and plastic behavior of the material by fitting the measured relaxed stresses for different strain amplitudes.

First, the least square approach will be used to identify the parameters. Since Eq. (312) is nonlinear in terms of the material parameters η_p and c_p , it will first be linearized with respect to certain initial values of $\hat{\eta}_p$ and \hat{c}_p . First, one has

$$\frac{\partial \tau_p}{\partial \eta_p} = 1 - \left(\frac{c_p}{\eta_p}\gamma_0 + 1\right) e^{-\frac{c_p}{\eta_p}\gamma_0}, \quad (313a)$$

$$\frac{\partial \tau_p}{\partial c_p} = \gamma_0 e^{-\frac{c_p}{\eta_p}\gamma_0}. \quad (313b)$$

Then the plastic stress can be approximated as

$$\begin{aligned} \tau_p(\hat{\eta}_p + \Delta\eta_p, \hat{c}_p + \Delta c_p) &= \tau_p(\hat{\eta}_p, \hat{c}_p) + \frac{\partial \tau_p}{\partial \eta_p}\Big|_{(\hat{\eta}_p, \hat{c}_p)} \Delta\eta_p + \frac{\partial \tau_p}{\partial c_p}\Big|_{(\hat{\eta}_p, \hat{c}_p)} \Delta c_p \\ &= b_p + \alpha_p \Delta\eta_p + \beta_p \Delta c_p, \end{aligned} \quad (314)$$

with

$$b_p = \hat{\eta}_p \left(1 - e^{-\frac{\hat{c}_p}{\hat{\eta}_p} \gamma_0} \right), \quad (315a)$$

$$\alpha_p = 1 - \left(\frac{\hat{c}_p}{\hat{\eta}_p} \gamma_0 + 1 \right) e^{-\frac{\hat{c}_p}{\hat{\eta}_p} \gamma_0}, \quad (315b)$$

$$\beta_p = \gamma_0 e^{-\frac{\hat{c}_p}{\hat{\eta}_p} \gamma_0}. \quad (315c)$$

The linearized version of Eq. (312) becomes

$$\tau_\infty = \tau_e + \tau_p = c_{e1} \gamma_0 + c_{e2} \gamma_0^3 + c_{e3} \gamma_0^5 + \alpha_p \Delta \eta_p + \beta_p \Delta c_p + b_p. \quad (316)$$

The least-squares method can then be applied.

If N experimental data points

$$\underline{\tau}_{exp} = \{ \tau_{exp}^{(1)}, \tau_{exp}^{(2)}, \dots, \tau_{exp}^{(N)} \}^T \quad (317)$$

were measured for N different strain amplitudes

$$\underline{\gamma}_0 = \{ \gamma_0^{(1)}, \gamma_0^{(2)}, \dots, \gamma_0^{(N)} \}^T, \quad (318)$$

then one can apply the least-squares method to identify the material parameters that minimize the error between Eq. (316) and the experimental data. Note that the number of experimental data should be at least as large as the number of parameters to be identified.

The least-squares solution would be

$$\underline{c} = (A^T A)^{-1} A^T \underline{b}, \quad (319)$$

with

$$A = \begin{bmatrix} \gamma_0^{(1)} & \gamma_0^{(1)3} & \gamma_0^{(1)5} & \alpha_p^{(1)} & \beta_p^{(1)} \\ \gamma_0^{(2)} & \gamma_0^{(2)3} & \gamma_0^{(2)5} & \alpha_p^{(2)} & \beta_p^{(2)} \\ & & \vdots & & \\ \gamma_0^{(N)} & \gamma_0^{(N)3} & \gamma_0^{(N)5} & \alpha_p^{(N)} & \beta_p^{(N)} \end{bmatrix}, \quad (320a)$$

$$\underline{c} = \left\{ c_{e1} \quad c_{e2} \quad c_{e3} \quad \Delta \eta_p \quad \Delta c_p \right\}^T, \quad (320b)$$

$$\underline{b} = \left\{ \tau_{exp}^{(1)} - b_p^{(1)} \quad \tau_{exp}^{(2)} - b_p^{(2)} \quad \dots \quad \tau_{exp}^{(N)} - b_p^{(N)} \right\}^T. \quad (320c)$$

Test runs were performed to verify the feasibility of this approach. In the test runs, the pseudo-experimental data in Table 13, were used to identify the material parameters, from Eq. (319),

$$c_{e1}, c_{e2}, c_{e3}, c_p, \eta_p. \quad (321)$$

Note that in the identification procedure, initial values should be given for $\hat{\eta}_p$ and \hat{c}_p to compute $\alpha_p^{(i)}$, $\beta_p^{(i)}$ and $b_p^{(i)}$ from Eqs. (315) and that iteration is needed to update $\hat{\eta}_p$ and \hat{c}_p . Table 16 shows the results with different initial values for η_p and c_p . When converged, the identified parameters are exactly the same as those assumed values in Table 10. The results in Table 16 indicate that the initial values are critical to the convergence of the least square procedure. “Good” initial values may lead to the correct values of the parameters in as few as two iterations while “bad” ones may result in a divergence. Hence, this least-squares procedure may become problematic when one has no prior knowledge of the material behavior.

Table 16: Identified elastic and plastic parameters

Initial values [MPa]	Converged?	Number of iterations
$\eta_p = 0.001$ $c_p = 0.06$	Yes	2
$\eta_p = 0.01$ $c_p = 0.60$	Yes	2
$\eta_p = 0.10$ $c_p = 6.0$	Yes	2
$\eta_p = 0.00001$ $c_p = 0.0006$	Yes	2
$\eta_p = 0.0001$ $c_p = 0.0006$	No	
$\eta_p = 0.00001$ $c_p = 0.00006$	No	

One may also try to minimize the error between Eq. (312) and the experimental data. The function to be minimized is the L_2 -norm of the error, which can be constructed as

$$\|\underline{\mathcal{E}}\|^2 = (\underline{\mathcal{I}}_\infty - \underline{\mathcal{I}}_{exp})^T (\underline{\mathcal{I}}_\infty - \underline{\mathcal{I}}_{exp}), \quad (322)$$

where $\underline{\mathcal{I}}_{exp}$ is given by Eq. (317) and the i th component of $\underline{\mathcal{I}}_\infty$ is given by Eq. (312) with $\gamma_0 = \gamma_0^{(i)}$. *Mathematica* can solve this minimization problem efficiently. A *Mathematica*

run, using the data in Table 13, predicted exactly the same material parameters as those assumed in Table 10.

12.2.5.3 Identification of viscous material parameters

After the parameters involved in the elastic and plastic behavior of the material are identified, the elastic and plastic response can be subtracted from the experimentally measured total stress. Then one can obtain the over-stress history, τ_v^{exp} , from which the parameters involved in the viscous behavior of the material can be identified.

Theoretically, one may fit the closed-form expression, Eq. (307), to the experimental data, τ_v^{exp} , to identify the viscous parameters and q related parameters. However, test runs failed due to the complexity and strong nonlinearity of the expressions. Thus, a robust step by step procedure is designed to identify the parameters one or several at each step.

Step 1: Considering the viscous response of the model at $t = 0$, it can be found that the response of the model with q effect should be the same as the one of the model with constant relaxation time $\tau_0 = \tau_{max}$ since $q(0) = 0$. From this observation, one can identify c_v .

Taking the time derivative of Eq. (300a) gives,

$$\frac{d\tau_v(t)}{dt} = c_v k e^{-\left(k\xi + \frac{1}{\tau_0}\right)t}, \quad (0 \leq t \leq t_0), \quad (323)$$

When $t \rightarrow 0^+$, one has, from Eq. (323),

$$\left. \frac{d\tau_v(t)}{dt} \right|_{t=0} = c_v k, \quad (324)$$

from which parameter c_v can be determined as

$$c_v = \frac{1}{k} \left. \frac{d\tau_v(t)}{dt} \right|_{t=0}. \quad (325)$$

It is also verified using *Mathematica* that when taking time derivative for Eq. (307) and setting $t \rightarrow 0^+$, same result as in Eq. (325) can be obtained.

Step 2: Considering two limiting cases for $q = 0$ and $q = 1$, one can find that these two cases correspond to $\tau_0 = \tau_{max}$ and $\tau_0 = \tau_{min}$ (see Eqs. (231) and (232)), respectively. Then the material model is degenerated to the model with constant relaxation time τ_0 . One

may use the viscous response for the model with constant relaxation time, Eq. (300b), to identify (ξ, τ_{max}) or (ξ, τ_{min}) , respectively. The procedure is as follows.

Taking the time derivative of Eq. (300b)

$$\frac{d\tau_v(t)}{dt} = \frac{c_vk}{k\xi + \frac{1}{\tau_0}} \left[1 - e^{-\left(k\xi + \frac{1}{\tau_0}\right)t_0} \right] \left(-\frac{1}{\tau_0} \right) e^{-\frac{1}{\tau_0}(t-t_0)}, \quad (t > t_0), \quad (326)$$

and setting $t = t_0^+$, one has

$$k_v = \left. \frac{d\tau_v(t)}{dt} \right|_{t=t_0} = \frac{c_vk}{k\xi + \frac{1}{\tau_0}} \left[1 - e^{-\left(k\xi + \frac{1}{\tau_0}\right)t_0} \right] \left(-\frac{1}{\tau_0} \right). \quad (327)$$

Here τ_0 may be τ_{max} or τ_{min} depending on $q = 0$ or $q = 1$. Thus the parameters ξ and τ_{max} (or τ_{min}) can be identified by fitting Eq. (327) to experimental data for the over-stress history. One may linearize Eq. (327) and use the least-squares method, or minimize the error between Eq. (327) and experimental data directly using *Mathematica*, to obtain the parameters. The error function to be minimized would be

$$\|\underline{e}\|^2 = (\underline{k}_v - \underline{k}_v^{exp})^T (\underline{k}_v - \underline{k}_v^{exp}). \quad (328)$$

It can be expected that the least-squares method will be sensitive to the initial values due to the strong nonlinearity in Eq. (327).

From the study of the characteristics of q in Section 12.2.2.2, for a very low strain rate k , $q \approx 0$; while for a large enough strain rate, $q \approx 1$. Hence, theoretically, one can obtain the two limiting cases for q . However, in practice, it is difficult to achieve these two limiting cases.

When applying a ramp strain with very large strain rate, q achieves its steady state very quickly; however, the time for q to be saturated is long enough for the strain to be way off the reasonable range since the strain rate is very high. Another problem is that the steady-state value of q is also determined by ζ and τ_q . In many cases, q_s is not even close to 1, even if the strain rate is high. For a low strain rate, although a reasonable strain level is not a problem and the value for q is really close to 0, the viscous effect is very weak, even unmeasurable. Hence, these two limiting cases are not practical.

When looking at the characteristics of q under harmonic strains, see Section 12.2.2.1, one can find that the steady-state value of q under harmonic strains with high frequency

and high amplitude is very close to 1. This means that the material behaves like the one with constant relaxation time τ_{min} . One may fit the expressions for storage and loss moduli, Eqs. (272), to experimental data obtained from high frequency and high amplitude harmonic strains to identify ξ and τ_{min} . The advantage for this approach is that the strain rate and strain amplitude are not related each other, *i.e.*, a high strain rate does not mean a high amplitude outside the reasonable range.

Step 3: After c_v , ξ , and τ_{min} have been identified, substitution of them into Eq. (307) gives a simpler expression for the over-stress. One can then fit that expression to experimental over-stress to identify the parameters τ_{max} , ζ , and τ_q .

An example for the parameters identification will be demonstrated in the following. One should note that the elastic and plastic contribution can be removed from the total stress to obtain the over-stress response since the parameters for the elastic and plastic behavior have already been identified in Section 12.2.5.2.

For identifying c_v , the stress rate at $t = 0$ is needed for the over-stress. The stress rate at $t = 0$ will be approximated by

$$\left. \frac{d\tau_v}{dt} \right|_{t=0} \approx \frac{\tau_v(\Delta t) - \tau_v(0)}{\Delta t}. \quad (329)$$

The sum of elastic and plastic stress at $t = \Delta t$ can be computed, from Eqs. (280) and (291), with $k = 0.05 \text{ sec}^{-1}$, $t = \Delta t = 0.01 \text{ sec}$ and the parameters listed in Table 10,

$$\tau_e(\Delta t) + \tau_p(\Delta t) = 0.289162 + 0.0310454 = 0.320208 \text{ kPa}. \quad (330)$$

Subtract Eq. (330) from Table 11, one has

$$\tau_v(\Delta t) = 0.418116 - 0.320208 = 0.0979082 \text{ kPa}. \quad (331)$$

Substituting Eq. (331) and $\tau_v(0) = 0$ into Eq. (329), one can obtain c_v from Eq. (325),

$$c_v = \frac{1}{k} \left. \frac{d\tau_v}{dt} \right|_{t=0} = \frac{1}{0.05} \frac{0.0979082 - 0.0}{0.01} = 195.816 \text{ kPa}. \quad (332)$$

This is very close to (or 0.7% different from) the assumed value in Table 10.

At this stage, the parameters, c_{e1} , c_{e2} , c_{e3} , c_p , η_p and c_v were identified. Next, the expressions for storage and loss moduli, Eqs. (272), will be fitted to experimental data, as

shown in Tables 14 and 15, obtained from high frequency and high amplitude harmonic strains to identify ξ and τ_{min} . Following the procedure discussed in Section 12.2.3.5, but in this case, only two instead of eight parameters need to be determined. One can obtain

$$\xi = 2.07435, \quad \tau_{min} = 0.00197659 \text{ sec.} \quad (333)$$

They are 8.0% and 2.8% different from the assumed values in Table 10, respectively.

Substituting Eqs. (332) and (333) into Eq. (307), τ_v becomes a function of τ_{max} , ζ , and τ_q . One can fit this expression for τ_v with three unknowns to the experimental over-stress history. A few test runs showed that the stress curve for $0 \leq t \leq t_0$ is not good for parameters identification. The reason might be that the approximate q , Eq. (245), does not exactly agree with the actual behavior of q at the begin of the time history. The stress response after $t = t_{rec}$ is not good for parameters identification either because the over-stress response is very weak after that time. The response data right after $t = t_0$ is good candidate for parameters identification. At $t = t_0$, the approximation for q is already quite good.

The stresses listed in Table 12 will be used to identify τ_{max} , ζ , and τ_q . First, the elastic and plastic response at the time instants listed in Table 12 will be computed and removed from the stresses in Table 12 to obtain the over-stress contribution. The elastic and plastic responses can be computed from Eqs. (280b) and (291b), respectively, for different strain levels, Eq. (310), and listed in Table 17. Note that after $t = t_0$, the elastic and plastic responses are constant for each strain level.

Table 17: Computed elastic stress τ_e [kPa] and plastic stress τ_p [kPa] after t_0

γ_0	0.01	0.03	0.06	0.10	0.20	0.30
τ_e	5.78302	17.3436	34.6496	57.5917	113.368	163.656
τ_p	0.472983	0.872415	1.01456	1.03977	1.04222	1.04223

After the computed elastic and plastic stresses, as shown in Table 17, are removed from the total stress, as listed in Table 12, one obtains the over-stress response as shown in Table 18. When fitting Eq. (307) to these over-stress response, one obtains,

$$\tau_{max} = 0.777411 \text{ sec}, \quad \zeta = 2.4142, \quad \tau_q = 744.564 \text{ sec.} \quad (334)$$

Table 18: Over-stresses τ_v [kPa] at sampling times t [sec]

$\gamma_0 = 0.01$					
t	0.25	0.40	0.55	0.70	0.90
τ_v	1.60662	1.31584	1.07769	0.882653	0.676371
$\gamma_0 = 0.03$					
t	0.65	0.75	0.90	1.05	1.20
τ_v	3.67329	3.19463	2.59102	2.10147	1.70444
$\gamma_0 = 0.06$					
t	1.30	1.50	1.70	1.80	1.90
τ_v	4.64641	3.44235	2.55036	2.19523	1.88956
$\gamma_0 = 0.10$					
t	2.10	2.20	2.40	2.55	2.70
τ_v	4.85829	4.11945	2.96186	2.31269	1.80585
$\gamma_0 = 0.20$					
t	4.10	4.20	4.45	4.60	4.70
τ_v	3.862	3.13301	1.85726	1.35721	1.10113
$\gamma_0 = 0.30$					
t	6.10	6.30	6.50	6.65	6.80
τ_v	2.87908	1.69476	0.997767	0.670678	0.450855

The first two parameters are 1.0% and 0.6% different from the assumed values in Table 10; however, τ_q is about 25% off the assumed value. This might be due to the fact that the viscous effect is not very sensitive to τ_q . A large change in τ_q does not affect the over-stress response much.

12.2.6 Numerical simulations

The H-S model discussed above was implemented in *Mathematica* and several numerical simulations were performed to evaluate its capability to capture the typical experimental observations for elastomeric materials. The assumed material parameters listed in Table 10 were used for all the following simulations, otherwise specified.

12.2.6.1 Initial and terminal modulus under ramp strains

The simplest simulation might be the ramp strain

$$\gamma(t) = kt. \tag{335}$$

In this simulation, the material behavior under ramp strains with different strain rates are studied. The strain rates are chosen as

$$k = \{2.5 \times 10^{-4}, 2.5 \times 10^{-3}, 0.025, 0.25, 2.5\} \text{ sec}^{-1}. \quad (336)$$

The stress-strain curve for different strain rates is shown in Fig. 56, where larger stress corresponds to larger strain rate. The stress-strain curves for the first three strain rates are almost coincident.

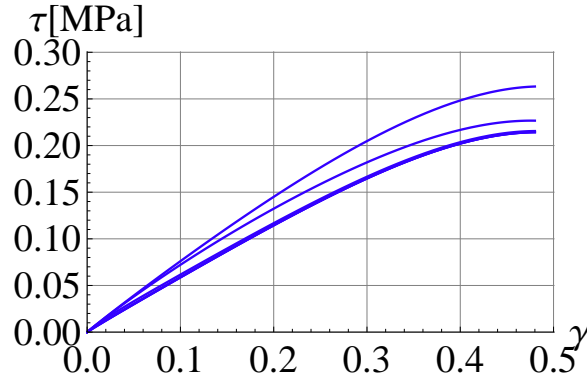


Figure 56: Stress-strain curves for ramp strain: strain rate decreases from top to bottom.

As reported in [35], the filled elastomeric materials under a ramp strain with different strain rates show different initial modulus (which is linearly dependent on the strain rate) but same terminal modulus. This section will check if the H-S model is capable to capture this behavior of the real elastomeric materials.

As discussed in Section 12.2.4, when the material is applied a ramp strain, the elastic and plastic response are, respectively,

$$\tau_e = c_{e1}(kt) + c_{e2}(kt)^3 + c_{e3}(kt)^5, \quad (337a)$$

$$\tau_p = \eta_p \left(1 - e^{-\frac{c_p}{\eta_p} kt} \right). \quad (337b)$$

The viscous response for the model with constant relaxation time τ_0 is

$$\tau_v(t) = \frac{c_v k}{k\xi + \frac{1}{\tau_0}} \left[1 - e^{-\left(k\xi + \frac{1}{\tau_0}\right)t} \right]. \quad (338)$$

When the material is applied a ramp strain the modulus can be computed as

$$G(t) = \frac{d\tau}{d\gamma} = \frac{1}{k} \frac{d\tau}{dt} = \frac{1}{k} \left(\frac{d\tau_e}{dt} + \frac{d\tau_p}{dt} + \frac{d\tau_v}{dt} \right) \equiv G_e + G_p + G_v. \quad (339)$$

From Eqs. (337a), (337b) and (338), one can compute

$$G_e = \frac{1}{k} \frac{d\tau_e}{dt} = c_{e1} + c_{e2}\gamma^2 + c_{e3}\gamma^4, \quad (340a)$$

$$G_p = \frac{1}{k} \frac{d\tau_p}{dt} = c_p e^{-\frac{c_p}{\eta_p} \gamma}, \quad (340b)$$

$$G_v = \frac{1}{k} \frac{d\tau_v}{dt} = c_v e^{-\xi\gamma - \frac{\gamma}{k\tau_0}}, \quad (340c)$$

It can be seen from Eqs. (340a), (340b) and (340c) that the elastic modulus and plastic modulus are rate-independent while the viscous modulus is rate-dependent. The amplitude-dependence of elastic modulus depends on the signs and relative values of the material constants c_{e2} and c_{e3} . However, the plastic and viscous moduli decrease with the increasing of the strain amplitude.

When considering the initial modulus, setting $\gamma = 0$ in Eqs. (340a), (340b) and (340c), it can be seen that the initial modulus is always, no matter what the strain rate k is,

$$G(t) = G_e + G_p + G_v = c_{e1} + c_p + c_v. \quad (341)$$

Hence, *the initial modulus of H-S model is not dependent on the strain rate.*

Considering the terminal modulus at certain strain amplitude γ obtained through different strain rate k , it can be seen that the elastic and plastic modulus depend on the strain amplitude only, not on the strain rate; thus, the total terminal modulus of the material is just an offset of the viscous modulus. The viscous modulus depends on both strain amplitude and strain rate. Thus, for a strain amplitude obtained through different strain rates, the elastic and plastic modulus are always the same. This agrees with the observation in the test. However, the viscous modulus is also rate-dependent, which means for a strain amplitude obtained through different strain rates, the viscous modulus are in general not the same. A close examination will be given to the viscous modulus, Eq. (340c).

For the model with constant τ_0 , the viscous modulus is always rate-dependent. This rate-dependency cannot be removed by adjusting the material parameters. The only case in which one may approximately consider the viscous modulus as rate-independent is $\xi \gg \frac{1}{k\tau_0}$. With the introduction of structural variable q , τ_0 is not a constant but a function of q which is in turn related to the strain rate k and two additional material parameters, ζ and λ_q . To

make the viscous modulus rate-independent, one should have $k\tau_0$ be a constant for different strain rate k . Roughly speaking, when k increases, τ_0 should decrease and accordingly q should increase since $\tau_0 = \tau_{max}(1 - q) + \tau_{min}q$ and $\tau_{max} > \tau_{min}$. From the discussion in Section 12.2.4.4, it can be found that q does increase with increasing of the strain rate. Thus, *the introduction of q makes the rate-independent terminal modulus possible.*

When considering the q effect, the relaxation time is not a constant but a parameter determined by strain rate k , and several additional material parameters, τ_{max} , τ_{min} , ζ , and λ_q . Thus one may adjust those material parameters to obtain different relaxation time τ_0 for different strain rates. Fig. 57 illustrates the stress-strain curve for the H-S material model under ramp strains, with different strain rates. From this figure, one can say that the terminal modulus tends to be rate-independent, *i.e.*, the slope of the stress-strain curve is constant for certain strain amplitude even through the strain rates are different. In conclusion, this H-S model with q effect is able to predict the rate-independent terminal modulus.

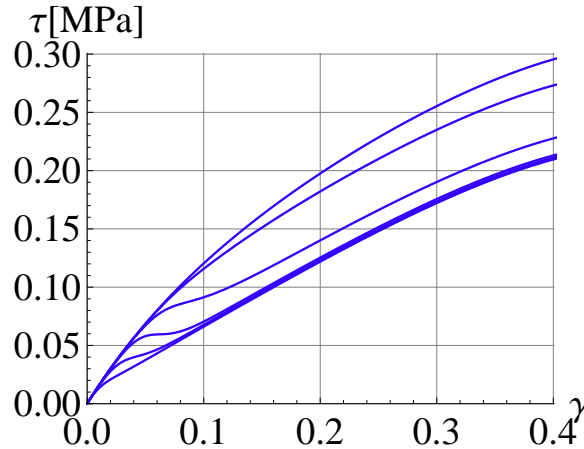


Figure 57: Stress-strain curves for ramp strain. Material parameters: $c_v = 0.985974$ MPa, $\xi = 10.0$, $\tau_{max} = 1000$ sec, $\tau_{min} = 1$ sec, $\zeta = 100$, $\tau_q = 1000$ sec and $k = 2.5, 0.25, 0.025, 2.5 \times 10^{-3}, 2.5 \times 10^{-4},$ and $2.5 \times 10^{-5} \text{ sec}^{-1}$ from top to bottom.

12.2.6.2 Relaxation tests

A set of relaxation tests were performed using step strains to determine the influence of the step size of the strain on the relaxation modulus, which is defined as relaxation stress

divided by the magnitude of the step strain. The strain histories used for the relaxation tests are given by Eqs. (240) with $k = 0.05 \text{ sec}^{-1}$ and strain steps given by Eq. (310).

The relaxation stress and relaxation modulus are shown in Fig. 58. In the left figure, a larger stress corresponds to larger strain; while in the right figure, a larger relaxation modulus corresponds to smaller strain step size, *i.e.*, the relaxation modulus decreases with the increasing of strain step size. This observation agrees with the experimental results reported by [8]. Fig. 59 presents the relaxation stress and relaxation modulus for $\gamma_0 = 0.06$.

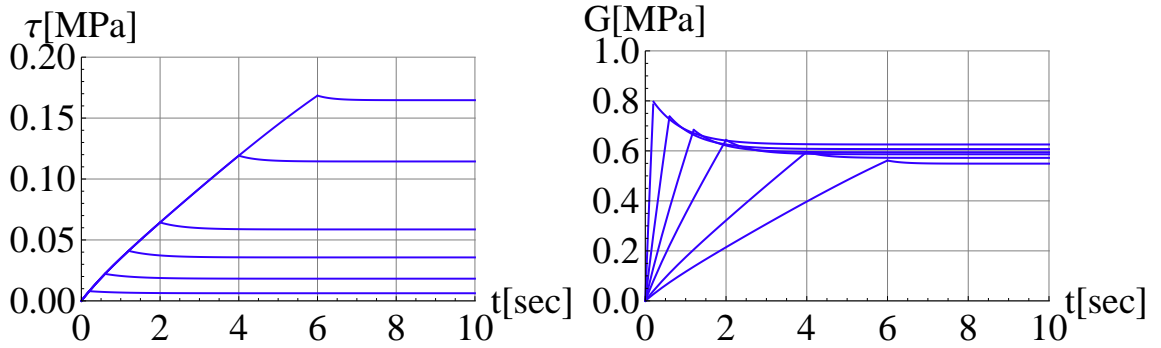


Figure 58: Relaxation test. Left: relaxation stress; right: relaxation modulus.

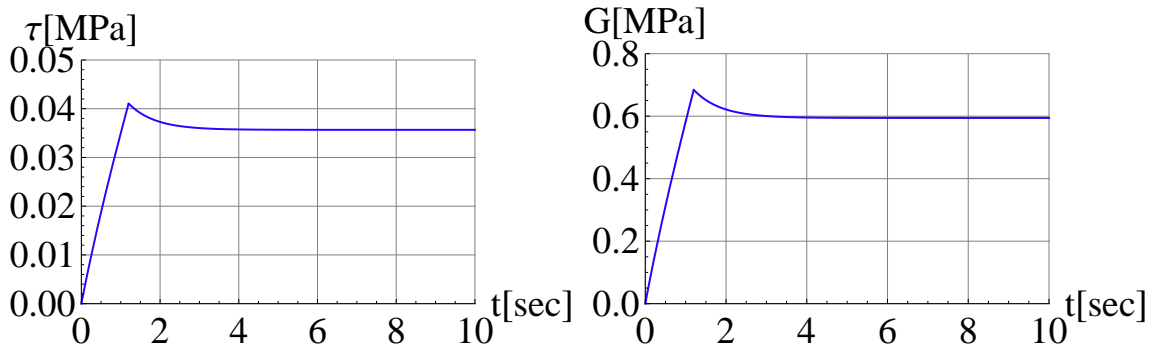


Figure 59: Relaxation test for $\gamma_0 = 0.06$. Left: relaxation stress; right: relaxation modulus.

12.2.6.3 Sinusoidal strain

A set of sinusoidal strain histories with different frequencies and amplitudes were prescribed and the steady state stress responses were measured. Fourier transformation was performed on the stress response and the storage and loss moduli are then computed according to Eqs. (253). The details of this test were discussed in Section 12.2.3.6 and Figs. 54 and 55

present the typical storage and loss moduli, respectively. It can be seen that this model is able to predict the dependency of the modulus on the strain amplitude and frequency.

12.2.6.4 Sinusoidal strain with increasing and decreasing amplitudes

To check the reversibility of the dynamic modulus amplitude dependency, a sinusoidal strain with increasing and then decreasing amplitude was prescribed, as qualitatively depicted in Fig. 60. The storage and loss moduli were computed from the stress response in the last period for each amplitude. The amplitudes for the increasing region are given by

$$A = \{0.01, 0.03, 0.06, 0.10, 0.20, 0.30\} \quad (342)$$

and for the decreasing region in the reverse order. Two frequencies, $f = 3.0$ and $f = 30.0$ Hz were simulated for the amplitude sequence.

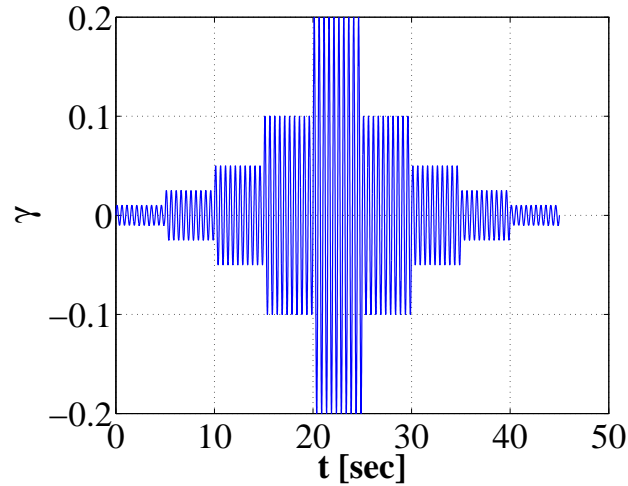


Figure 60: Sinusoidal strain with increasing and decreasing amplitudes

The simulations were first run for 200 periods for each amplitude. With this long time, the structural variable q has enough time to saturate. It can be expected that the storage and loss moduli for this case should be the same as those obtained from applying sinusoidal strain with different amplitudes individually. The data listed in Table 19 verified this prediction. The moduli for the same amplitude, no matter it is in the increasing or decreasing sequence, are the same. They are also identical to those obtained by applying a sinusoidal strain with same constant amplitude for sufficient time to ensure that the steady

state response is achieved. This observation indicates that the decline in the modulus due to the increasing of the strain amplitude is recoverable, which is in accordance with the experimental results reported by [8]. Note that the storage and loss moduli obtained from steady state response are denoted G'_{steady} and G''_{steady} , respectively, in Tables 19 and 20.

However, when the simulations were run for a shorter time, 10 periods, for each amplitude, the situation changed. In this case, the structural variable q does not have enough time to saturate, especially for the low amplitude strains. Table 20 lists the storage and loss moduli for each amplitude with 10-period simulation. It can be seen that the storage and loss moduli are different from G'_{steady} and G''_{steady} , respectively, especially for low amplitude strains. The reason is that the structural variable q needs longer time to saturate for low amplitudes than it needs for high amplitudes.

Figs. 61 and 62 show two typical histories for the structural variable q . It can be seen, from Fig. 61, that when the simulation lasts 200 periods for each amplitude, q is saturated at each strain amplitude no matter it is in the increasing or decreasing sequence. The saturated value for q in this case is the same for same strain amplitudes. This explains the fact that the modulus are same for same amplitudes. However, when the simulation runs only 10 periods for each amplitude, it can be seen, from Fig. 62, that q does not saturate for low amplitude strains, while q achieved its steady state for high amplitude strains. This explains the fact that the moduli are different from those G'_{steady} and G''_{steady} for low amplitude strains while the same for high amplitude strains. Another observation is that the values of q for the strains with same amplitude but in increasing and decreasing sequence are different in this 10-period simulation. This results in the difference between the modulus for strains with same amplitude but in increasing and decreasing sequence, see Table 20.

Note that the difference of the modulus between increasing and decreasing amplitude sequences is related to the recovery time of the material damage and the simulation time. If the simulation time is long enough comparing with the recovery time, the difference will be negligible; otherwise, the difference will be significant. Fig. 63 presents the storage modulus of elastomeric materials with different recovery times under sinusoidal strains with

Table 19: Storage and loss moduli [kPa]: 200-period simulation for each amplitude

f [Hz]	A	0.01	0.03	0.06	0.1	0.2	0.3	0.2	0.1	0.06	0.03	0.01
3.0	G' (this test)	635.237	608.151	590.92	583.163	572.6	556.813	572.6	583.163	590.92	608.151	635.238
	G'_{steady}	635.24	608.151	590.92	583.163	572.6	556.813					
3.0	G'' (this test)	30.9959	31.4955	24.7654	19.1409	13.6193	11.5076	13.6194	19.1409	24.7654	31.4949	30.995
	G''_{steady}	30.9942	31.4949	24.7654	19.1408	13.6192	11.5076					
30.0	G' (this test)	662.277	631.825	613.293	604.568	592.278	575.093	592.278	604.568	613.293	631.825	662.279
	G'_{steady}	662.288	631.825	613.293	604.568	592.278	575.092					
30.0	G'' (this test)	83.3006	85.5095	78.4476	71.9056	63.8908	59.4033	63.8909	71.9056	78.4476	85.5095	83.3011
	G''_{steady}	83.3105	85.5095	78.4476	71.9056	63.8909	59.4031					

Table 20: Storage and loss moduli [kPa]: 10-period simulation for each amplitude

f [Hz]	A	0.01	0.03	0.06	0.1	0.2	0.3	0.2	0.1	0.06	0.03	0.01
3.0	G' (this test)	823.908	637.062	590.952	583.163	572.6	556.813	572.6	583.163	590.92	608.139	634.805
	G'_{steady}	635.24	608.151	590.92	583.163	572.6	556.813					
3.0	G'' (this test)	48.0315	90.7812	25.0314	19.1412	13.6194	11.5076	13.6193	19.141	24.7628	31.3897	28.3689
	G''_{steady}	30.9942	31.4949	24.7654	19.1408	13.6192	11.5076					
30.0	G' (this test)	830.72	792.816	616.	604.568	592.277	575.092	592.277	604.568	613.29	631.739	660.487
	G'_{steady}	662.288	631.825	613.293	604.568	592.278	575.092					
30.0	G'' (this test)	18.7774	61.3831	81.4836	71.906	63.8892	59.4031	63.8895	71.9056	78.4441	85.4122	81.4516
	G''_{steady}	83.3105	85.5095	78.4476	71.9056	63.8909	59.4031					

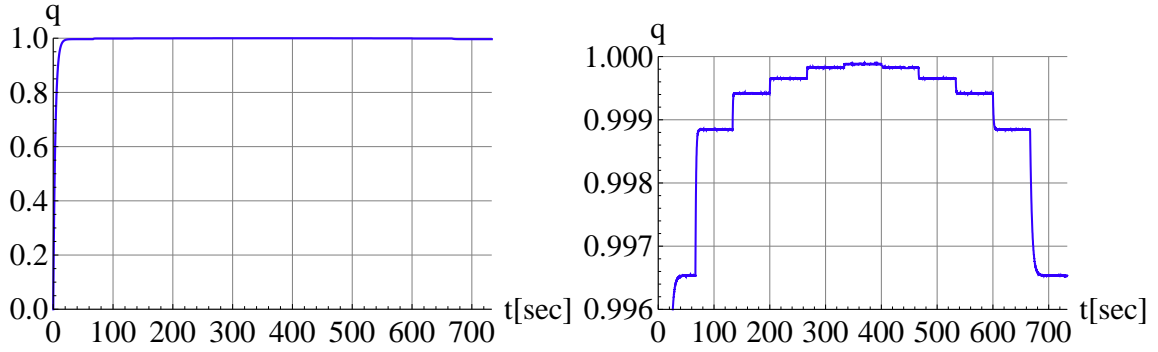


Figure 61: Time history for q : $f = 3$ Hz and 200-period simulation for each amplitude.

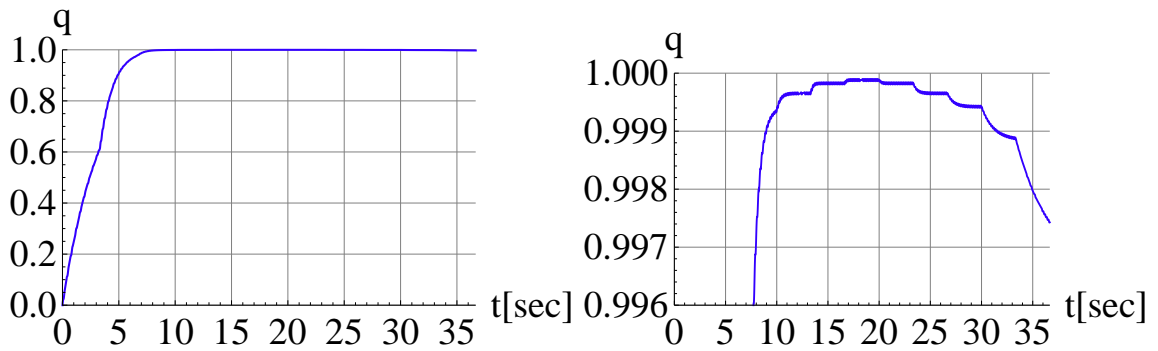


Figure 62: Time history for q : $f = 3$ Hz and 10-period simulation for each amplitude.

increasing and decreasing amplitudes. The frequency for the sinusoidal strain is 3 Hz. In the figure, each curve with same symbol represents an increasing and decreasing sequence of the strain. The modulus in the amplitude decreasing sequence is always smaller than that for the same strain amplitude in the increasing sequence. The recovery time is reflected by ζ : a large ζ represents a short recovery time. The figure was generated with 10 period simulation for each strain amplitude. It can be seen from the figure that when the recovery time is short (or ζ is large), the difference of the modulus for same strain amplitude in the increasing and decreasing sequences is small; however, for case with long recovery time (or small ζ), this difference is quite significant, for instants, the cases with $\zeta = 0.15$ and $\zeta = 0.075$.

12.2.6.5 Effect of static strain offset on dynamic modulus

Simulations with strain history as qualitatively illustrated in Fig. 64 were performed to study the effect of the static strain offset on the dynamic modulus. The frequency for the

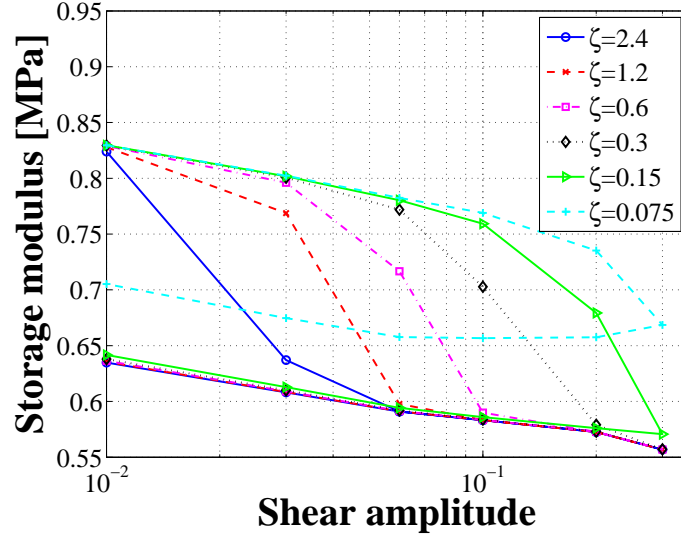


Figure 63: Storage modulus for different recovery times.

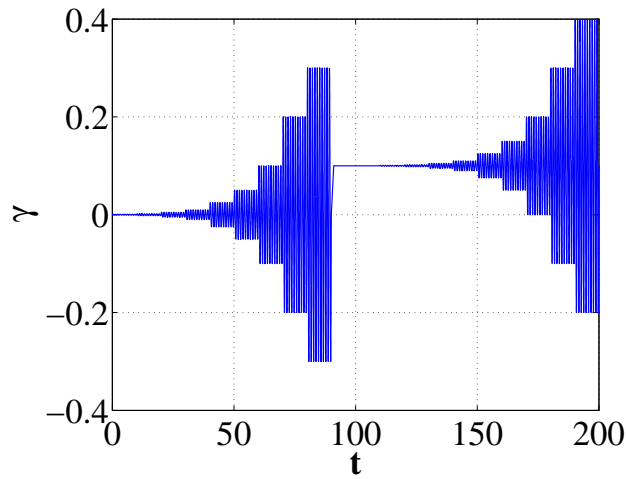


Figure 64: Sinusoidal strain with static strain offset.

sinusoidal strain is 3 Hz; and the amplitudes are given by Eq. (342). The static strain offsets are chosen as 0.05, 0.10, 0.15, and 0.20, respectively. The storage and loss moduli were computed for each of the amplitudes and shown in Fig. 65. It is found that the effect of the static strain offset on the storage modulus is small when the offset is not very large, for instance, $\gamma \leq 15\%$; however, the difference is significant when the strain offset is large. The effect of the static strain offset on the loss modulus is negligible for all offsets investigated when the dynamic strain amplitudes are large. Chazeau *et al.* [35] reported similar experimental observations: the imposition of a strain offset up to 10% has little

effect on both the storage and loss moduli. Test data for strain offset larger than 10% was not reported in [35].

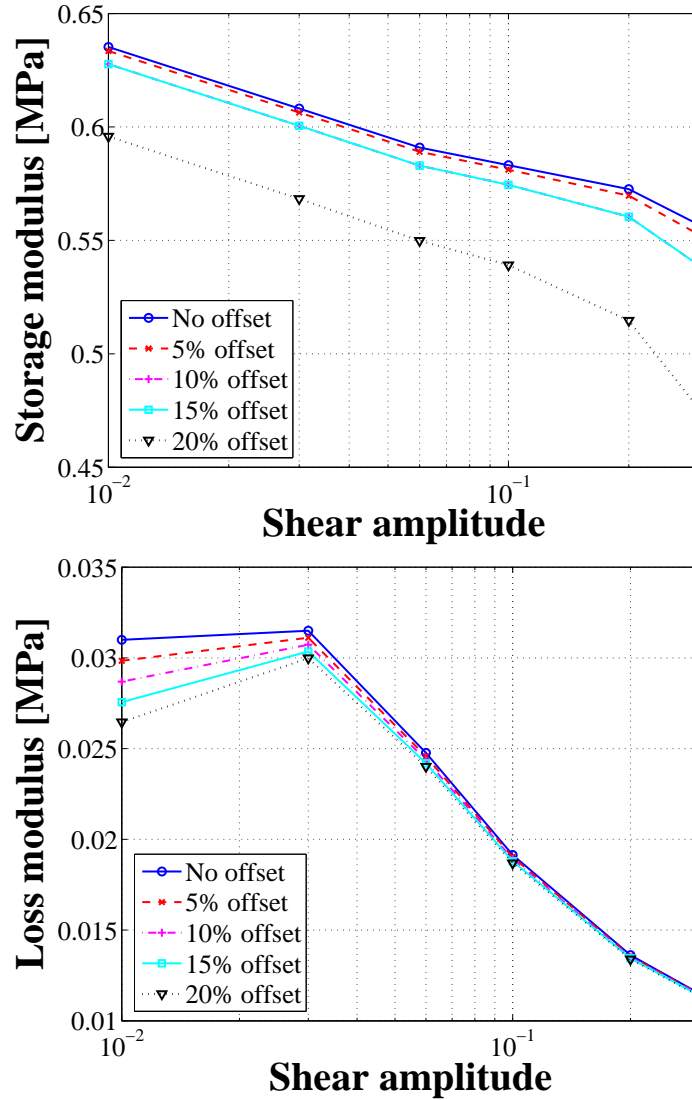


Figure 65: Effect of static strain offset on dynamic modulus.

It is interesting to note that the waiting time between the application of the static strain offset and the starting of the second sequence of sinusoidal strains is not important for this H-S model as long as the sinusoidal strain lasts sufficient time for the saturation of structural variable q . Theoretically, when the waiting time is sufficiently long, q will recover from certain value to 0. If the sinusoidal strains are applied after that time, the modulus would be the same as those obtained from virgin material. If the waiting time is not long

enough for q to recover, the modulus would be different from those obtained from virgin material. However, different waiting times, longer or less than the recovery time for q , were tested and same results as in Fig. 65 were obtained. The reason is that the structural variable q saturates to its steady state when the sinusoidal strain is applied for sufficient time no matter q is recovered or not in the waiting time.

What is the reason for the storage modulus changing between cases with different strain offsets? When a sinusoidal strain with a static offset A_0 ,

$$\gamma = A_0 + A \sin(\omega t), \quad (343)$$

is applied, it can be found the strain rate is the same as that of a sinusoidal strain, *i.e.*,

$$\dot{\gamma} = A\omega \cos(\omega t). \quad (344)$$

Hence, Eqs. (230) to (233) for the H-S model are not different from those for a sinusoidal strain without a static component. Following the procedure in Sections 12.2.3.2 and 12.2.3.3, one can obtain the same c_{pk} , d_{pk} , c_{vk} , and d_{vk} for the case with static offset as those for the case without offset. However, for the case with offset, one has $c_{p0} = c_{v0} = A_0$ instead of $c_{p0} = c_{v0} = 0$ for the case without offset. This makes Eqs. (238) to be the same for both cases. It can be expected that the static strain offset will have no influence on the plastic and viscous contributions to the dynamic modulus, see Eqs. (274) and (275).

However, the situation for the elastic contribution to the dynamic modulus is different. Substituting Eq. (343) into Eq. (237), one can obtain the elastic contribution to the dynamic modulus as, from Eq. (253),

$$G'_e = \left(c_{e1} + \frac{3}{4}c_{e2}A^2 + \frac{5}{8}c_{e3}A^4 \right) + A_0^2 \left[3c_{e2} + \left(\frac{15}{2}A^2 + 5A_0^2 \right) c_{e3} \right], \quad (345a)$$

$$G''_e = 0; \quad (345b)$$

Note that the elastic storage modulus in Eq. (345a) is different from that one in Eq. (273a) by the appearance of the second term. This second term involves the strain offset A_0 and material parameters c_{e2} and c_{e3} , which means that the static strain offset will affect the storage modulus of the material as long as the constitutive law for the elastic response is

nonlinear. If the constitutive law for the elastic response is linear, *i.e.*, $c_{e2} = c_{e3} = 0$, it can be seen that Eqs. (345a) and (273a) are the same. Fig. 66 presents the adjusted storage modulus, where the second term in Eq. (345a) was removed from the computed storage modulus for cases with strain offset. It can be seen that the curves for cases with and without static strain offset are on top of each other after the adjustment. Thus, as long as the material presents nonlinear stress-strain behavior, the static strain offset will influence the dynamic modulus, at least the storage modulus, more or less.

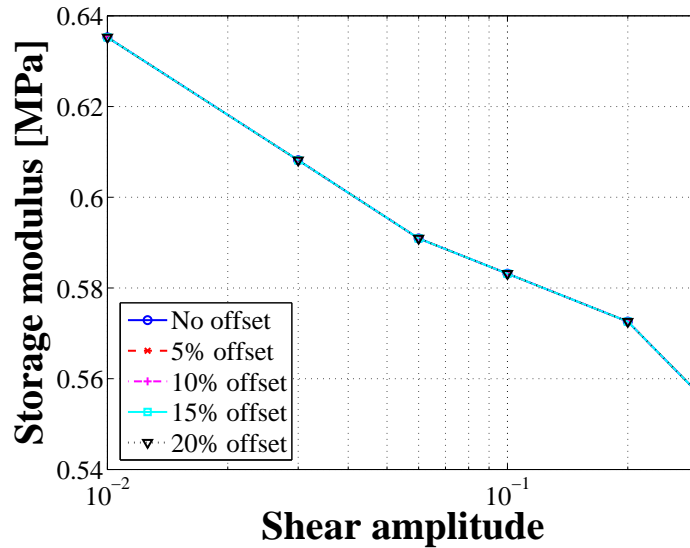


Figure 66: Effect of static strain offset on dynamic modulus (adjusted storage modulus).

12.2.7 Summary on the evaluations of H-S model

The H-S model includes the necessary elements for modeling elastomeric materials, which are elastic, plastic, and viscous elements; hence, theoretically, it should be able to model the behavior of the elastomeric materials if the material parameters are well tuned. However, it is very difficult, if not impossible, to model all the behavior of the elastomeric materials in practice since some of the behavior of elastomeric materials are not even well understood by researchers at this time. From the analytical studies and numerical simulations in previous sections, some conclusions may be made for the H-S model:

- The H-S model is capable to capture the frequency and amplitude dependency of the

storage and loss moduli; especially, with the introduction of the structural variable q .

- The predictions from H-S model under relaxation tests agree with the typical experimental observations for elastomeric materials under relaxation test.
- When a ramp strain applied, the introduction of the structural variable q makes the rate-independent terminal modulus possible; however, the initial modulus is always the same no matter what the rate of the ramp strain is.
- Simulation results for sinusoidal strains with increasing and then decreasing amplitudes showed that whether the strain amplitude is increasing or decreasing does not affect the storage and loss moduli of the material as long as the application time of the strain is long enough for each amplitude. This is in accordance with the experimental results. However, if the application time is not long enough comparing with the recovery time, the modulus for same amplitude in increasing and decreasing sequence is different, the former is greater than the latter.
- The static strain offset does not affect the loss modulus; however, it influences the storage modulus as long as the material presents nonlinearity in the stress-strain relationship. This influence on the storage modulus is small when the strain offset is small.

One important thing that should be pointed out is that the previous analysis and discussions are all based on the fact that the H-S model consists of one elastic, one plastic and one viscous path in parallel. However, as indicated in Eq. (229), the H-S model can involve several plastic and/or viscous paths in parallel. It can be expected that the predictions from H-S model will have a better agreement with the actual behavior of elastomeric materials when more plastic and/or viscous paths are included in the model. Figs. 67 and 68 present the storage and loss moduli fitting to the same test data as in Figs. 52 and 53 but this time with three viscous paths (or Maxwell elements). It can be seen that the fitted results are much better than those shown in Figs. 52 and 53 where only one Maxwell element was used.

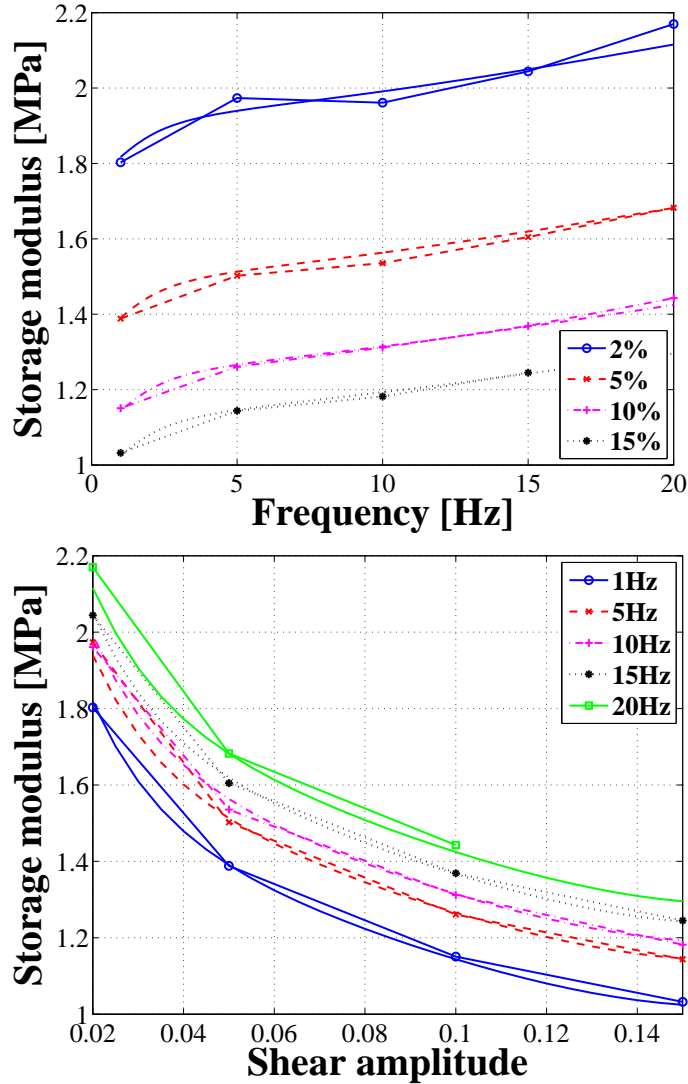


Figure 67: Storage modulus fitting. With symbols: test data from [8]; without symbols: Eq. (272a) with three Maxwell elements

However, two problems are likely to show up with the inclusion of more plastic and/or viscous paths. First, more experimental data may be required to identify the material parameters because the material model involves more parameters when more plastic and/or viscous paths are included. Second, difficulties may be encountered in the curve fitting procedure when the number of the material parameters is very large. Including more plastic and/or viscous paths in the model does not complicate the derivation of its analytical solutions; however, more material parameters will lead to computational difficulties in minimizing the error function. When confronted with a large number of material parameters,

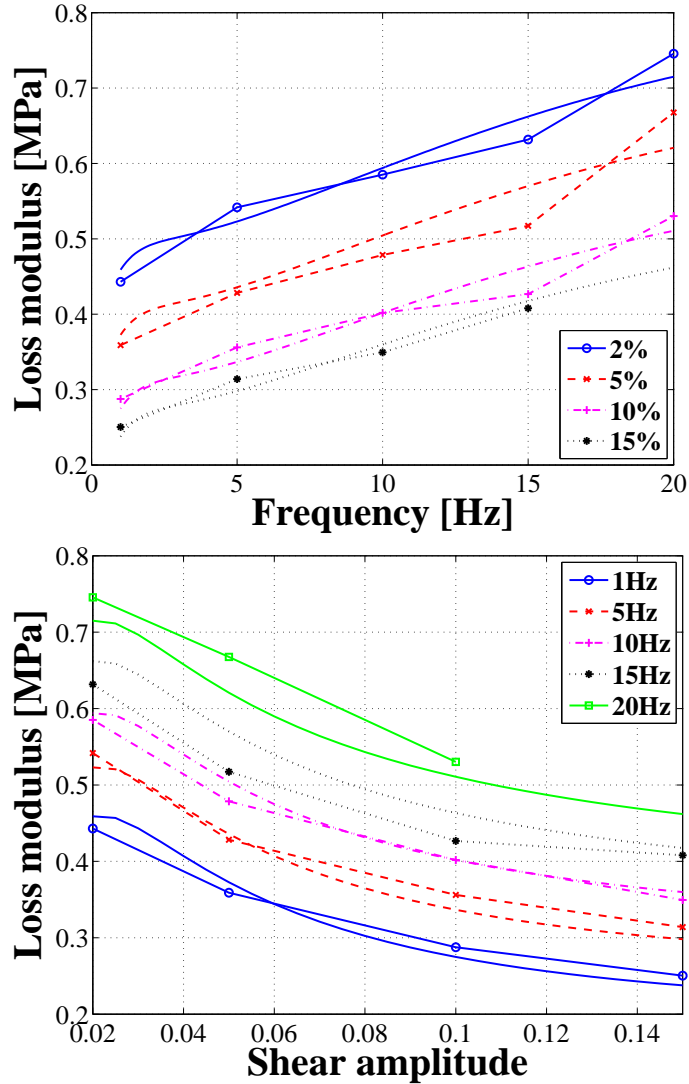


Figure 68: Loss modulus fitting. With symbols: test data from [8]; without symbols: Eq. (272b) with three Maxwell elements

identification procedure becomes computationally inefficient, and might not converge. If the minimization algorithm is efficient and robust enough, involving more material parameters does not bring significant challenges to the identification procedure. From the experience with *Mathematica*, one might encounter convergence problem when the number of Maxwell elements reaches five or more.

12.3 Höfer-Lion Model

The second elastomeric model to be evaluated was proposed by Höfer and Lion [64], which will be referred as H-L model in the following. This model is based on the concept of stress decomposition and its one-dimensional version consists of one elastic path and one or more Maxwell elements in parallel, as depicted in Fig. 69.

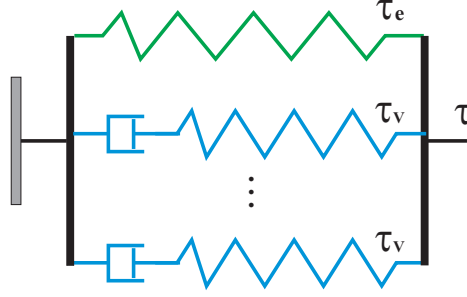


Figure 69: Höfer-Lion Model: one-dimensional version

12.3.1 Constitutive equations for H-L model

For the one-dimensional version of H-L model, the total shear stress can be additively decomposed as

$$\tau = \tau_e + \sum_{m=1}^M \tau_{vm}, \quad (346)$$

where τ_e is the elastic equilibrium shear stress and can be given by any physically meaningful stress-strain relationship, for example,

$$\tau_e = c_e \gamma. \quad (347)$$

In Eq. (346), τ_{vm} is the over-stress in the m th Maxwell element, given by,

$$\dot{\tau}_{vm} = c_{vm} \dot{\gamma} - \frac{\dot{z}_m}{\tau_{0m}} \tau_{vm} \quad \text{for } m = 1, 2, \dots, M. \quad (348)$$

Here z_m is an intrinsic time scale and τ_{0m} the relaxation time. Note that if $z_m = t$, Eq. (348) becomes the equation for standard linear Maxwell element with viscosity $\eta_{vm} = c_{vm} \tau_{0m}$, which is well suited for modeling the frequency-dependent properties of elastomeric materials but cannot describe any amplitude dependent phenomena. To model both the

amplitude and frequency dependent behavior of elastomeric materials, the evolution of z_m is given by differential equation

$$\dot{z}_m(t) = \alpha_m (\bar{\tau}_m |\dot{\gamma}| + 1) + (1 - \alpha_m) \left(\sum_{i=1}^L d_{mi} q_i + 1 \right) \quad \text{for } m = 1, 2, \dots, M. \quad (349)$$

Here α_m , $\bar{\tau}_m$ and d_{mi} are material parameters and q_i are internal variables to describe the amplitude dependence of the material. q_i are given by a set of first order differential equations in the form of

$$\dot{q}_i(t) = \frac{1}{\tau_{qi}} (\tau_{q0} |\dot{\gamma}| - q_i) \quad \text{for } i = 1, 2, \dots, L. \quad (350)$$

The parameters τ_{qi} are relaxation times describing the dynamic behavior of the material's microstructure and the constant $\tau_{q0} = 1$ sec is introduced for dimensional reasons.

The two terms in the right-hand side of Eq. (349) were proposed for different purposes. The first term describes the short-term behavior of the material between amplitude steps, while the second term is included to describe the long-term recovery behavior of the modulus. The characteristic of these two terms will be discussed in following. When $\alpha = 1$, the H-L model consists of only the first term, which will be referred as *α -1 model*; while the model consists of only the second term when $\alpha = 0$, which will be referred as *α -0 model* in the following.

12.3.1.1 α -1 model

For a α -1 model, Eq. (348) becomes (with the subscript m omitted),

$$\dot{\tau}_v = c_v \dot{\gamma} - \frac{\bar{\tau} |\dot{\gamma}| + 1}{\tau_0} \tau_v. \quad (351)$$

This is the differential equation for a Maxwell element with relaxation time

$$\tau_R = \frac{\tau_0}{\bar{\tau} |\dot{\gamma}| + 1}; \quad (352)$$

accordingly the viscosity for the Maxwell element is

$$\eta_v = c_v \tau_R = \frac{c_v}{\xi |\dot{\gamma}| + 1/\tau_0}. \quad (353)$$

with $\xi = \bar{\tau}/\tau_0$. Note that this viscosity is the same as Eq. (231), which means that the α -1 model is the same as the H-S model but with a constant τ_0 . Hence, the behavior of the α -1

model will not be repeated here. Any discussions in Section 12.2 with constant τ_0 apply for α -1 model.

12.3.1.2 α -0 model

For a α -0 model, Eq. (348) becomes

$$\dot{\tau}_v = c_v \dot{\gamma} - \frac{\sum_{i=1}^L d_i q_i + 1}{\tau_0} \tau_v. \quad (354)$$

with evolution equations given by Eq. (350) for q . The behavior of this α -0 model is in general different from the α -1 model. However, considering the case where q achieves a steady state (constant) so that $\dot{q} = 0$, one can find $q = \tau_{q0} |\dot{\gamma}|$. Then Eq. (354) becomes,

$$\dot{\tau}_v = c_v \dot{\gamma} - \frac{\tau_{q0} \left(\sum_{i=1}^L d_i \right) |\dot{\gamma}| + 1}{\tau_0} \tau_v. \quad (355)$$

It can be found that α -0 model in this case is the same as α -1 model with $\bar{\tau} = \tau_{q0} \left(\sum_{i=1}^L d_i \right)$, see Eq. (351).

In the following sections, the harmonic response of α -1 model and α -0 model will first be compared by fitting these two models with the test data used in Section 12.2 and experimental data reported in [64]; then the response of α -0 model under relaxation tests will be discussed in detail since the relaxation behavior of the α -1 model has been studied in Section 12.2. Some numerical simulations with the combination of α -1 and α -0 model will also be presented.

12.3.2 Storage and loss moduli: response of H-L model under harmonic strain

In Figs. 52, 53, 67 and 68, the H-S model with constant τ_0 was fitted to experimentally measured storage and loss moduli, respectively, for one and three Maxwell elements in parallel. In this section, the same fitting procedure will be conducted for the α -1 and α -0 model to study their capability to model the amplitude and frequency dependency of the elastomeric materials. For α -1 model, the expressions for the storage and loss moduli have been derived in Section 12.2.3. For α -0 model, the harmonic balance analysis procedure introduced in Section 12.2.3 can be applied to obtain the expressions for storage and loss

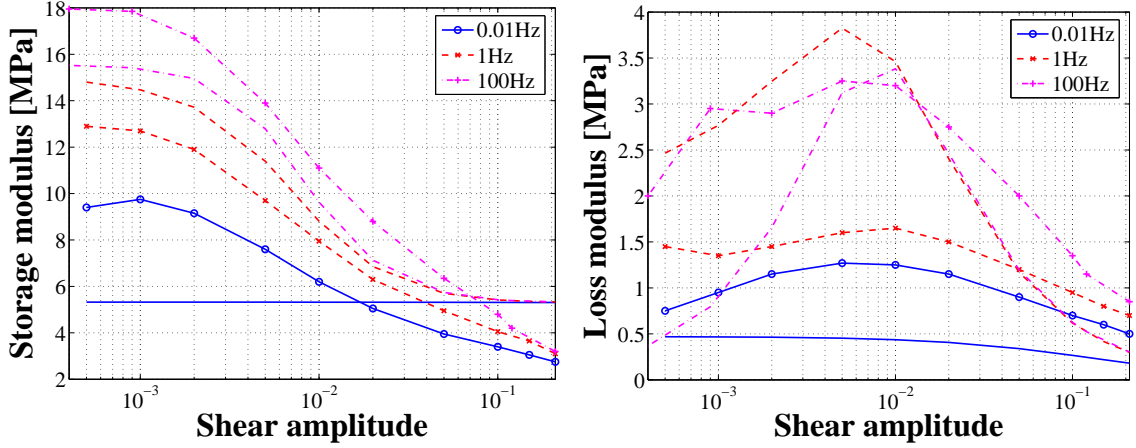


Figure 70: Storage and loss moduli fitting (average error: 1.61306 MPa). With symbols: test data from [64]; without symbols: α -1 model fitting with one Maxwell element

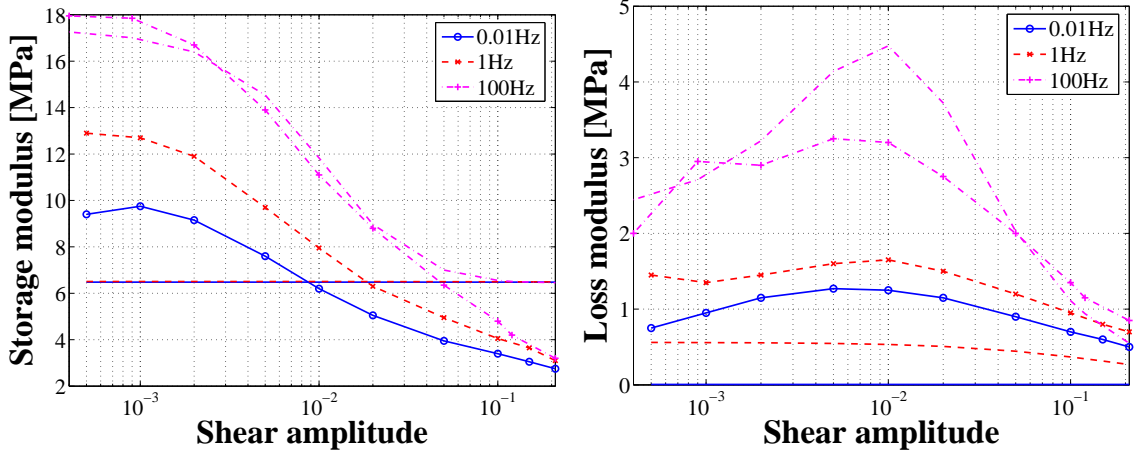


Figure 71: Storage and loss moduli fitting (average error: 2.08715 MPa). With symbols: test data from [64]; without symbols: α -0 model fitting with one Maxwell element

moduli. The details are not shown here. The only difference is that an expression for q needs to be obtained first.

Figs. 70 to 73 present the storage and loss moduli fitting for the α -1 and α -0 model with one and three Maxwell elements in parallel. The test data is obtained from [64]. For α -0 model, as suggested by [64], three q 's were used for each Maxwell element and d_{mi} were set as $d_{m1} = 0.7$, $d_{m2} = 0.15$, and $d_{m3} = 0.15$. A constraint, $\tau_{q1} = 10\tau_{q2} = 100\tau_{q3}$, was also enforced for the recovery times of q . Some key observations from the figures are:

- the overall fit for the storage modulus is better than that for loss modulus;

- α -1 model performs better than α -0 model for the storage modulus fitting; while the α -0 model works better than α -1 model for loss modulus fitting;
- the fit for the α -1 model becomes much better when the number of parallel Maxwell elements increases; while the fitting improvement with the increasing of the number of parallel Maxwell elements is not apparent for the α -0 model. This might be due to the fact that d_i and q_i are the same for each Maxwell element.

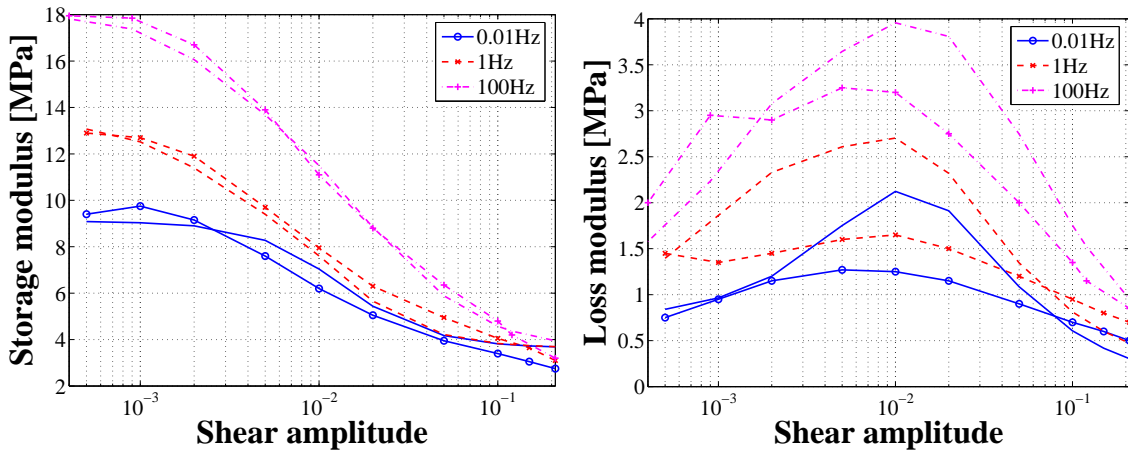


Figure 72: Storage and loss moduli fitting (average error: 0.520227 MPa). With symbols: test data from [64]; without symbols: α -1 model fitting with three Maxwell elements

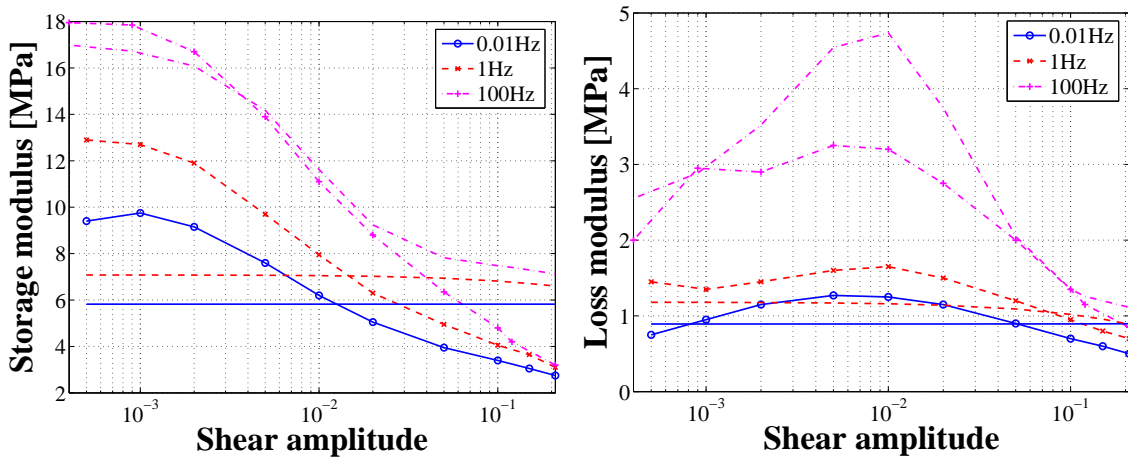


Figure 73: Storage and loss moduli fitting (average error: 2.02253 MPa). With symbols: test data from [64]; without symbols: α -0 model fitting with three Maxwell elements

Figs. 74 to 77 present similar storage and loss moduli fitting for the test data reported in [8] and used in Section 12.2. Similar observations can be seen from these figures.

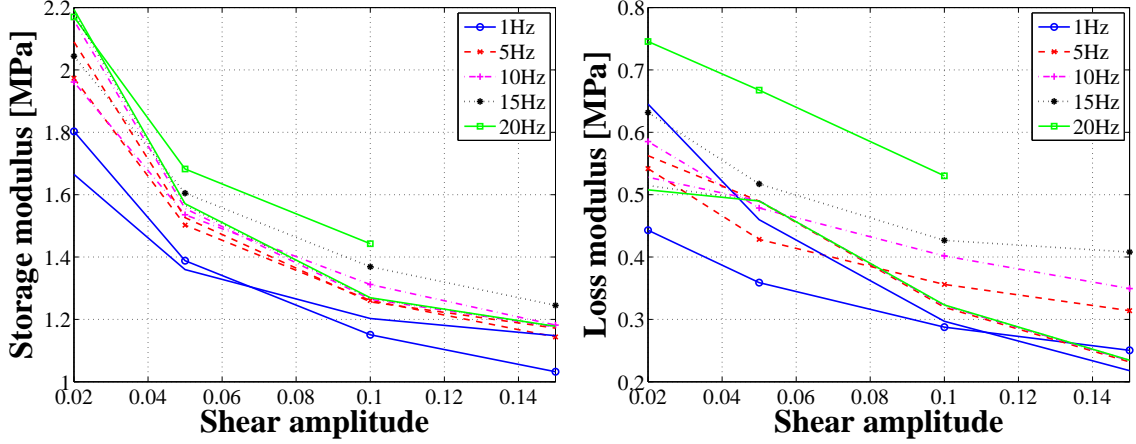


Figure 74: Storage and loss moduli fitting (average error: 0.108241 MPa). With symbols: test data from [8]; without symbols: α -1 model fitting with one Maxwell element

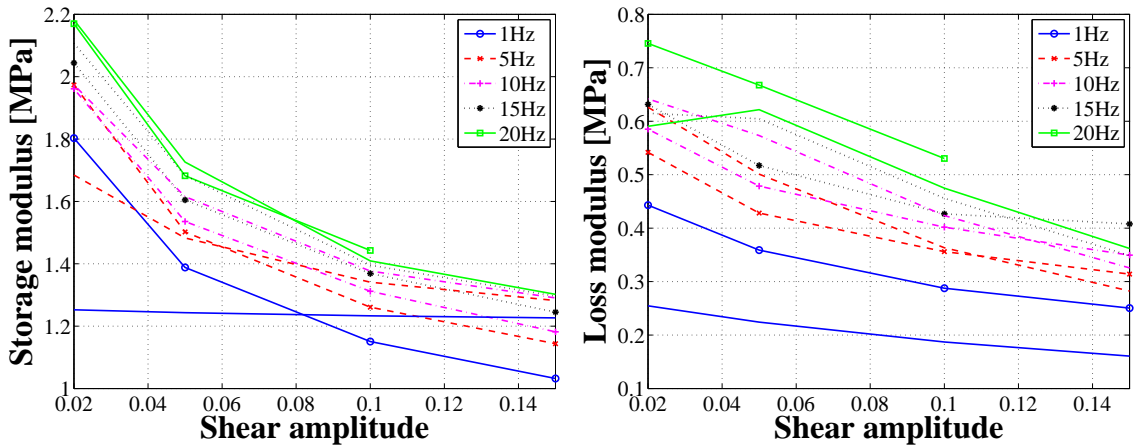


Figure 75: Storage and loss moduli fitting (average error: 0.131517 MPa). With symbols: test data from [8]; without symbols: α -0 model fitting with one Maxwell element

12.3.3 Response of α -0 model under relaxation test

This section studies the response of the α -0 model under a strain history given by Eqs. (240), *i.e.*, a ramp strain followed by a relaxation test. For this case, Eq. (350) becomes (with the subscript i omitted),

$$\dot{q} = \frac{1}{\tau_q} (k - q) \quad \text{for } 0 \leq t \leq t_0; \quad (356a)$$

$$\dot{q} = -\frac{1}{\tau_q} q \quad \text{for } t > t_0. \quad (356b)$$

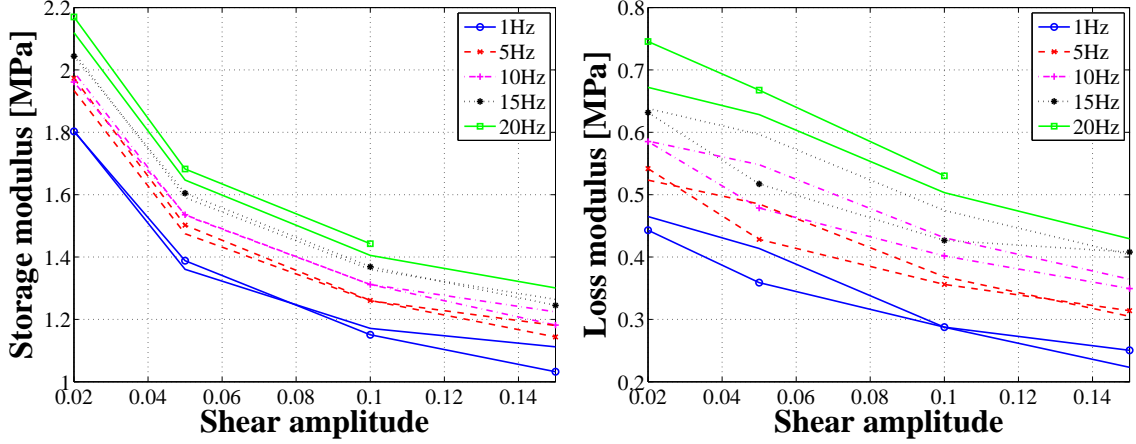


Figure 76: Storage and loss moduli fitting (average error: 0.0364108 MPa. With symbols: test data from [8]; without symbols: α -1 model fitting with three Maxwell elements

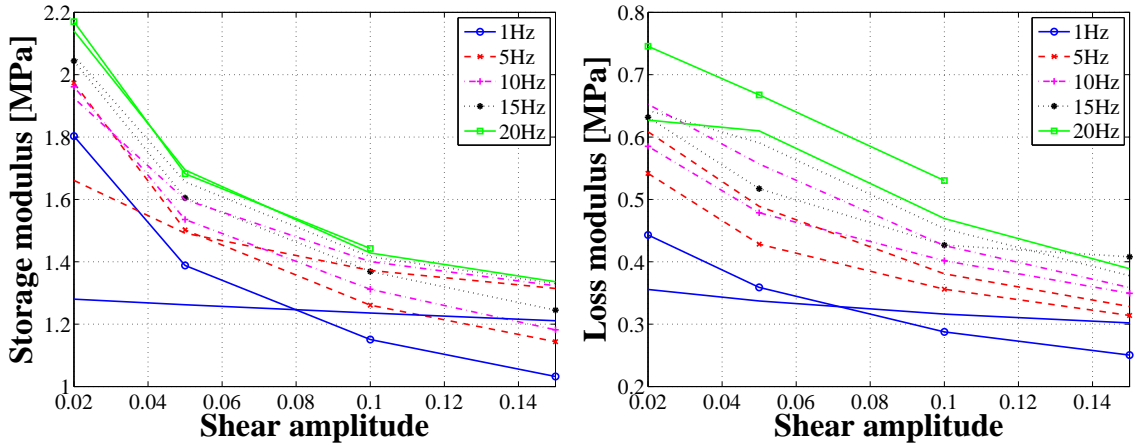


Figure 77: Storage and loss moduli fitting (average error: 0.122971 MPa). With symbols: test data from [8]; without symbols: α -0 model fitting with three Maxwell elements

These two equations can be solved for q ,

$$q = k \left(1 - e^{-t/\tau_q}\right) \quad \text{for } 0 \leq t \leq t_0; \quad (357a)$$

$$q = \left(e^{t_0/\tau_q} - 1\right) k e^{-t/\tau_q} \quad \text{for } t > t_0, \quad (357b)$$

where the initial condition $q(0) = 0$ and the continuity of q at $t = t_0$ were used. It can be seen that q increases from 0 to $q_0 = k \left(1 - e^{-t_0/\tau_q}\right)$ at $t = t_0$, and then decays exponentially with time constant τ_q . When the time is long enough, q becomes 0, which means the material is completely recovered. Note that the maximum value of q depends on and is equal to the strain rate k . This is different from the structural variable used in H-S model.

Substitution of Eqs. (357) into Eq. (354) leads to,

$$\dot{\tau}_v = c_v k - \frac{1+k-k\sum_{i=1}^L d_i e^{-t/\tau_{qi}}}{\tau_0} \tau_v \quad \text{for } 0 \leq t \leq t_0; \quad (358a)$$

$$\dot{\tau}_v = -\frac{1+k\sum_{i=1}^L d_i (e^{t_0/\tau_{qi}} - 1) e^{-t/\tau_{qi}}}{\tau_0} \tau_v \quad \text{for } t > t_0, \quad (358b)$$

where $\sum_{i=1}^L d_i = 1$ was used. The solution to Eq. (358a) can be written as, for $0 \leq t \leq t_0$,

$$\begin{aligned} \tau_v &= c_v k e^{-\int (1+k-k\sum_{i=1}^L d_i e^{-t/\tau_{qi}})/\tau_0 dt} \int_0^t e^{\int (1+k-k\sum_{i=1}^L d_i e^{-t_1/\tau_{qi}})/\tau_0 dt_1} dt_1 \\ &= c_v k e^{-[(1+k)t+k\sum_{i=1}^L d_i \tau_{qi} e^{-t/\tau_{qi}}]/\tau_0} \int_0^t e^{[(1+k)t_1+k\sum_{i=1}^L d_i \tau_{qi} e^{-t_1/\tau_{qi}}]/\tau_0} dt_1. \end{aligned} \quad (359)$$

The solution to Eq. (358b) can be written as, for $t > t_0$,

$$\begin{aligned} \tau_v &= \tau_{v0} e^{-\int_{t_0}^t [1+k\sum_{i=1}^L d_i (e^{t_0/\tau_{qi}} - 1) e^{-t_1/\tau_{qi}}]/\tau_0 dt_1} \\ &= \tau_{v0} e^{-[(t-t_0)-k\sum_{i=1}^L d_i \tau_{qi} (1-e^{-t_0/\tau_{qi}})](e^{-(t-t_0)/\tau_{qi}} - 1)}/\tau_0, \end{aligned} \quad (360)$$

where $\tau_{v0} = \tau_v(t_0)$ should be computed from Eq. (359).

Taking the derivative of the over-stress, Eq. (359), with respect to the strain, one can obtain the modulus of the α -0 model under ramp strain history as

$$\begin{aligned} G_v(t) &= \frac{d\tau_v}{d\gamma} = \frac{1}{k} \frac{d\tau_v}{dt} \\ &= c_v - \frac{c_v}{\tau_0} \left[(1+k) + k \sum_{i=1}^L d_i e^{-\frac{t}{\tau_{qi}}} \right] e^{-\frac{(1+k)t+k\sum_{i=1}^L d_i \tau_{qi} e^{-\frac{t}{\tau_{qi}}}}{\tau_0}} \int_0^t e^{\frac{(1+k)t_1+k\sum_{i=1}^L d_i \tau_{qi} e^{-\frac{t_1}{\tau_{qi}}}}{\tau_0}} dt_1. \end{aligned} \quad (361)$$

It is found that $G_v(0) = c_v$ for any strain rate, which means this α -0 model is not able to predict a rate-dependent initial modulus. However, this model may predict a rate-dependent or rate-independent terminal modulus by adjusting the material parameters.

Fig. 78 shows typical stress histories for α -0 model under relaxation tests. The stress increases with increasing of strain before the strain reaches γ_0 ; after that the stress decays.

12.3.4 Numerical simulations

The H-L model discussed above was implemented in *Mathematica* and several numerical simulations were performed to evaluate its capability to capture the typical experimental observations for elastomeric materials.

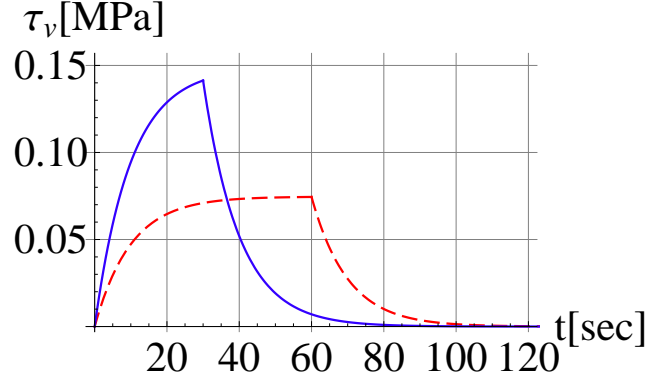


Figure 78: Typical stress histories for α -0 model under relaxation tests. Solid line: $k = 0.01 \text{ sec}^{-1}$ and $\gamma_0 = 0.30$; dashed line: $k = 0.005 \text{ sec}^{-1}$ and $\gamma_0 = 0.30$.

12.3.4.1 Relaxation tests

A set of relaxation tests were performed using step strains to determine the influence of the step size of the strain on the relaxation modulus, which is defined as relaxation stress divided by the magnitude of the step strain. The strain histories used for the relaxation tests are given by Eqs. (240) with $k = 0.05 \text{ sec}^{-1}$ and strain steps given by Eq. (310).

In the relaxation simulations, five Maxwell elements were used, three of them are α -1 model and two of them are α -0 model. For each α -0 model, three structural variable q 's were used and they are the same for all α -0 models. The parameters related to q are $d_{m1} = 0.7$, $d_{m2} = 0.15$, and $d_{m3} = 0.15$, and $\tau_{q1} = 10\tau_{q2} = 100\tau_{q3} = 0.111564 \text{ sec}$. The elastic modulus is $c_e = 0.551907 \text{ MPa}$ and the other material parameters are presented in Table 21.

Table 21: Assumed material parameters for H-L model

m	α_m	c_{vm} [MPa]	τ_{0m} [sec]	$\bar{\tau}_m$ [sec]
1	1.0	0.0490169	8.43262×10^{28}	8.46308×10^{30}
2	1.0	0.092102	0.00502916	0.0116266
3	1.0	0.0583368	0.154327	1.12503
4	0	0.06	0.927418	-
5	0	0.04	1039.28	-

The relaxation stress and relaxation modulus are illustrated in Fig. 79. In the left figure, a larger stress corresponds to larger strain; while in the right figure, a larger relaxation modulus corresponds to smaller strain step size, *i.e.*, the relaxation modulus decreases with the increasing of strain step size. This observation agrees with the experimental results

reported by [8]. Fig. 80 shows the relaxation stress and relaxation modulus for $\gamma_0 = 0.06$.

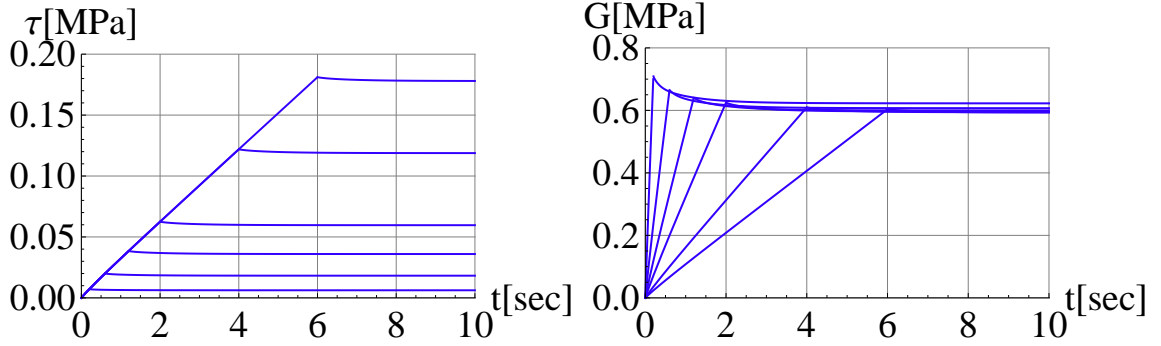


Figure 79: Relaxation test. Left: relaxation stress; right: relaxation modulus.

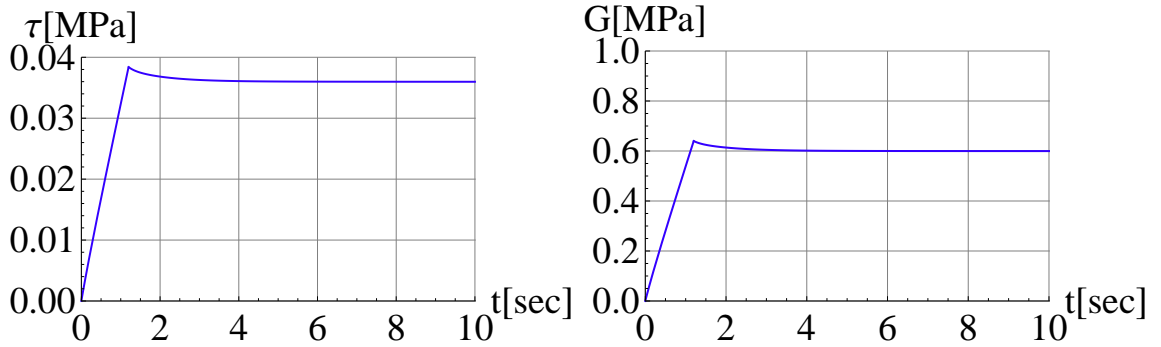


Figure 80: Relaxation test for $\gamma_0 = 0.06$. Left: relaxation stress; right: relaxation modulus.

12.3.4.2 Sinusoidal strain with increasing and decreasing amplitudes

Similar to Section 12.2.6.4, to check the reversibility of the dynamic modulus amplitude dependency, a sinusoidal strain with increasing and then decreasing amplitude was prescribed, as shown in Fig. 60, and the storage and loss moduli were computed from the stress response in the last period for each amplitude. The amplitudes are given by Eq. (342) for increasing region and then decreasing in the reverse order. The frequency for the sinusoidal strain is 3.0 Hz for every strain amplitude.

Fig. 81 presents the storage modulus of elastomeric materials with different recovery times τ_q under sinusoidal strain with increasing and decreasing amplitudes. In the figure, each curve with same symbol represents an increasing and decreasing sequence of the strain. The modulus in the amplitude decreasing sequence is always smaller than that for the same

strain amplitude in the increasing sequence. It can be seen from the figure that when the recovery time is short, the difference of the modulus for same strain amplitude in the increasing and decreasing sequences is small; however for case with long recovery time, this difference is quite significant.

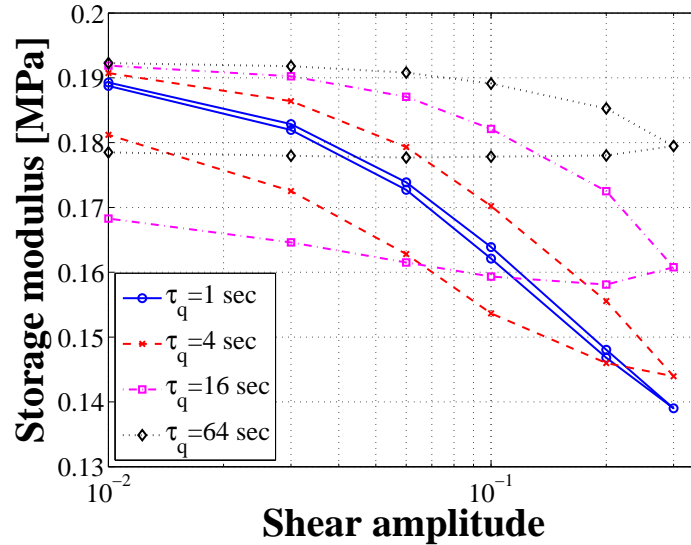


Figure 81: Storage modulus for different recovery times.

Fig. 81 was generated with 10-period simulation for each strain amplitude. The simulations were also run for 200 periods for each amplitude. In this case the curves for the amplitude decreasing and increasing sequences are identical. Hence, the difference of the modulus between increasing and decreasing amplitude sequences is related to the recovery time of the material damage and the simulation time. If the simulation time is long enough comparing with the recovery time, the difference will be negligible; otherwise, the difference will be significant.

Fig. 82 shows two typical histories for the structural variable q . It can be seen, from the right figure, that when the simulation lasts 200 periods for each amplitude, q is saturated at each strain amplitude no matter it is in the increasing or decreasing sequence. The saturated value for q in this case is the same for same strain amplitudes. This explains the fact that the modulus are same for same amplitudes. However, when the simulation lasts only 10 periods for each amplitude, it can be seen, from the left figure, that q was not saturated at all. This results in the difference between the modulus for strains with same

amplitude but in increasing and decreasing sequence.

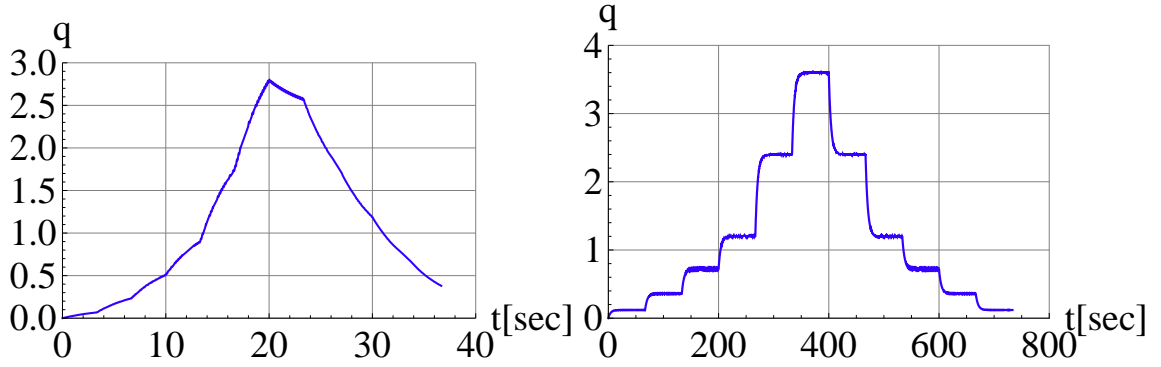


Figure 82: Time history for q : $f = 3$ Hz, $\tau_q = 4$ sec. Left: 10-period simulation for each amplitude; right: 200-period simulation for each amplitude.

Note that in this simulation only one α -1 model and one α -0 model were used to make simple the change of the recovery time τ_q . The parameters for the α -1 model are: $c_v = 0.08$ MPa, $\tau_0 = 50$ sec, and $\bar{\tau} = 50$ sec; and those related to the α -0 model are: $c_v = 0.08$ MPa and $\tau_0 = 0.1$ sec. Only one q was used for the α -0 model in the simulation with different recovery times τ_q as shown in Fig. 81. The elastic modulus is $c_e = 0.05$ MPa.

12.3.4.3 Effect of static strain offset on dynamic modulus

Similar simulations, as in Section 12.2.6.5, with strain history as shown in Fig. 64 were performed to study the effect of the static strain offset on the dynamic modulus. The frequency for the sinusoidal strain is 3 Hz; and the amplitudes are given by Eq. (342). The static strain offsets are chosen as 0.05, 0.10, 0.15, and 0.20, respectively. The material model is the same as used in Section 12.3.4.2.

The storage and loss moduli were computed for each of the amplitudes and demonstrated in Fig. 83. It is found that the effect of the static strain offset on both the storage and loss moduli is negligible for the offsets investigated. Note that for this H-L model, the effect of the strain offset on the storage modulus is much weaker than that for the H-S model as shown in Fig. 65. This is due to the fact that the stress-strain relationship for the elastic response in this H-L model is linear. As discussed in Section 12.2.6.5, the strain offset has no influence on the elastic modulus when the stress-strain relationship is linear.

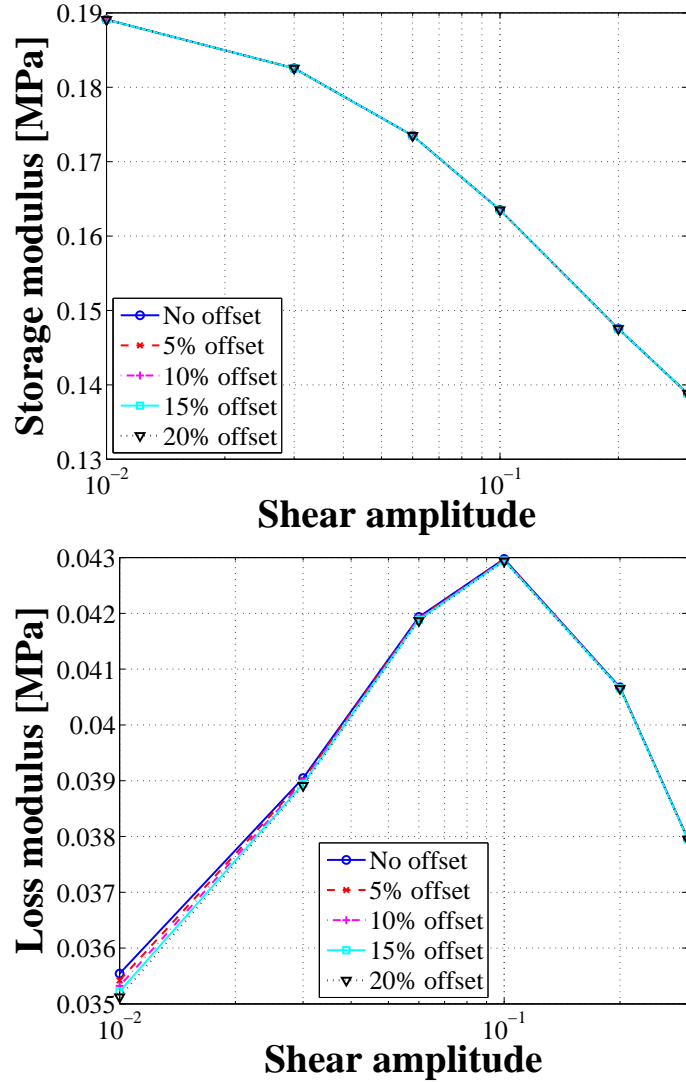


Figure 83: Effect of static strain offset on dynamic modulus.

Here again the waiting time between the application of the static strain offset and the starting of the second sequence of sinusoidal strains is not important as long as the sinusoidal strain lasts long enough for the saturation of structural variable q . The reason is that the structural variable q will saturate to its steady state when the sinusoidal strain is applied for enough time no matter q is recovered or not during the waiting time.

12.3.5 Summary on the evaluations of H-L model

From the analytical studies and numerical simulations in previous sections, some conclusions similar to those for H-S model in Section 12.2.7 may be made for the H-L model:

- The H-L model is capable of capturing the frequency and amplitude dependency of the storage and loss moduli.
- The predictions from H-L model under relaxation tests agree with the typical experimental observations for elastomeric materials under relaxation tests.
- Simulation results for sinusoidal strain with increasing and then decreasing amplitude showed that whether the strain amplitude is increasing or decreasing does not affect the storage and loss moduli of the material as long as the settling time is long enough for each amplitude. However, if the settling time is not long enough as compared to the recover time, the modulus for same amplitude in increasing and decreasing sequence is different.
- The static strain offset does not affect the storage and loss moduli.

The material parameters identification procedure for this H-L model would be easier than that for the H-S model since closed-form expressions for the stress history of H-L model under harmonic strain or relaxation test can be obtained. One can fit these expressions to the experimental data to identify the material parameters.

12.4 Summary

In this chapter two elastomeric material models, Haupt-Sedlan model and Höfer-Lion model, were thoroughly analyzed. The analysis was based on a simple shear deformation which is a deformation state close to the real work state of the lead-lad dampers involved in rotorcraft. From the studies, it can be found that both H-S and H-L models are capable of predicting some typical experimental observations for the elastomeric materials, and the predictions from these two models are quite similar.

The H-S model includes the necessary elements for modeling elastomeric materials, which are elastic, plastic, and viscous elements; hence, theoretically, it should be able to model the behavior of the elastomeric materials if the material parameters are well tuned. However, the equation governing the structural variable q is more difficult to solve analytically, even for very simple strain history, than the one for the H-L model.

The H-L model does not have a plastic element and the stress-strain relationship for the elastic response is linear. However, this drawback can be overcome by including one or more plastic elements in the H-L model and replacing the stress-strain relationship for the elastic response with a nonlinear one, which will improve the performance of the H-L model.

For the material parameters identification, two types of experimental tests, which are very common for the elastomeric material testing, are required. One is the ramp strain followed by a relaxation test, from which the stress history should be recorded from $t = 0$ to the time at which the change of stress is negligible. This relaxation test should be performed for different strain levels. Another type of test is the harmonic strain test, from which the storage and loss moduli should be measured or calculated for different strain amplitudes and frequencies.

Chapter XIII

CONCLUSIONS AND FUTURE WORK

13.1 Conclusions

To avoid the high maintenance costs associated with hydraulic dampers, industry has used elastomeric dampers that feature simpler mechanical design, lower part count, and result in “dry” rotors. However, the design of robust elastomeric dampers is hampered by a lack of reliable analytical tools that can be used to predict their damping behavior in the presence of the large multi-frequency nonlinear motion experienced by the rotor.

The present research has proposed a first-principles-based strategy for modeling the elastomeric dampers within the framework of multibody dynamics analysis. This modeling approach presents advantages as compared to the classical lumped-parameter device modeling approach.

- The geometric configuration of the damper is taken into account through finite element modeling.
- The elastomeric material behavior is represented by constitutive laws that are available in the literature.
- Although experimental testing is required for the identification of material parameters, the identified parameters can be used for dampers with different geometric configurations but made from the same elastomeric material.
- The damper behavior is predicted from material properties and geometric configuration. Thus, the modeling approach does not require the damper to exist; instead, it could be used to design dampers.
- The model can capture some fundamental properties/phenomena inherent in elastomeric materials by nature, for instance, the hysteresis loop and dual frequency effect.

- The damper model can be seamlessly integrated with finite element based multibody dynamics analysis codes.

The proposed first-principles-based damper modeling approach was integrated into the finite element method. First, a finite element tool was developed. This tool consists of a two-dimensional continuum finite element, meshing tool, numerical solver and elastic and elastomeric material models, and is capable of modeling plane strain, plane stress, and axisymmetric problems. After this finite element tool was validated, it was coupled with a finite element based multibody dynamics analysis code for the comprehensive simulation of a realistic helicopter rotor, the UH-60 utility helicopter. The results showed the feasibility of the overall coupling strategy that has been developed.

The elastomeric material model, and especially the proper modeling of material inelastic behavior, is key to the successful modeling of elastomeric dampers. In verifying the feasibility of the proposed road map, a simple material model for elastomeric materials was used, which is not capable of modeling the actual behavior of elastomeric dampers. Hence, different elastomeric material models available in literature were reviewed and material parameters identification procedures were developed based on experimental data from relaxation test and harmonic test.

In conclusion of this work, a validated, first-principles-based tool for the modeling of elastomeric devices is available. A strategy was developed for coupling this tool with finite element based multibody dynamics formulation for the comprehensive simulation of vehicles such as cars, trucks or helicopters.

13.2 Future work

The recommended future work for the present research is as follows.

1. **Evaluate additional elastomeric material models and compare their behavior with experimental data.** Due to the lack of experimental data for materials specifically used in the manufacturing of lead-lag dampers, the current evaluation of elastomeric material models did not compare material behavior with relevant experimental data. This comparison is important because various elastomers behave in

different manners, and it is unlikely that a single model will be appropriate for all materials. The final version of this first-principles-based damper modeling tool is likely to include various elastomeric material models, which can be selected by the user for optimal performance.

2. **Implement selected elastomeric models into finite element framework.**
3. **Correlate predictions from the developed model with experimental results.**
The predictions from the developed first-principles-based elastomeric damper model will be correlated with experimental data.
4. **Predict the behavior of realistic elastomeric dampers.** For actual elastomeric dampers used in industry, finite element models can be developed and their behavior investigated. The predictions from the finite element tool will be compared to experimental results.
5. **Predict the response of coupled multibody system with elastomeric components.** The developed finite element model of elastomeric components can be coupled with a comprehensive multibody dynamics code to predict the behavior of complex systems featuring elastomeric components, for example, rotorcraft with elastomeric lead-lag dampers. The predictions can then be compared with the actual rotorcraft flight test data.
6. **Tight coupling between the elastomeric model and the multibody dynamics code.** Develop a methodology for the simultaneous solution of the governing equations for the elastomeric components and multibody system.
7. **Perform parametric study of the effects of damper configurations and material properties on rotorcraft performance.**
8. **Investigate thermal effects on the behavior of elastomeric materials.** An important aspect of the elastomeric material behavior is the energy dissipation. It is well known that elastomeric materials will heat up when inelastic deformations are

imposed, and that the properties of elastomeric materials are temperature-dependent. Temperature changes will affect both the mechanical behavior and energy dissipation behavior of elastomeric materials. Thus, elastomeric material models that are capable of modeling the thermal effects should be developed.

Appendix A

STRAIN MEASURES IN A NONLINEAR CONTINUUM

A.1 Kinematics of the Problem

In the analysis of the deformation in the neighborhood of a material point in a solid, one considers the body in a *reference configuration*, and a Cartesian frame of reference \mathcal{I} defined by three mutually orthogonal unit vectors $\mathcal{I} = (\bar{i}_1, \bar{i}_2, \bar{i}_3)$; and a *deformed configuration* of the same solid as depicted in Fig. 84. Note that the following notational convention will be adopted: lower case symbols refer to entities defined in the reference configuration, whereas upper case symbols refer to the corresponding quantities in the deformed configuration.

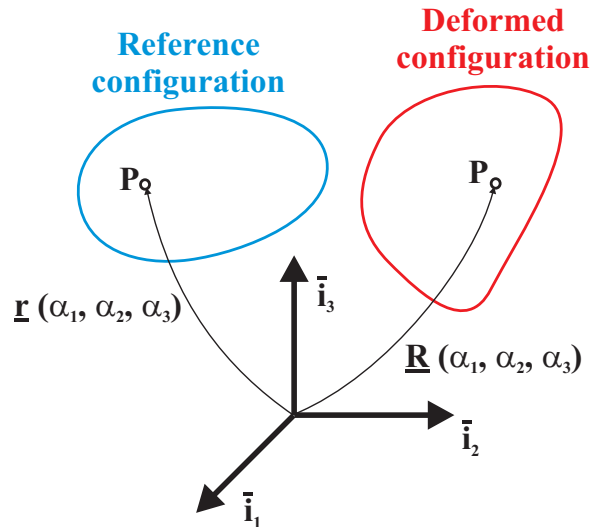


Figure 84: The reference and deformed configurations of a body.

Let \mathbf{P} be a material point in the body, and be identified by a label consisting of a triplet of real numbers, denoted $(\alpha_1, \alpha_2, \alpha_3)$. This label is called the *material coordinates* of point \mathbf{P} and will remain attached to the material particle throughout the deformation process. Let the position vector of point \mathbf{P} be \underline{r} , and \underline{R} , in the reference, and deformed configuration,

respectively,

$$\underline{r} = \underline{r}(\alpha_1, \alpha_2, \alpha_3), \quad (362)$$

$$\underline{R} = \underline{R}(\alpha_1, \alpha_2, \alpha_3).$$

Since the material coordinates are an identifying label for a material particle, they can be chosen arbitrarily. A convenient choice for the material coordinates consist of the components of the position vector in \mathcal{I} . This means

$$\underline{r}(\alpha_1, \alpha_2, \alpha_3) = \alpha_1 \bar{v}_1 + \alpha_2 \bar{v}_2 + \alpha_3 \bar{v}_3. \quad (363)$$

This particular choice of the material coordinates is called the *Lagrangian representation*.

A *material line* consists of a set of particles aligned with one of the coordinate directions at one point of the body, as depicted in Fig. 85. For a Cartesian reference frame

$$\underline{g}_i = \frac{\partial \underline{r}}{\partial \alpha_i} = \bar{v}_i. \quad (364)$$

As the deformation takes place, the material lines are convected with the body. The convected material lines are now curves in space intersecting at the new location of the particle. The base vectors in the deformed configuration are defined in a manner similar to those of the reference configuration

$$\underline{G}_i = \frac{\partial \underline{R}}{\partial \alpha_i}. \quad (365)$$

These base vectors are not mutually orthogonal, nor are they unit vectors.

The state of strain at a point of a body is a quantification of the deformation in the neighborhood of that point. Fig. 86 shows the neighborhood of point \mathbf{P} in the reference and deformed configurations. In the reference configuration, this neighborhood is described by a rectangular parallelepiped spanned by the vectors $\underline{g}_1 d\alpha_1$, $\underline{g}_2 d\alpha_2$, and $\underline{g}_3 d\alpha_3$. Increments in position vector are denoted $d\underline{r}$ and $d\underline{R}$ in the reference and deformed configurations, respectively, they writes

$$\begin{aligned} d\underline{r} &= \frac{\partial \underline{r}}{\partial \alpha_i} d\alpha_i = \underline{g}_i d\alpha_i; \\ d\underline{R} &= \frac{\partial \underline{R}}{\partial \alpha_i} d\alpha_i = \underline{G}_i d\alpha_i. \end{aligned} \quad (366)$$

The lengths of these increments, denoted ds and dS in the reference and deformed

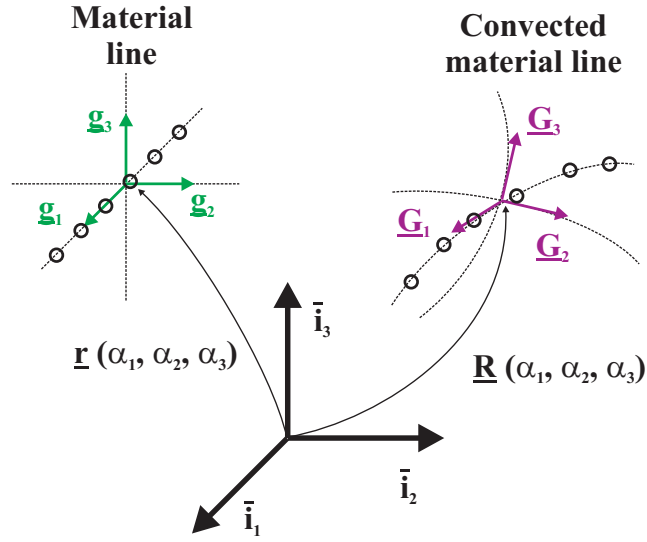


Figure 85: The base vectors in the reference and deformed configurations.

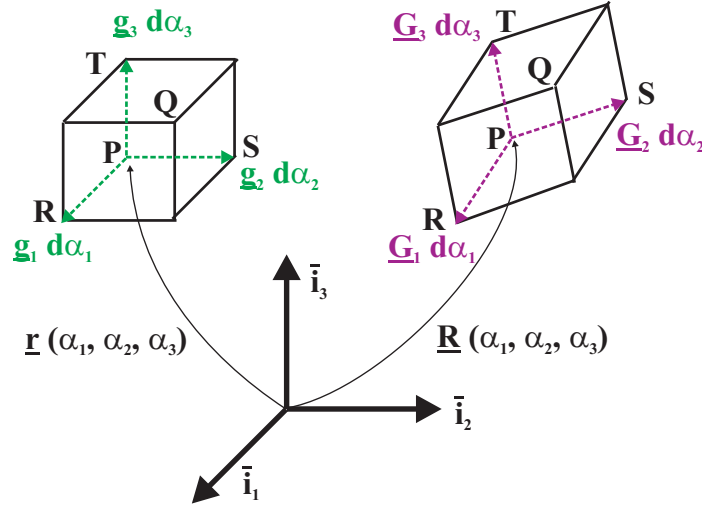


Figure 86: Volume elements in the reference and deformed configurations.

configurations, respectively, are readily found as

$$ds^2 = d\underline{r} \cdot d\underline{r} = \underline{g}_i \cdot \underline{g}_j d\alpha_i d\alpha_j = g_{ij} d\alpha_i d\alpha_j; \quad (367a)$$

$$dS^2 = d\underline{R} \cdot d\underline{R} = \underline{G}_i \cdot \underline{G}_j d\alpha_i d\alpha_j = G_{ij} d\alpha_i d\alpha_j. \quad (367b)$$

These relationships define the components of the metric tensor in the reference and deformed configurations, respectively, as

$$g_{ij} = \underline{g}_i \cdot \underline{g}_j, \quad (368a)$$

$$G_{ij} = \underline{G}_i \cdot \underline{G}_j. \quad (368b)$$

The symmetry of both tensors is apparent from these definitions.

A.2 Displacement Field

The difference between the positions of a material point in the deformed and reference configurations defines the *displacement vector* as

$$\underline{u}(\alpha_1, \alpha_2, \alpha_3) = \underline{R} - \underline{r}. \quad (369)$$

The displacement vector is now resolved along the base vectors of the reference configuration as

$$\underline{u} = u_i \underline{g}_i. \quad (370)$$

Similarly, the position vector in the deformed configuration is resolved as

$$\underline{R} = X_i \underline{g}_i. \quad (371)$$

With these definitions, Eq. (369) now writes

$$X_i = \alpha_i + u_i. \quad (372)$$

The base vector in the deformed configuration is related to the displacement field as

$$\underline{G}_i = \frac{\partial \underline{R}}{\partial \alpha_i} = \frac{\partial(\underline{r} + \underline{u})}{\partial \alpha_i} = \delta_{ij} \underline{g}_j + \frac{\partial(u_j \underline{g}_j)}{\partial \alpha_i}. \quad (373)$$

When using a Cartesian reference frame, the base vectors \underline{g}_j are constant vectors, and the following result is obtained

$$\underline{G}_i = (\delta_{ij} + u_{j,i}) \underline{g}_j, \quad (374)$$

where the notation $(\cdot)_{,i}$ indicates a derivative with respect to the material coordinate α_i .

A.3 Strain Measures

A.3.1 Deformation gradient tensor

A widely used strain measure is the *deformation gradient tensor* which is defined as

$$F_{ij} = \frac{\partial X_i}{\partial \alpha_j}. \quad (375)$$

Resolving the base vector in the deformed configuration Eq. (365) along the reference frame yields

$$\underline{G}_i = \frac{\partial \underline{R}}{\partial \alpha_i} = F_{ji} \underline{g}_j. \quad (376)$$

Dotting this relationship by \underline{g}_ℓ yields an alternative definition of the deformation gradient tensor

$$F_{ij} = \underline{g}_i \cdot \underline{G}_j. \quad (377)$$

With the help of the chain rule for derivatives, an explicit expression of the inverse of the deformation gradient tensor can be obtained

$$F_{ij}^{-1} = \frac{\partial \alpha_i}{\partial X_j}. \quad (378)$$

Introducing the displacement field, Eq. (372) into Eq. (375) yields the deformation gradient tensor in terms of the displacement field as

$$F_{ij} = \delta_{ij} + u_{i,j}. \quad (379)$$

The determinant of the deformation gradient tensor is defined as

$$J = \det F_{ij} = \det \left(\frac{\partial X_i}{\partial \alpha_j} \right). \quad (380)$$

This determinant can be interpreted as the determinant of the Jacobian of the coordinate transformation from the coordinates in the reference configuration α_i to those in the deformed configuration X_i .

A.3.2 Metric tensor

Relationship (367b) shows that the metric tensor G_{ij} can be used as a measure of the deformation. When used as strain measure, the metric tensor is also called the *Green deformation tensor*, or the *Cauchy-Green deformation tensor*.

The metric tensor in the deformed configuration is closely related to the deformation gradient tensor. Introducing Eq. (376) into the definition of the metric tensor, Eq. (368b) yields

$$G_{ij} = F_{ki} F_{kj}. \quad (381)$$

The determinant G of the metric tensor is related to that of the deformation gradient tensor

$$G = \det(G_{ij}) = \det(F_{ki}F_{kj}) = (\det F_{ij})^2 = J^2. \quad (382)$$

A.3.3 Green-Lagrange strain tensor

A widely used strain measure is the *Green-Lagrange strain tensor*, defined as

$$e_{ij} = \frac{1}{2}(G_{ij} - g_{ij}). \quad (383)$$

It is also called the *Lagrangian strain tensor*, or the *Green-Saint Venant strain tensor*.

The Green-Lagrange strain tensor is closely related to the deformation gradient tensor. Indeed, introducing Eq. (381) into Eq. (383) yields

$$e_{ij} = \frac{1}{2}(F_{ki}F_{kj} - g_{ij}). \quad (384)$$

The Green-Lagrange strain tensor is also closely related to the change in length of the increment of the position vector. Indeed, Eqs. (367a) and (367b) yield

$$\frac{1}{2}(dS^2 - ds^2) = \frac{1}{2}(G_{ij} - g_{ij}) d\alpha_i d\alpha_j = e_{ij} d\alpha_i d\alpha_j. \quad (385)$$

Finally, the Green-Lagrange strain tensor is readily expressed in terms of displacement by introducing Eq. (379) into Eq. (384) to find

$$e_{ij} = \frac{1}{2}(u_{i,j} + u_{j,i} + u_{k,i}u_{k,j}). \quad (386)$$

A.3.4 Almansi strain tensor

The *Almansi strain tensor* is introduced by considering once again the change of the increment of the position vector. Combining Eqs. (367a) and (367b) yields

$$\frac{1}{2}(dS^2 - ds^2) = \frac{1}{2} \left(\frac{\partial \underline{R}}{\partial X_i} \cdot \frac{\partial \underline{R}}{\partial X_j} - \frac{\partial \underline{r}}{\partial X_i} \cdot \frac{\partial \underline{r}}{\partial X_j} \right) dX_i dX_j. \quad (387)$$

Introducing Eqs. (371) and the inverse deformation gradient tensor, Eq. (378), this becomes

$$\begin{aligned} \frac{1}{2}(dS^2 - ds^2) &= \frac{1}{2} \left(\delta_{ij} - \frac{\partial \alpha_k}{\partial X_i} \frac{\partial \alpha_k}{\partial X_j} \right) dX_i dX_j \\ &= \frac{1}{2} \left(\delta_{ij} - X_{ki}^{-1} X_{kj}^{-1} \right) dX_i dX_j. \end{aligned} \quad (388)$$

The Almansi strain tensor is defined as

$$\epsilon_{ij} = \frac{1}{2} \left(\delta_{ij} - F_{ki}^{-1} F_{kj}^{-1} \right), \quad (389)$$

so that

$$\frac{1}{2} (dS^2 - ds^2) = \epsilon_{ij} dX_i dX_j. \quad (390)$$

The Almansi strain tensor is directly related to the Green-Lagrange strain tensor. Indeed, comparing Eqs. (385) and (390)

$$\begin{aligned} e_{ij} &= F_{ki} F_{lj} \epsilon_{kl}; \\ \epsilon_{ij} &= F_{ki}^{-1} F_{lj}^{-1} e_{kl}. \end{aligned} \quad (391)$$

The Almansi strain tensor can also be expressed in terms of displacements. Starting from Eq. (389), and introducing Eqs. (378) and (372) yields

$$\epsilon_{ij} = \frac{1}{2} \left(\delta_{ij} - \frac{\partial \alpha_k}{\partial X_i} \frac{\partial \alpha_k}{\partial X_j} \right) = \frac{1}{2} \left[\delta_{ij} - \frac{\partial (X^k - u_k)}{\partial X_i} \frac{\partial (X^k - u_k)}{\partial X_j} \right]. \quad (392)$$

After simplification, this becomes

$$\epsilon_{ij} = \frac{1}{2} \left(\frac{\partial u_i}{\partial X_j} + \frac{\partial u_j}{\partial X_i} - \frac{\partial u_k}{\partial X_i} \frac{\partial u_k}{\partial X_j} \right). \quad (393)$$

A.3.5 Volume dilatation

The previous sections has focused on the state of strain at a point of a three-dimensional solid. However, it is often useful to characterize the volume dilatation of a volume element. Consider the volume defined by vectors $\underline{g}_1 d\alpha_1$, $\underline{g}_2 d\alpha_2$, and $\underline{g}_3 d\alpha_3$ as shown in Fig. 86. The particles contained in that volume before deformation are located in the volume defined by vectors $\underline{G}_1 d\alpha_1$, $\underline{G}_2 d\alpha_2$, $\underline{G}_3 d\alpha_3$ after deformation. The volume dv in the reference configuration is found as

$$dv = \underline{g}_1 \cdot (\underline{g}_2 \times \underline{g}_3) d\alpha_1 d\alpha_2 d\alpha_3 = d\alpha_1 d\alpha_2 d\alpha_3. \quad (394)$$

The volume dV in the deformed configuration is

$$dV = \underline{G}_1 \cdot (\underline{G}_2 \times \underline{G}_3) d\alpha_1 d\alpha_2 d\alpha_3 = \sqrt{G} d\alpha_1 d\alpha_2 d\alpha_3 \quad (395)$$

The *volumetric strain*, or relative change in volume is now defined as

$$\Delta = \frac{dV - dv}{dv} = \sqrt{G} - 1 = J - 1. \quad (396)$$

The relationship between elements of volume in the reference and deformed configuration is found by comparing Eqs. (394) and (395)

$$dV = \sqrt{G} dv = J dv \quad (397)$$

The integral of a function f over the reference and deformed configuration of the body are related by the following formula

$$\int_V f(X^1, X^2, X^3) dV = \int_v f(\alpha_1, \alpha_2, \alpha_3) J dv. \quad (398)$$

A.3.6 Virtual strain components

When dealing with variational principles, extensive use will be made of the concept of virtual strains. Taking a variation of Eq. (385) yields

$$\delta \left[\frac{1}{2} (dS^2 - ds^2) \right] = \delta e_{ij} d\alpha_i d\alpha_j. \quad (399)$$

A similar result can be obtained in terms of the deformation gradient tensor. Starting from Eqs. (367a) and (367b) leads to

$$\delta \left[\frac{1}{2} (dS^2 - ds^2) \right] = \delta \left[\frac{1}{2} (d\underline{R} \cdot d\underline{R} - d\underline{r} \cdot d\underline{r}) \right] = \delta (dX_i) dX_i. \quad (400)$$

Recalling the definition, Eq. (375), of the deformation gradient tensor, this becomes

$$\delta \left[\frac{1}{2} (dS^2 - ds^2) \right] = \delta \left(\frac{\partial X_i}{\partial \alpha_j} \right) dX_i d\alpha_j = \delta X_{ij} dX_i d\alpha_j. \quad (401)$$

Finally, the variation of the Green-Lagrange strain tensor can be expressed in terms of the variation of the deformation gradient tensor. From Eq. (383) it follows that

$$\delta e_{ij} = \frac{1}{2} (\delta F_{pi} F_{pj} + \delta F_{pj} F_{pi}). \quad (402)$$

A.4 Decomposition of Deformation Gradient Tensor

A.4.1 Multiplicative spherical/deviatoric decomposition of deformation gradient tensor

In order to characterize volumetric and volume preserving deformations in the presence of large strains, the following multiplicative decomposition of the deformation gradient tensor is introduced

$$F_{ij} = \left(J^{\frac{1}{3}} \delta_{ik} \right) \left(J^{-\frac{1}{3}} F_{kj} \right). \quad (403)$$

The first factor represents the spherical part of the deformation gradient tensor

$$F_{ij}^{sph} = J^{\frac{1}{3}} \delta_{ij}, \quad (404)$$

and the second factor its deviatoric part

$$\bar{F}_{ij} = J^{-\frac{1}{3}} F_{ij}. \quad (405)$$

In view of Eq. (380), it is clear that

$$\det(\bar{F}_{ij}) = J^{-1} J = 1. \quad (406)$$

In other words, for Eq. (396), \hat{F}_{ij} corresponds to a constant volume deformation, or *isochoric deformation*. Of course, by construction

$$\det(F_{ij}^{sph}) = J. \quad (407)$$

The corresponding decomposition for the metric tensor is

$$G_{ij} = \left(J^{\frac{2}{3}} \delta_{ik} \right) \left(J^{-\frac{2}{3}} G_{kj} \right), \quad (408)$$

where the deviatoric part of the metric tensor is defined as

$$\bar{G}_{ij} = J^{-\frac{2}{3}} G_{ij}. \quad (409)$$

Here again it is clear that $\det(\bar{G}_{ij}) = 1$.

A.4.2 Polar decomposition of deformation gradient tensor

Consider the deformation gradient tensor F_{ij} . The polar decomposition theorem implies the following decompositions

$$F_{ij} = R_{ik} U_{kj} = U_{ik}^* R_{kj}, \quad (410)$$

where R_{ij} is an orthogonal (rotation) tensor, and U_{ij} and U_{ij}^* the *right*, and *left symmetric stretch tensors*, respectively. The physical interpretation of the polar decomposition theorem applied to the deformation gradient tensor is as follows. For the first decomposition in Eq. (410), the deformation gradient tensor is viewed as two successive operations: first a rigid body rotation (application of the rotation operator R_{ik}), then a stretching (application

of the right stretch tensor). For the second decomposition in Eq. (410), the deformation gradient tensor is again viewed as two successive operations: first a stretching (application of the left stretch tensor), then a rigid body rotation (application of the rotation operator R_{kj}). The following tensors are associated with the polar decomposition

$$\begin{aligned} G_{ij} &= F_{ki}F_{kj} = U_{ki}U_{kj}; \\ G_{ij}^* &= F_{ik}F_{jk} = U_{ik}^*U_{jk}^*. \end{aligned} \quad (411)$$

These tensor are called the *right* and *left Cauchy-Green deformation tensors*, respectively. The right Cauchy-Green deformation tensor was introduced earlier, and was simply called the Cauchy-Green deformation tensor, or metric tensor.

The Green-Lagrange strain tensor can also be expressed in terms of the right symmetric stretch tensor. Introducing Eq. (411) into Eq. (384) yields

$$e_{ij} = \frac{1}{2}(U_{ki}U_{kj} - g_{ij}). \quad (412)$$

This important result shows that the Green-Lagrange strain measure is a measure of the sole deformation and is not affected by a rigid body rotation. This contrasts with the deformation gradient tensor which includes effects of both deformation and rigid body motions, as evident from Eq. (410).

The spectral decomposition of the right and left Cauchy-Green deformation tensors is readily obtained

$$\begin{aligned} G_{ij} &= \sum_k \lambda_{(k)}^2 P_{ik}P_{jk}; \\ G_{ij}^* &= \sum_k \lambda_{(k)}^2 P_{ik}^*P_{jk}^*; \end{aligned} \quad (413)$$

where the $\lambda_{(k)}^2$ are the eigenvalues of the metric tensor; and P_{ij} and P_{ij}^* store the eigenvector of G_{ij} , and G_{ij}^* , respectively. Additional results obtained from the polar decomposition theorem are

$$U_{ij} = \sum_k \lambda_{(k)} P_{ik}P_{jk}; \quad U_{ij}^* = \sum_k \lambda_{(k)} P_{ik}^*P_{jk}^*; \quad (414)$$

$$F_{ij} = \sum_k \lambda_{(k)} P_{ik}^*P_{jk}^*; \quad F_{ik}P_{kj} = \sum_k \lambda_{(j)} P_{ij}^*. \quad (415)$$

A.5 Principal Stretches

The eigenvalues of the metric tensor are the solution of

$$\det (G_{ij} - \lambda^2 \delta_{ij}) = 0. \quad (416)$$

Expanding the determinant yields

$$\lambda^6 - I_1 \lambda^4 + I_2 \lambda^2 - I_3 = 0, \quad (417)$$

where I_1 , I_2 , and I_3 are the invariants of the metric tensor defined as

$$\begin{aligned} I_1 &= G_{ii} &&= \lambda_{(1)}^2 + \lambda_{(2)}^2 + \lambda_{(3)}^2, \\ I_2 &= \frac{1}{2} (G_{ii} G_{jj} - G_{ij} G_{ij}) &&= \lambda_{(2)}^2 \lambda_{(3)}^2 + \lambda_{(1)}^2 \lambda_{(3)}^2 + \lambda_{(1)}^2 \lambda_{(2)}^2, \\ I_3 &= \det(G_{ij}) &&= \lambda_{(1)}^2 \lambda_{(2)}^2 \lambda_{(3)}^2. \end{aligned} \quad (418)$$

The eigenvalues $\lambda_{(k)}^2$ of the metric tensor are called the *principal stretches*. They can be viewed as just another measure of the straining at a point. Note that the principal stretches are not a complete measure of the state of strain at a point until the directions of the corresponding eigenvectors are also known.

The deviatoric principal stretches $\bar{\lambda}_{(k)}^2$ are defined as the eigenvalues of the deviatoric metric tensor \bar{G}_{ij} , eq. (409), *i.e.*

$$\det (\bar{G}_{ij} - \bar{\lambda}^2 \delta_{ij}) = 0. \quad (419)$$

It is clear from this definition that the deviatoric principal stretches are related to the principal stretches simply as

$$\bar{\lambda}_{(k)} = J^{-\frac{1}{3}} \lambda_{(k)}. \quad (420)$$

The invariants of the deviatoric metric tensor are readily related to the invariants of the metric tensor and evaluated as

$$\bar{I}_1 = I_3^{-1/3} I_1, \quad (421a)$$

$$\bar{I}_2 = I_3^{-2/3} I_2, \quad (421b)$$

$$\bar{I}_3 = 1. \quad (421c)$$

Appendix B

STRESS MEASURES IN A CONTINUUM MEDIUM

B.1 Stress Vector per Unit Area of Deformed Configuration

The state of stress in a solid can be visualized by cutting the body in the deformed configuration by a plane. The effect of the removed portion of the body is represented by forces acting on the remaining portion. Fig. 87 shows the reference and deformed configurations of the body, and the plane cutting the deformed body. The outer normal to this plane is denoted \underline{N} . Consider now a small element of area dA_n located in this plane, at point \mathbf{P} . Let \underline{F}_n be the *force vector* acting on that small element at point \mathbf{P} . The *stress vector* $\underline{\tau}_n$ acting at that point is defined as

$$\underline{\tau}_n = \lim_{dA_n \rightarrow 0} \left(\frac{\underline{F}_n}{dA_n} \right). \quad (422)$$

The existence of the stress vector, *i.e.* the existence of the limit in Eq. (422) is a fundamental assumption of continuum mechanics. The total force acting on a differential element of area dA_n is

$$\underline{F}_n = dA_n \underline{\tau}_n. \quad (423)$$

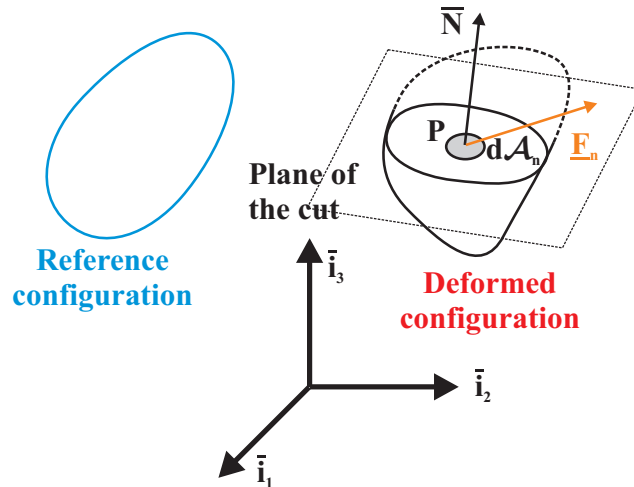


Figure 87: A body in the reference and deformed configurations.

Of course, the force and stress vectors acting on a differential element of area depend on the orientation of that element. In fact, an oriented differential element of area can be defined as

$$d\underline{\mathcal{A}}_n = d\mathcal{A}_n \underline{N}, \quad (424)$$

where \underline{N} is the normal to the differential element. Let \underline{F}_1 , \underline{F}_2 , and \underline{F}_3 be the force vectors obtained by cutting the body by three planes aligned the Cartesian reference frame \bar{v}_1 , \bar{v}_2 , and \bar{v}_3 , and $\underline{\tau}_1$, $\underline{\tau}_2$, and $\underline{\tau}_3$ be the corresponding stress vectors. Fig. 88 shows a tetrahedron with three forces oriented normal to the reference frame, and the fourth face with an outer normal \underline{N} .

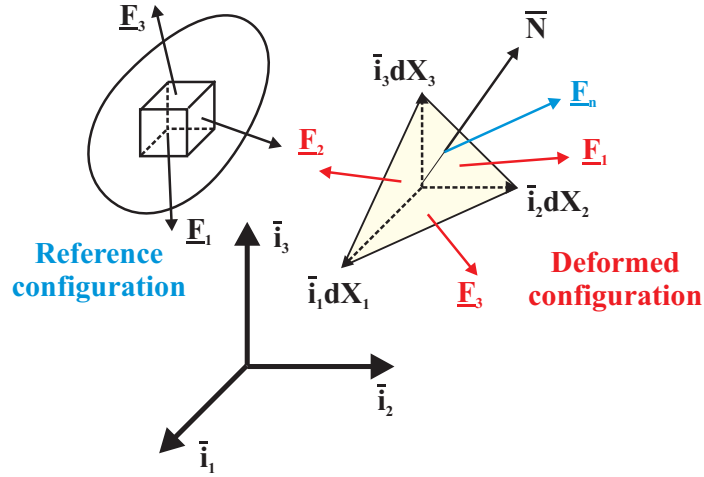


Figure 88: A differential element of volume in the deformed configuration

Three sides of the tetrahedron, denoted **PR**, **PS**, and **PT** are parallel to the reference frame axes, and are of length dX_1 , dX_2 , and dX_3 , respectively. These correspond to increments in the position vector of the deformed configuration defined in Eq. (371). The equilibrium condition for the forces acting on the tetrahedron writes

$$\underline{\tau}_n d\mathcal{A}_n - \frac{1}{2}dX_2dX_3 \underline{\tau}_1 - \frac{1}{2}dX_1dX_3 \underline{\tau}_2 - \frac{1}{2}dX_1dX_2 \underline{\tau}_3 = 0. \quad (425)$$

Let the components of the outer normal \underline{N} in the Cartesian reference frame be

$$\underline{N} = \mathcal{N}_i \underline{g}_i. \quad (426)$$

It is then clear that

$$\begin{aligned}\mathcal{N}_1 &= \frac{1}{2} \frac{dX_2 dX_3}{d\mathcal{A}_n}; \\ \mathcal{N}_2 &= \frac{1}{2} \frac{dX_1 dX_3}{d\mathcal{A}_n}; \\ \mathcal{N}_3 &= \frac{1}{2} \frac{dX_1 dX_2}{d\mathcal{A}_n}.\end{aligned}\tag{427}$$

The equilibrium equation (425) now simply writes

$$\underline{\tau}_n = \mathcal{N}_i \underline{\tau}_i.\tag{428}$$

This important result shows that the stress vector $\underline{\tau}_n$ acting on a differential element of area with an arbitrary orientation \underline{N} can be evaluated once the stress vectors $\underline{\tau}_i$ are known.

In other words, the stress vectors $\underline{\tau}_i$ fully define the state of stress at a point.

B.2 Cauchy stress tensor

Since the stress vectors $\underline{\tau}_i$ fully define the state of stress at a point, they are used to define a stress tensor τ_{ij}

$$\underline{\tau}_i = \tau_{ij} \underline{g}_j,\tag{429}$$

where the τ_{ij} are the covariant components of the *Cauchy stress tensor*. Fig. 89 shows the geometric interpretation of the Cauchy stress components in a two dimensional case.

The stress components τ_{11} , τ_{22} , and τ_{33} can be interpreted as direct stresses, whereas the components τ_{12} , τ_{13} , etc. are shearing stresses.

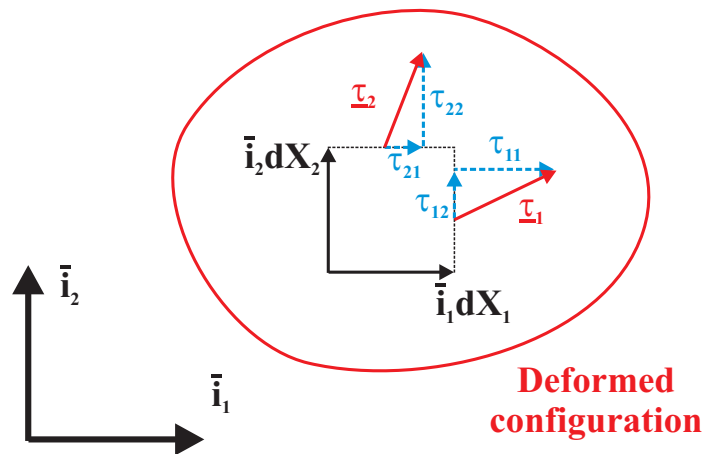


Figure 89: The Cauchy stress components in a two dimensional case.

The tensorial nature of the Cauchy stress tensor must be proven. This can be achieved by studying its transformation law for its components under a change of coordinates. Since the stress vector is a vector, Eq. (428) can be written as

$$\underline{\tau}_n = \mathcal{N}_i \underline{\tau}_i = \bar{\mathcal{N}}_i \bar{\underline{\tau}}_i. \quad (430)$$

Using the transformation law for the contra-variant components of the outer normal vector \underline{N} , and introducing the definition (429) of the Cauchy stress yields

$$\mathcal{N}_i \tau_{ij} \underline{g}_j = \frac{\partial \alpha_k}{\partial \bar{\alpha}_i} \mathcal{N}_k \bar{\tau}_{il} \bar{\underline{g}}_l = \frac{\partial \alpha_k}{\partial \bar{\alpha}_i} \frac{\partial \alpha_m}{\partial \bar{\alpha}_l} \mathcal{N}_k \bar{\tau}_{il} \underline{g}_m, \quad (431)$$

where the transformation law for the base vector was used. Dotting by \underline{g}_p yields

$$\mathcal{N}_i \tau_{ip} = \frac{\partial \alpha_k}{\partial \bar{\alpha}_i} \frac{\partial \alpha_p}{\partial \bar{\alpha}_l} \mathcal{N}_k \bar{\tau}_{il}. \quad (432)$$

This relationship must hold for any orientation of the outer normal \underline{N} . In particular, one can choose $\mathcal{N}_i = (1, 0, 0)$, or $\mathcal{N}_i = (0, 1, 0)$, or finally $\mathcal{N}_i = (0, 0, 1)$. Combining the results then leads to

$$\tau_{ij} = \frac{\partial \alpha_i}{\partial \bar{\alpha}_k} \frac{\partial \alpha_j}{\partial \bar{\alpha}_l} \bar{\tau}_{kl}. \quad (433)$$

This transformation law proves the tensorial nature of the Cauchy stress tensor.

The Cauchy stress tensor, sometimes called the *true stress tensor*, fully characterizes the stress state at a point. However, its use in finite deformation theory of elasticity is not convenient. Indeed, the stress vectors $\underline{\tau}_i$ act on a differential element of volume $\underline{g}_1 dX_1, \underline{g}_2 dX_2, \underline{g}_3 dX_3$ which location is unknown since the determination of the deformed configuration of the body is goal of the theory. In particular, the material particles located in the differential element of volume $\underline{g}_1 dX_1, \underline{g}_2 dX_2, \underline{g}_3 dX_3$ occupied an unknown volume of the reference configuration.

To overcome this problem, it is necessary to determine the stress acting on a differential element of volume of the deformed configuration which had a specified location in the reference configuration.

B.3 Stress Vector per Unit Area of Reference Configuration

The stress vector per unit area of the reference configuration is defined as

$$\underline{\sigma}_n = \lim_{d\mathcal{A}_n \rightarrow 0} \left(\frac{\underline{F}_n}{d\mathcal{A}_n} \right). \quad (434)$$

Here again, the existence of the stress vector per unit area of the reference configuration is a basic assumption of continuum mechanics. This definition of the stress vector is similar to that given in section B.1 but leads to a different way of visualizing the stress state, as depicted in Fig. 90. Here the reference configuration of a body has been cut by a plane normal to \underline{N} . A differential element of area $d\mathcal{A}_n$ at a point P is considered. All the material particles within this differential element are convected to the differential element of area $d\mathcal{A}_n$ of the deformed configuration. Note that due to the deformation of the body, the differential element of area $d\mathcal{A}_n$ is not normal to \underline{N} but rather to \underline{N} . The total force acting on the differential element $d\mathcal{A}_n$ of the deformed configuration is

$$\underline{F}_n = d\mathcal{A}_n \underline{\sigma}_n. \quad (435)$$

Let da_1 be the differential element of area of the reference configuration defined by vectors $\underline{g}_2 d\alpha_2$ and $\underline{g}_3 d\alpha_3$. In the deformed configuration, this element becomes $d\mathcal{A}_1$ and is defined by vectors $\underline{G}_2 d\alpha_2$ and $\underline{G}_3 d\alpha_3$. The stress vector $\underline{\sigma}_1$ is defined to act on this differential element. The stress vectors $\underline{\sigma}_2$ and $\underline{\sigma}_3$ can be defined in a similar manner.

B.3.1 Relationships between normals in reference and deformed configurations

It will be important to relate the stress vector per unit area of the deformed configuration as described in section B.1 with the stress vector per unit area of the reference configuration. To that effect, it is necessary to relate elements of area in both configuration as well as the orientation of the normal to both elements. Consider a tetrahedron defined by three faces oriented along the Cartesian reference frame, and a fourth face with an \underline{N} , as depicted in Fig. 91. In the reference configuration the area $d\mathcal{A}_n$ of the face RST is

$$2d\mathcal{A}_n \underline{N} = \mathbf{RS} \times \mathbf{RT}. \quad (436)$$

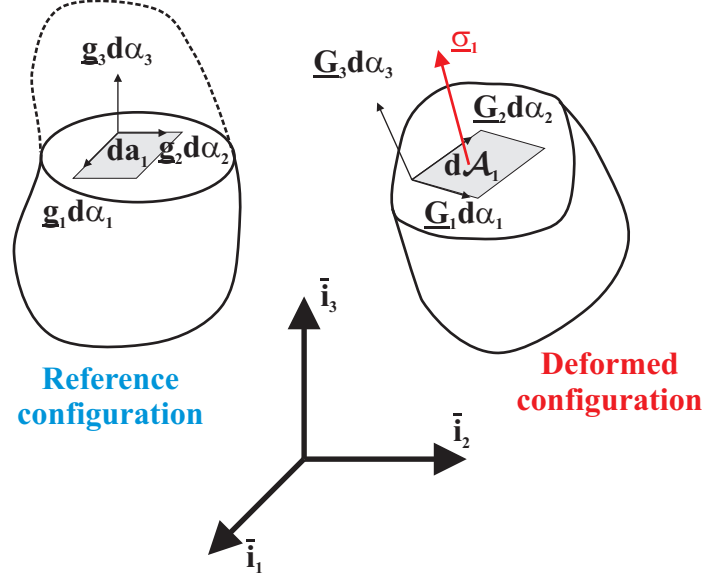


Figure 90: The stress vector per unit area of the reference configuration acting on a convected element of area.

Expressing \mathbf{RS} and \mathbf{RT} in terms of the base vectors yields

$$2d\mathcal{A}_n \underline{N} = (\underline{g}_2 d\alpha_2 - \underline{g}_1 d\alpha_1) \times (\underline{g}_3 d\alpha_3 - \underline{g}_1 d\alpha_1) = da_i \underline{g}_i. \quad (437)$$

Dotting this result by \underline{g}_i yields

$$da_i = 2(\underline{N} \cdot \underline{g}_i) d\mathcal{A}_n. \quad (438)$$

Finally, the contra-variant components of the outer normal are defined by $\underline{N} = n_i \underline{g}_i$, and Eq. (438) becomes

$$da_i = 2n_i d\mathcal{A}_n \quad (439)$$

All the material particles contained in the tetrahedron $\underline{g}_1 d\alpha_1, \underline{g}_2 d\alpha_2, \underline{g}_3 d\alpha_3$ in the reference configuration are contained in the tetrahedron $\underline{G}_1 d\alpha_1, \underline{G}_2 d\alpha_2, \underline{G}_3 d\alpha_3$ in the deformed configuration. In this deformed configuration the area $d\mathcal{A}_n$ of the face \mathbf{RST} is

$$2d\mathcal{A}_n \underline{N} = \mathbf{RS} \times \mathbf{RT}. \quad (440)$$

Proceeding as before leads to

$$2d\mathcal{A}_n \underline{N} = (\underline{G}_2 d\alpha_2 - \underline{G}_1 d\alpha_1) \times (\underline{G}_3 d\alpha_3 - \underline{G}_1 d\alpha_1) = \sqrt{G} da_i \underline{g}_i. \quad (441)$$

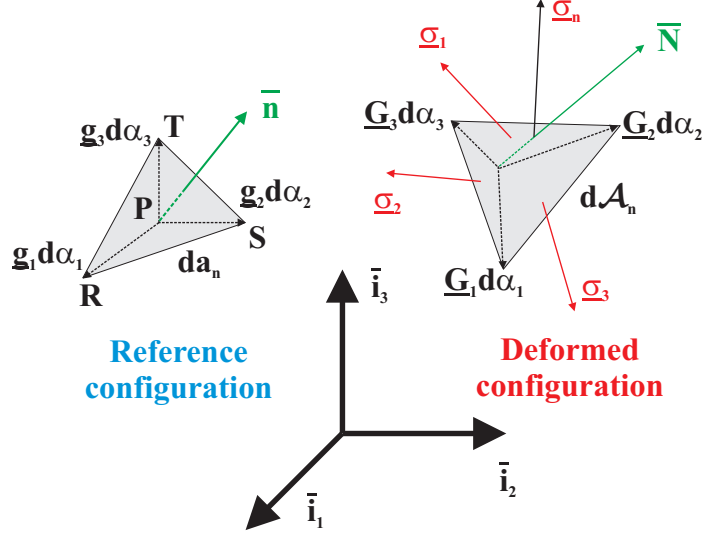


Figure 91: The tetrahedron in the reference and deformed configurations

Dotting this result by \underline{G}_j leads to

$$\sqrt{G} da_i = 2(\underline{N} \cdot \underline{G}_i) d\mathcal{A}_n. \quad (442)$$

Finally, using the relation of the elements of area in the reference and deformed configuration

$$dA_i = \sqrt{GG^{ii}} da_i, \quad \text{no sum on } i \quad (443)$$

yields

$$\frac{dA_i}{\sqrt{G^{ii}}} = 2(\underline{N} \cdot \underline{G}_i) d\mathcal{A}_n, \quad \text{no sum on } i. \quad (444)$$

Here again, the contra-variant components of the outer normal in the deformed configuration $\underline{N} = N_i \underline{g}_i$ are defined, and (444) becomes

$$\frac{dA_i}{\sqrt{G^{ii}}} = 2N_i d\mathcal{A}_n, \quad \text{no sum on } i. \quad (445)$$

The components of the outer normal in the reference and deformed configuration can be related by comparing Eqs. (439) and (442) to find

$$d\mathcal{A}_n N_i = \sqrt{G} d\mathcal{A}_n n_i. \quad (446)$$

The Cartesian components of the outer normal in the deformed configuration were defined in Eq. (426). It can be readily shown that

$$\begin{aligned} N_i &= F_{ki} \mathcal{N}_k; \\ \mathcal{N}_i &= F_{ki}^{-1} N_k. \end{aligned} \quad (447)$$

so that Eq. (446) becomes

$$d\mathcal{A}_n \mathcal{N}_i = \sqrt{G} F_{ki}^{-1} d\mathcal{A}_n n_k. \quad (448)$$

This formula is known as *Nanson's formula*.

B.3.2 Equilibrium equations

Equilibrium of the differential element of volume **PRST** of the deformed configuration depicted in Fig. 91 requires the forces to sum up to zero, *i.e.*

$$\underline{\sigma}_n d\mathcal{A}_n - \underline{\sigma}_i \frac{da_i}{2} = 0. \quad (449)$$

Introducing (439) then yields

$$\underline{\sigma}_n = n_i \underline{\sigma}_i \quad (450)$$

This important relationship relates the stress vector acting on a face with an arbitrary orientation to the stress vector $\underline{\sigma}_i$. Clearly, the knowledge of stress vectors $\underline{\sigma}_1$, $\underline{\sigma}_2$, and $\underline{\sigma}_3$ allows the computation of the stress vector $\underline{\sigma}_n$ acting on a differential element of arbitrary orientation at that point.

Relationship (450) is very similar to Eq. (428). However, important differences exist. First, both $\underline{\tau}_n$ and $\underline{\sigma}_n$ are stress vectors acting on a face with an arbitrary orientation, but $\underline{\tau}_n$ is the stress vector per unit area of the deformed configuration, whereas $\underline{\sigma}_n$ is the stress vector per unit area of the reference configuration. Second, the stress vectors $\underline{\tau}_i$ act in the deformed configuration on faces normal to the axes \bar{v}_i of the Cartesian reference frame, whereas the stress vectors $\underline{\sigma}_i$ act in the deformed configuration on faces that were normal to the Cartesian reference frame in the reference configuration. Finally, both $\underline{\tau}_n$ and $\underline{\sigma}_n$ act on a face with the same orientation, but \mathcal{N}_i are the components of the outer normal in the deformed configuration expressed in the Cartesian reference frame, whereas n_i are the components of the outer normal in the reference configuration expressed in the Cartesian reference frame.

B.4 The 1st Piola-Kirchhoff stress tensor

The stress vectors $\underline{\sigma}_i$ can be used to define a stress tensor s_{ij}

$$\underline{\sigma}_i = s_{ij} \underline{g}_j, \quad (451)$$

where the s_{ij} are the components of the *1st Piola-Kirchhoff stress tensor*. Fig. 92 shows the geometric interpretation of these stress components for a two dimensional situation.

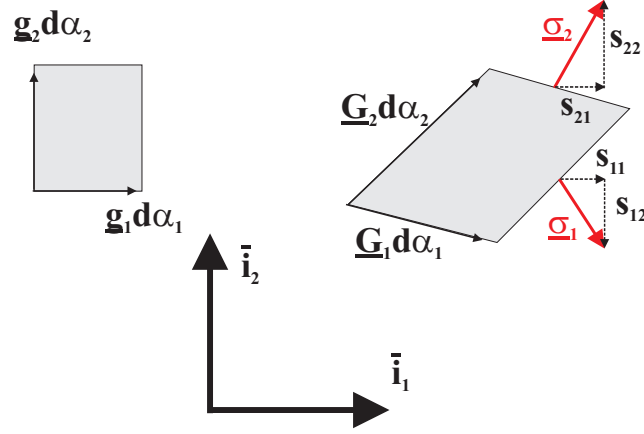


Figure 92: The 1st Piola-Kirchhoff stress components in a two dimensional case.

Note that the s_{ij} are the components of the stress vector per unit area of the reference configuration, resolved along the axes \underline{g}_1 , \underline{g}_2 , and \underline{g}_3 . The stress components s_{11} or s_{22} are not normal to the faces on which they act, and the stress components s_{12} and s_{21} cannot be interpreted as shearing stresses.

It is important to prove that the 1st Piola-Kirchhoff stress tensor is indeed a tensor. To study the transformation law of its components under a change of coordinate, it is noted that (450) writes

$$\underline{\sigma}_n = n_i \underline{\sigma}_i = \bar{n}_i \bar{\underline{\sigma}}_i. \quad (452)$$

Introducing the definition (451) of the 1st Piola-Kirchhoff stress tensor yields

$$n_i s_{il} \underline{g}_l = \frac{\partial \alpha_k}{\partial \bar{\alpha}_i} n_k \bar{s}^{im} \bar{\underline{g}}_m = \frac{\partial \alpha_k}{\partial \bar{\alpha}_i} \frac{\partial \alpha_p}{\partial \bar{\alpha}_m} n_k \bar{s}^{im} \underline{g}_p. \quad (453)$$

Dotting this result by \underline{g}_q results in

$$n_i s_{iq} = \frac{\partial \alpha_k}{\partial \bar{\alpha}_i} \frac{\partial \alpha_q}{\partial \bar{\alpha}_m} n_k \bar{s}^{im}. \quad (454)$$

This relationship must hold for any orientation of the outer normal. In particular, one can choose $n_i = (1, 0, 0)$, or $n_i = (0, 1, 0)$, or $n_i = (0, 0, 1)$. Combining these results then leads to

$$s_{ij} = \frac{\partial \alpha_i}{\partial \bar{\alpha}_k} \frac{\partial \alpha_j}{\partial \bar{\alpha}_l} \bar{s}^{kl}, \quad (455)$$

which proves the tensorial nature of the 1st Piola-Kirchhoff stress tensor.

B.5 The 2nd Piola-Kirchhoff stress tensor

The stress vectors $\underline{\sigma}_i$ can be resolved in an alternate manner, namely

$$\underline{\sigma}_i = \sigma_{ij} \underline{G}_j, \quad (456)$$

where the σ_{ij} define the components of the *2nd Piola-Kirchhoff stress tensor*. Fig. 93 shows the geometric interpretation of these stress components for a two dimensional situation.

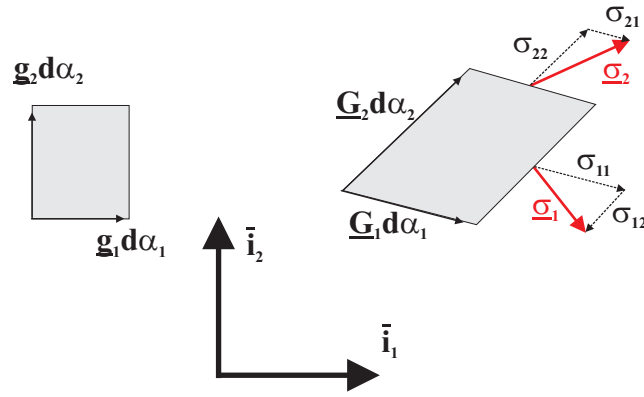


Figure 93: The 2nd Piola-Kirchhoff stress components in a two dimensional case.

Note that the σ_{ij} are the components of the stress vector per unit area of the reference configuration, resolved in the base vectors \underline{G}_1 , \underline{G}_2 , and \underline{G}_3 of the deformed configuration. The 2nd Piola-Kirchhoff contra-variant stress component are the contra-variant component of a vector resolved in a skew coordinate system, as the \underline{G}_i are neither unit vectors, nor mutually orthogonal.

Fig. 92 and 93 show that the Piola-Kirchhoff stress components are not as simple to interpret as the Cauchy stress components depicted in figure 89. For that reason, the Piola-Kirchhoff stress components are sometimes called “*pseudo*” stresses, or “*generalized*” stresses. It should be noted, however, that all three stress measures fully characterize the state of stress at a point.

Here again, it is important to establish the tensorial nature of the 2nd Piola-Kirchhoff stress tensor. Introducing the definition (456) of the 2nd Piola-Kirchhoff stress into Eq. (452)

yields

$$n_i \sigma_{il} \underline{G}_l = \frac{\partial \alpha_k}{\partial \bar{\alpha}_i} n_k \bar{\sigma}_{im} \underline{\bar{g}}_m = \frac{\partial \alpha_k}{\partial \bar{\alpha}_i} \frac{\partial \alpha_p}{\partial \bar{\alpha}_m} n_k \bar{\sigma}_{im} \underline{G}_p. \quad (457)$$

Dotting this result by \underline{g}_q yields

$$n_i \sigma_{iq} = \frac{\partial \alpha_k}{\partial \bar{\alpha}_i} \frac{\partial \alpha_q}{\partial \bar{\alpha}_m} n_k \bar{\sigma}_{im}. \quad (458)$$

Here again the orientation of the normal is arbitrary, hence

$$\sigma_{ij} = \frac{\partial \alpha_i}{\partial \bar{\alpha}_k} \frac{\partial \alpha_j}{\partial \bar{\alpha}_l} \bar{\sigma}_{kl}. \quad (459)$$

which proves the tensorial nature of the 2nd Piola-Kirchhoff stress tensor.

Finally, the 1st and 2nd Piola-Kirchhoff stress tensor can be readily related to each other. Indeed, comparing Eqs. (451) and (456) leads to

$$\begin{aligned} s_{ij} &= F_{jk} \sigma_{ik}; \\ \sigma_{ij} &= F_{jk}^{-1} s_{ik}. \end{aligned} \quad (460)$$

B.6 Relationship Between Cauchy and Piola-Kirchhoff stress tensors

Both Cauchy and Piola-Kirchhoff stress tensors fully define the state of stress at a point, and should, therefore, be closely related to each other. Consider the tetrahedron of Fig. 91. The face **RST** is a face with an arbitrary orientation, and the force acting in this face can be written $d\mathcal{A}_n \underline{\tau}_n$. As a result, the equilibrium equation for this tetrahedron writes

$$d\mathcal{A}_n \underline{\tau}_n - \frac{da_i}{2} \underline{\sigma}_i = 0. \quad (461)$$

Introducing Eq. (442) then yields

$$\underline{\tau}_n = \frac{1}{\sqrt{G}} N_i \underline{\sigma}_i. \quad (462)$$

Expressing the outer normal in the Cartesian reference frame by Eq. (447) leads to

$$\underline{\tau}_n = \frac{1}{\sqrt{G}} \mathcal{N}_k F_{kj} \underline{\sigma}_j. \quad (463)$$

This relationship holds for any orientation of the outer normal. In particular, if the outer normal in the deformed configuration is chosen along any of the Cartesian reference vector, then

$$\underline{\tau}_i = \frac{1}{\sqrt{G}} F_{ij} \underline{\sigma}_j. \quad (464)$$

This important result relates the two types of stress vectors. Introducing the definition, Eq. (429), of the Cauchy stress tensor, and Eq. (451) of the 1st Piola-Kirchhoff stress tensor then yields

$$\tau_{ik} \underline{g}_k = \frac{1}{\sqrt{G}} F_{ij} s_{jl} \underline{g}_l. \quad (465)$$

Dotting this result by \underline{g}_p leads to

$$\begin{aligned} \tau_{ij} &= \frac{1}{\sqrt{G}} F_{ik} s_{kj}; \\ s_{ij} &= \sqrt{G} F_{ik}^{-1} \tau_{kj}; \end{aligned} \quad (466)$$

which relates the Cauchy and 1st Piola-Kirchhoff stress tensors.

On the other hand, introducing the definition, Eq. (429), of the Cauchy stress tensor and the definition, Eq. (456), of the 2nd Piola-Kirchhoff stress tensor into Eq. (464) gives

$$\tau_{ik} \underline{g}_k = \frac{1}{\sqrt{G}} F_{ij} \sigma_{jl} \underline{G}_l = \frac{1}{\sqrt{G}} F_{ij} F_{ml} \sigma_{jl} \underline{g}_m. \quad (467)$$

Dotting this result by \underline{g}_p leads to

$$\begin{aligned} \tau_{ij} &= \frac{1}{\sqrt{G}} F_{ik} F_{jl} \sigma_{kl}; \\ \sigma_{ij} &= \sqrt{G} F_{ik}^{-1} F_{jl}^{-1} \tau_{kl}; \end{aligned} \quad (468)$$

which relates the Cauchy and 2nd Piola-Kirchhoff stress tensors.

The same relationship can be obtained by expressing the total force \underline{F}_n acting on a face with an arbitrary orientation as

$$\underline{F}_n = d\mathcal{A}_n \underline{\sigma}_n = d\mathcal{A}_n \underline{\tau}_n. \quad (469)$$

Introducing Eqs. (450) and (428) then yields

$$d\mathcal{A}_n n_i \underline{\sigma}_i = d\mathcal{A}_n \mathcal{N}_i \underline{\tau}_i \quad (470)$$

Using the definition, Eq. (451) of the 1st Piola-Kirchhoff stress tensor, and Eq. (429) of the Cauchy stress tensor then leads to

$$d\mathcal{A}_n n_i s_{ij} = d\mathcal{A}_n \mathcal{N}_i \tau_{ij} \quad (471)$$

Finally, using Eq. (448), then regrouping the term yields

$$d\mathcal{A}_n n_i \left(s_{ij} - \sqrt{G} F_{ik}^{-1} \tau_{kj} \right) = 0 \quad (472)$$

This result must hold for an arbitrary orientation of the normal, and hence the term in parenthesis must vanish, giving Eq. (466) once again.

Appendix C

GOVERNING EQUATIONS OF FINITE DEFORMATION ELASTICITY

C.1 Equations of Equilibrium

Consider a differential element of volume defined by vectors $\underline{g}_1 d\alpha_1$, $\underline{g}_2 d\alpha_2$, $\underline{g}_3 d\alpha_3$, as depicted in Fig. 94. All the material particles contained in that volume are convected to the volume defined by vectors $\underline{G}_1 d\alpha_1$, $\underline{G}_2 d\alpha_2$, $\underline{G}_3 d\alpha_3$ in the deformed configuration. On three faces of this differential element of volume the stress vectors per unit area of the reference configuration are $\underline{\sigma}_1$, $\underline{\sigma}_2$, and $\underline{\sigma}_3$. On the opposite faces, the corresponding stress vectors present increments $\partial\underline{\sigma}_1/\partial\alpha_1 d\alpha_1$, $\partial\underline{\sigma}_2/\partial\alpha_2 d\alpha_2$, and $\partial\underline{\sigma}_3/\partial\alpha_3 d\alpha_3$, respectively. Let \underline{b} be the body forces per unit volume of the reference configuration acting on this differential element of volume. Equilibrium of all the forces acting on this differential element of volume implies

$$\begin{aligned} & d\alpha_1 d\alpha_2 d\alpha_3 \underline{b} + \left(\underline{\sigma}_1 + \frac{\partial\underline{\sigma}_1}{\partial\alpha_1} d\alpha_1 - \underline{\sigma}_1 \right) d\alpha_2 d\alpha_3 \\ & + \left(\underline{\sigma}_2 + \frac{\partial\underline{\sigma}_2}{\partial\alpha_2} d\alpha_2 - \underline{\sigma}_2 \right) d\alpha_1 d\alpha_3 + \left(\underline{\sigma}_3 + \frac{\partial\underline{\sigma}_3}{\partial\alpha_3} d\alpha_3 - \underline{\sigma}_3 \right) d\alpha_1 d\alpha_2 = 0. \end{aligned} \quad (473)$$

After simplification, this becomes

$$\underline{\sigma}_{i,i} + \underline{b} = 0. \quad (474)$$

Equilibrium of the moments acting on the same differential element of volume implies

$$(d\alpha_2 d\alpha_3 \underline{\sigma}_1) \times (d\alpha_1 \underline{G}_1) + (d\alpha_1 d\alpha_3 \underline{\sigma}_2) \times (d\alpha_2 \underline{G}_2) + (d\alpha_1 d\alpha_2 \underline{\sigma}_3) \times (d\alpha_3 \underline{G}_3) = 0, \quad (475)$$

which simplifies to

$$\underline{\sigma}_i \times \underline{G}_i = 0. \quad (476)$$

At the outer surface of the body, the internal stresses must equilibrate the externally applied tractions. In view of Eq. (450), this condition writes

$$n_i \underline{\sigma}_i = \underline{t}, \quad (477)$$

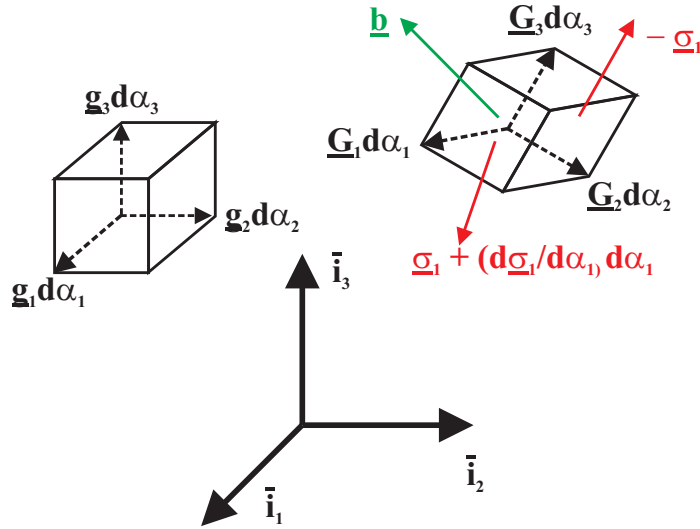


Figure 94: Forces acting on a differential element of volume in the deformed configuration.

where \underline{t} are externally applied traction per unit area of the reference configuration, and \underline{n} the outer normal to the outer surface of the body in the reference configuration.

Let v denote the volume of the body in the reference configuration, and s its outer surface. Equations (474) and (476) express the equilibrium of a differential element of volume dv defined by vector $\underline{g}_1 d\alpha_1$, $\underline{g}_2 d\alpha_2$, $\underline{g}_3 d\alpha_3$ in the reference configuration. Similarly, Eq. (477) expresses the equilibrium of a differential element ds of the outer surface of the body. The body is said to be in equilibrium if Eqs. (474) and (476) are satisfied at all points in v , and Eq. (477) at all points on s . Note that though Eqs. (474) and (476) express the equilibrium of forces acting on the unknown deformed configuration of the body, they must hold at all points in v , the known reference configuration of the body.

C.1.1 Equilibrium equations in terms of the 1st Piola-Kirchhoff stress tensor

The equations of equilibrium developed in the previous section were expressed in terms of the stress vectors $\underline{\sigma}_i$. These stress vectors can be written in terms of the 1st Piola-Kirchhoff stress as Eq. (451). The force equilibrium equation, Eq. (474) then becomes

$$\left(s_{ki} \underline{g}_i \right)_{,k} + b^i \underline{g}_i = 0 \quad (478)$$

where b^i are the components of the applied force vector. Since \underline{g}_i are constant vectors, this becomes

$$s_{ki,k} + b^i = 0. \quad (479)$$

With the help of Eq. (451), the moment equilibrium equation, Eq. (476) becomes

$$\left(s_{ij} \underline{g}_j \right) \times \left(F_{ki} \underline{g}_k \right) = s_{ij} F_{ki} \epsilon_{jkl} \underline{g}_l = 0. \quad (480)$$

Dotting this result by \underline{g}_l yields

$$F_{ki} s_{ij} \epsilon_{jkl} = 0. \quad (481)$$

From the definition of the permutation tensor it follows that

$$F_{ik} s_{kj} = F_{jk} s_{ki}. \quad (482)$$

Finally, the outer surface equilibrium equation, Eq. (477) becomes

$$n_k s_{ki} = t^i. \quad (483)$$

where t^i are the components of the externally applied traction $\underline{t} = t^i \underline{g}_i$.

In summary, the equilibrium equations of a body expressed in terms of the 1st Piola-Kirchhoff stress tensor write

$$\begin{aligned} s_{ki,k} + b^i &= 0; \\ F_{ik} s_{kj} &= F_{jk} s_{ki}; \\ n_k s_{ki} &= t^i. \end{aligned} \quad (484)$$

The first equation represent the force equilibrium condition, the second the moment equilibrium condition, and the last the outer surface equilibrium condition.

C.1.2 Equilibrium equations in terms of the 2nd Piola-Kirchhoff stress tensor

Equation (460) relates the 1st and 2nd Piola-Kirchhoff stress tensor. With the help of this relationship, the equilibrium equations (484) become

$$\begin{aligned} (F_{ij} \sigma_{kj})_{,k} + b^i &= 0; \\ \sigma_{ij} &= \sigma_{ji}; \\ n_k F_{ij} \sigma_{kj} &= t^i. \end{aligned} \quad (485)$$

C.1.3 Equilibrium equations in terms of Cauchy stress tensor

The equilibrium equations, Eq. (484), can also be expressed in term of the Cauchy stress tensor with the help of Eq. (466) to find

$$\begin{aligned} \left(\sqrt{G} F_{kj}^{-1} \tau_{ji} \right)_{,k} + b^i &= 0; \\ \tau_{ij} &= \tau_{ji}; \\ n_k \sqrt{G} F_{kj}^{-1} \tau_{ji} &= t^i. \end{aligned} \tag{486}$$

The following comments can be made from comparing the equilibrium equations written in terms of the 1st Piola-Kirchhoff stress tensor, Eq. (484), the 2nd Piola-Kirchhoff stress tensor, Eq. (485), and the Cauchy stress tensor (486). The 1st Piola-Kirchhoff stress tensor is very attractive because the force and outer surface equilibrium equations become linear equations. Unfortunately, the 1st Piola-Kirchhoff stress tensor is un-symmetric. The equilibrium equations, Eq. (485) in terms of the 2nd Piola-Kirchhoff stress tensor are nonlinear since the unknown displacement field appears in these equations through the deformation gradient tensor. However, this stress tensor is symmetric. The Cauchy stress tensor also enjoys the symmetry property, but the equilibrium equations are more complex.

C.2 Principle of Virtual Work

Consider a body in equilibrium under the effect of applied loads and prescribed displacements. This implies that equilibrium equations, Eqs. (474) and (477) are satisfied at all points in the reference volume v of the body, and at all points of the reference externally surface s of the body, respectively. The following variational statement can be constructed

$$\int_v -(\underline{\sigma}_{i,i} + \underline{b}) \cdot \delta \underline{u} \, dv + \int_s (n_i \underline{\sigma}_i - \underline{t}) \cdot \delta \underline{u} \, ds = 0, \tag{487}$$

where $\delta \underline{u}$ is an arbitrary variation of the displacement field. If statement (487) holds for an arbitrary variation $\delta \underline{u}$, it is entirely equivalent to equilibrium equations (474) and (477). Integrating the first term by parts yields

$$\int_v \underline{\sigma}_i \cdot \delta \underline{u}_{,i} \, dv - \int_v \underline{b} \cdot \delta \underline{u} \, dv - \int_s \underline{t} \cdot \delta \underline{u} \, ds = 0. \tag{488}$$

Introducing the definition, Eq. (456), of the 2nd Piola-Kirchhoff stress, the first integrand becomes

$$\underline{\sigma}_i \cdot \delta \underline{u}_{,i} = \sigma_{ij} \underline{G}_j \cdot \delta \underline{G}_i = \frac{1}{2} (\sigma_{ij} \underline{G}_j \cdot \delta \underline{G}_i + \sigma_{ji} \underline{G}_i \cdot \delta \underline{G}_j). \quad (489)$$

In view of the symmetry of the 2nd Piola-Kirchhoff stress tensor, Eq. (485), and recalling the definition of the Green-Lagrange strain tensor, Eq. (383), this writes

$$\underline{\sigma}_i \cdot \delta \underline{u}_{,i} = \sigma_{ij} \frac{1}{2} (\underline{G}_j \cdot \delta \underline{G}_i + \underline{G}_i \cdot \delta \underline{G}_j) = \sigma_{ij} \frac{1}{2} \delta G_{ij} = \sigma_{ij} \delta e_{ij}, \quad (490)$$

where the definition of the metric tensor, Eq. (368b) in the deformed configuration was used.

The principle of virtual work now becomes

$$\int_v \sigma_{ij} \delta e_{ij} \, dv = \int_v \underline{b} \cdot \delta \underline{u} \, dv + \int_s \underline{t} \cdot \delta \underline{u} \, ds. \quad (491)$$

This principle reads: “A body is in equilibrium if the virtual work of the 2nd Piola-Kirchhoff due to a virtual change in the Green-Lagrange strain equals the virtual work done by the externally applied forces and surface tractions for all admissible virtual displacement field and associated kinematically admissible strains.” It is important to note that though the principle of virtual work express the equilibrium condition for a body in its deformed configurations the integrals in Eq. (491) are written over the reference configuration of the body.

The principle of virtual work can also be expressed in terms of the Cauchy stress tensor. Introducing Eq. (468) in the first integral of Eq. (491) yields

$$\int_v \sigma_{ij} \delta e_{ij} \, dv = \int_v \sqrt{G} F_{ik}^{-1} F_{jl}^{-1} \tau_{kl} \delta e_{ij} \, dv. \quad (492)$$

Considering the relationship between variations in the Green-Lagrange and infinitesimal strain tensors

$$\begin{aligned} \delta e_{ij} &= F_{ki} F_{lj} \delta \varepsilon_{kl}; \\ \delta \varepsilon_{ij} &= F_{ki}^{-1} F_{lj}^{-1} \delta e_{kl}. \end{aligned} \quad (493)$$

Eq. (492) becomes

$$\int_v \sigma_{ij} \delta e_{ij} \, dv = \int_v \tau_{kl} \delta \varepsilon_{kl} \sqrt{G} \, dv. \quad (494)$$

The last integral can be transformed to an integral over the deformed configuration of the body, see Eq. (398)

$$\int_v \sigma_{ij} \delta e_{ij} \, dv = \int_V \tau_{kl} \delta \varepsilon_{kl} \, dV. \quad (495)$$

Proceeding in a similar manner for the last two terms of Eq. (491) leads to

$$\int_V \tau_{ij} \delta \varepsilon_{ij} \, dV = \int_V \underline{\underline{B}} \cdot \delta \underline{u} \, dV + \int_S \underline{\underline{T}} \cdot \delta \underline{u} \, dS, \quad (496)$$

where $\underline{\underline{B}}$ are the body force per unit volume of the deformed configuration, and $\underline{\underline{T}}$ the surface traction per unit area of the deformed configuration.

It should be noted that statement of the principle of virtual work, Eq. (496) is identical to that obtained based on the linear theory of elasticity. Though this principle is correct, it is very difficult to use for nonlinear analysis because the Cauchy stress and infinitesimal strain are referred to the unknown deformed configuration, and all the integrals appearing in the principle must be performed over the unknown deformed volume and outer surface of the body. This contrasts with statement (491) of the principle of virtual work which involves the 2nd Piola-Kirchhoff stress and Green Lagrange strains which are referred to the reference configuration, and integrals to be performed over the known volume and outer surface of the body in its reference configuration.

Appendix D

CONSTITUTIVE LAWS FOR A NONLINEAR CONTINUUM

D.1 Introduction

The solution of elastic problems requires three types of relationships. First, adequate strain measures are defined and related to the displacement field. This purely kinematic problem was analyzed in Appendix A. Second, adequate stress measures were defined in Appendix B, and equilibrium conditions were derived in Appendix C. These equilibrium conditions stem from Newton's laws, and can be enforced through equilibrium equations or variational principles. Finally, the stress and strain measures must be related through constitutive laws. These constitutive laws characterize the mechanical behavior of the material, and consist of a mathematical idealization of the observed behavior of the material.

Various different types of constitutive laws exist to represent the many types of experimentally observed material behaviors. A limited number of highly idealized constitutive laws will be presented in this chapter. Section D.2 introduces the fundamental concept of strain energy density function. The constitutive laws for linear elastic materials are presented in section D.3 and D.4, for anisotropic and isotropic behavior, respectively. A general introduction of the strain energy density function for elastomeric materials will be described in terms of strain invariants in section D.5.

D.2 Strain Energy Density Function

The principle of virtual work, Eq. (491) states that a body is in equilibrium if the virtual work done by the internal stresses is equal to the work done by the externally applied forces for all admissible virtual displacement fields and associated stress fields. The virtual work done by the internal stresses writes

$$\delta W_i = \int_v \sigma_{ij} \delta e_{ij} \, dv. \quad (497)$$

Note that $\sigma_{ij}\delta e_{ij}$ represents the virtual work done by the internal stress per unit volume of the reference configuration. A strain energy density function $W(e_{ij})$ is assumed to exist

$$\sigma_{ij} = \frac{\partial W(e_{ij})}{\partial e_{ij}}. \quad (498)$$

This relationship describes the constitutive behavior of the material as it relates stress to strain. It is, however, important to note that the existence of the strain energy density function is an assumption. Not all constitutive laws can be written in the form of Eq. (498), although the behavior of several important classes of material can be indeed be characterized by a relationship of this form. Introducing Eq. (498) into Eq. (497) leads to

$$\delta W_i = \delta \int_v W(e_{ij}) \, dv = \delta A. \quad (499)$$

Clearly, the existence of a strain energy density function implies that the virtual work done by the internal stress is equal to virtual changes in the total strain energy of the body, defined as

$$A = \int_v W(e_{ij}) \, dv. \quad (500)$$

It should be noted that strain energy density function defined by Eq. (498) is measured per unit volume of the reference configuration. The strain density function must be a positive definite function of the strain state only. It does not depend on the straining history.

D.3 Linear Elastic Anisotropic Material

When the displacements and deformations of a body remain very small, the stress-strain relationship can often be approximated by a linear relationship

$$\tau_{ij} = c^{ijkl}\varepsilon_{kl}. \quad (501)$$

where the c^{ijkl} are constant stiffness moduli. The strain energy density function is readily found as

$$W(\varepsilon_{ij}) = \frac{1}{2}c^{ijkl}\varepsilon_{ij}\varepsilon_{kl}. \quad (502)$$

Since the indices i , j , k , and l can be varied independently, $3^4 = 81$ independent elastic moduli exist. However, these various moduli are not all different from each other. Indeed,

due to the symmetry of the strain tensor the first two, and the last two indices can be interchanged. Furthermore, since the strain energy density function is definite positive the indices ij and kl can be interchanged. This leaves a total of 21 independent elastic moduli. If the material possesses symmetry planes, some of these 21 constants can be show to vanish.

The linear behavior characterized by Eq. (501) is a reasonable approximation for very small displacements and strains only. For small strains, the Green-Lagrange strain e_{ij} is identical to the infinitesimal strain ε_{ij} , and the 2nd Piola-Kirchhoff stress σ_{ij} is identical to Cauchy stress τ_{ij} . Hence, Eqs. (501) and (502) could be written as

$$\begin{aligned}\sigma_{ij} &= c^{ijkl} e_{kl}; \\ W(e_{ij}) &= \frac{1}{2} c^{ijkl} e_{ij} e_{kl}.\end{aligned}\tag{503}$$

It is important to realize that this linear relation between the 2nd Piola-Kirchhoff stress and Green-Lagrange stain tensors corresponds to a linear elastic material if the displacements and strains are indeed small, but a nonlinear elastic material if large strains are present.

D.4 Linear Elastic Isotropic Material

If the linear elastic material is isotropic, it can be shown that only two of the elastic moduli does not vanish. The tensor of elastic moduli writes

$$c^{ijkl} = \lambda \delta_{ij} \delta_{kl} + \mu (\delta_{ik} \delta_{jl} + \delta_{il} \delta_{jk}),\tag{504}$$

where λ and μ are called *the Lamé constants*. They are related to the better known *engineering constants* as

$$\begin{aligned}\lambda &= \frac{E\nu}{(1+\nu)(1-2\nu)}; \\ \mu &= \frac{E}{2(1+\nu)},\end{aligned}\tag{505}$$

where E is *Young's modulus* and ν *Poisson's ratio*. Note that μ is equal to the shearing modulus. The strain energy density function is found by introducing Eq. (504) into Eq. (502) to find

$$W = \frac{1}{2} (\lambda \varepsilon_{ii} \varepsilon_{jj} + 2\mu \varepsilon_{ij} \varepsilon_{ij}).\tag{506}$$

The stress-strain relationship is readily found by introducing Eq. (504) into Eq. (503) to find

$$\tau_{ij} = \lambda \varepsilon_{kk} \delta_{ij} + 2\mu \varepsilon_{ij}. \quad (507)$$

This relationship is known as Hooke's Law for a linear elastic, isotropic material. It is a good approximation to the behavior of many material subjected to small strains.

D.5 Nonlinear Elastic, Isotropic, Incompressible Materials

Elastomeric materials are highly elastic. This means that, at a fixed temperature, such materials present very little hysteresis effect even for large deformation. It is common to consider these materials to be perfectly elastic, and to assume the existence of strain energy density function. Elastomeric materials present an isotropic behavior, and even more, the deformation is often assumed to take place without volume change. The deformation is said to be isochoric. Equivalently one speaks of an incompressible material.

The invariants of the metric tensor do not give a complete deformation of the state of strain at a point until the directions of the corresponding eigenvectors are also unknown. However, if the material behavior is isotropic, the strain energy density function should depend on the magnitude of the deformation but not on direction in which this deformation is taking place. As a result, the following form of the strain energy density function was proposed

$$W(e_{ij}) = W(I_1, I_2), \quad (508)$$

subjected to the incompressibility condition

$$I_3 = 1, \quad (509)$$

where the strain invariants I_1, I_2 and I_3 were defined by Eq. (418). In view of the incompressibility condition, Eq. (509), the strain invariants write

$$I_1 = \lambda_{(1)}^2 + \lambda_{(2)}^2 + \lambda_{(3)}^2; \quad (510a)$$

$$I_2 = \lambda_{(2)}^2 \lambda_{(3)}^2 + \lambda_{(3)}^2 \lambda_{(1)}^2 + \lambda_{(1)}^2 \lambda_{(2)}^2 = \lambda_{(1)}^{-2} + \lambda_{(2)}^{-2} + \lambda_{(3)}^{-2}. \quad (510b)$$

The 2nd Piola-Kirchhoff stress can be readily computed as

$$\sigma_{ij} = 2 \frac{\partial W}{\partial G_{ij}} = 2 \left(\frac{\partial W}{\partial I_1} \frac{\partial I_1}{\partial G_{ij}} + \frac{\partial W}{\partial I_2} \frac{\partial I_2}{\partial G_{ij}} \right). \quad (511)$$

In view of Eq. (418) this writes as

$$\sigma_{ij} = 2 \frac{\partial W}{\partial I_1} \delta_{ij} + 2 \frac{\partial W}{\partial I_2} (I_1 \delta_{ij} - G_{ij}). \quad (512)$$

Finally, the Cauchy stress follows from Eq. (468)

$$\tau_{ij} = 2 \left(\frac{\partial W}{\partial I_1} + I_1 \frac{\partial W}{\partial I_2} \right) G_{ij}^* - 2 \frac{\partial W}{\partial I_2} G_{ik}^* G_{jk}^*. \quad (513)$$

It is important to note that for a truly incompressible material as is the case here, the hydrostatic pressure cannot be determined from the constitution laws. In fact, an arbitrary hydrostatic pressure can be added to expression (513). To remove any ambiguity in the definition of the Cauchy stress, only the deviatoric part of Eq. (513) is used to yield

$$\tau_{ij} = 2 \left(\frac{\partial W}{\partial I_1} + I_1 \frac{\partial W}{\partial I_2} \right) \left(G_{ij}^* - \frac{1}{3} G_{pp}^* \delta_{ij} \right) - 2 \frac{\partial W}{\partial I_2} \left(G_{ik}^* G_{jk}^* - \frac{1}{3} G_{pq}^* G_{pq}^* \delta_{ij} \right) + p \delta_{ij}. \quad (514)$$

REFERENCES

- [1] ALEXANDER, H., “A constitutive relation for rubber-like materials,” *International Journal of Engineering Science*, vol. 6, no. 9, pp. 549–563, 1968.
- [2] AMBACHER, H., ENDERLE, H. F., KILIAN, H. G., and SAUTER, A., “Relaxation in permanent networks,” *Progress in Colloid and Polymer Science*, vol. 80, pp. 209–220, 1989.
- [3] AMIN, A. F. M. S., LION, A., SEKITA, S., and OKUI, Y., “Nonlinear dependence of viscosity in modeling the rate-dependent response of natural and high damping rubbers in compression and shear: Experimental identification and numerical verification,” *International Journal of Plasticity*, vol. 22, pp. 1610–1657, 2006.
- [4] ANAND, L., “On h. hencky’s approximate strain-energy function for moderate deformations,” *Journal of Applied Mechanics*, vol. 46, pp. 78–82, 1979.
- [5] ANAND, L., “Moderate deformations in extension-torsion of incompressible isotropic elastic materials,” *Journal of the Mechanics and Physics of Solids*, vol. 34, no. 3, pp. 293–304, 1986.
- [6] ARMSTRONG-HÉLOUVRY, B., *Control of Machines with Friction*. Boston, MA: Springer, 1978.
- [7] ARRUDA, E. M. and BOYCE, M. C., “A three-dimensional constitutive model for the large stretch behavior of rubber elastic materials,” *Journal of the Mechanics and Physics of Solids*, vol. 41, no. 2, pp. 389–412, 1993.
- [8] AUSTRELL, P. E., *Modeling of Elasticity and Damping for Filled Elastomers*. PhD thesis, Lund Institute of Technology, Division of Structural Mechanics, Lund, Sweden, 1993.
- [9] AUSTRELL, P. E., OLSSON, A. K., and JONSSON, M., “A method to analyze the non-linear dynamic behavior of rubber components using standard FE codes,” in *Proceedings of the First M.I.T. Conference on Fluid and Solid Mechanics, Cambridge, MASS, June 12-15, 2001*. Paper no 464.
- [10] BAGLEY, R. L. and TORVIK, P. J., “Fractional calculus - a different approach to the analysis of viscoelastically damped structures,” *AIAA Journal*, vol. 21, no. 5, pp. 741–748, 1983.
- [11] BAGLEY, R. L. and TORVIK, P. J., “A theoretical basis for the application of fractional calculus to viscoelasticity,” *Journal of Rheology*, vol. 27, no. 3, pp. 201–210, 1983.
- [12] BAGLEY, R. L. and TORVIK, P. J., “Fractional calculus in the transient analysis of viscoelastically damped structures,” *AIAA Journal*, vol. 23, no. 6, pp. 918–925, 1985.

- [13] BAGLEY, R. L. and TORVIK, P. J., “On the fractional calculus model of viscoelastic behavior,” *Journal of Rheology*, vol. 30, no. 1, pp. 133–155, 1986.
- [14] BALL, R. C., DOI, M., EDWARDS, S. F., and WARNER, M., “Elasticity of entangled networks,” *Polymer*, vol. 22, pp. 1010–1018, 1981.
- [15] BANERJEE, A. K. and KANE, T. T., “Modeling and simulation of rotor bearing friction,” *Journal of Guidance, Control and Dynamics*, vol. 17, pp. 1137–1151, 1994.
- [16] BATHE, K. J., *Finite Element Procedures*. Englewood Cliffs, New Jersey: Prentice Hall, Inc., 1996.
- [17] BAUCHAU, O. A., “Computational schemes for flexible, nonlinear multi-body systems,” *Multibody System Dynamics*, vol. 2, no. 2, pp. 169–225, 1998.
- [18] BAUCHAU, O. A. and RODRIGUEZ, J., “Modeling of joints with clearance in flexible multibody systems,” *International Journal of Solids and Structures*, vol. 39, pp. 41–63, 2002.
- [19] BAUCHAU, O., BOTTASSO, C., and NIKISHKOV, Y., “Modeling rotorcraft dynamics with finite element multibody procedures,” *Mathematical and Computer Modeling*, vol. 33, no. 10-11, pp. 1113–1137, 2001.
- [20] BAUCHAU, O. A., *DYMORE User’s Manual*. Atlanta, Georgia: School of Aerospace Engineering, Georgia Institute of Technology, 2009.
- [21] BAUMEISTER, T., AVALLONE, E. A., and (EDS.), T. B. I., *Marks’ Mechanical Engineers Handbook*. New-York: McGraw-Hill Book Company, 1978.
- [22] BERGSTRÖM, J. S. and BOYCE, M. C., “Constitutive modeling of the large strain time-dependent behavior of elastomers,” *Journal of the Mechanics and Physics of Solids*, vol. 46, no. 5, pp. 931–954, 1998.
- [23] BERGSTRÖM, J. S. and BOYCE, M. C., “Large strain time-dependent behavior of filled elastomers,” *Mechanics of Materials*, vol. 32, pp. 627–644, 2000.
- [24] BIDERMAN, V. L., “Calculations of rubber parts (in Russian),” *Rascheti na Prochnost*, p. 40, 1958.
- [25] BISCHOFF, J. E., ARRUDA, E. M., and GROSH, K., “A new constitutive model for the compressibility of elastomers at finite deformations,” *Rubber Chemistry and Technology*, vol. 74, no. 4, pp. 541–559, 2001.
- [26] BONET, J., “Large strain viscoelastic constitutive models,” *Internal Journal of Solids and Structures*, vol. 38, pp. 2953–2968, 2001.
- [27] BOYCE, M. C. and ARRUDA, E. M., “Constitutive models of rubber elasticity: a review,” *Rubber Chemistry and Technology*, vol. 73, no. 3, pp. 504–523, 2003.
- [28] BRACKBILL, C. R., LESIEUTRE, G. A., SMITH, E. C., and GOVINDSWAMY, K., “Thermomechanical modeling for elastomeric materials,” *Smart Materials and Structures*, vol. 5, pp. 529–539, 1996.

- [29] BRACKBILL, C. R., LESIEUTRE, G. A., SMITH, E. C., and RUHL, L. E., “Characterization and modeling of the low strain amplitude and frequency dependent behavior of elastomeric damper materials,” *Journal of the American Helicopter Society*, vol. 45, no. 1, pp. 34–42, 2000.
- [30] BRACKBILL, C. R., SMITH, E. C., and LESIEUTRE, G. A., “Application of a refined time domain elastomeric damper model to helicopter rotor aeroelastic response and stability,” *Journal of the American Helicopter Society*, vol. 47, no. 3, pp. 186–197, 2002.
- [31] BRACKBILL, C. R., *Helicopter Rotor Aeroelastic Analysis Using Refined Elastomeric Damper Model*. PhD thesis, The Pennsylvania State University, Department of Aerospace Engineering, Pennsylvania, USA, 2000.
- [32] CANUDAS DE WIT, C., OLSSON, H., ASTROM, K. J., and LISCHINSKY, P., “A new model for control of systems with friction,” *IEEE Transactions on Automatic Control*, vol. 40, pp. 419–425, 1995.
- [33] CARDONA, A. and GÉRADIN, M., “Kinematic and dynamic analysis of mechanisms with cams,” *Computer Methods in Applied Mechanics and Engineering*, vol. 103, pp. 115–134, 1993.
- [34] CHAGNON, G., MARCKMANN, G., and VERRON, E., “A comparison of the hart-smith model with arruda-boyce and gent formulations for rubber elasticity,” *Rubber Chemistry and Technology*, vol. 77, no. 4, pp. 724–735, 2004.
- [35] CHAZEAU, L., BROWN, J. D., YANYO, L. C., and STERNSTEIN, S. S., “Modulus recovery kinetics and other insights into the payne effect for filled elastomers,” *Polymer Composites*, vol. 21, no. 2, pp. 202–222, 2000.
- [36] COLEMAN, B. D. and NOLL, W., “The thermodynamics of elastic materials with heat conduction and viscosity,” *Archive for Rational Mechanics and Analysis*, vol. 13, pp. 167–178, 1963.
- [37] DAHL, P. R., “Solid friction damping of mechanical vibrations,” *AIAA Journal*, vol. 14, pp. 1675–1682, 1976.
- [38] DROZDOV, A. D., “Fractional differential models in finite viscoelasticity,” *Acta Mechanica*, vol. 124, pp. 155–180, 1997.
- [39] DROZDOV, A. D. and DORFMANN, A., “Modeling the response of filled elastomers at finite strains by rigid-rod networks,” *Archive of Applied Mechanics*, vol. 72, pp. 52–76, 2002.
- [40] DROZDOV, A. D. and DORFMANN, A., “A micro-mechanical model for the response of filled elastomers at finite strains,” *International Journal of Plasticity*, vol. 19, pp. 1037–1067, 2003.
- [41] ENDERLE, H. F. and KILIAN, H. G., “Relaxation in permanent networks,” *Progress in Colloid and Polymer Science*, vol. 75, pp. 55–61, 1987.

- [42] ERMAN, B. and FLORY, P. J., "Relationships between stress, strain, and molecular constitution of polymer networks. comparison of theory with experiments," *Macromolecules*, vol. 15, no. 3, pp. 806–811, 1982.
- [43] FELKER, F. F., LAU, B. H., MCLAUGHLIN, S., and JOHNSON, W., "Nonlinear behavior of an elastomeric lag damper undergoing dual-frequency motion and its effect on rotor dynamics," *Journal of the American Helicopter Society*, vol. 32, no. 4, pp. 45–53, 1987.
- [44] FERRI, A. A., "Friction damping and isolation systems," *ASME Journal of Vibration and Acoustics*, vol. 117B, pp. 196–206, 1995.
- [45] FLETCHER, W. P. and GENT, A. N., "Non-linearity in the dynamic properties of vulcanised rubber compounds," *Transactions of the Institution of the Rubber Industry*, vol. 29, pp. 266–280, 1953.
- [46] FLÜGGE, W., *Viscoelasticity*. New York, Berlin: Springer-Verlag, second revised ed., 1975.
- [47] FLORY, P. J., "Network structure and the elastic properties of vulcanized rubber," *Chemical reviews*, vol. 35, no. 1, pp. 51–75, 1944.
- [48] FLORY, P. J. and ERMAN, B., "Theory of elasticity of polymer networks. 3," *Macromolecules*, vol. 15, no. 3, pp. 800–806, 1982.
- [49] GANDHI, F. and CHOPRA, I., "Analysis of bearingless main rotor aeroelasticity using an improved time domain nonlinear elastomeric damper model," *Journal of the American Helicopter Society*, vol. 41, no. 3, pp. 267–277, 1996.
- [50] GENT, A. N., "A new constitutive relation for rubber," *Rubber Chemistry and Technology*, vol. 69, pp. 59–61, 1996.
- [51] GENT, A. N. and THOMAS, A. G., "Forms for the stored (strain) energy function for vulcanized rubber," *Journal of Polymer Science*, vol. 28, no. 118, pp. 625–628, 1958.
- [52] GOVINDJEE, S. and REESE, S., "A presentation and comparison of two large deformation viscoelasticity models," *Journal of Engineering Materials and Technology*, vol. 119, pp. 251–255, 1997.
- [53] GREEN, M. S. and TOBOLSKY, A. V., "A new approach to the theory of relaxing polymeric media," *The Journal of Chemical Physics*, vol. 14, no. 2, pp. 80–92, 1946.
- [54] HAESSIG, D. A. and FRIEDLAND, B., "On the modeling and simulation of friction," *ASME Journal of Dynamic Systems, Measurement, and Control*, vol. 113, pp. 354–362, 1991.
- [55] HART-SMITH, L. J., "Elasticity parameters for finite deformations of rubber-like materials," *Zeitschrift für angewandte Mathematik und Physik*, vol. 17, no. 5, pp. 608–626, 1966.
- [56] HARWOOD, J. A. C., MULLINS, L., and PAYNE, A. R., "Stress softening in natural rubber vulcanizates. part II: Stress softening effects in pure gum and filler loaded rubbers," *Journal of Applied Polymer Science*, vol. 9, pp. 3011–3021, 1965.

- [57] HAUPT, P., *Continuum mechanics and theory of materials*. Berlin: Springer-Verlag, 2000.
- [58] HAUPT, P. and LION, A., “On finite linear viscoelasticity of incompressible isotropic materials,” *Acta Mechanica*, vol. 159, pp. 87–124, 2002.
- [59] HAUPT, P. and SEDLAN, K., “Viscoplasticity of elastomeric materials: experimental facts and constitutive modeling,” *Archive of Applied Mechanics*, vol. 71, pp. 89–109, 2001.
- [60] HAUPT, P., LION, A., and BACKHAUS, E., “On the dynamic behaviour of polymers under finite strains: constitutive modelling and identification of parameters,” *International Journal of Solids and Structures*, vol. 37, pp. 3633–3646, 2000.
- [61] HEINRICH, G. and KALISKE, M., “Theoretical and numerical formulation of a molecular based constitutive tube-model of rubber elasticity,” *Computational and Theoretical Polymer Science*, vol. 7, pp. 227–241, 1997.
- [62] HENCKY, H., “The law of elasticity for isotropic and quasi-isotropic substances by finite deformations,” *Journal of Rheology*, vol. 2, pp. 169–176, 1931.
- [63] HENCKY, H., “The elastic behavior of vulcanized rubber,” *Rubber Chemistry and Technology*, vol. 6, pp. 217–224, 1933.
- [64] HÖFER, P. and LION, A., “Modelling of frequency- and amplitude-dependent material properties of filler-reinforced rubber,” *Journal of the Mechanics and Physics of Solids*, vol. 57, pp. 500–520, 2009.
- [65] HOLZAPFEL, G. A., “On large strain viscoelasticity: continuum formulation and finite element applications to elastomeric structure,” *International Journal for Numerical Methods in Engineering*, vol. 39, pp. 3903–3926, 1996.
- [66] HOLZAPFEL, G. A. and SIMO, J. C., “A new viscoelastic constitutive model for continuous media at finite thermomechanical changes,” *International Journal of Solids and Structures*, vol. 33, no. 20-22, pp. 3019–3034, 1996.
- [67] HU, W. and WERELEY, N. M., “Distributed rate-dependent elastoslide model for elastomeric lag dampers,” *Journal of Aircraft*, vol. 44, no. 6, pp. 1972–1984, 2007.
- [68] HUBER, N. and TSAKMAKIS, C., “Discussion of finite deformation viscoelasticity laws with reference to torsion loading,” *Continuum Mechanics and Thermodynamics*, vol. 12, pp. 303–323, 2000.
- [69] HUBER, N. and TSAKMAKIS, C., “Finite deformation viscoelasticity laws,” *Mechanics of Materials*, vol. 32, pp. 1–18, 2000.
- [70] HUNT, K. H. and CROSSLEY, F. R. E., “Coefficient of restitution interpreted as damping in vibroimpact,” *Journal of Applied Mechanics*, vol. 112, pp. 440–445, 1975.
- [71] IWAN, W. D., “On a class of models for the yielding behavior of continuous and composite systems,” *ASME Journal of Applied Mechanics*, vol. 89, pp. 612–617, 1967.

- [72] JAMES, A. G., GREEN, A., and SIMPSON, G. M., "Strain energy functions of rubber I. characterization of gum vulcanizates," *Journal of Applied Polymer Science*, vol. 19, no. 7, pp. 2033–2058, 1975.
- [73] JAMES, H. M. and GUTH, E., "Theory of the elastic properties of rubber," *The Journal of Chemical Physics*, vol. 11, no. 10, pp. 455–481, 1943.
- [74] JOHNSON, C., *Numerical Solutions of Partial Differential Equations by the Finite Element Method*. Cambridge: Cambridge University Press, 1987.
- [75] KALISKE, M. and HEINRICH, G., "An extended tube-model for rubber elasticity: Statistical-mechanical theory and finite element implementation," *Rubber Chemistry and Technology*, vol. 72, no. 4, pp. 602–632, 1999.
- [76] KANE, T. R., "Impulsive motions," *Journal of Applied Mechanics*, vol. 15, pp. 718–732, 1962.
- [77] KHULIEF, Y. A. and SHABANA, A. A., "Dynamic analysis of constrained systems of rigid and flexible bodies with intermittent motion," *ASME Journal of Mechanisms, Transmissions, and Automation in Design*, vol. 108, pp. 38–44, 1986.
- [78] KHULIEF, Y. A. and SHABANA, A. A., "A continuous force model for the impact analysis of flexible multi-body systems," *Mechanism and Machine Theory*, vol. 22, pp. 213–224, 1987.
- [79] KILIAN, H. G., ENDERLE, H. F., and UNSELD, K., "The use of the van der waals model to elucidate universal aspects of structure-property relationships in simply extended dry and swollen rubbers," *Macromolecules*, vol. 264, no. 10, pp. 866–876, 1986.
- [80] KILIAN, H. G., "Equation of state of real networks," *Macromolecules*, vol. 22, no. 2, pp. 209–217, 1981.
- [81] KUHN, W. and GRÜN, F., "Beziehungen zwischen elastischen konstanten und dehnungsdoppelbrechung hochelastischer stoe," *Kolloideitschrift*, vol. 101, pp. 248–271, 1942.
- [82] KUNZ, D. L., "Influence of elastomeric damper modeling on the dynamic response of helicopter rotors," *AIAA Journal*, vol. 35, no. 12, pp. 349–354, 1997.
- [83] LAIARINANDRASANA, L., PIQUES, R., and ROBISSON, A., "Visco-hyperelastic model with internal state variable coupled with discontinuous damage concept under total lagrangian formulation," *International Journal of Plasticity*, vol. 19, pp. 977–1000, 2003.
- [84] LAMPAERT, V., SWEVERS, J., and AL-BENDER, F., "Modification of the leuven integrated friction model structure," *IEEE Transactions on Automatic Control*, vol. 47, no. 4, pp. 683–687, 2002.
- [85] LESIEUTRE, G. A., "Finite elements for dynamic modeling of uniaxial rods with frequency dependent material properties," *International Journal of Solids and Structures*, vol. 29, no. 12, pp. 1567–1579, 1992.

- [86] LESIEUTRE, G. A., BIANCHINI, E., and MAIANI, A., “Finite element modeling of one-dimensional viscoelastic structures using anelastic displacement fields,” *Journal of Guidance, Control and Dynamics*, vol. 19, no. 3, pp. 520–527, 1996.
- [87] LESIEUTRE, G. A. and BIANCHINI, E. B., “Time-domain modeling of linear viscoelasticity using anelastic displacement fields,” *Journal of Vibration and Acoustics*, vol. 117, pp. 424–430, 1995.
- [88] LESIEUTRE, G. A. and GOVINDSWAMY, K., “Finite element modeling of frequency-dependent and temperature-dependent dynamic behavior of viscoelastic materials in simple shear,” *Internal Journal of Solids and Structures*, vol. 33, no. 3, pp. 419–432, 1996.
- [89] LESIEUTRE, G. A. and MINGORI, D. L., “Finite element modeling of frequency-dependent material damping using augmenting thermodynamic fields,” *Journal of Guidance, Control, and Dynamics*, vol. 13, no. 6, pp. 1040–1050, 1990.
- [90] LION, A., “A constitutive model for carbon black filled rubber: Experimental investigations and mathematical representation,” *Continuum Mechanics and Thermodynamics*, vol. 8, no. 3, pp. 153–169, 1996.
- [91] LION, A., “On the large deformation behavior of reinforced rubber at different temperatures,” *Journal of the Mechanics and Physics of Solids*, vol. 45, no. 11/12, pp. 1805–1834, 1997.
- [92] LION, A., “On the thermodynamics of fractional damping elements,” *Continuum Mechanics and Thermodynamics*, vol. 9, pp. 83–96, 1997.
- [93] LION, A., “A physically based method to represent the thermo-mechanical behaviour of elastomers,” *Acta Mechanica*, vol. 123, pp. 1–25, 1997.
- [94] LION, A., “Thixotropic behavior of rubber under dynamic loading histories: experiments and theory,” *Journal of the Mechanics and Physics of Solids*, vol. 46, no. 5, pp. 895–930, 1997.
- [95] LU, Y. C., “Fractional derivative viscoelastic model for frequency-dependent complex moduli of automotive elastomers,” *International Journal of Mechanics and Materials in Design*, vol. 3, pp. 329–336, 2006.
- [96] LUBLINER, J., “A model of rubber viscoelasticity,” *Mechanics Research Communications*, vol. 12, no. 2, pp. 93–99, 1985.
- [97] MARK, J. E., ERMAN, B., and EIRICH, F. R., *The science and technology of rubber*. Elsevier Academic Press, 2005.
- [98] MIEHE, C. and KECK, J., “Superimposed finite elastic-viscoelastic-plastoelastic stress response with damage in filled rubbery polymers. experiments, modeling and algorithmic implementation,” *Journal of the Mechanics and Physics of Solids*, vol. 48, pp. 323–365, 2000.
- [99] MOONEY, M., “A theory of large elastic deformation,” *Journal of Applied Physics*, vol. 11, no. 9, pp. 582–592, 1940.

- [100] MUHR, A. H., “Modeling the stress-strain behavior of rubber,” *Rubber Chemistry and Technology*, vol. 78, no. 3, pp. 391–425, 2005.
- [101] MULLINS, L. and TOBIN, N. R., “Theoretical model for the elastic behavior of filler reinforced vulcanized rubber,” *Rubber Chemistry and Technology*, vol. 30, pp. 551–571, 1957.
- [102] MULLINS, L. and TOBIN, N. R., “Stress softening in rubber vulcanizates. part I: Use of a strain amplification factor to describe the elastic behavior of filler-reinforced vulcanized rubber,” *Journal of Applied Polymer Science*, vol. 9, pp. 2993–3009, 1965.
- [103] NUTTING, P. G., “A new generalized law of deformation,” *Journal of the Franklin Institute*, vol. 191, pp. 679–685, 1921.
- [104] ODEN, J. C. and J. A. C. MARTINS, J., “Models and computational methods for dynamic friction phenomena,” *Computer Methods in Applied Mechanics and Engineering*, vol. 52, pp. 527–634, 1985.
- [105] OGDEN, R. W., “Large deformation isotropic elasticity: On the correlation of theory and experiment for compressible rubberlike solids,” *Proceedings of the Royal Society of London*, vol. A 328, pp. 567–583, 1972.
- [106] OGDEN, R. W., “Large deformation isotropic elasticity: On the correlation of theory and experiment for incompressible rubberlike solids,” *Proceedings of the Royal Society of London*, vol. A 326, pp. 565–584, 1972.
- [107] PAYNE, A. R., “The dynamic properties of carbon black-loaded natural rubber vulcanizates. part I,” *Journal of Applied Polymer Science*, vol. 6, no. 19, pp. 57–63, 1962.
- [108] PAYNE, A. R., “A note on the existence of a yield point in the dynamic modulus of loaded vulcanizates,” *Journal of Applied Polymer Science*, vol. 3, no. 1, p. 127, 1962.
- [109] PETERS, D. and HE, C., “Finite state induced flow models. Part II: Three-dimensional rotor disk,” *Journal of Aircraft*, vol. 32, no. 2, pp. 323–333, 1995.
- [110] PETERS, D., KARUNAMOORTHY, S., and CAO, W., “Finite state induced flow models. Part I: Two-dimensional thin airfoil,” *Journal of Aircraft*, vol. 32, no. 2, pp. 313–322, 1995.
- [111] PFEIFFER, F. and GLOCKER, C., *Multi-Body Dynamics with Unilateral Contacts*. New York: John Wiley & Sons, Inc, 1996.
- [112] REESE, S., “A micromechanically motivated material model for the thermo-viscoelastic material behaviour of rubber-like polymers,” *International Journal of Plasticity*, vol. 19, pp. 909–940, 2003.
- [113] REESE, S. and GOVINDJEE, S., “A theory of finite viscoelasticity and numerical aspects,” *International Journal of Solids and Structures*, vol. 35, no. 26-27, pp. 3455–3482, 1998.
- [114] RIVLIN, R. S., “Large elastic deformations of isotropic materials I. fundamental concepts,” *Philosophical Transactions of the Royal Society of London. Series A*, vol. 240, no. 882, pp. 459–490, 1948.

- [115] RIVLIN, R. S., “Large elastic deformations of isotropic materials IV. further developments of the general theory,” *Philosophical Transactions of the Royal Society of London. Series A*, vol. 241, no. 835, pp. 379–397, 1948.
- [116] RIVLIN, R. S. and SAUNDERS, D. W., “Large elastic deformations of isotropic materials VII. experiments on the deformation of rubber,” *Philosophical Transactions of the Royal Society of London. Series A*, vol. 243, no. 865, pp. 251–288, 1951.
- [117] SHIGLEY, J. E. and MISCHKE, C. R., *Mechanical Engineering Design*. New York: McGraw-Hill Book Company, 1989.
- [118] SIMO, J. C., “On a fully three-dimensional finite-strain viscoelastic damage model: Formulation and computational aspects,” *Computer Methods in Applied Mechanics and Engineering*, vol. 60, pp. 153–173, 1987.
- [119] SLONIMSKY, G. L., “Laws of mechanical relaxation processes in polymers,” *Journal of Polymer Science: Part C*, vol. 16, pp. 1667–1672, 1967.
- [120] SMITH, E. C., GOVINDSWAMY, K., BEALE, M. R., and LESIEUTRE, G. A., “Formulation validation, and application of a finite element model for elastomeric lag dampers,” *Journal of the American Helicopter Society*, vol. 41, no. 3, pp. 247–256, 1996.
- [121] SMITH, E. C., GOVINDSWAMY, K., BEALE, M. R., VASCSINEC, M. J., and LESIEUTRE, G. A., “Aeroelastic response and stability of a helicopter with elastomeric lag dampers,” *Journal of the American Helicopter Society*, vol. 41, no. 3, pp. 257–266, 1996.
- [122] STERN, H. J., *History, in Rubber Technology and Manufacture*. London: Newnes-Butterworths, 1977.
- [123] SWEVERS, J., AL-BENDER, F., GANESMAN, C. G., and PRAJOGO, T., “An integrated friction model structure with improved presliding behavior for accurate friction compensation,” *IEEE Transactions on Automatic Control*, vol. 45, no. 4, pp. 675–686, 2000.
- [124] TIMOSHENKO, S. P. and GERE, J. M., *Theory of Elastic Stability*. New York: McGraw-Hill Book Company, 1961.
- [125] TRELOAR, L. R. G., “The elasticity of a network of long-chain molecules I,” *Transaction of Faraday Society*, vol. 39, pp. 36–41, 1943.
- [126] TRELOAR, L. R. G., “The elasticity of a network of long-chain molecules II,” *Transaction of Faraday Society*, vol. 39, no. 7, pp. 241–246, 1943.
- [127] TRELOAR, L. R. G., “Stress-strain data for vulcanized rubber under various types of deformation,” *Transaction of Faraday Society*, vol. 40, no. 9, pp. 59–70, 1944.
- [128] VALANIS, K. C., “A theory of viscoplasticity without a yield surface: Part I, general theory,” *Archives of Mechanics*, vol. 23, pp. 517–533, 1971.
- [129] VALANIS, K. C. and LANDEL, R. F., “The strain-energy function of a hyperelastic material in terms of the extension ratios,” *Journal of Applied Physics*, vol. 38, no. 7, pp. 2997–3002, 1967.

- [130] WANG, M. C. and GUTH, E., “Statistical theory of networks of non-gaussian flexible chains,” *The Journal of Chemical Physics*, vol. 20, no. 7, pp. 1144–1157, 1952.
- [131] XIAO, H. and CHEN, L. S., “Hencky’s elasticity model and linear stress-strain relations in isotropic finite hyperelasticity,” *Acta Mechanica*, vol. 157, pp. 51–60, 2002.
- [132] YEOH, O. H., “Characterization of elastic properties of carbon-black filled rubber vulcanites,” *Rubber Chemistry and Technology*, vol. 4, no. 2, pp. 792–805, 1990.
- [133] YEOH, O. H., “Some forms of the strain energy function for rubber,” *Rubber Chemistry and Technology*, vol. 66, no. 5, pp. 754–771, 1993.
- [134] YEOH, O. H. and FLEMING, P. D., “A new attempt to reconcile the statistical and phenomenological theories of rubber elasticity,” *Journal of Polymer Science Part B: Polymer Physics*, vol. 35, no. 12, pp. 1919–1931, 1997.